Contribution to the study of electromagnetic gears for renewable energy applications

Haidar Diab

Normandie Université

THÈSE

Pour obtenir le diplôme de doctorat

Spécialité GENIE ELECTRIQUE

Préparée au sein de l'Université Le Havre Normandie

Contribution à l'étude des engrenages électromagnétiques pour les applications énergies renouvelables

Présentée et soutenue par
HAIDAR DIAB

Thèse soutenue le 07/11/2022 devant le jury composé de		
MME ELENA LOMONOVA	PROFESSOR, EINDHOVEN UNIVERSITY OF TECHNOLOGY	Rapporteur du jury
M. SMAIL MEZANI	MAÎTRE DE CONFERENCES (HDR), UNIVERSITE DE LORRAINE	Rapporteur du jury
M. MAZEN GHANDOUR	DOCTEUR, UNIVERSITE LIBANAISE	Membre du jury
M. JEAN LEBESNERAIS	PRESIDENT, EOMYS ENGINEERING	Membre du jury
M. CHRISTOPHE ESPANET	PROFESSEUR DES UNIVERSITES, UNIVERSITE DE FRANCHE-COMTE	Président du jury
M. YACINE AMARA	PROFESSEUR DES UNIVERSITES, Université Le Havre Normandie	Directeur de thèse
M. GEORGES BARAKAT	PROFESSEUR DES UNIVERSITES, Université Le Havre Normandie	Co-directeur de thèse

Thèse dirigée par YACINE AMARA (Groupe de Recherche en Electrotechnique et Automatique du Havre) et GEORGES BARAKAT (Groupe de Recherche en Electrotechnique et Automatique du Havre)

UNIVERSITÉ LE HAVRE NORMANDIE

ED 591 PSIME

GREAH

ACKNOWLEDGEMENTS

The research presented in this dissertation was conducted at GREAH laboratory, part of the University of Le Havre Normandy. It has been fully funded by the region of Normandy.

I would like first to thank Prof. Christophe Espanet, professor at University of Franche-Comté, and scientific director at Sonceboz Group for accepting to examine this work and chair the jury of the thesis. Also, I am delighted to have Prof. Elena Lomonova, professor at Eindhoven University of Technology, and Dr. HDR Smaïl Mezani, researcher and lecturer at University of Lorraine, as thesis jury participants, and I would like to thank them for taking the time to examine my work and report on it. Additionally, I am honored that Dr. Jean Lebesnerais, CEO of EOMYS Engineering, and Prof. Mazen Ghandour, professor at the Lebanese University, accepted the invitation to take part and participate in the thesis jury.

I want to express my sincere appreciation to my supervisor Prof. Yacine Amara who guided me during my three years of PhD. His trust and belief empowered me throughout this journey. In addition, his knowledge, expertise, and comprehension paved my way and helped me stay on the right direction.

Besides, I was very honored to have Prof. Georges Barakat, the director of GREAH group, as my co-supervisor. He accompanied me not only during my PhD studies but also throughout my MSc research training. Having someone like him with experience and deep knowledge has always kept me motivated and helped me in observing new perspectives.

Then, I would like to thank my laboratory colleagues and friends for the nice opportunity of having them as part of the GREAH family. My appreciation also goes to the GREAH laboratory staff and members, and to the university and doctoral school administration staff.

Finally, I would like to thank my family and friends for their comprehension and continuous support through all the times.

CONTRIBUTIONS

Journal Papers:

H. Diab, Y. Amara, G. Barakat and M. Ghandour, "Translator Eccentricity Analysis in Tubular Linear Machines Using Quasi-3-D Finite Element Method Modeling," in IEEE Transactions on Magnetics, vol. 58, no. 2, pp. 1-5, Feb. 2022, Art no. 8101105.

H. Diab, Y. Amara, and G. Barakat, "Open Circuit Performance of Axial Air Gap Flux Switching Permanent Magnet Synchronous Machine for Wind Energy Conversion: Modeling and Experimental Study," Energies, vol. 13, no. 4, p. 912, Feb. 2020.

H. Diab, Y. Amara, S. Hlioui, and J. J. H. Paulides, "Design and Realization of a Hybrid Excited Flux Switching Vernier Machine for Renewable Energy Conversion," Energies, vol. 14, no. 19, p. 6060, Sep. 2021.

Conference Presentations:

H. Diab, Y. Amara and G. Barakat, "Comparison of Two Tubular Linear Permanent Magnet Machines with Translator Eccentricity," 2020 International Conference on Electrical Machines (ICEM), 2020, pp. 612-618.

H. Diab, Y. Amara and G. Barakat, "Translator Eccentricity Analysis in Tubular Linear Machines using Quasi-3D Finite Element Method Modeling," INTERMAG 2021, 2021, Underline Science Inc. doi: 10.48448/55vc-6n77.

H. Diab, Y. Amara and G. Barakat, "3D Permeance Network Modeling for an Axial Field Flux Focusing Magnetic Gear," 15th Joint MMM-INTERMAG Conference, Jan. 2022. doi: 10.48448/SJMM-WH69.

H. Diab, Y. Amara and G. Barakat, "A 3D Nonlinear Magnetic Equivalent Circuit Model for an Axial Field Flux Focusing Magnetic Gear: Comparison of Fixed-Point and Newton-Raphson Methods," 14th International Conference of TC-Electrimacs Committee (Electrimacs), Nancy, France, May 2022.

H. Diab, Y. Amara and G. Barakat, " End-Effects Modeling in an Axial Field Flux Focusing Magnetic Gear using a Quasi-3D Reluctance Network Model," 2022 International Conference on Electrical Machines (ICEM), September 2022.

H. L. Ali, H. Diab and Y. Amara, "Study of Eccentricity in a Tubular Linear Flux Switching Machine Using 3D Finite Element Analysis," 2021 13th International Symposium on Linear Drives for Industry Applications (LDIA), 2021, pp. 1-6.

H. Diab and Y. Amara, "Mechanical Construction and Bearing Function Integration in Tubular Linear Flux Switching Machines," 2021 13th International Symposium on Linear Drives for Industry Applications (LDIA), 2021, pp. 1-6.

H. Diab, A. Bensalah, M. Hatoum, Y. Amara, and G. Barakat, "Etat de l'art des convertisseurs électromécaniques pour les énergies marines renouvelables," SYMPOSIUM DE GENIE ELECTRIQUE (SGE), Nantes, 2020.

H. Diab, S. Asfirane, and Y. Amara, "Power capability of shifted inductances axes permanent magnet machines," presented at the 2022 Joint MMM-INTERMAG, Dec. 2021. doi: 10.48448/14PD-4Z92.

H. Diab, S. Asfirane, Y. Amara, H. Ben Ahmed, and M. Gabsi, "Efficiency maps of synchronous machines based on electrical circuits modelling," presented at the 14th International Conference of TC-Electrimacs Committee, Nancy, France, May 2022.

Honorable mentions:

Won the ICEM Jan Melkebeek Best Poster Presentation Award for the work "End-Effects Modeling in an Axial Field Flux Focusing Magnetic Gear using a Quasi-3D Reluctance Network Model".

TABLE OF CONTENTS

ACKNOWLEDGEMENTS ..... **II**

CONTRIBUTIONS ..... **III**

TABLE OF CONTENTS ..... **V**

GLOSSARY ..... **VIII**

GENERAL INTRODUCTION ..... **IX**

CHAPTER I - MAGNETIC GEARS: AN OVERVIEW **1**

Introduction 1

1. Historical Background 1
2. Magnetic Gears: Motivation and Advantages 7
3. Principle of Operation of Magnetic Gears 11
4. Key Design Factors for Magnetic Gears 14
5. Magnetic Gear Types and Topologies 16

5.1. Coaxial Radial Field Magnetic Gears *18*

5.2. Coaxial Axial Field Magnetic Gears *23*

5.3. Transverse Flux Magnetic Gears *26*

5.4. Special Magnetic Gears *28*

5.5. Linear Magnetic Gears *30*

5.6. Magnetically Geared Machines *32*

6. Magnetic Gears Volumetric Torque Density Analysis 34

Conclusion 41

CHAPTER II - MAGNETIC EQUIVALENT CIRCUIT FOR MODELING MAGNETIC GEARS **42**

Introduction 42

1. Magnetic Materials 42

1.1. The B-H relationship *43*

1.2. Soft Magnetic Materials *46*

1.3. Hard Magnetic Materials *49*

2. Finite Element Method 53
3. Magnetic Equivalent Circuit 57

3.1. The Nodal Formulation *61*

3.2. The Mesh Formulation *63*

4. The Aspects of Implementing a 3D MEC 64
4.1. Non-Conformal Meshing and Motion Simulation 65
4.2. Choosing the 3D MEC Mesh Parameters 67
4.3. Maxwell Stress Tensor 69
4.4. Magnetic Saturation Consideration: Nonlinear Iterative Solvers 72
4.5. The End-Effects in Magnetic Gears 81
4.6. Numerical Aspects 82
5. Nonlinear 3D PN Modeling of an Axial Field Magnetic Gear 84
6. End-Effects Modeling in Magnetic Gears using 3D PN 92
6.1. Linear Case Results 94
6.2. Magnetic Saturation Case Results 97
6.3. Analysis and Discussion 99
7. Quasi-3D RN for Modeling the End-Effects in Axial Field MGs 104
Conclusion 110
CHAPTER III - MAGNETIC GEARS FOR MARINE RENEWABLE ENERGY 112
Introduction 112
1. An Overview on Marine Renewable Energy Conversion Systems 112
1.1. Tidal Stream Energy 113
1.2. Wave Energy 114
1.3. Tidal Impoundment Energy 115
1.4. Offshore Wind Energy 115
2. Applications of Magnetic Gears in Marine Renewable Energy 121
1.5. Rotational Radial Field Structures 122
1.6. Rotational Axial Field Structures 127
1.7. Tubular Linear Structures 128
3. Proposal of a MG for Marine Energy Conversion 130
Conclusion 139
CHAPTER IV - TRANSLATOR ECCENTRICITY IN TUBULAR LINEAR STRUCTURES 140
Introduction 140
1. Tubular Linear Machines and Eccentricity 140
2. Eccentricity Analysis in TLPM using 3D FEM 142
2.1. Open-Circuit Case 146
2.2. On-Load Case 149
2.3. Discussion and Comparison of the Results 151
3. Eccentricity Analysis in TLPM using Quasi-3D FEM 153
2.4. Modeling of Structure A 155
2.1. Modeling of Structure B 156

2.2. Discussion and Evaluation 161

4. Eccentricity Analysis in Tubular Linear Magnetic Gears..... 161

Conclusion 171

GENERAL CONCLUSION..... 172

REFERENCES..... 177

GLOSSARY

MG	Magnetic Gear
MMF	Magnetomotive Force
PM	Permanent Magnet
VTD	Volumetric Torque Density
MTD	Mass Torque Density
IPM	Interior Permanent Magnets
SMPM	Surface-Mounted Permanent Magnets
PDD	Pseudo-Direct Drive
MGM	Magnetically Geared Machine
FEM	Finite Element Method
MEC	Magnetic Equivalent Circuit
PN	Permeance Network
RN	Reluctance Network
MST	Maxwell Stress Tensor
AFFMG	Axial Field Flux Focusing Magnetic Gear
SMPMG	Axial Field Surface-Mounted PM Magnetic Gear
Q3D	Quasi-3D
DD	Direct Drive
PTO	Power Take-Off
O&M	Operation And Maintenance
PPR	Modulation Pole Pieces Rotor
TLPM	Tubular Linear Permanent Magnet Machines
EMF	Electromotive Force
TLMG	Tubular Linear Magnetic Gear
HSM	High Speed Mover
LSM	Low Speed Mover

GENERAL INTRODUCTION

Most mechanical applications rely on a gearing arrangement to transmit power from one shaft to another. The aim is usually to extract high speed from a low-speed application or obtain high torque from a low torque input. Mechanical gears and gearboxes are mostly used for this purpose and can be found in almost any mechanical application. Like other applications, energy conversion systems for renewable energy rely on mechanical gearboxes to transmit mechanical power to the electrical machine at higher speeds and to avoid having very large generators. The main issue and problem with mechanical gears is their low reliability and requirement for regular lubrication and maintenance, which increases the operation and maintenance costs for renewable energy applications especially those installed in remote locations like offshore wind sites. In addition, the low reliability of the mechanical gears would lead to possible failures and service interruptions of the energy conversion system. These problems that are associated with mechanical gears are mostly caused by the frictional forces, and this is where the search for frictionless alternatives started.

Since the beginning of the 20th century, electromagnetic devices called magnetic gears were proposed to transmit power between two ports through the frictionless interaction of magnetic forces. This idea didn't receive enough attention for a long time because of the poor torque capability of the proposed designs back then. Then, near the end of the 20th century, the development of the magnets and the appearance of strong rare-earth permanent magnets provided the magnetic gearing idea with huge potential, where suddenly magnetic gear designs with impressive torque densities comparable to those of mechanical gears appeared. Therefore, the development and research on magnetic gears have been ever rising and increasing for twenty years now. Meanwhile, renewable energy conversion systems found huge potential in the high torque density magnetic gears because on one hand magnetic gears are suitable for low-speed high torque applications, and on the other hand they could provide some remarkable advantages over mechanical gears that would improve the system's reliability and performance. Some of the potential advantages of using magnetic gears are reduced maintenance and increased reliability, possible isolation between input and output shafts, inherent overload protection, possibility of integration into electrical machines to provide a compact and high efficiency design. In the meantime, there is still a substantial room for improvements and contributions that can be added

to the development and research of magnetic gears. For example, the development of the methods and techniques that could be used for modeling magnetic gears is very important and interesting as modeling forms the foundation that directs any improvement or practical implementation of an application. Moreover, acquiring lightweight modeling tools that could provide good estimations for low computational cost is very important for any optimization problem where different parameters are varying.

Therefore, multiple objectives could be defined for this work which would serve as a contribution to the development of magnetic gears in specific and electromagnetic devices in general. First, laying out and analyzing the literature on magnetic gears to understand the current state of the technology. Second, the proposition and implementation of lightweight numerical modeling techniques that could be used to describe important physical aspects in magnetic gears. Then, briefly studying the literature on marine renewable energy as it stands as a very good potential candidate for magnetic gear application, and then attempting to propose a magnetic gear design that could be suitable for marine energy applications. Furthermore, analyzing the impact of a mechanical defect on the electromagnetic performance of tubular linear machines and magnetic gears, as this type of machines is being widely proposed and researched for the application in marine renewable energy like wave energy.

The first chapter will seek to provide an up-to-date overview of magnetic gears. It will begin with a historical overview of magnetic gears to demonstrate how this technology has developed through time. It will then explain the rationale and benefits of utilizing magnetic gears. After that, the operating concept of typical contemporary magnetic gears together with major design characteristics and terminologies will be discussed. Next, the various magnetic gear types and topologies will be presented which will serve as a presentation for the existing literature on magnetic gears as well as a showcase for the suggested new and old designs. Finally, the acquired data from the literature will be compiled and examined in order to summarize and draw some observations.

The purpose of the second chapter will be to describe and implement modeling approaches for magnetic gears, with a particular emphasis on modeling axial field magnetic gears. Its ultimate objective is to develop a modeling tool for early design phases that can account for the 3D characteristics of axial field magnetic gears while maintaining a quick calculation time. First, a quick introduction of the behaviors and classes of magnetic materials will be provided. Next, a theoretical presentation for the modeling approaches that will be employed will be done,

illustrating the implementation of the finite element method and presenting the formulations of the magnetic equivalent circuit method. The implementation details of the magnetic equivalent circuit approach are then detailed in numerous parts. Then, the provided modeling technique is assessed by evaluating and comparing its nonlinear solvers, where a comparison between the fixed-point and Newton-Raphson methods is done to assess the practicality and performance of each method when applied to magnetic equivalent circuit. Afterwards, the end-effects of axial field magnetic gears are investigated and modeled using a 3D magnetic equivalent circuit model, and two magnetic gear designs are compared. The chapter is then concluded with the presentation and evaluation of an alternate quasi-3D technique for simulating also the end-effects in axial field magnetic gears.

The next chapter begins with an introduction to marine renewable energy systems. First, diverse conversion technologies and energy sources will be discussed briefly, and offshore wind energy will be studied in more depth. The difficulties and requirements of offshore wind conversion systems will be investigated. Next, an overview of the uses of magnetic gears in maritime energy systems will be presented, including the implementations of magnetic gears and magnetically geared machines documented in the literature. Lastly, a parametric sweep analysis will be performed employing the modeling techniques given in the preceding chapter, with the objective of proposing an axial field magnetic gear design appropriate for deployment in a maritime renewable energy conversion system.

The final chapter will address the topic of eccentricity in tubular linear constructions. The eccentricity problem is first defined and described. Next, the 3D FEM model used for eccentricity impact analysis is explained. Then, two tubular linear permanent magnet machines with distinct architectures are evaluated and compared under varying eccentricity and operation circumstances. Next, a quasi-3D FEM modeling approach for assessing eccentricity in tubular linear machines will be presented and evaluated, and it will be applied to the previously mentioned structures and compared with the 3D FEM. Finally, to conclude the chapter, the eccentricity in two tubular linear magnetic gear systems will studied using 3D FEM.

Chapter I - Magnetic Gears: An Overview

Introduction

This chapter aims at providing a state-of-the-art presentation on magnetic gears. It will start by a historical background section on magnetic gears to discover how this technology evolved over the years. Then, it will go on with showing the motivation and advantages of using and developing magnetic gears. Afterwards, the principle of operation of the standard modern magnetic gears will be presented alongside some key design aspects and terms. Next, the different magnetic gear types and topologies will be presented which will serve as a presentation for the literature published on magnetic gears as well as a showcase for the new and old designs proposed. Finally, the data collected from the literature will be gathered and analyzed to summarize some key points and conclusions on magnetic gears.

1. Historical Background

In 1901, one of the first works about geared power transmission using electromagnetic forces was published as a patent by C. G. Armstrong [1]. The device, shown in Fig. I-1, represents the electromagnetic device proposed by Armstrong, and which he described as capable of transmitting rotary motion of a driving-wheel to a driven wheel through the effect of magnetic forces without actual contact of the wheels or without any mechanical wear or noises. The whole device resembles an electromagnetic frictionless analogy to the operation of mechanical spur gears. It used electromagnets to generate the magnetic field at the teeth of the driving-wheel which in turn will cause the ferromagnetic teeth on the driven wheel to interact with the induced electromagnetic forces and rotate. The device suffered from multiple issues, first the small contact area between the two wheels limited the torque capability and density of the device. Then, generating the required magnetic fields required a large current which reduced the total efficiency of the system. Hence, although this device was a breakthrough in terms of the advantages its frictionless power transmission could provide, it couldn't rival mechanical gears in terms of practicality and efficiency. A couple years later, A. H. Neuland patented another electromagnetic apparatus that may transfer power between two rotatable components rotating

at the same or different speeds and in the same or opposite directions [2]. Unlike the device proposed by Armstrong, this apparatus, shown in Fig. I-2, is composed of two rotating elements and a stationary member arranged between the surfaces of the rotating elements. The shafts of the elements are aligned together, and the coupling and interaction is done through the magnetic field generated by the electric current flowing through the coils wound around the teeth of the stationary member. The direction of the current in the coils is varied to obtain consecutive magnetic north and south poles. By changing the number of teeth on each element the rotating elements can be configured to rotate at the same speed or with different speed ratios.

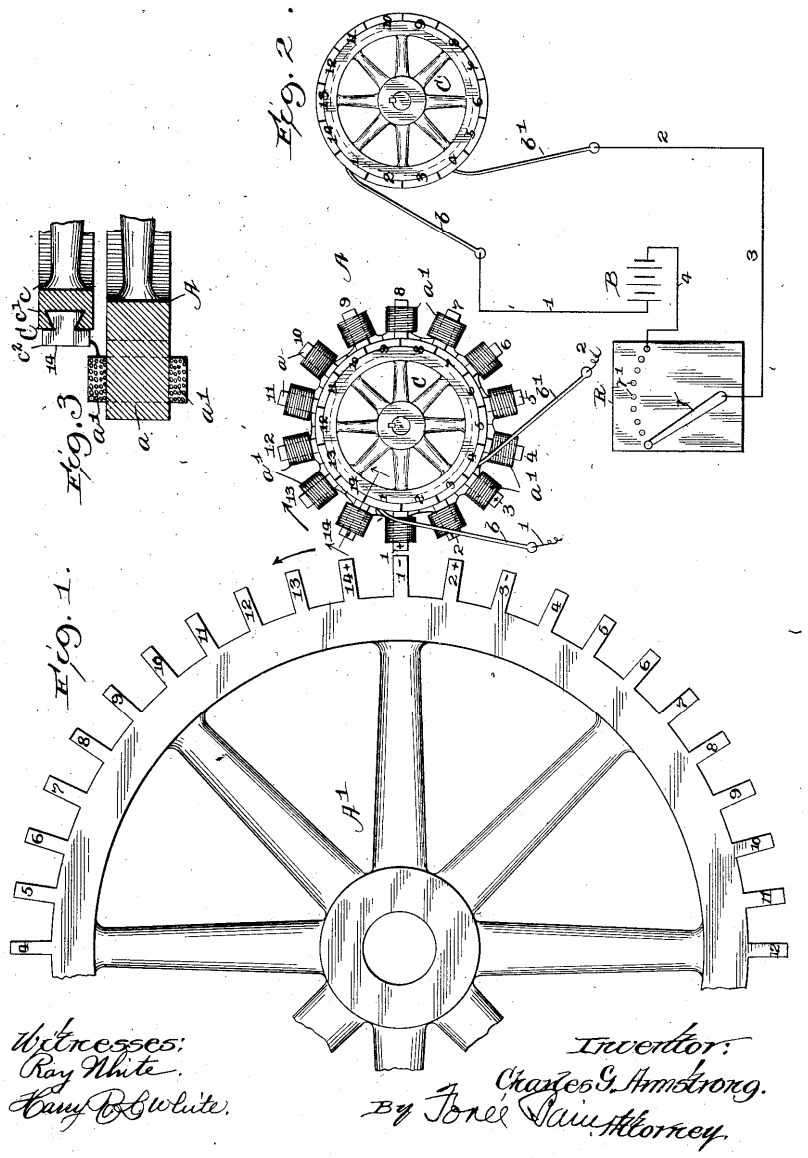

Fig. I-1 The electromagnetic device proposed by Armstrong in 1901 [1].

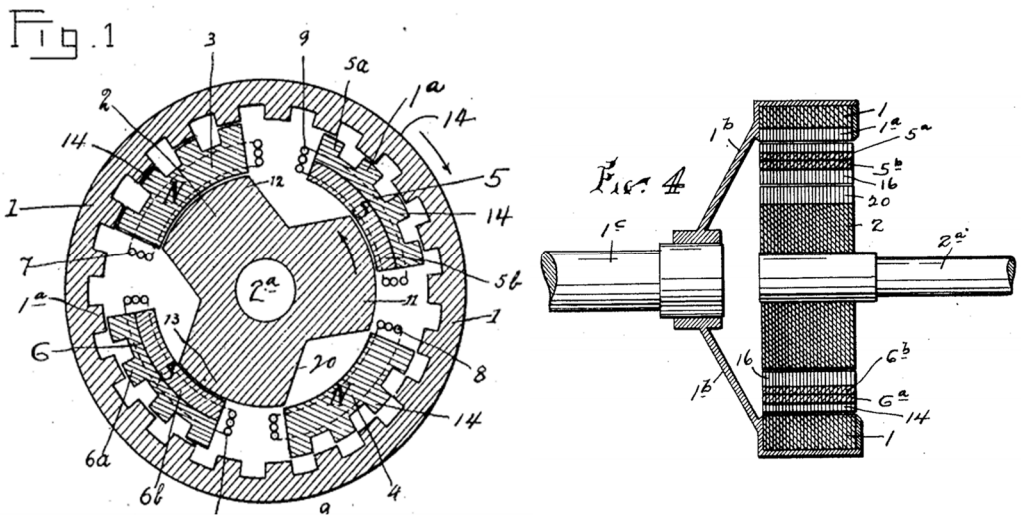

Fig. I-2 The electromagnetic apparatus proposed by Neuland in 1916 [2].

Thus, this device provided an advantage by utilizing the full contact surface between the elements improving the possibility of acquiring high torque densities, and its construction was compact and cheap. However, it still suffered from the issue of requiring large current values for higher powers, and the use of permanent magnets was possible but limited only to low power applications due to the low coercivity of the permanent magnets back then, so it still couldn't compete with mechanical gears. Many years later, the term "magnetic gearing" appeared, probably for the first time, in the patent established by G. A. Reese in 1967 [3]. It is based on the same principles operating the former devices presented but with a modified structure and arrangement. Again, the key advantages proposed were the frictionless and vibration free operation and the cheap manufacturing costs. As can be seen in Fig. I-3, the device is composed of three coaxial members a high-speed rotor, a low-speed rotor, and a fixed stator. Only the high-speed rotor contains magnetic flux sources which were realized using permanent magnets. In contrast to the design proposed by Neuland, the fixed member is now enclosing and surrounding the high and low speed rotors, and the magnetic flux source is on one of the rotors and not on the fixed member. This work also demonstrated the relationship between the number of teeth on each member and illustrated the magnetic gear behavior in torque overload situations. One year later, T. B. Martin established a patent on a magnetic transmission device [4] whose design could be considered as the closest to modern high-torque density magnetic gear designs.

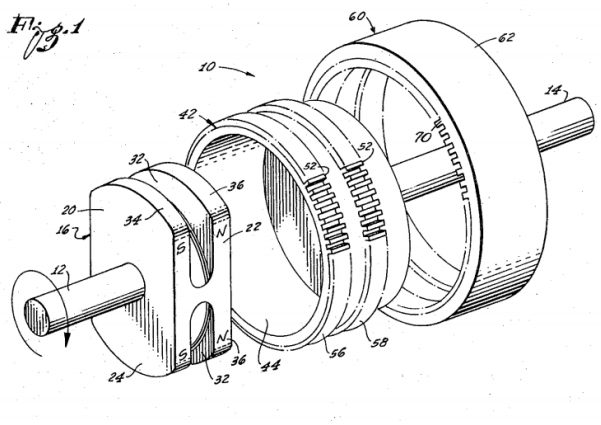

Fig. I-3 The magnetic gearing arrangement proposed by Reese in 1967 [3].

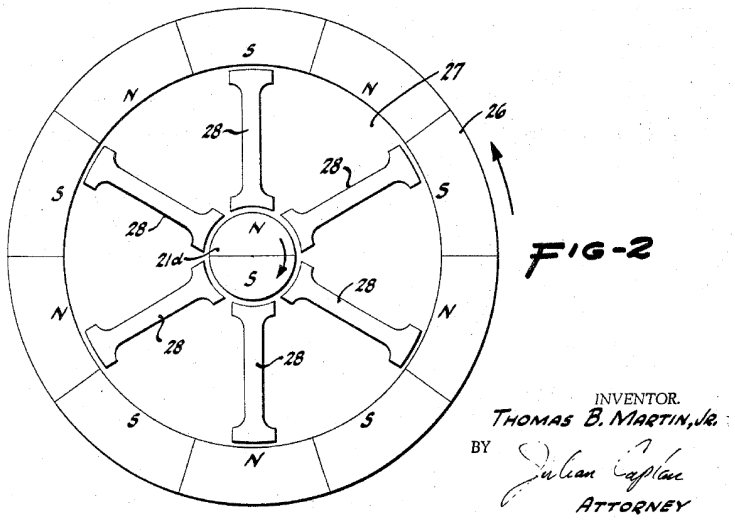

Fig. I-4 The magnetic transmission device proposed by Martin in 1968 [4].

The device illustrated in Fig. I-4 consisted of three coaxial members: an inner high-speed rotor with magnetic excitation; a middle structure that has fixed radially-directed, magnetically-permeable bar, having curved ends so that they are in close proximity to the rotors at the opposite ends; and an outer ring magnet with multiple north and south pole pairs considered as the low-speed rotor.

Some years later, the magnetic gearing concept started to gain rising interest, and multiple research papers started to emerge on the subject, each presenting a proposal on how magnetic gears should be operated and implemented. For example, in 1980 Hesmondhalgh proposed a

structure based on cascading multiple elementary magnetic gears [5].The multielement magnetic gear is shown in Fig. I-5, and the teeth of its adjacent elements are shifted by certain angle. This system was designed so that it doesn't have large changes of stored magnetic energy in the exciting coil if the inner and outer rotors are rotated at speeds inversely proportional to their numbers of teeth. The overall efficiency of the device wasn't satisfactory providing a total efficiency of 34% where the main reason for this was the core loss occurring at a very large volume in the device. Taking advantage of the advances in the permanent magnet technology, a new magnetic gear design using rare-earth magnets was proposed in [6]. The magnetic gear, shown in Fig. I-6, resembled an analogy to a mechanical internal gear set (gear and pinion) where magnetic interaction forces operated the device without direct contact between the pinion and gear.

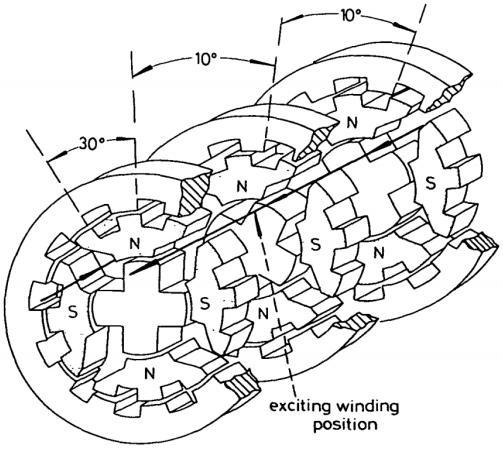

Fig. I-5 A multielement magnetic gear using three 4-pole elements [5].

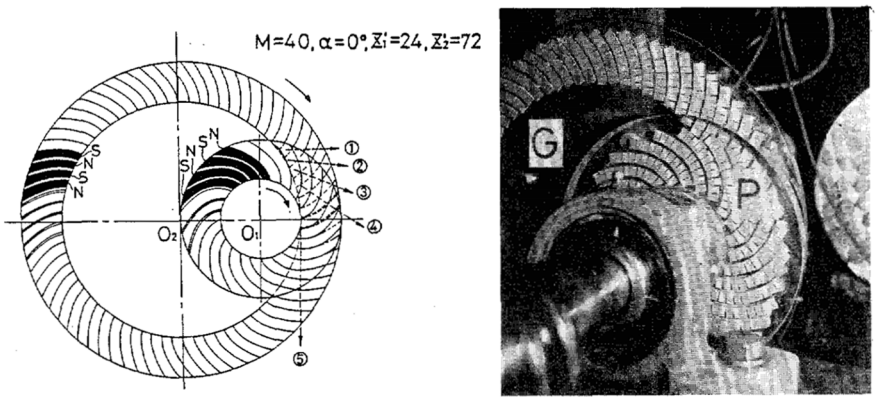

Fig. I-6 A new magnetic gear set (pinion and gear) using permanent magnets [6]

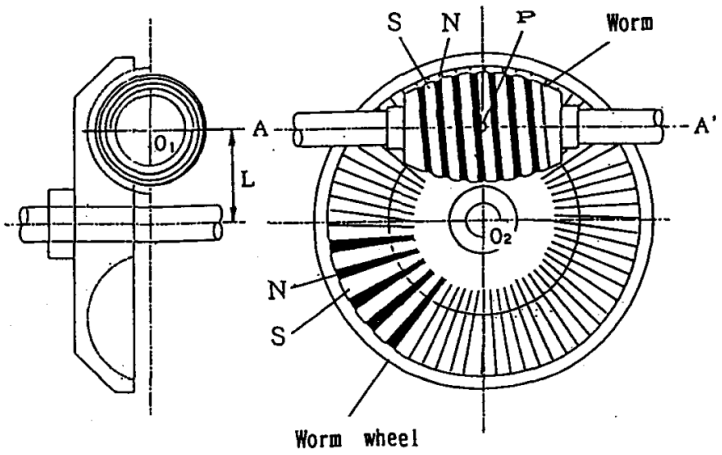

Fig. I-7 Configuration of the magnetic worm gear proposed in [7]

A rotary speed converter implemented in a small-scale application for a record player was proposed in [8]. The device used magnetic interaction forces and Samarium-Cobalt magnets to operate, but it suffered from durability and wear issues because direct contact through a thin rubber film was used to transfer motion. Another application for magnetic gears was proposed in [9] for a micro-transmission mechanism. This miniature device was deemed suitable for some medical and home robots where high-speed and precision are not important criteria, but highly safe, silent, and clean mechanisms are required, but it couldn't be used for industrial applications due to its low torque capability. A magnetic worm gear using permanent magnets [7] was proposed by Kikuchi (see Fig. I-7). Although the design used rare-earth magnets ($SmCo_5$), it had a low torque density due to the mechanical resonance of the gear and the poor mating between the worm and worm wheel. Finally, an improvement for the design proposed by T. Martin was patented by B. Ackermann and L. Honds in 1997 [10] (see Fig. I-8), and a variation of the design was provided by Ackermann in 1999 [11].

Essentially, all the designs that tried to mimic a certain mechanical gear type, by replacing the contact teeth with magnets, didn't succeed in competing with their mechanical counterparts in terms of torque density and efficiency. However, the potential advantages from the magnetic gearing concept remained highly anticipated and sought after until eventually more successful designs that could rival mechanical gears started to emerge. The key was in thinking about the design from an electromagnetic perspective, finding the best way to optimize the magnetic circuit, and taking full advantage of the magnetic components, rather than trying to mimic the operation and structure of mechanical gears.

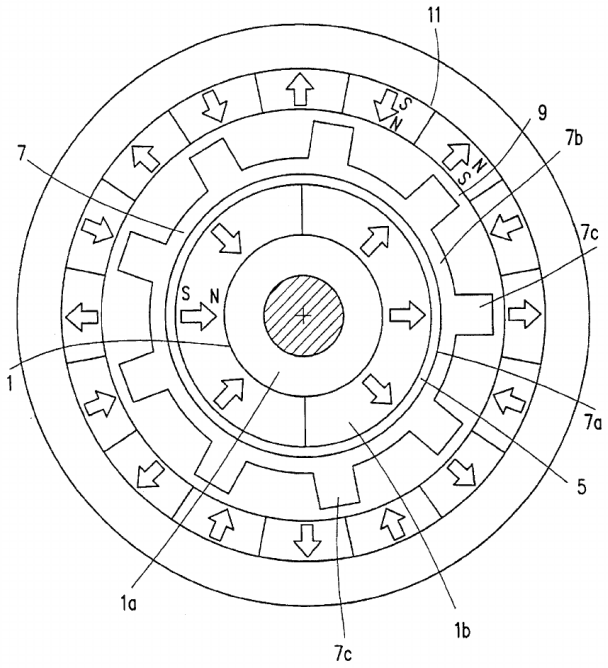

Fig. I-8 The magnetic drive arrangement proposed by Ackermann and Honds in 1997 [10].

Moreover, the advancement in the permanent magnet technology, manufacturing and machining technologies, and the introduction of rare-earth magnets with high coercivity and remanence, like the Neodymium magnet, all contributed to improving the performance of the magnetic gears and achieving high torque densities comparable to mechanical gears. This section tried listing some of the main contributions that paved the way to researchers working on this topic and laid the foundation to some works that came later and formed the cornerstone of the research in this domain.

2. Magnetic Gears: Motivation and Advantages

Gears are used to transmit power while increasing or decreasing the speed and decreasing or increasing the torque. Mechanical gears and gearboxes are very widely used and can be found in almost any mechanical application or device. The term "mechanical" is added to distinguish them from magnetic gears and to describe the nature of their operation, where it depends on the physical engagement of the gears' teeth in some sort of sliding contact. Precision machined teeth are required to provide a perfect fit, but even in the most expensive and well machined gears, the matching of the different teeth causes significant noise and vibrations in the driving

and driven parts. In addition, the gears will need to be lubricated and serviced on a regular basis and are vulnerable to wear and fatigue failure. Furthermore, when the mechanical gears are fully loaded, it has been shown to be difficult or impossible to release them from each other. Due to the fact that gears must be in direct contact, if the driven member experiences a significant overload or stall, then the whole system (including the gear train, load and/or motor) will be similarly over-loaded and/or stalled. In the worst-case scenario, this might cause irreparable damage to the system and/or the motor to explode. Moreover, high gear ratios can only be achieved by using a large number of gears or by using an elaborate gear system.

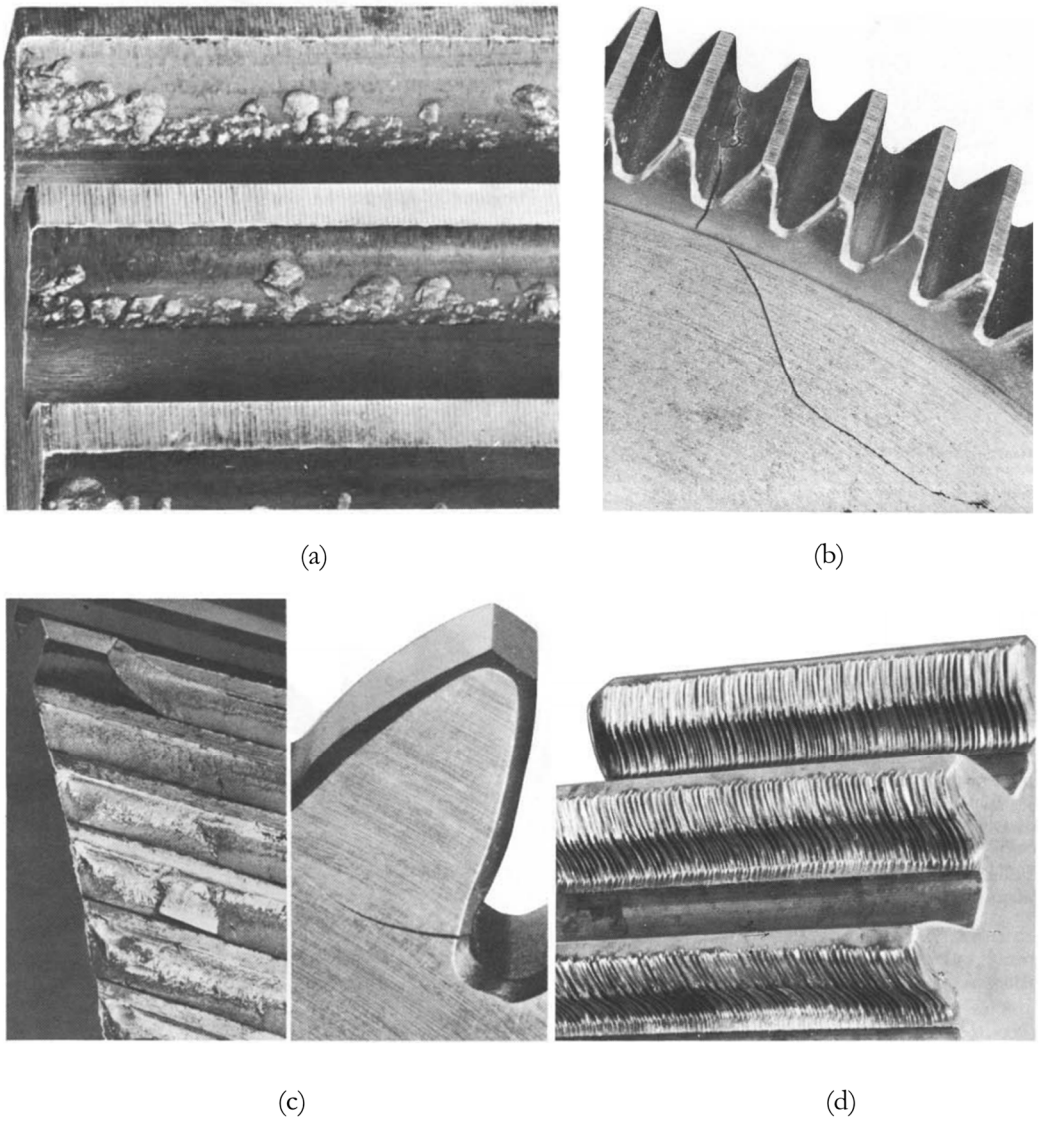

Fig. I-9 Some typical failure classes: (a) destructive pitting, (b) rim and web failure, (c) beam bending fatigue, and (d) abrasive wear [12].

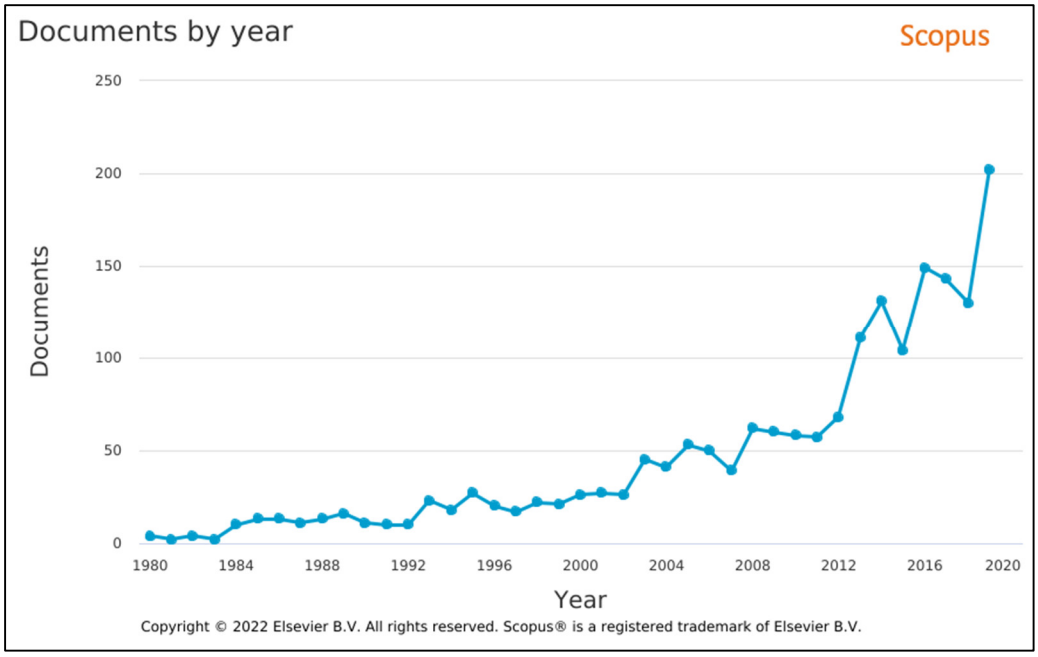

Fig. I-10 The evolution of the number of contributions on mechanical gear failures over the years.

Material-wise, steel's strength, durability, and cost efficiency make it the most used mechanical gear-making material. Carbon and alloy content affect steel hardness and hardenability. Heat-treat reaction and surface treatment affect a gear material's microstructure, wear, and fatigue. Gear performance relies on metallurgical variables, lubrication, contamination, misalignment, surface quality, machining damage, and severe loading or impact loading [13], [14]. Some of the classes and types of mechanical gear failures are wear, scuffing, hertzian fatigue, cracking, fracture, and bending fatigue [15]. All these failures could pose a hazard in safety critical applications and would, in best case scenarios, cause a service interruption in the system. Some mechanical gear failure types are summarized in Fig. I-9. Due to the importance and criticality of this issue, investigating mechanical gear failure causes and searching for methods to avoid them has been a research topic of rising interest for the past few decades. Fig. I-10 shows how the number of papers published about mechanical gear failures has been increasing throughout the past few decades.

All these issues drove researchers into searching for and an alternative to mechanical gears, and magnetic gears, with their contact-less power transmission, proved to be a very good candidate that could solve most of the problems encountered with mechanical gears.

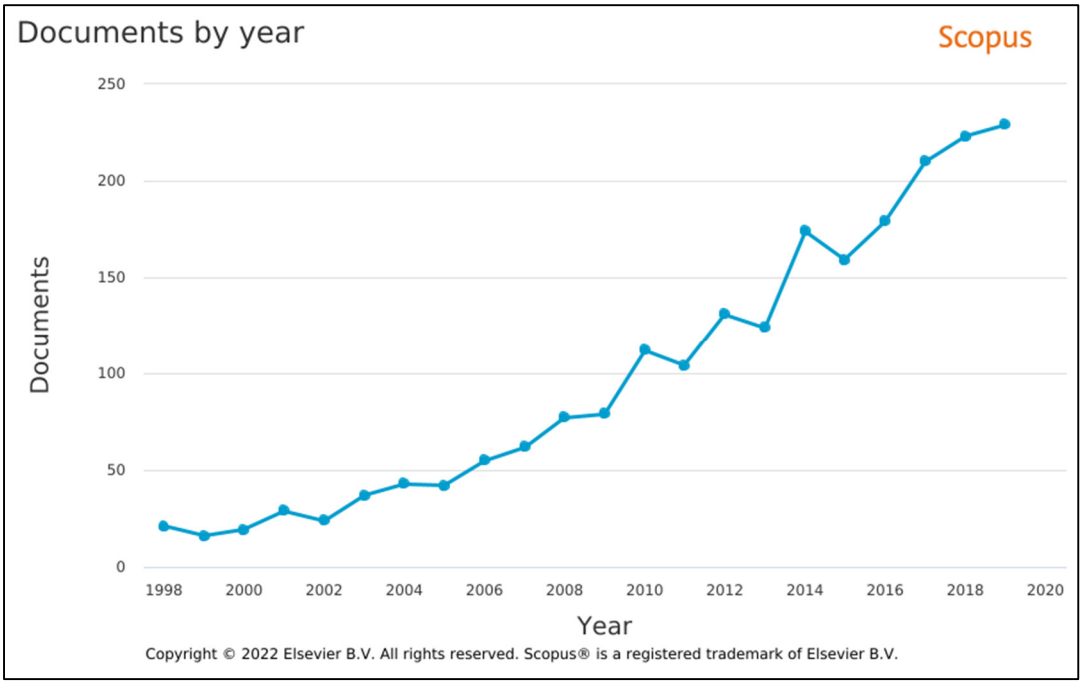

Fig. I-11 The variation of the number of contributions on magnetic gears over the past two decades.

Eventually, the interest in researching and developing magnetic gears increased through the past two decades (see Fig. I-11). A magnetic gear was found to be easier to manufacture, reliable, and less prone to failures. It may ensure a silent and vibration-free operation, and it could be arranged in a compact spatial configuration including axial and coaxial even while providing relatively high gear ratios. Another very important benefit of a magnetic gear is its inherent overload protection. It could be easily clutched and declutched even under full load, and during operation if the load torque exceeds a maximum torque value, the rotors will just slip and mitigate the damaging overload. In summary, some of the main advantages and features of magnetic gears are listed as follows:

- Silent noiseless running
- Vibration-less operation
- No need for oil or lubrication
- No backlash
- Can operate in harsh environments (better resistivity to water and dust)
- Robustness against large torque fluctuations
- Better overall reliability and reduced maintenance requirements

- Inherent overload protection and easy clutching/declutching
- Could be designed in a small and compact volume
- Could be embedded into electric machines or coupled to them

All these advantages and more are potentially obtainable by using a magnetic gear, but there are also a lot of challenges and difficulties to overcome in order to unlock the full potential of this device.

3. Principle of Operation of Magnetic Gears

In 2001, K. Atallah published one of most important and popular works on magnetic gears [16], and although the concept behind this work is not new, it was considered a breakthrough in this domain at that time. The main element that gave this work a great value was the remarkable torque density that was deemed achievable by the magnetic gear proposed (i.e., $100\ kNm/m^3$). In addition, this paper illustrated the fundamental equations to be used for determining the gear ratio and number of poles, and it introduced the concept of magnetic modulation through the ferromagnetic pieces as an essential factor to obtain a high-performance magnetic gear. Three years later Atallah established an extended version of his original work including a design study and experimental realization of the magnetic gear [17].

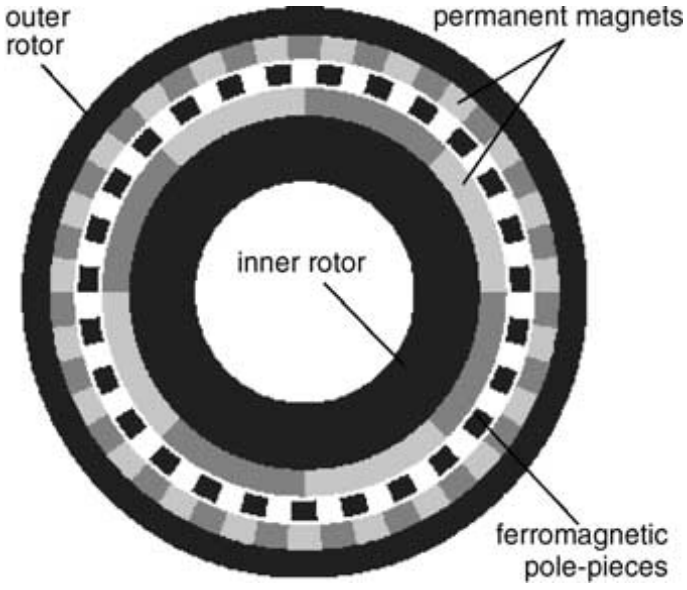

Fig. I-12 The high-performance magnetic gear proposed by K. Atallah [17].

The proposed magnetic gear, shown in Fig. I-12, is a coaxial magnetic gear with three main members or elements: an inner rotor, an intermediary member composed of ferromagnetic segments that will perform the job of magnetic modulation, and an outer rotor, where permanent magnets are mounted on the inner and outer rotors. The power is transmitted from the inner to the outer rotor at a different rotational speed and torque, whereas the member holding the ferromagnetic pieces is held fixed. In practice, depending on the application and the required gear ratio, the outer rotor could be held fixed, and the intermediary member can be rotated instead, so all three members can be practically called "rotors". The number of poles on each member should be chosen to properly match the appropriate space harmonics, and hence they are bound by a specific relationship and equation.

The modulation of the magnetic fields produced by each of the permanent magnet rotors is done through the ferromagnetic segments located in the intermediary member, and it is essential to obtain a high torque density and performance. In simple terms, it makes the interaction between the magnetic fields produced at the inner and outer rotors more efficient, and hence the modulating ferromagnetic pole-pieces became an indispensable part for the operation of any high-performance magnetic gear.

To properly choose the number of poles on each member in accordance with a relationship that will allow the gearing action to occur, a simplified expression of the magnetomotive force (MMF) produced by either permanent magnet rotor could be used. The MMF function of either permanent magnet rotor, which is a function of the angular position (θ), could be expressed in Fourier series. Then, using these expressions multiplied by the modulation function representing the ferromagnetic modulating pieces, one can determine the spatial harmonics of the MMF functions and their relative angular velocities. The space harmonics are split in two groups: a synchronous group having angular velocities same as the magnetic angular velocity of the rotor they belong to, and an asynchronous group with different angular velocities. Below are the equations expressed in Fourier series with F_I and F_O being the MMF forces produced by the inner and outer permanent magnet rotors respectively. The permeance change caused due to the presence of the modulating ferromagnetic pieces is represented through the function P_f.

$$F_I(\theta) = \sum_{m=1,3,5,\ldots,\infty} F_{I,m} \cos\left(m\, p_I(\theta - \omega_I\, t) + m\, p_I\, \theta_{0,I}\right) \tag{I-1}$$

$$F_O(\theta) = \sum_{n=1,3,5,\ldots,\infty} F_{O,n} \cos\left(n\, p_O(\theta - \omega_O\, t) + n\, p_O\, \theta_{0,O}\right) \tag{I-2}$$

$$P_f(\theta) = P_{f,0} + \sum_{k=1,2,3,\ldots,\infty} P_{f,k} \cos\left(k\, n_f\left(\theta - \omega_f\, t\right) + k\, n_f\, \theta_{0,f}\right) \tag{I-3}$$

The terms p_I and p_O represent the number of pole-pairs on the permanent magnet inner and outer rotors respectively, and n_f represents the number of ferromagnetic pole pieces of the intermediary member. The angular velocities (mechanical rotational speeds) ω_I, ω_O, and ω_f belong to the inner, outer, and modulating rotors respectively. After multiplying the MMF functions by the modulation function, a set of spatial asynchronous harmonics will appear, and to achieve the magnetic gearing, a set of synchronous spatial harmonics from the inner rotor should match a set of asynchronous spatial harmonics from the outer rotor, and similarly, a set of synchronous spatial harmonics from the outer rotor should match a set of asynchronous spatial harmonics from the inner rotor. The expressions of the spatial synchronous and asynchronous harmonics for the inner and outer rotors are summarized in Table I-1. Based on the harmonics' expressions and the required coupling between the inner and outer rotors, the equation relating the number of poles on each member could be seen in (I-4) , and similarly, an equation relating the angular velocities of the three members could be obtained (I-5). To reach the proper relationship, the harmonics indices should be substituted by the values that represent the fundamental asynchronous harmonic for both rotors (i.e., $m = 1, n = 1, \pm k = -1$). Hence, the resulting equations that relate the number of poles on each member and the angular velocities of each member are shown in (I-6) and (I-7) respectively.

$$n\, p_O = |m\, p_I \pm k\, n_f| \tag{I-4}$$

$$\left(m\, p_I \pm k\, n_f\right) \omega_O = m\, p_I\, \omega_I \pm k\, n_f\, \omega_f \tag{I-5}$$

Table I-1 Summary of the spatial synchronous and asynchronous harmonics from the MMF produced by the inner and outer rotors.

	Inner Rotor	**Outer Rotor**
Synchronous Spatial Harmonics	$m\, p_I$	$n\, p_O$
Asynchronous Spatial Harmonics	$\lvert m\, p_I \pm k\, n_f \rvert$	$\lvert n\, p_O \pm k\, n_f \rvert$

$$p_I + p_O = n_f \tag{I-6}$$

$$p_I\,\omega_I + p_O\,\omega_O = n_f\,\omega_f \tag{I-7}$$

Using the above equations and depending on which member is chosen as the fixed member, the gear ratio and direction of rotation of the elements could be determined. The three rotors could practically rotate at the same time resulting in what is called a magnetic continuously variable transmission device [18], [19], but for this work only two rotors will be rotating, and one will be fixed.

4. Key Design Factors for Magnetic Gears

Before classifying and identifying the different types and structures of magnetic gears, it is important to list some of the important factors and variables that are considered when designing or evaluating a magnetic gear:

- **Gear ratio** which is the quantity on which a magnetic gear design is based, and it is chosen to satisfy the torque/speed transformation requirements for the application in which the gear is being installed. It is the transformation ratio for the speed and torque between the input and output shafts and can be determined directly from (I-7). Depending on which rotor is chosen to be fixed, the gear ratio formula can have two forms:
  - If the ferromagnetic pole pieces rotor is fixed ($\omega_f = 0$):

$$G_{r1} = -\frac{p_O}{p_I}, \text{ with } \omega_I = G_{r1}\,\omega_O. \tag{I-8}$$

  - If the outer rotor holding the magnets is fixed ($\omega_O = 0$):

$$G_{r2} = \frac{n_f}{p_I}, \text{ with } \omega_I = G_{r2}\,\omega_f. \tag{I-9}$$

  It can be seen from the above equations that, for the same number of pole-pairs on all the rotors, a higher gear ratio could be achieved by fixing the outer rotor instead of the modulating rotor, but in this case more attention should be paid to the rigidity and stiffness of the ferromagnetic pieces structure since it will be rotating and transmitting torque. Also, for applications where the direction of rotation matters, it should be noted that the equation of G_{r1} contains a negative sign which signifies that the input and output shafts will rotate in opposite directions.

- **Cogging torque factor** which represents the influence of some design parameters on the cogging torque value and the torque ripple. It was first established by Z. Q. Zhu in [20] for permanent magnet machines, and according to them, the factor is used to indicate how good a combination of slot and pole numbers is from the perspective of cogging torque. In the same fashion, this factor could be used for magnetic gears to determine how good a combination of magnetic pole pairs (p_I) and ferromagnetic pole-pieces (n_f) will be from the point of view of cogging torque. The equation of the cogging torque factor is given by:

$$C_T = \frac{2\, p_I\, n_f}{LCM(2\, p_I, n_f)} \tag{I-10}$$

  From the above equation, it can be seen that the larger the least common multiple between the number of poles on the high-speed rotor (inner rotor) and the number of ferromagnetic pieces, and the smaller the number of poles, the smaller will be the amplitude of the cogging torque. In addition, the cogging torque factor doesn't change for the same gear ratio value. An ideal cogging torque factor would be 1, and hence, when choosing the number of poles or the gear ratio, minimizing the cogging torque factor should be an essential consideration. It is worth noting that to acquire a small cogging torque factor and to minimize the torque ripple, a rational non-integer gear ratio should be chosen for the system in a lot of situations, which could be challenging when modeling the magnetic gear because it might eliminate any possible symmetry or periodicity which will increase the total size of the model.
- **Stall torque** which represents the highest torque the low-speed rotor could withstand before slipping out of synchronization. Depending on which structure is chosen to be fixed, the low-speed rotor could be either the structure with the higher number of magnetic poles or the structure holding the ferromagnetic pole-pieces. This quantity is very important because it can help in evaluating the performance of the magnetic gear and determining its torque capability and density. It is also essential for the mechanical and structural study and design of the magnetic gear because the rotor should be mechanically structured and supported to bear the maximum torque value without any mechanical failure or deformation.
- **Torque density** is probably the most important quantity that is being used to evaluate the performance of a magnetic gear and its suitability for a certain application. It provides an insight on how effective a certain magnetic gear design is from the perspective of volume, materials used, or cost. In addition, it allows to perform a comparison with mechanical gears

and whether a magnetic gear can replace the mechanical gear installed in the application. There are two types of densities: volumetric torque density which is used more often, and the mass torque density. The volumetric torque density (VTD) depends on the stall torque value and the active region volume of the magnetic gear. Some references even suggest calculating two volumetric torque densities: one depends on the active region volume, and another depends on the total volume (including magnetically inactive components like bearings or housing). Throughout this work, and unless mentioned otherwise, the term volumetric torque density will refer to the torque density that depends on the active region volume. On the other hand, the mass torque density (MTD) depends on the stall torque and the active region mass. This leads to the equations below expressing the VTD and MTD:

$$VTD = \frac{Stall\ Torque}{Active\ Region\ Volume}\ [N \cdot m/L] \tag{I-11}$$

$$MTD = \frac{Stall\ Torque}{Active\ Region\ Mass}\ [N \cdot m/kg] \tag{I-12}$$

5. Magnetic Gear Types and Topologies

With the increasing research interest magnetic gears have gained over the past few decades, a variety of structures and types were proposed for different application. Some were conventional known structures and others tried to provide an innovative and new design, and the main goal was to always achieve the best and most efficient performance. There are a lot of criteria from which one can choose for the classification of magnetic gears, but there are no absolute rules for nomenclature, as different names or definitions might appear in different references. Multiple contributions could be found providing a literature overview on magnetic gears and listing the different types and structures [21]–[26]. Fig. I-13 list some criteria and types that could be used to identify and classify magnetic gears where any combination of the listed criteria could form a unique magnetic gear type or structure. Some might consider that the majority of rotational magnetic gears could be split into two main types: a radial field type (i.e., coaxial radial field structure), and an axial field type (i.e., coaxial discoidal structure).

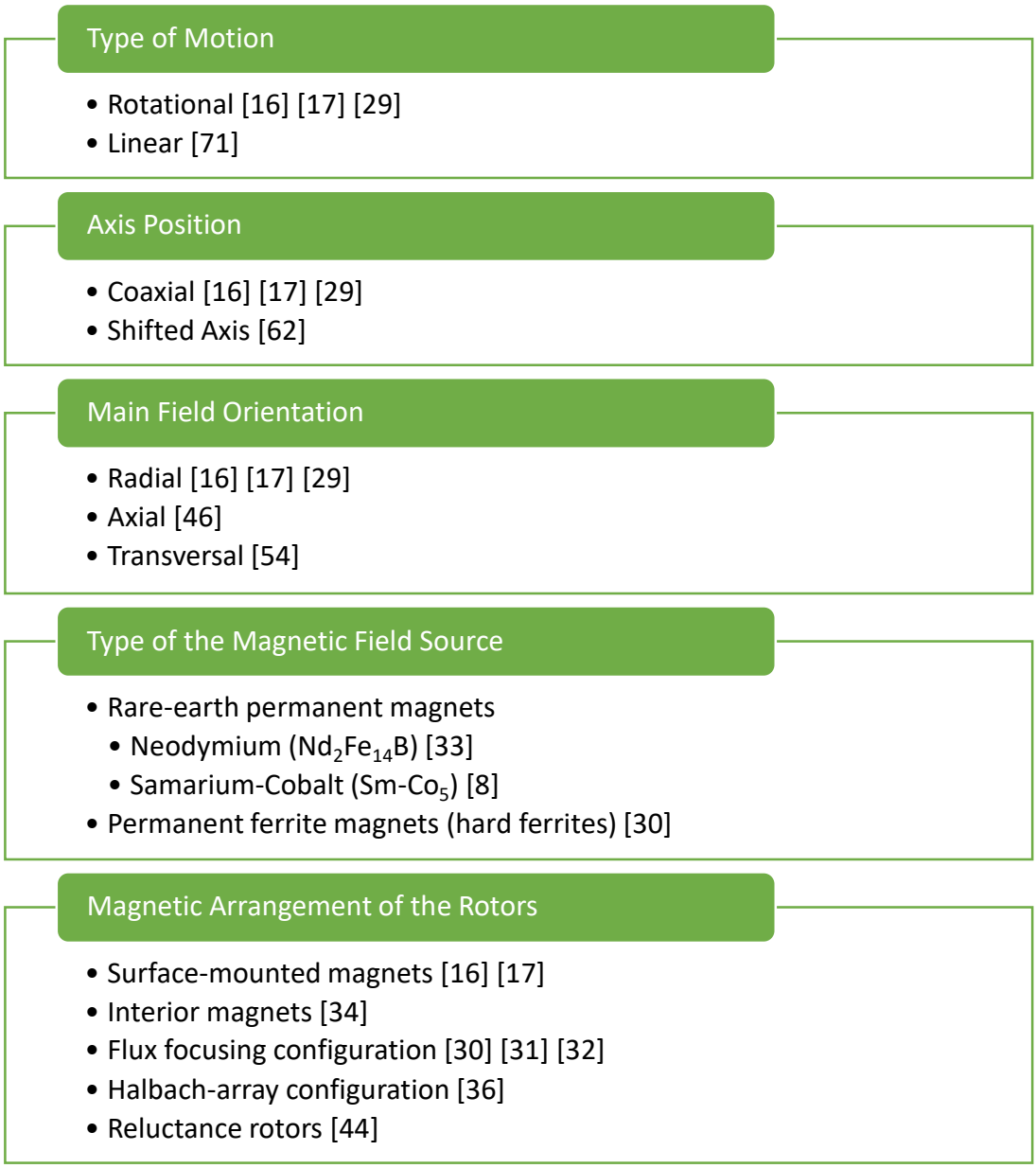

Fig. I-13 Main criteria used for classifying and identifying magnetic gears.

Moreover, if one wants to pick two main criteria to classify magnetic gears from the list shown in Fig. I-13 Main criteria used for classifying and identifying magnetic gears., they will probably choose the field orientation and the magnetic arrangement of the rotors. In the following sections, the main magnetic gear types and structures will be identified and presented, in addition to some special structures and types that could not clearly fit into a single category or scheme.

5.1. Coaxial Radial Field Magnetic Gears

The coaxial radial field structure is the most popular and used structure among magnetic gears as well as electric machines. The term "radial field" defines the magnetic flux main orientation which aligns with the radial direction with respect to the center of rotation of the device, and the term coaxial signifies that all the structures of the device share the same axis or center of rotation, and in the case of magnetic gears, the three rotors are aligned at single axis of rotation. One of the most popular contributions about magnetic gears, the high-performance magnetic gear that was presented in the "Principle of Operation of Magnetic Gears" section was a coaxial radial field magnetic gear with surface-mounted permanent magnet rotors [16], [17]. The surface-mounted PM rotors define the magnetic arrangement of the magnetized rotors, meaning that the permanent magnets are placed on top of the surface of the rotor back iron which is usually composed of a ferromagnetic lamination, and the polarities of the permanent magnets are alternating between north and south poles (see Fig. I-14). The same magnetic gear type but with a modified ferromagnetic pole-pieces shape was proposed in [27], [28]. The idea there was to add a supporting bridge for the ferromagnetic pieces and optimize their shape to achieve the desired performance (see Fig. I-15).

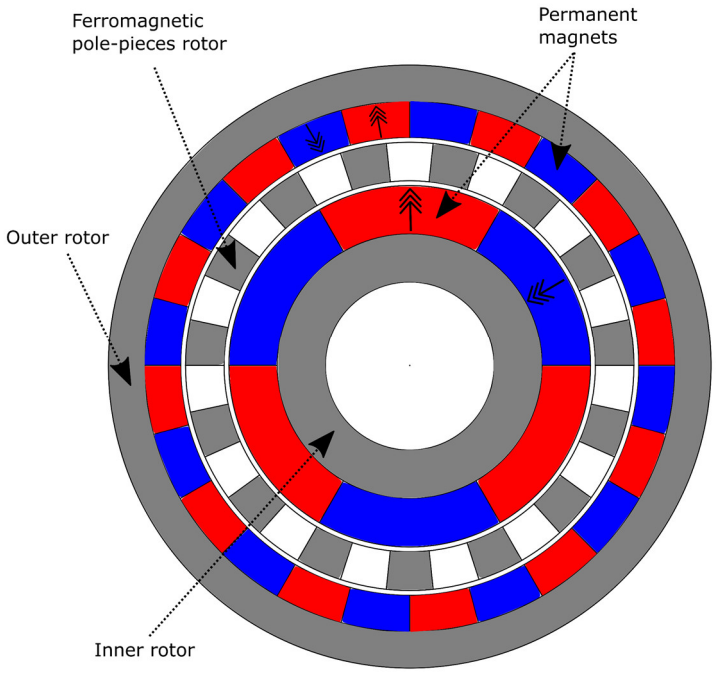

Fig. I-14 A coaxial radial field magnetic gear with surface-mounted permanent magnets.

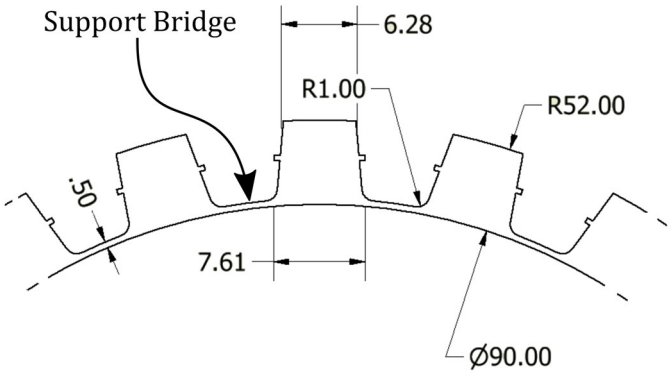

Fig. I-15 A cross-section of the modified ferromagnetic pole-pieces rotor with a support bridge [28].

It has been demonstrated that the support bridge would simplify the mechanical construction and eliminate some high-order unwanted harmonics. In fact, using the bridge is the most common practice to support the modulating pieces, but it might provide a leakage path for flux which would reduce the stall torque and affect the overall performance.

In one of the original publications about magnetic gears [29], the authors proposed a radial field structure with a spoke type flux focusing inner rotor and a surface-mounted PM outer rotor (see Fig. I-16). The simulation of the structure was very promising providing a volumetric torque density of $92\ N.m/L$, but the performance of the prototype was underwhelming due to end-effects and mechanical issues.

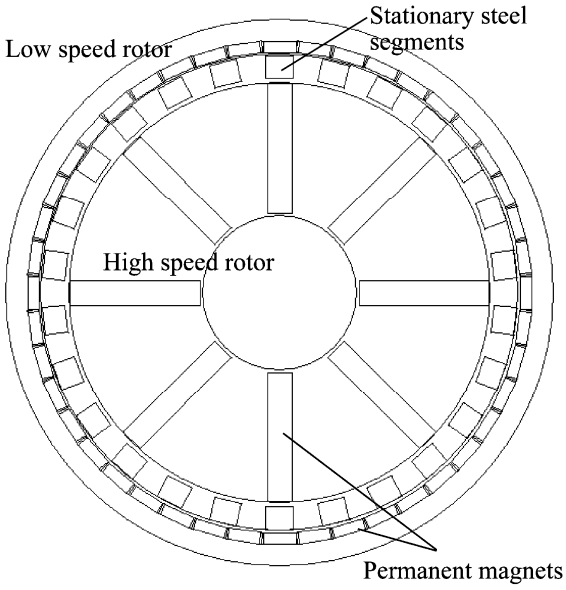

Fig. I-16 The spoke-type inner rotor coaxial radial field magnetic gear proposed in [29].

Similarly, a flux-focusing radial field magnetic gear (see Fig. I-17) was proposed and studied throughout multiple works testing different magnet types [30]–[32]. The works tested using ferrite magnets for cost reduction, neodymium magnets, and a hybrid combination of neodymium magnets on the inner rotor and ferrite magnets on the outer rotor. The predicted and experimentally verified VTDs of the magnetic gear using ferrite magnets only were $56\ N.m/L$ and $33\ N.m/L$ respectively. For the magnetic gear using the hybrid combination, the predicted and experimentally verified VTDs were $81\ N.m/L$ and $66.3\ N.m/L$ respectively. Finally, the magnetic gear using neodymium magnets only provided predicted and experimentally verified VTDs of $154\ N.m/L$ and $151.2\ Nm/L$ respectively. This illustrates the performance-boost acquired when using rare-earth magnets and highlights their importance for magnetic gears aiming to achieve high torque densities. Subsequently, after optimizing the design, shown in Fig. I-17, using a parametric sweep analysis and while using neodymium permanent magnets, the authors have managed to experimentally achieve an impressive VTD of $239\ N.m/L$, knowing that the predicted value through simulations was $245\ N.m/L$ [33].

A radial field design, shown in Fig. I-18, with interior PM inner rotor and surface-mounted PM outer rotor was proposed in [34]. The work also proposed three possible configurations for the ferromagnetic pole-pieces support bridge and compared between them. The experimental prototype for this design had a torque density of $42\ N.m/L$ while the calculated value was $66\ N.m/L$.

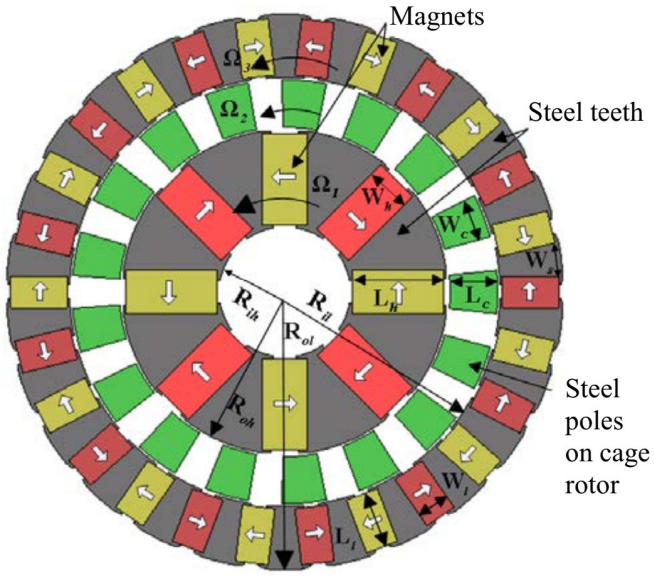

Fig. I-17 The flux-focusing radial field magnetic gear proposed in [30].

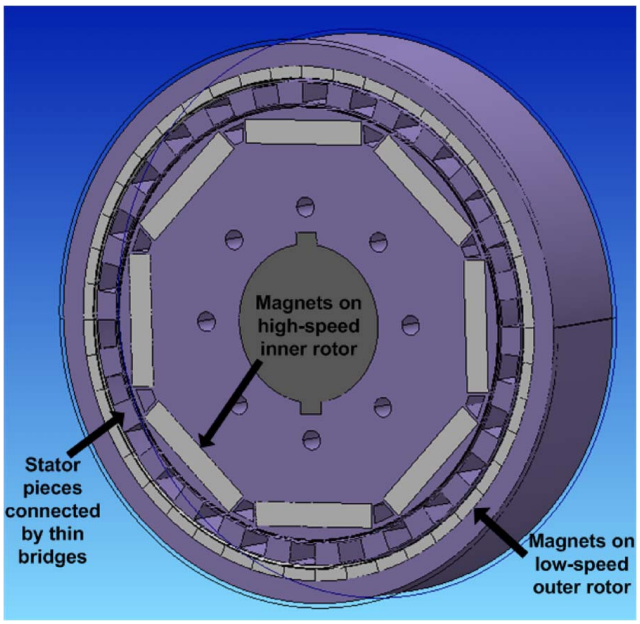

Fig. I-18 The interior permanent magnet radial field magnetic gear proposed in [34].

Another radial field interior PM magnetic gear was proposed in [35], but for this design the PMs on the outer rotor were interior and were surface mounted on the inner rotor (see Fig. I-19). Moreover, instead of the traditional alternating polarity, the permanent magnets on the outer rotor were homopolar. While the predicted VTD value of this design was $55.3\ N.m/L$, the reported experimental value was $53.3\ N.m/L$.

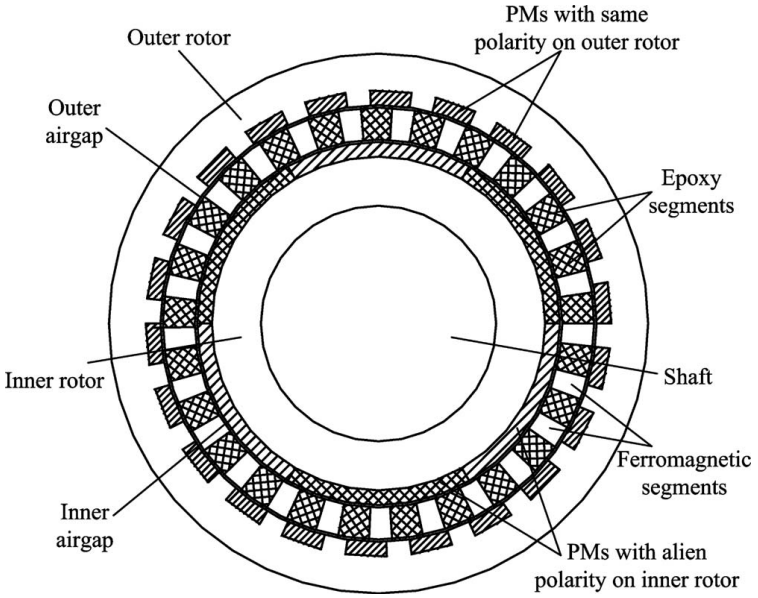

Fig. I-19 The interior PM outer rotor radial field homopolar magnetic gear proposed in [35].

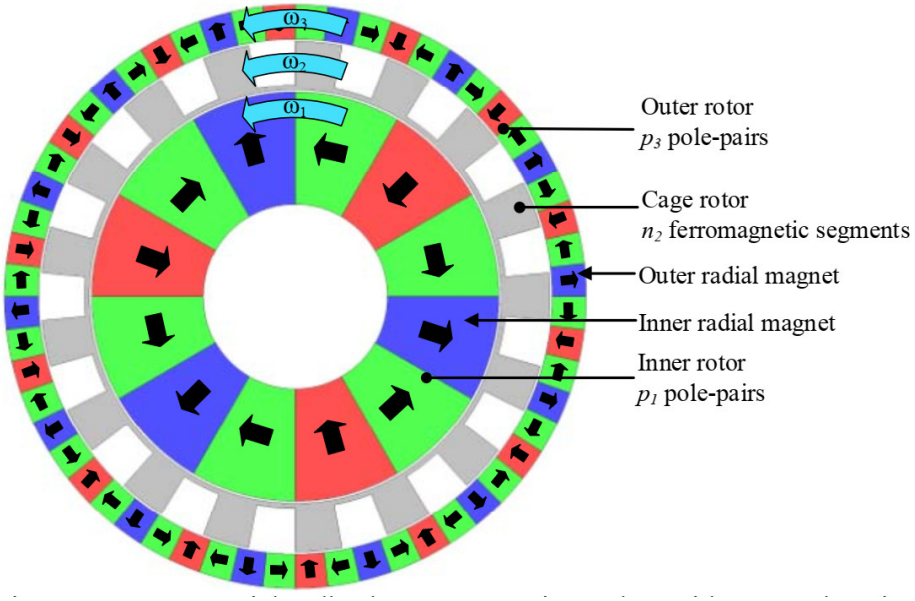

Fig. I-20 A coaxial radial field magnetic gear with Halbach array rotors [36].

An additional popular magnetic arrangement of the rotors is the Halbach array configuration. A coaxial radial field magnetic gear using neodymium Halbach array permanent magnets was proposed in [36] (see Fig. I-20). The design was computed to obtain a VTD of $284\ N.m/L$ using just a 120mm outside diameter for the active region, and the experimental prototype achieved a VTD of $261.4\ N.m/L$. More studies and works on radial field coaxial magnetic gears using Halbach array could be found in [37]–[43].

For high-speed applications, reluctance type magnetic gears are proposed where the inner rotor is completely passive, and the permanent magnets only exist on the outer rotor. In [44], the authors proposed such a design (see Fig. I-21), but it suffered from a very low torque density both through simulation and experimentally ($19.49\ N.m/L$ and $12.66\ N.m/L$ respectively). Nevertheless, the advantages shown for this design were the ability to operate in high-speed region due to the simplicity and robustness of the inner rotor, and, in comparison with the surface-mounted PM magnetic gear, the reluctance design have shown higher efficiencies in the high-speed region.

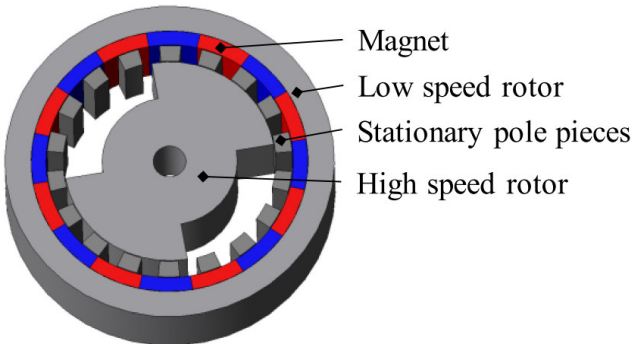

Fig. I-21 The reluctance type coaxial magnetic gear proposed in [44].

5.2. Coaxial Axial Field Magnetic Gears

The axial field topology has gained significant research interest in the domain of electric machines in the past few decades. This topology could be also applied to magnetic gears, and, eventually, works have been established on studying axial field magnetic gears and their performance. There are multiple advantages and situations that could make the axial field structure more favorable than the radial field one. For example, in applications where spatial restrictions limit the stack length of the device but allow radial expansion, axial field structures could be a perfect fit, and this discoidal structure could facilitate the implementation of multi-stage systems. In addition, they could be very suitable for systems that require isolation between the input and output shafts or where the mechanical power should be transmitted through a flat barrier. Despite all the mentioned advantages, the radial field topology might still be the more favorable in most applications due to the unbalanced axial forces that the axial field structure experience on each rotor. These forces could cause different mechanical problems and most of the times will lead to a non-uniform air gap between the rotors, so more consideration should be given to the rigidity and strength of an axial field structure which might increase the cost and complexity of the device. An interesting study comparing axial and radial field surface-mounted PM magnetic gears could be found in [45].

One of the first contributions about axial field magnetic gears was the work established by S. Mezani in 2006 [46]. The proposed design was an axial field surface-mounted PM magnetic gear utilizing neodymium magnets (see Fig. I-22). After performing a basic optimization study, the calculated VTD of the structure with the optimal parameters was shown to be around $70\ N.m/L$, and the calculated axial forces on the rotors were shown to be relatively small.

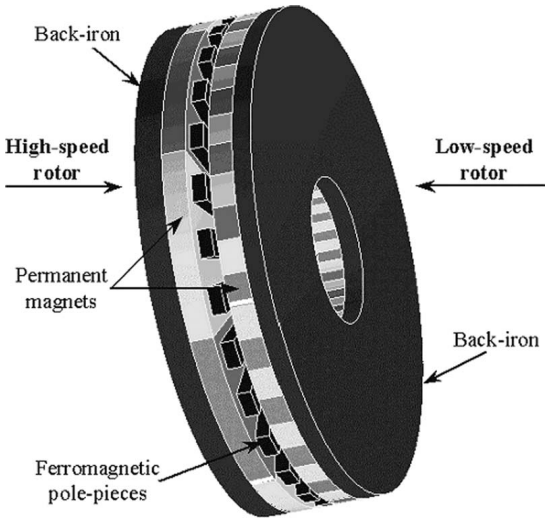

Fig. I-22 The high-performance axial field magnetic gear proposed in [46].

A flux focusing axial field magnetic gear was proposed in [47]. The study proposed using ferrite magnets and included only simulation results (see Fig. I-23). The study performed a parametric sweep analysis to determine the values that maximize the torque densities, and the calculated VTD of the final design was $65\ N.m/L$. In the same work, the calculated VTD of a surface-mounted PM axial field magnetic gear with similar size and properties was $41\ N.m/L$ which highlights the advantage of using the flux focusing configuration especially when using ferrite magnets. Another study by the same team was proposed in [48], where it kept the same configuration and used neodymium magnets instead of ferrite. The design parameters were optimized to obtain minimal torque ripple and high torque density, where the calculated VTD of the final design was $257.6\ N.m/L$. Afterwards, the team finally realized an experimental setup for their design and presented it in [49]. The design was meant for an ocean generator application, and it was experimentally verified that it could achieve a VTD of $152.3\ N.m/L$ knowing that the simulated value was $173\ N.m/L$.

Likewise, an axial field surface-mounted PM magnetic gear was designed and experimentally realized in [50]. According to the authors, this work presented the first known experimental prototype of an axial field magnetic gear and during the design phase they faced a lot of challenges to make the construction feasible, so they had to consider some design choices that weren't necessarily optimal for obtaining a high torque density like having an air gap of 5 mm.

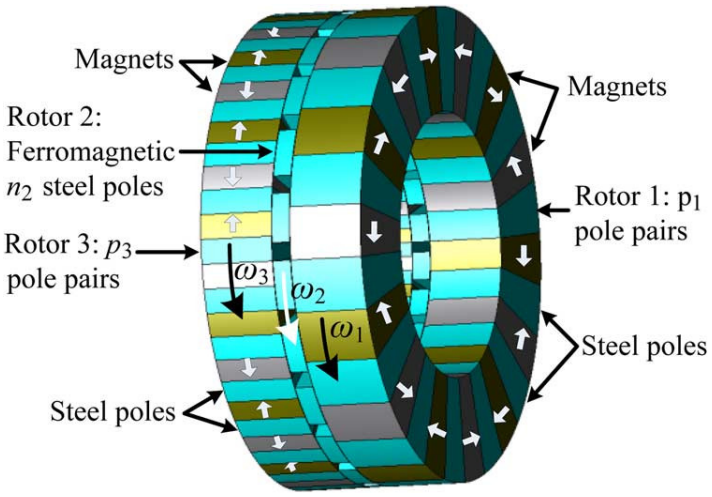

Fig. I-23 The axial field flux focusing magnetic gear proposed in [47].

Eventually, the calculated and experimentally reported VTDs from the magnetic gear in [50] were $21.1\ N.m/L$ and $22.4\ N.m/L$. Subsequently, the same team proposed an axial field magnetic gear with Halbach array rotors in [51]. The work included an analysis study, where multiple advantages of using Halbach array were demonstrated like decreasing iron losses and lowering the torque ripple. It was shown also that using the Halbach array could increase the torque density of the structure. For example, for a gear ration of 4.14, the calculated VTD increased from $128\ Nm/L$ to $183.9\ Nm/L$ when using Halbach arrays on both rotors.

Furthermore, an interesting new design of an axial field flux focusing magnetic gear with L-shaped ferromagnetic pieces was proposed in [52]. The unique L shape of the ferromagnetic pieces was suggested to reduce the flux leakage (see Fig. I-24). However, this design might not be easy to fabricate using traditional techniques, so the 3D printing was proposed to overcome this difficulty. Nevertheless, the authors still faced difficulties when making the prototype, and its performance at the end turned out to be very underwhelming. The authors reported that the 3D-printed design might not also withstand high axial attraction forces. Finally, it was reported that the calculated VTD of the design using neodymium magnets was $74\ N.m/L$, but the prototype, which used ferrite magnets, achieved a torque density of $2\ N.m/L$ only.

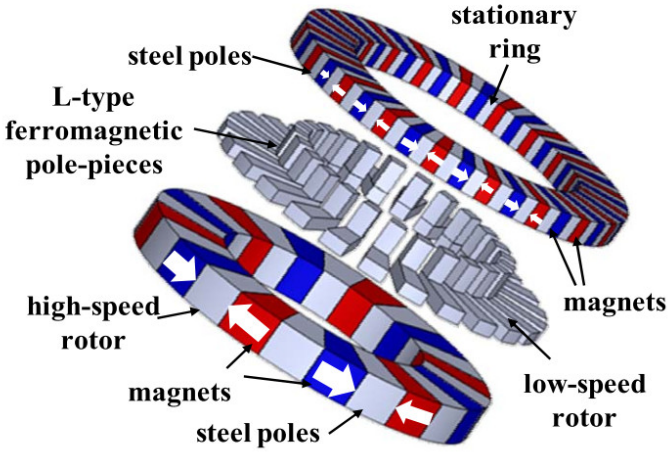

Fig. I-24 The axial field flux focusing magnetic gear with L-shaped ferromagnetic pieces [52].

5.3. Transverse Flux Magnetic Gears

Despite the potential that the transverse flux MG might hold, it is still one of the immature types that not a lot of research has been put into it and still requires much more investigation. The potential mainly lies around obtaining higher torque densities similar to transverse flux motors that were shown to have the potential for significantly higher torque densities than their radial counterparts [53]. A transverse flux magnetic gear enables the 3D circulation of magnetic flux which necessitates the use of 3D modeling techniques to study and analyze the structure[54]–[57]. In [58], the analysis of a flux focusing transverse flux magnetic gear was done (see Fig. I-25). After properly sizing the structure and optimizing the parameters, the calculated VTD was $20.2\ N.m/L$ when using ferrite magnets and $80.6\ N.m/L$ when using neodymium magnets. In comparison with a radial field magnetic gear, the VTD of the transverse flux design was much lower. Afterwards, an experimental prototype of a transverse flux magnetic gear was presented in [59]. This prototype was based on the original design shown in [60] which used surface-mounted PM rotors (see Fig. I-26). The work suggested using neodymium magnets and implemented an instrumentation setup to measure the electromotive force induced in the ferromagnetic pole-pieces. However, the measured VTD of the prototype was only $14.9\ N.m/L$, and it has been reported that large iron losses are occurring in the ferromagnetic segments independent of the load.

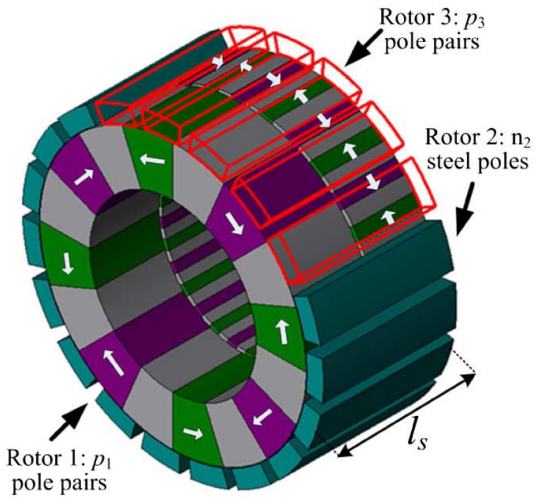

Fig. I-25 The transverse flux focusing magnetic gear from [58].

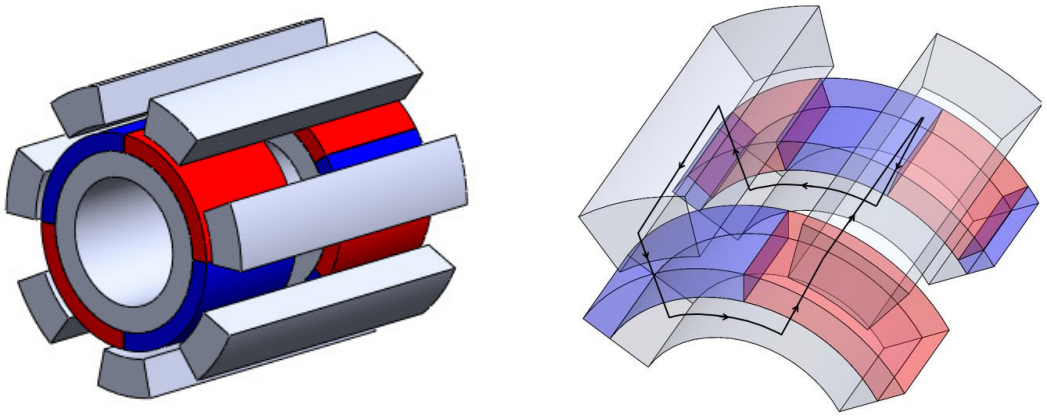

(a) (b)

Fig. I-26 The (a) transverse flux magnetic gear with (b) the 3D flow of its magnetic flux [59], [60].

A novel design which could be considered as a hybrid axial transverse flux type was proposed in [61]. The work discussed a flux focusing magnetic gear with special T-shaped ferromagnetic pole pieces (see Fig. I-27). It was shown that the special shape of the pole pieces reduced the saturation and flux leakage in the modulating rotor as compared to conventional axial field magnetic gears. In addition, it was demonstrated that the proposed design could achieve higher torque density than an axial field structure, where the calculated VTD using optimized parameters was evaluated at $282.5\ N.m/L$. However, it is yet to be proven how practical and plausible the fabrication of this design will be.

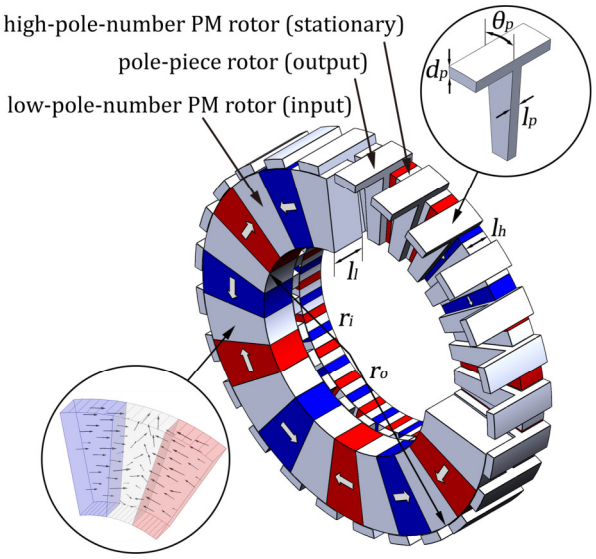

Fig. I-27 The axial transverse flux focusing magnetic gear with T-shaped pole pieces proposed in [61].

5.4. Special Magnetic Gears

This section is concerned with magnetic gears that don't clearly fit into any of the previous mentioned categories, and especially, MG topologies that try to imitate their mechanical counterparts. It has been shown that a lot of these implementations didn't succeed because of the poor utilization of the magnetic energy like the spur magnetic gear for example, but there are some topologies that were proven to have some great potential.

The planetary magnetic gear, shown in Fig. I-28, is one of the types that have shown some potential and are being studied. It consists of an outer rotor ring gear, an inner rotor sun gear, and a set of planet gears where the numbers of pole-pairs on each member are p_1, p_2, and p_3 respectively. According to [62], which is one of the first works on planetary magnetic gears, the relationship between the number of poles on each member could be given as $p_3 = p_1 + 2\,p_2$, and if the ring gear is kept stationary, the gear ratio would be expressed as $G_r = (p_1 + p_3)/p_1$. In [62], the calculated VTD of the planetary magnetic gear was $97.3\,N.m/L$, but the experimentally measured VTD decreased significantly to $15.8\,N.m/L$. More works on planetary magnetics gears were proposed, where it has been shown that the predicted VTD of some designs could reach values as high as $300\,N.m/L$ [63]–[65].

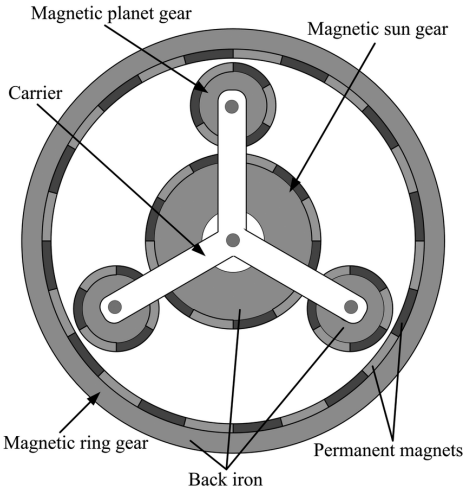

Fig. I-28 The planetary magnetic gear proposed in [62].

Then, there is the cycloidal magnetic gear that is inspired by the cycloidal mechanical drive or gear. This type is one of the more interesting and sought-after types due to its capability of providing very high gear ratios using minimal volume and number of poles. Its operation principle is similar to its mechanical counterpart, where the outer ring gear is kept fixed while the inner rotor is forced to rotate with two different rotary motions. The first cycloidal magnetic gear was proposed by F. Jørgensen in [66]. With the previously described operation, if the number of poles on the inner and outer rotors is p_1 and p_2 respectively, the gear ratio between the two rotary motions becomes $G_r = p1/(p1 - p2)$. According to [66], for a cycloidal magnetic gear with a gear ratio of -21, the calculated VTD was $141.9\ N.m/L$, and the measured value through the experimental prototype made was $106.6\ N.m/L$.

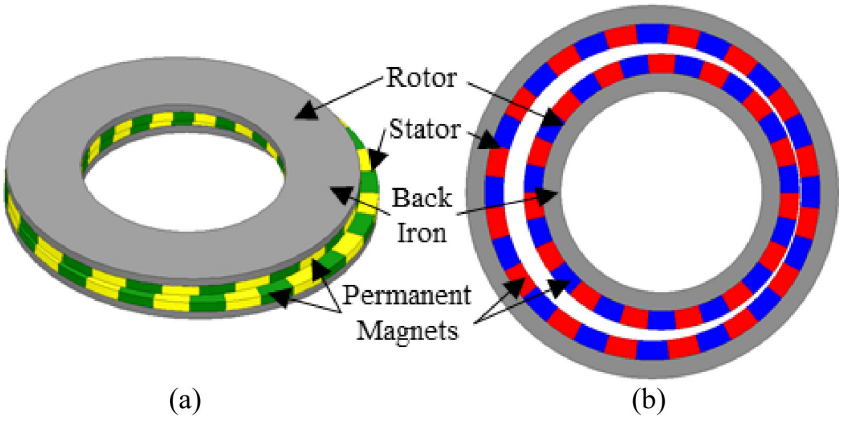

Fig. I-29 The concept of an (a) axial and (b) radial cycloidal magnetic gear [67].

In addition, an axial cycloidal magnetic gear was first proposed in [68] with the purpose of countering the problems caused by the bearing wear issues occurring in the radial cycloidal magnetic gears due to the non-uniform air gap radial forces. In [67], a cycloidal magnetic gear design combining both axial and radial field topologies was presented (see Fig. I-29). The authors have done an analysis study on the structure and constructed a proof-of-concept prototype. Furthermore, three configurations for the design were studied, where the configuration combining both the radial and axial topologies had a calculated VTD of $20.6\ N.m/L$ and an experimentally measured one of $17.6\ N.m/L$. More theoretical studies and simulations on cycloidal magnetic gears could be found in [69]–[74].

5.5. Linear Magnetic Gears

Different types and topologies of magnetic gears have been presented in the previous few sections, but they all performed rotary motion transformation or transmission, and likewise there are also magnetic gears that could perform linear motion transmission. In other words, linear magnetic gears would transform the linear motion from one moving part while changing the speed of motion and force, and, of course, without any physical contact. Similar to linear electric machines, one could obtain the linear magnetic gear in a flat or tubular configuration, but the tubular configuration has gained more attention because it could be more practically valid. The principle of operation of the linear magnetic gear is the same as the conventional rotary magnetic gear having three main members, where two members hold the magnet poles and a member holds the modulation ferromagnetic segments, and the equations for the number of poles and gear ratio could be applied in the same manner. The first tubular linear magnetic gear was proposed by K. Atallah in 2005 [75], where the design has shown that it could achieve a volumetric thrust force density of $1.7\ kN/L$ when using rare-earth magnets (see Fig. I-30). A year later, the same author proposed an improved and optimized design [76] that used quasi-Halbach array magnetization on the high-speed mover which attained a volumetric thrust force density of $2\ kN/L$. Later, the authors of the original design constructed a prototype for their design and presented it in [77], [78]. The comparison of the calculated and measured values from the prototype, whose schematic can be seen in Fig. I-31, has shown that the spacing between the pole-piece rings has a significant impact on the transmitted force, where the measured transmitted force decreased by 30% from the simulated value. Finally, a novel tubular linear MG topology that uses high temperature superconductor (HTS) bulks in the modulating mover was

proposed in [79]. The structure, shown in Fig. I-32, could achieve remarkable improvement in the thrust force density as compared the conventional structures.

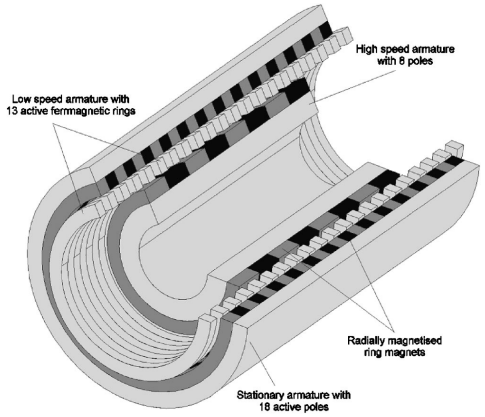

Fig. I-30 The first tubular linear magnetic gear proposed in [75].

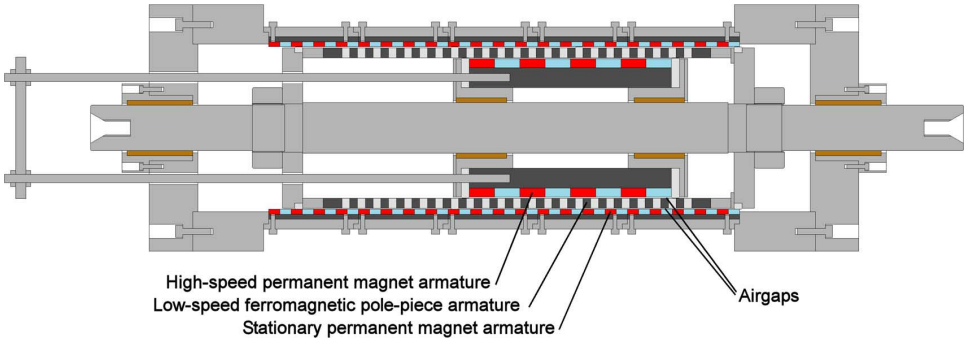

Fig. I-31 The tubular linear magnetic gear prototype cross-section presented in [77].

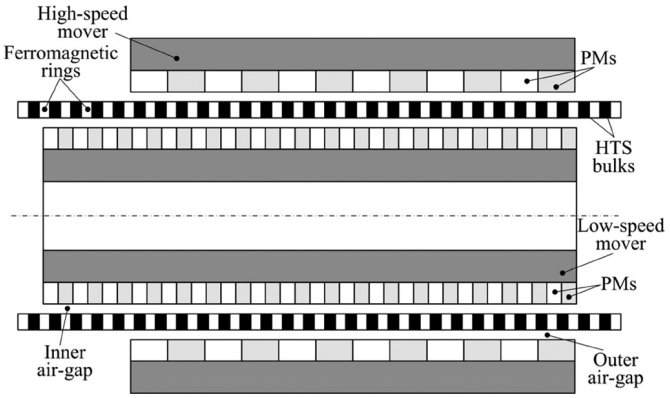

Fig. I-32 The HTS tubular linear magnetic gear shown in [79].

5.6. Magnetically Geared Machines

A magnetic gear is a transmission device with no electrical connection (unless it is excited using coils which is not typical), and conveniently, it can be designed to replace a mechanical gear operating in a certain application in a simple manner, where no changes have to be made to the system and only the mechanical gear is to be replaced by a magnetic gear. An alternative proposal for utilizing a magnetic gear is to integrate it with an electrical machine forming what could be called a pseudo-direct drive system (PDD). This refined proposal could be very beneficial and useful for acquiring compact volume, low cost, high-performance devices for energy conversion applications which are defined in the literature as magnetically geared machines (MGMs). An MGM is said to be smaller, lighter, and more efficient than the standard direct drive machine while still using less magnet material [80]. The opportunities and advantages proposed by MGMs lead many researchers to pursue and study this idea over the past decade, which made the literature rich with many unique designs and structures. The classification of MGMs is rather complex and different identifications could be found in different references, however, a main aspect that could classify an MGM design is whether the combined magnetic gear and electrical machine are magnetically coupled or not. Some designs require magnetic coupling, while others leave it optional, and some can only operate when magnetically decoupled. In addition, the radial and axial field topologies are also possible for MGMs and the position of the stator, and the windings could also change the type and operation of the device.

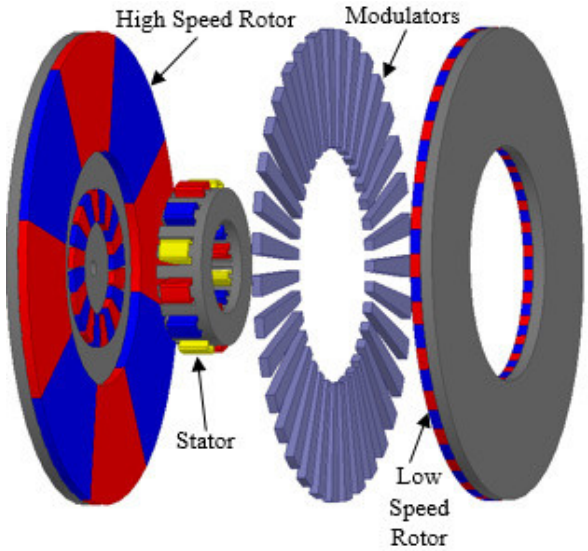

Fig. I-33 A disc-type magnetically geared machine [81].

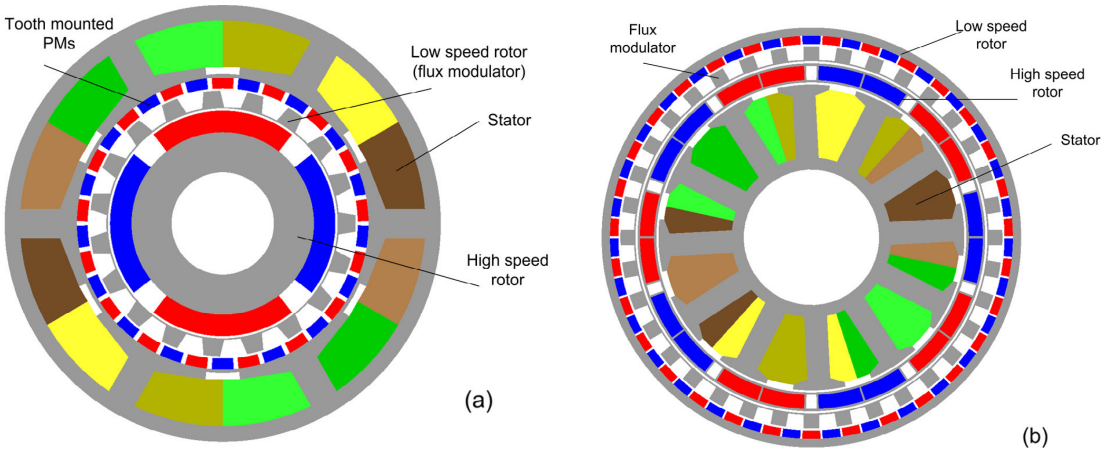

Fig. I-34 Radial field magnetically geared machines with (a) outer stator and (b) inner stator configurations [82].

In Fig. I-33, an axial field magnetically geared machine can be shown which was proposed in [81]. The proposed topology integrated an axial field permanent magnet machine into the bore of an axial field magnetic gear, where for this topology to function properly the magnetic gear and the electrical machine should be magnetically decoupled. Additionally, a radial field MGM with an outer stator configuration was proposed in [83], and another with an inner stator configuration was presented in [84] (see Fig. I-34). One of the differences between the inner and outer stator configurations is the magnetic coupling where the inner stator configuration can be magnetically coupled or decoupled whereas the outer stator configuration should be magnetically decoupled. Another difference is related to the volume of the MGM where in the inner stator configuration the electrical machine doesn't increase the total volume of the system unlike the outer stator configuration. On the other hand, some of the disadvantages of the inner stator configuration is that it possesses three air gaps instead of two, and the cooling of its inner stator could be hard to achieve. These are some of the popular MGM types, and since this work will be mainly focused on pure MGs, the discussion was limited to these few types. In fact, to properly cover the subject of the MGMs a full chapter might be required due to the wide variety of designs available and the different aspects to discuss. Finally, more works and revisions on MGMs can be found in [85]–[92].

6. Magnetic Gears Volumetric Torque Density Analysis

To properly summarize and review the designs and topologies that have been presented in the previous section, a comparative study for the torque capability of the different designs should be done. In addition, since one of the goals of developing magnetic gears was to rival or replace mechanical gears, it is good to take a look at the torque densities that some mechanical gears possess. There are multiple design factors to look at and consider when comparing between magnetic gears and mechanical gears like:

- Gear ratio
- Torque and speed
- Safety level required
- Ease of accessibility to the installation or application for maintenance
- Cost and total mass
- Volume and spatial constraints
- System operating temperature and installation environment temperature

Each one of these factors plays a role in deciding which is better for the application in hand. In general, and from what have been discussed previously, the magnetic gear can "potentially" have the upper hand and advantage with respect to most of the factors, but, to this date, there are still a lot of practical design challenges that continue to form an obstacle in the way of widely implementing and using magnetic gears, and here's where comes the incentive to continuously develop and improve magnetic gears.

For this work, the main factors that will be used to compare mechanical and magnetic gears are the volumetric torque density and the gear ratio. However, other factors that could be related to material, mass, cost, efficiency, etc., are equally important, and especially when discussing the practical implementation in a live application, the economic feasibility, the mass production of the device, etc. Interesting studies discussing the optimization of magnetic gears with respect to the cost, mass, gear ratio, magnet material grade, and temperature could be found in [93]–[95]. Before listing the VTD summary of the magnetic gears that have been proposed, a table listing the VTD of some mechanical gear types and models with different gear ratios is good for the comparison (see Table I-2), and this table is mainly summarized and extracted from multiple previous works that addressed this subject [96]–[98]. It is important to note that the VTDs listed in Table I-2 for mechanical gears are calculated with respect to a rough estimation of the

mechanical gear's volume [98], unlike the VTDs of the magnetic gears, which are usually calculated with respect to a definite active magnetic region volume. In addition, the output rated torque of a mechanical gear is dependent on the input speed, and hence the values mentioned in the table are provided by the manufacturers for a specified input speed and could vary with varying the speeds. For instance, the output torque specified for a certain input speed could decrease with the increase of the input speed, so the VTD value for one magnetic gear model mentioned in the table below could vary depending on multiple factors.

Table I-2 Summary of the torque capabilities of some commercial mechanical gears with different types and gear rations

Topology	Stages	Model	Gear Ratio	Rated Torque ($N.m$)	VTD ($N.m/L$)
Spur	2	Bonfiglioli C11 2P-4.9-P90	4.9	48	16
Spur	2	Bonfiglioli C11 2P-20,6_P80	20.6	82	27
Spur	2	Bonfiglioli C41 2P-44,8-P90	44.8	500	51
Spur	3	Bonfiglioli C100 3P-150,4-P132	150.4	12000	83
Planetary	1	Neugart PLS90 HP	5	220	265
Planetary	2	Neugart PLS90 HP, 2 stage	20	220	189
Planetary	2	Neugart PLS60 HP, 2 stage	64	120	103
Cycloidal	1	Nabtesco RV-6E	31	58	131.9
Cycloidal	1	Nabtesco RV-20E	57	167	204.9
Cycloidal	1	Nabtesco RV-40E	81	412	256.1
Harmonic	1	HarmonicDrive CSD-50-50-2UH	50	172	142.1
Harmonic	1	HarmonicDrive CSD-50-80-2UH	80	260	214.9
Harmonic	1	HarmonicDrive CSD-50-100-2UH	100	329	271.9
Worm	1	Winsmith DB961 Series	5	2274	33
Worm	1	Winsmith DB961 Series	20	3386	49
Worm	1	Winsmith DB961 Series	100	2588	38

Furthermore, large differences can be observed between the different mechanical gear types listed in Table I-2, and a unique trend for the relationship of the "gear ratio vs VTD" couldn't be specified. However, some observations could be made like the poor VTD values recorded by the spur and worm gear types with respect to the other types. In essence, the list of the torque and VTD values is only to provide an overview on the specifications of some mechanical gears and to have a perspective that could be useful when observing the VTDs of different magnetic gears. On the other hand, to perform a systematic comparison and to deduce the general trends and relationships of the quantities, a larger collection of mechanical gears should be presented, and the mechanical and magnetic gears used for the comparison should be rated for the same speed and designed for similar applications.

Table I-3 Summary of the volumetric torque densities of magnetic gears available in the literature

Magnetic Gear Type	**Magnet Type**	**Gear Ratio**	**Simulated VTD ($N.m/L$)**	**Experimental VTD ($N.m/L$)**	**Ref.**
Radial field – Halbach array	Neodymium	5.67	284	261.4	[36]
Radial field – flux focusing	Neodymium	4.25	245	239	[33]
Axial field – flux focusing	Neodymium	4.16	173	152.3	[49]
Radial field – flux focusing	Neodymium	4.25	154	151.2	[32]
Radial field – Halbach array and flux focusing	Neodymium	4.25	152	112	[99]
Radial field – SMPM	Neodymium	10.5	115.7	110	[28]
Radial field – Halbach array	Neodymium	4.25	110.7	108.3	[100]
Radial field – cycloidal	Neodymium	21	141.9	106.64	[66]
Radial field – SMPM	Neodymium	4.25	97.1	95.4	[100]

Radial field – flux focusing	Neodymium	4.25	126.67	95	[101]
Axial field – cycloidal	Neodymium	30	-	91.5	[68]
Radial field – SMPM	Neodymium	5.75	111.2	77.9	[17]
Radial field – harmonic – dual stage	Neodymium	360	78	75	[74]
Radial field – flux focusing	Neodymium and Ferrite	4.25	81	66.3	[32]
Radial field – SMPM	Neodymium	10.33	-	60	[102]
Radial field – Halbach array	Neodymium	4.25	148.6	57.2	[103]
Radial field – SMPM and flux focusing	Neodymium	5.5	92	54.6	[29]
Radial Field – IPM and SMPM (homopolar)	Neodymium	7.33	55.3	53	[35]
Radial field – SMPM	Neodymium	10.5	80.8	49	[104]
Radial field – IPM and SMPM	-	5.5	66	42	[34]
Radial field – SMPM	Neodymium	5.5	53.1	41.6	[105]
Radial field – SMPM	Neodymium	5.5	-	36.9	[42]
Radial field – flux focusing	Ferrite	4.25	56	33	[30]
Axial field – SMPM	Neodymium	8	21.1	22.4	[50]
Radial and axial field – cycloidal	Neodymium	20	20.6	17.6	[67]
Radial field – planetary	Neodymium	3	97.3	15.8	[62]

Transverse flux – SMPM	Neodymium	3.25	-	14.9	[59]
Radial field – reluctance rotor	Neodymium	6	19.49	12.66	[44]
Axial field – flux focusing with L-shaped segments	Ferrite	4.16	74	2	[52]

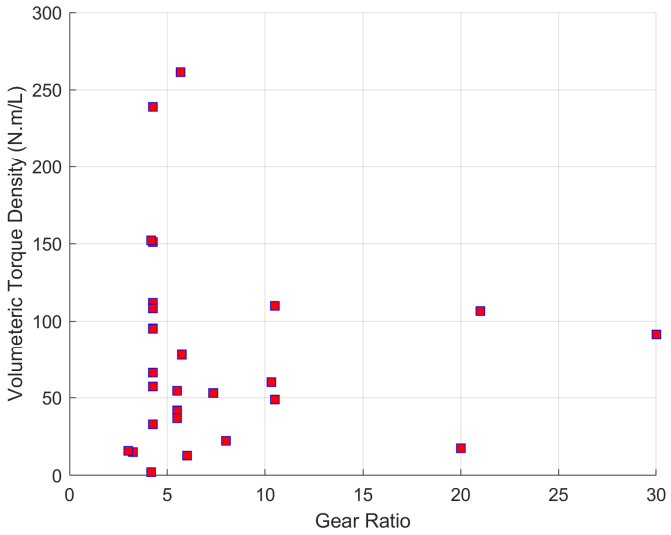

Fig. I-35 The experimental VTD of magnetic gears with different types and gear ratios.

A summary of the characteristics of magnetic gears that have been experimentally realized is shown in Table I-3. The table describes the type of each magnetic gear, the gear ratio, and the calculated and measured VTDs. Most of the entries were presented in the previous sections, and in this table, they have been arranged and sorted in decreasing order with respect to the experimental VTD value. In addition, to better visualize the interesting and important relationship between the gear ratio and the VTD of the magnetic gears, the values from the columns of the gear ratio and experimental VTD from Table I-3 have been used to realize a scatter plot shown in Fig. I-35. Also, the table only mentioned the magnetic gears that had a prototype and experimental measurements to increase the validity of the analysis and comparison, but there are still much more theoretical designs and concepts that have been presented in the literature and could hold a lot of potential. After reviewing the literature and

analyzing the data presented, some of the main points and takeaways that could be mentioned are:

- To this date, the radial field topology seems to be the dominant structure for magnetic gears where the majority of the successful prototypes constructed are of the radial field type, and the highest measured VTDs are for radial field magnetic gears. However, this doesn't mean that the axial field topology isn't receiving enough research interest. In fact, the axial field topology has received a lot of attention from researchers and several designs have been proposed, but the main challenge lied always in successfully constructing a prototype and applying the design. The axial attraction forces in the axial field topology cause multiple issues, challenge the structural integrity of the device, and complicate the fabrication process. In addition, aligning the three discoidal rotors of an axial field structure and maintaining the alignment in the presence of the attraction forces is a big challenge, where most of the times the structure ends up having non-uniform air gaps between the rotors which increases the severity of the attraction forces even more. Hence, more research is still required for the axial field topology, whether it is by optimizing the structure itself from a magnetic point of view to improve its performance, or by improving the design structurally and mechanically to overcome the construction challenges.
- Among the different magnetic arrangements of the rotors, the flux focusing and the Halbach array seem to be the best performing arrangements, where currently the highest and second highest measured VTDs are for magnetic gears with Halbach array and flux focusing arrangements respectively. This doesn't exclude any other possible arrangement or configuration from having a high-performance when properly designed and optimized, where every arrangement has its advantages and disadvantages, and the design should be ultimately tailored to properly suit the application and constraints in hand. Moreover, it has been demonstrated that the design and shape of the ferromagnetic pole-pieces have an impact on the overall performance, and the method to support the modulating segments should be properly investigated during the design process.
- By checking the values of the VTDs in Table I-3, one can see a significant discrepancy between the simulated and experimental VTD values in most of the cases where only a few of the designs have managed to keep the expected and measured values close enough. One of the most reported causes for this discrepancy is the end-effects which weren't properly taken into account in the simulation. In addition, another cause reported by a lot of works

was the difference between the design values used in the simulation and the experimental values realized in the prototype where many values had to be changed during the construction process to make the fabrication possible. In essence, before going into the construction phase, it is always important to use proper modeling methods that could take into account different phenomena and predict the performance accurately. Moreover, developing proper and efficient modeling tools could always form a positive contribution to the whole design process. It is not to be ignored also that the current measured performances of the available magnetic gears are coming from prototypes constructed at laboratories for testing and experimentation, so it is not fair to strictly compare them to mechanical gear technologies that have been manufactured and mass produced for over a century. Hence, as the magnetic gears technology evolve and develop over the next few years, their performance will continue to rise, especially when the designs start to be practically implemented into systems and manufactured by industrial societies that could optimize the fabrication of the product for maximal performance.

- After observing Fig. I-35, it seems that predicting a general trend for the gear ratio vs the VTD relationship might not be straightforward. For the conventional magnetic gear types which have been presented in the previous sections, one can assume that the VTD is decreasing with the increase of the gear ratio, which is in agreement with what have been presented in [106], where the authors tried to compare between mechanical and planetary magnetic gears. According to [106], this trend is also true for planetary mechanical gears, but the two gear types react differently to varying the external diameter, where the mechanical gear had almost the same torque density no matter what the value of the external diameter while the magnetic gears VTD increase with the increase of the external diameter. On the other hand, this trend might not fully stand when discussing special magnetic gear types that are designed to achieve higher gear ratios like the cycloidal magnetic gear, where multiple works on this type have shown that it could achieve high VTD with high gear ratios. An in-depth investigation is required to identify the variation trend for some of the special magnetic gear types.
- It has been reported by multiple works that the losses occurring in a magnetic gear depend primarily on the speed of rotation rather than the load [107]. In addition, the losses appear to be lower at full torque load than at no load or reduced load, where the losses can be divided into two types: electromagnetic losses related to iron core and permanent magnet

losses, and mechanical losses related to bearings and friction. Therefore, magnetic gears could be considered more suitable and efficient for low-speed high-torque applications.

Conclusion

A literature overview and state-of-the-art presentation on magnetic gears were shown in this chapter. The potential advantages provided by magnetic gears were presented to clarify the motives behind researching and developing this technology. After presenting the principle of operation of modern magnetic gears, the different types and topologies of magnetic gears were presented. Finally, a summarizing analysis has been conducted by gathering and analyzing the data available in the literature, then the result of this analysis is summarized in some key points. The principles and information discussed and presented in this chapter are supposed to provide the reader with an orientation towards the type of the problem this work is tackling and should serve as an important reference for next the chapters.

Chapter II - Magnetic Equivalent Circuit for Modeling Magnetic Gears

Introduction

In this chapter, the objective is to present and implement modeling methods for magnetic gears, where the main focus is directed towards the modeling of axial field magnetic gears. The ultimate goal behind this is to obtain a modeling tool for early design stages, which can consider the 3D aspects of axial field magnetic gears while having a short computation time. First, a brief overview on magnetic materials behaviors and types is done. Next, a theoretical presentation for the modeling techniques that are going to be used is conducted which illustrates the implementation of the finite element method technique and presents the formulations of the magnetic equivalent circuit method. Then, the details of the implementation of the magnetic equivalent circuit method are illustrated through multiple sections. Furthermore, the presented modeling method is evaluated through testing its nonlinear solvers and comparing between them. Additionally, the end-effects in axial field magnetic gears are analyzed and modeled using a 3D magnetic equivalent circuit model, and a comparison between two magnetic gear configurations is conducted. Finally, an alternative quasi-3D method for modeling the end-effects is presented and evaluated.

1. Magnetic Materials

Understanding the magnetic material properties and behavior is essential for the design of electric machines and magnetic gears. Ignoring some magnetism principles and phenomena while modeling an electromagnetic device will definitely lead to an inaccurate model and wrong predictions. Hence, some of the practical aspects for magnetism and magnetic materials, that will be mostly useful for the modeling approaches to be presented later, will be presented in a rather compact fashion because diving into the details of magnetism might be out of the scope of this work.

The following categories may be used to classify magnetic materials: diamagnetic paramagnetic, ferromagnetic, antiferromagnetic, and ferrimagnetic (see Fig. II-1). Diamagnetic materials don't have a net magnetic moment at the atomic or molecular level. As for the

paramagnetic materials, they have a net magnetic moment at the atomic level, but the coupling between proximity moments is weak. On the other hand, ferromagnetic materials have a net magnetic moment at the atomic level, and, in contrast to paramagnetic materials, there is a tight coupling between neighboring moments. The moments spontaneously align across macroscopic areas known as domains as a result of this interaction. When the material is exposed to an applied field, the domains further align. Finally, atomic moments in ferrimagnetic and antiferromagnetic materials are arranged such that they are antiparallel to one another [108]. This makes the ferromagnetic materials the best candidate for creating flux tubes, storing magnetic energy, and transferring it across the different regions of an electromagnetic device. Therefore, the discussion will be limited to the behavior and nature of the ferromagnetic materials.

1.1. The B-H relationship

The relationship between the magnetic flux density and the magnetic field intensity defines the macroscopic properties of the material. It is called the constitutive relationship and is given by:

$$\mathbf{B} = \mu\,\mathbf{H} \tag{II-1}$$

where $\mathbf{B}$ is the magnetic flux density expressed in (T or $Wb.m^{-2}$), $\mathbf{H}$ is the magnetic field intensity expressed in ($A.m^{-1}$), and μ is the permeability expressed in ($H.m^{-1}$).

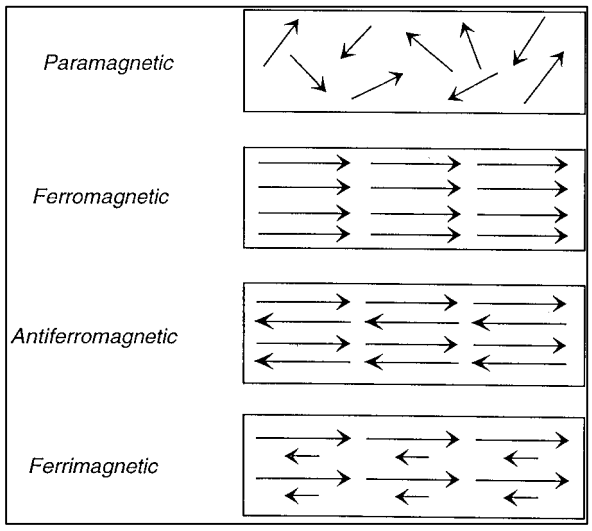

Fig. II-1 Magnetic materials classification showing the orientation of the magnetic moments of each category [109].

The permeability μ is scalar for isotropic media but might become tensor for anisotropic materials. This is due to the fact that anisotropic materials have different magnetic properties in different directions. In other words, magnetic anisotropy is the characteristic of a material that maximizes certain magnetic properties in a favored direction. It is unlike isotropic materials which have the same magnetic properties regardless of the direction. Moreover, if the behavior of the material is magnetically nonlinear, the value of the permeability becomes dependent on the intensity field value. In addition, a material is called non-homogeneous if the permeability is a function of position [110]. Finally, another important and more general form of the constitutive equation is given by:

$$\mathbf{B} = \mu_0 (\mathbf{H} + \mathbf{M}) \tag{II-2}$$

This equation is expressed according to the Sommerfeld convention where $\mu_0 = 4\pi.10^{-7}\ H.m^{-1}$ is the vacuum or free space permeability, and **M** is called the Magnetization which is a measure of the net magnetic dipole moment per unit volume. From (II-1) and (II-2), the following equation can be derived:

$$\mathbf{M} = \chi_m \mathbf{H} \tag{II-3}$$

where χ_m is the susceptibility of the material and its relationship with the permeability is given by:

$$\chi_m = \frac{\mu}{\mu_0} - 1 \tag{II-4}$$

Plotting the magnetic flux density **B** or the magnetization **M** as a function of **H** is a very good way to represent graphically the macroscopic properties of a magnetic material. The B-H plot is used more often, knowing that it is based on the constitutive equations presented in (II-1) and (II-2), so the M-H plot also could be easily deduced using these equations. A demonstrative B-H plot is shown in Fig. II-2, the plot is nonlinear, and it is usually called a hysteresis loop or magnetization curve. It reveals the hysteresis phenomenon attributed to the ferromagnetic materials which basically means that the present state of a material depends on its prior magnetization state. To understand some of the useful information that could be extracted from a hysteresis loop, it is useful to briefly present the magnetization cycle.

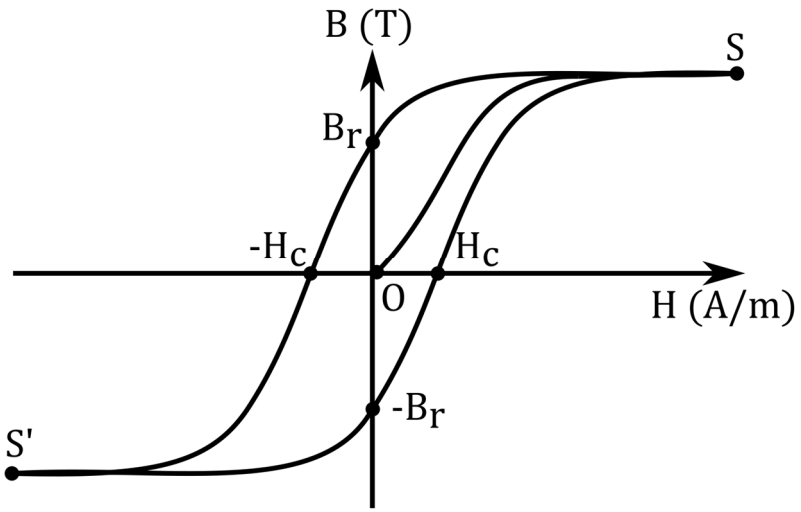

Fig. II-2 A typical B-H plot or hysteresis loop.

Referring to the points shown in Fig. II-2, starting at point O with an unmagnetized specimen, an **H**-field is applied. As the magnetic field intensity value increases in the plus direction, the domains having the same alignment as **H** expand which eventually increases the value of the magnetic flux density. As the magnitude of **H** gradually increases from weak to moderate then from moderate to high, the magnetic moments that were not initially aligned with the direction of **H** start to gradually align depending on the strength of the applied field and the extent of their initial misalignment. The magnitude of **B** will in turn gradually increase until eventually reaching the saturation point S, and afterwards the increase rate of the magnitude of **B** becomes much slower no matter how high the magnitude of **H** reaches. Reaching the saturation phase indicates that the majority of the magnetic moments are aligned or close to alignment with the direction of **H**. This phenomenon is called magnetic saturation, and it is essential to understand and consider when analyzing electromagnetic devices that use soft magnetic materials.

After tracing the segment OS which is called the initial magnetization curve, the magnetic field intensity value is decreased gradually to zero. However, some of the magnetic moments retain their orientation, and others that were initially aligned in an opposite direction to the magnetic field don't return to their initial opposite alignment. This will form a net positive alignment for the magnetic moments in the plus direction which will remain even when the

magnetic field is reduced to zero, so the material at this stage will exhibit a residual induction value B_r which will be called magnetic remanence. Then, the direction of **H** is reversed to trace the remaining part of the loop starting from the residual induction point. As the magnetic field value is increased in the negative direction, the moments flip their orientation and try to align themselves with the new direction of the magnetic field until eventually cancelling out the positive net magnetic moment and reducing the magnitude of **B** to zero. At the point where this occurs the value of the magnetic field is denoted H_c, and it is called the coercivity. After the magnitude of **H** is increased beyond $-H_c$, a similar behavior to what has been seen in the initial magnetization segment occurs but in the negative direction, until consequently reaching the saturation point S' attributed to the same saturation induction value the point S had but in the negative direction. In a similar fashion, when the magnitude of **H** is returned to zero, and it is reversed to the positive direction again, the path (S', S) is traced in a symmetrical fashion passing through the point $(0, -B_r)$ which closes and completes the hysteresis loop. It is worth noting that the loop that has been described is called the major hysteresis loop where minor hysteresis loops could be obtained by cycling through magnetic field values such that $-H_c < H < H_c$.

1.2. Soft Magnetic Materials

Considered as a class of ferromagnetic materials, the soft magnetic materials serve as the magnetic core for a wide variety of applications. Their "soft" label originated from the fact that they could be easily magnetized and demagnetized. These materials are characterized by their low coercivity ($H_c < 1000\ A/m$) and high permeability making them perfect for magnetic flux conduction and channeling. Their hysteresis loop could be distinguished by its thin body and small enclosed area as compared to the loop of hard magnetic materials which are the second family of ferromagnetic materials (see Fig. II-3). These properties make soft magnetic materials substantially used in electric machines, transformers, inductors, transducers, electromagnets, etc.

There are different types of soft magnetic materials suitable for different applications and possess different qualities and responses to frequency, temperature, and magnetic field intensity. Some of the important quantities that play a role in the choice and classification of soft magnetic materials are the saturation magnetization, coercivity, permeability, and resistance. High permeability and saturation magnetization are preferred for applications where high magnetic field values are anticipated.

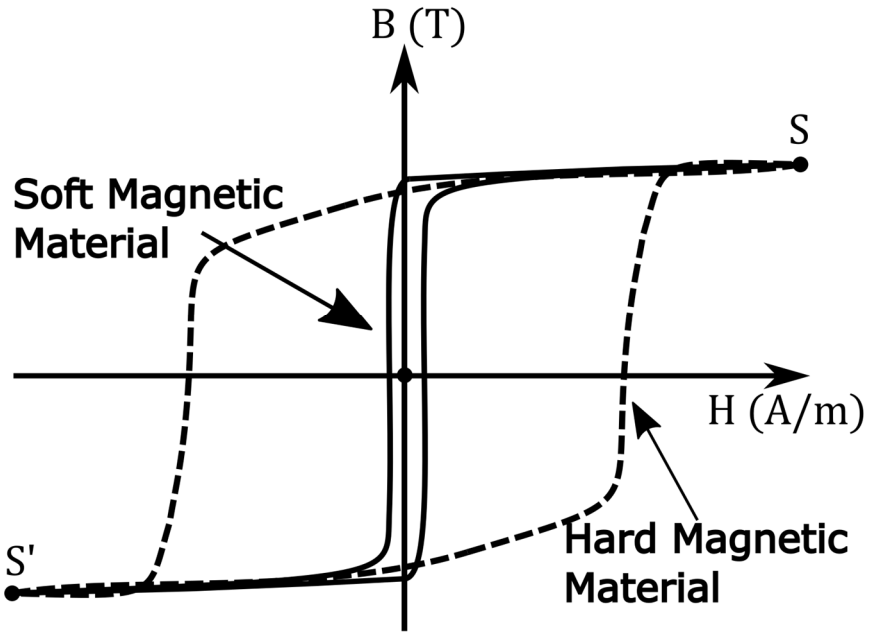

Fig. II-3 Illustrative hysteresis loops for soft and hard magnetic materials.

On the other hand, high-frequency applications might prioritize having very low coercivity and high resistivity values. Low coercivity and high resistivity mean reducing losses caused by hysteresis and eddy currents respectively. In addition, as shown in Fig. II-4, a linear segment could be identified in the magnetization curve of almost every soft magnetic material. This segment represents the state of the material before hitting the magnetic saturation, and the relative permeability along it is constant. The relative permeability μ_r which is normalized to the free space permeability μ_0 is given by:

$$\mu_r = \frac{\mu}{\mu_0} \tag{II-5}$$

Whether it is purified from any impurities then used in its pure form or mixed with other elements to form alloys, iron (Fe) constitutes the main chemical element of almost all soft magnetic materials. Different alloys and compositions possess different chemical and physical properties. For example, silicon steel (Fe-Si) is mostly used in motors and transformers due to its high permeability and increased resistivity and hence reduced eddy current losses and improved magnetic flux conduction.

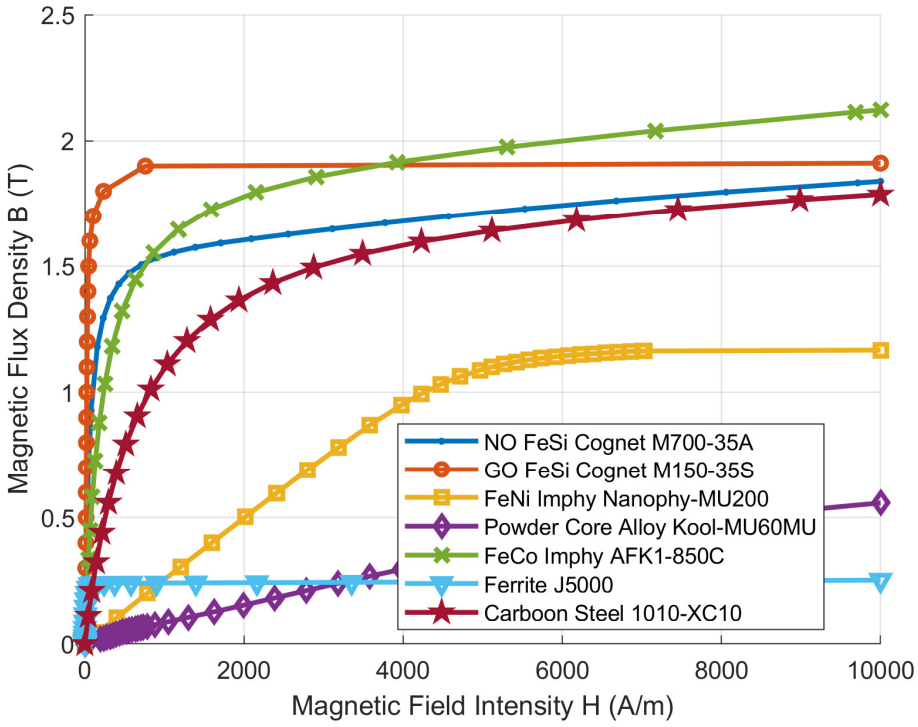

Fig. II-4 The B-H curves for different soft magnetic materials [111]–[116].

In addition, it can be divided into two types: grain-oriented (GO) Fe-Si and non-grain-oriented (NO) Fe-Si, where it is known that the grain-oriented Fe-Si is used for static applications like transformers whereas the non-grain-oriented Fe-Si is used for rotating applications like motors and generators. Nickel-iron alloys (Fe-Ni) are another kind of alloys that have very high permeability values but lower saturation magnetization than silicon steel or soft iron. Applications for Fe-Ni alloys include the cores of audio frequency transformers, magnetic amplifiers, and inductors [108], [117]. Moreover, there is the cobalt-iron alloys which are characterized by their very high saturation induction (up to 2.4 T), so they are considered very suitable for all applications that require high flux density like, for example, applications with flux focusing configuration, but they can be quite expensive.

The magnetization BH curves of a variety of magnetic materials from different manufacturers are shown in Fig. II-4. It is worth noting that these are presented just for illustration and not necessarily for strict comparison because each curve is traced under different conditions, and the user should always refer to the data sheet of the manufacturer to identify the key quantities of the material they are aiming to use and decide whether or not it can fit their specific

application. In general, for magnetic gears, the main priority is having a soft magnetic material with high saturation induction, permeability, and resistivity. In addition, reducing hysteresis losses might become a priority if the magnetic gear is designed to operate at very high speeds. Hence, the situation is similar to electric machines, so silicon steel, cobalt-iron alloy, carbon steel, or pure iron could all serve as good candidates for the use in the magnetic core of a MG.

1.3. Hard Magnetic Materials

Unlike soft magnetic materials, hard magnetic materials are identified by their high coercivity and low permeability, and, as their name suggest, the high coercivity makes it "hard" to magnetize and demagnetize them. They are also called permanent magnets since once magnetized they can maintain their magnetization and act as a magnetic field source. Permanent magnets are essential for the functioning of many applications, and they are extensively used in electric machinery. For magnetic gears, it has been demonstrated in the first chapter that the development of the PM materials and capabilities played the biggest role in improving the performance of magnetic gears and rising the interest in them.

Permanent magnets operate in the second quadrant of the magnetization curve (Fig. II-2), and it is due to what is called the demagnetization field which is a self-field that opposes the magnetization field, where it develops inside the material when the material is magnetized. Some of the main properties that should be inspected when selecting a magnet are the remanence B_r, the coercivity, the shape of the BH curve in the second quadrant, the Curie temperature, and the energy density. The remanence has been identified in the previous section as the intersection of the hysteresis loop with the H-axis ($B = B_r$ at $H = 0$), and similarly the coercivity was defined as the magnetic field value at $B = 0$. However, since the coercivity values in permanent magnets tend to be very high, two types of coercivities are defined corresponding to the B-H and J-H curves. First, there is the normal coercivity H_{cb} which is the point at which the magnetic flux density is nullified, and it corresponds to the magnetic field value in the B-H curve at which $B = 0$. Then, the value that corresponds to the J-H curve is known as the intrinsic coercivity H_{cj} which is the point at which the polarization of the magnet reaches zero. This is knowing that the polarization $\mathbf{J}$ is attributed to the magnetization $\mathbf{M}$ and defined as $\mathbf{J} = \mu_0 \mathbf{M}$. After reaching one of the coercivity points, the magnet is completely demagnetized and can be re-magnetized if it hasn't endured any physical damage.

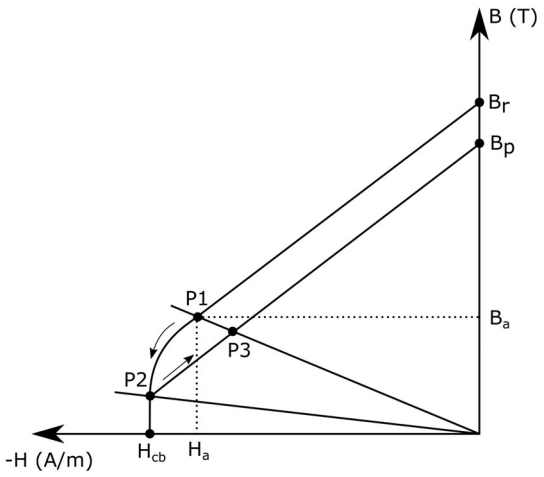

Fig. II-5 The B-H demagnetization curve of a permanent magnet with a knee point P1.

In addition, the Curie temperature is the temperature value at which the ferromagnetic material loses its magnetic properties and becomes paramagnetic, and usually permanent magnets manufacturers will set a maximum operating temperature below the curie temperature point. Furthermore, the energy density is represented as the product of the values of **B** and **H** acquired at any point along the B-H demagnetization curve. There appears a maximum value for the energy density among the points of the demagnetization curve denoted $(BH)_{max}$, and it is used usually to grade the hard magnetic materials.

Finally, the B-H curve in the second quadrant is usually linear or possesses a large linear segment with a knee point at which the B-H relationship turns nonlinear. By looking into Fig. II-5, the original linear segment of the B-H demagnetization curve is identified by the points B_r and P1, where the relative permeability of along this segment is constant denoted as the "recoil permeability", and its value is usually close to unity. It is good to note that even with low relative permeability, the hard magnetic materials are still considered ferromagnetic because their internal structure is designed to have the maximum energy storage capability. The operating point of the permanent magnet is determined by the geometry of the magnet and the geometry and properties of the magnetic circuit it is placed in. In static systems, the structure can be designed to choose an operating point for the magnet at the maximum energy density position, but in dynamic systems like rotating machine it should be kept along the linear segment of the magnetization curve. If the operating point of the magnet passes below the knee point P1, irreversible losses occur. As can be seen in Fig. II-5, if the operating point passes from P1 to P2

then shifts upward, it will not return to its initial line connecting B_r and P1, but it will trace a new demagnetization path passing through P3 and B_p with the new remanence value being smaller than the original one ($B_p < B_r$).

Different chemical compositions significantly change a permanent magnet properties and usages. Some of the commercially available and used hard magnetic materials are alnico, samarium cobalt (SmCo), hard ferrites, and neodymium-iron-boron (NdFeB). A summary of some of the main properties of these magnets can be found in Table II-1. It is worth noting that properties can differ even for magnets the have the same type and chemical elements, and this difference depends on many factors like heat treatment, whether it was prepared by sintering or casting, and the magnetic orientation of its particles which determines if the magnet is isotropic or anisotropic. For example, alnico magnets can have excellent stability over a wide temperature range higher than 500 °C, strong corrosion resistance, but relatively low coercivity and energy density. On the other hand, hard ferrites are the most commonly used and least expensive hard magnetic material. They are produced by powder metallurgical methods and are usually called ceramic magnets. In addition, they are characterized by good temperature stability, high coercivity, high electrical resistivity, and excellent corrosion resistance.

Then, there are the rare-earth permanent magnets which are known to have the highest energy density, coercivity, and remanence among all the magnets. The two most known rare-earth magnets are the neodymium iron (NdFeB) and the samarium cobalt (SmCo), where they both possess very high energy density and coercivity, so they are amongst the best in terms of resistance to demagnetization, and they are both produced using powder metallurgical methods. The main difference between them is in the optimum operating temperature, where the neodymium magnets possess the highest energy density and remanence but at low temperatures (below 200 °C). At high temperatures, the strength of the neodymium magnets decreases rapidly, and the samarium cobalt magnets gain the advantage of having excellent thermal stability (SmCo magnets possess excellent temperature coefficients). Additionally, another important difference is the corrosion resistance, where the neodymium magnets are among the most vulnerable magnets to corrosion and require special treatment and coating if they are meant to be installed in harsh environments, but SmCo magnets have excellent corrosion resistance thanks to the large percentage of cobalt. Finally, some neodymium and samarium cobalt magnets grades and properties are summarized in Table II-2 and Table II-3 respectively. For magnetic gears, it should be clear by now that the neodymium magnets are the preferred choice to obtain a high

torque density design due to their superiority in terms of energy density and remanence, but their limitations in terms of the operating temperatures are not to be disregarded. Eventually, it will all depend on the application environment and conditions.

Table II-1 The physical properties of some of the commercially available permanent magnets [118].

Magnet Type	Curie Temperature (°C)	Maximum Operating Temperature (°C)	Density (g/cm3)	Relative Recoil Permeability
Alnico	860	525-550	6.9-7.3	1.7-4.7
Hard Ferrites (Ceramic)	450	250	4.8-4.9	1.05-1.2
SmCo	700-800	250-350	8-8.5	1.1
NdFeB	310-370	80-240	7.4	1.05

Table II-2 Neodymium (NdFeB) magnets grades and properties [118].

Magnet Grade	Max. Operating Temperature (°C)	Remanence B_r (T)	Normal Coercivity H_{cb} (kA/m)	Intrinsic Coercivity H_{cj} (kA/m)	Max. energy product $(BH)_{max}$ (J/m^3)
N35	80	1.22	925	955	279
N42	80	1.33	925	955	334
N50	80	1.43	860	875	398
N38H	120	1.26	960	1353	303
N45H	120	1.37	1036	1353	358
N48H	120	1.4	1047	1353	382
N30EH	200	1.14	862	2387	239
N33EH	200	1.17	900	2387	263
N40EH	200	1.28	1000	2387	318

Table II-3 Samarium cobalt magnets grades and properties [118].

Material Composition	Magnet Grade	Remanence B_r (mT)	Normal Coercivity H_{cb} (kA/m)	Intrinsic Coercivity H_{cj} (kA/m)	Max. energy product $(BH)_{max}$ (J/m^3)
SmCo5	S16	790-840	612-660	1830	118-135
	S20	890-930	684-732	1830	150-167
	S24	960-1000	740-788	1830	183-199
Sm2Co17	S220	930-970	676-740	1433	160-183
	S240	950-1020	692-764	1433	175-191
	S280	1030-1080	756-812	1433	207-220
	S320	1100-1130	812-860	1433	230-255

2. Finite Element Method

The finite element method (FEM) is the most widely used numerical method for solving electromagnetic problems. In the FEM, a given domain is considered as a collection of subdomains, called "finite elements", and the governing equation is estimated across each subdomain using any of the conventional variational methods. The primary motivation for finding approximate solutions on a collection of subdomains is that it is simpler to describe a complex function as a collection of simple polynomials. Obviously, each segment of the solution must link with its neighbors in the sense that the function and, if desired, its derivatives are continuous at the connecting points. It may be used to solve static and transient, linear and nonlinear, isotropic and anisotropic, homogeneous and inhomogeneous electromagnetic problems. Some of the advantages that make this method powerful are linked to the concept of subdivision of the whole domain, where this subdivision allows for accurate representation of complex geometries and easy treatment of dissimilar material properties. In addition, the subdivision facilitates the representation of the total solution through functions defined within each element that detect local effects. On the other hand, the FEM is only useful for computations in bounded regions but is inconvenient when the region is unbounded. Moreover, a factor that really makes the FEM quite popular and practical amongst researchers and engineers is the availability of a large number of numerical implementations for the method through software packages and applications [108], [110], [119]. This provides the user with readily available and powerful FEM software tools for modeling electromagnetic problems but without worrying about the underlying complex mathematics of the FEM. It is worth noting that the terms finite element method (FEM) and finite element analysis (FEA) are used interchangeably in references, where some references consider that they point to the same thing, but others consider that the FEA represents the simulation created by applying the mathematical equations behind the FEM. For this work, the term FEM will be used exclusively to point to both the technique and the numerical model.

As previously mentioned, there are so many excellent FEM commercial software, and they all provide a trusted and powerful tool for researchers and engineers to solve all kinds of physical problems, and in the context of this work, to model and design electrical machines and electromagnetic devices.

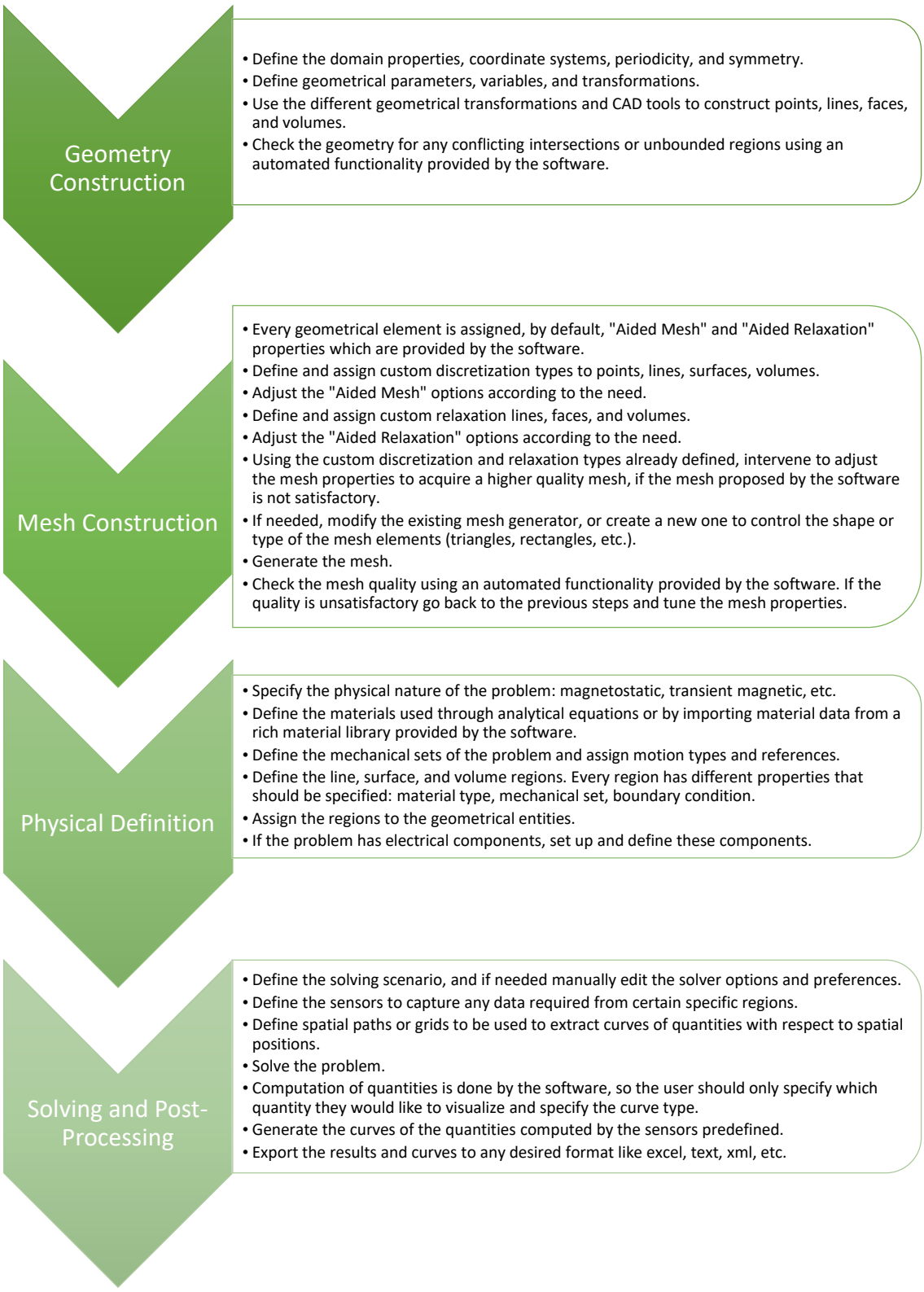

Fig. II-6 A flowchart demonstrating the basic steps for constructing a FEM model using the FLUX software.

As the main goal of this chapter is to present an implementation of a certain modeling technique, a trusted modeling method should be always present to validate the results from the proposed implementation, so the FEM fits perfectly in this slot to provide a perspective for comparison and validation. The software that was used to create the FEM models throughout this work was the Altair FLUX which is a popular and powerful product that contains CAD tools to create 2D and 3D geometries, and of course the FEM numerical implementation. A flowchart showing the steps followed to create an FEM model using FLUX is shown in Fig. II-6. One of the most important steps while creating an FEM model is the mesh creation step because the quality of the mesh will decide the accuracy and performance of the model. If the mesh is bad, the generated results will be random or inaccurate, and if the mesh elements are too small across the whole domain, the system size will become too large and the time to solve the problem will increase significantly. Hence, it is all about tuning the mesh to keep a good balance between the accuracy and the computation time which might not be very easy or simple to achieve especially for inexperienced users. Furthermore, an essential meshing aspect that is provided by the FLUX software and almost any other FEM software is the mesh relaxation.

Mesh relaxation allows to have different element sizes in different regions which is very suitable and practical for most applications. For example, the air gap is a usually a small but very important region for calculating quantities, and it hosts a lot of flux variations and orientations which should be detected, so usually multiple layers of small and equally sized elements are utilized to mesh this region in order to get the most accurate estimation of the quantities in it. On the other hand, big regions that don't hold a lot of flux variations and transitions could be meshed using larger mesh elements because there might not be any important local flux variations to detect, so having small mesh elements, as the size of the elements used in the air gap for example, will significantly increase the number of nodes and the size of the system without adding any benefits or gains. Hence, it is generally more suitable and practical to implement the mesh relaxation by to changing the mesh density and size elements in the regions throughout the whole domain in accordance with nature and size of the region. In the FLUX software, this feature is already implemented by default and could be easily adjusted and edited by the user to help in tuning the quality and size of the mesh. The mesh of a 2D cross-section of a flux focusing magnetic gear where the mesh relaxation is implemented is shown in Fig. II-7, and it can be seen how the size of the mesh elements is gradually increased as the distance away from the air gap increases. Another important feature offered by FLUX and many other FEM

software, is the ability to create sketches and even animations to visualize the flux lines, induction arrows and many other quantities that are useful for understanding and analyzing the functioning of a device (see Fig. II-8).

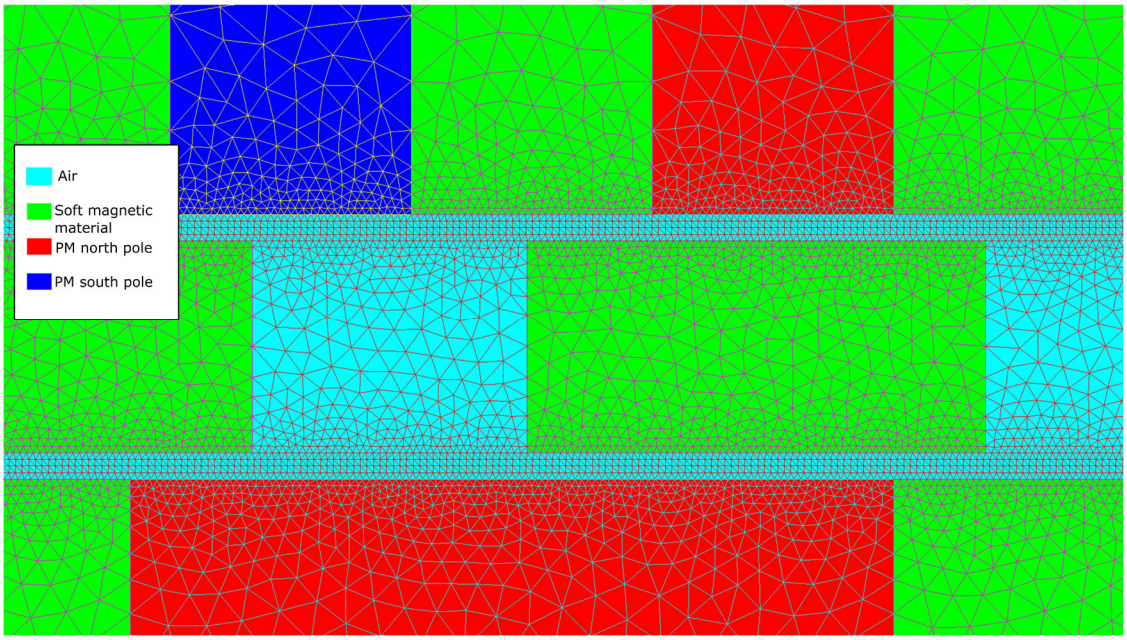

Fig. II-7 A 2D-cross section of a flux focusing magnetic gear meshed using FLUX.

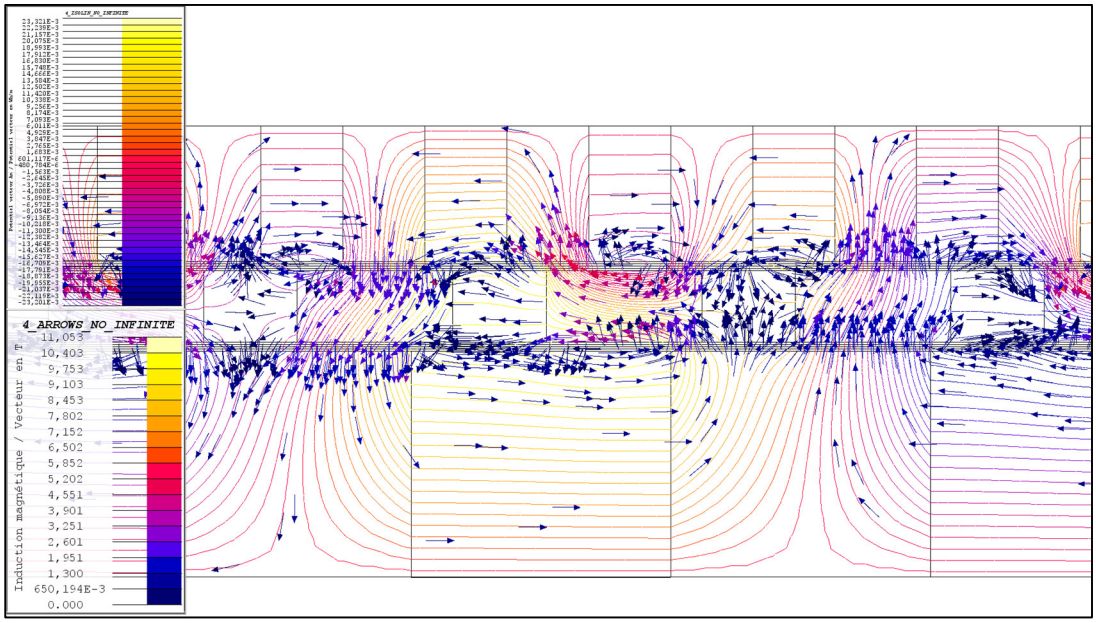

Fig. II-8 A sketch generated using FLUX showing the magnetic potential vector isolines and the magnetic induction arrows distribution.

3. Magnetic Equivalent Circuit

Magnetic equivalent circuit (MEC) is a very well established and known technique for modeling and representing the magnetic aspect of an electromagnetic device. It can be considered a branch of the more general "lumped parameter network" concept which is based on representing a certain physical aspect of a device using connected parameters that form a circuit or a network. In MEC, the lumped parameter represents the reluctance or permeance of a flux tube, and, hence, the network is formed by dividing the domain into elementary flux tubes and then representing them using a circuit of reluctances or permeances. An analogy between this "magnetic circuit" and an electrical circuit can be created, where the basic electrical circuital laws could be translated into magnetic circuital laws. The theory and equations of the MEC can be also derived directly from basic magnetism laws like Ampere's and Gauss's laws but mentioning the analogy with electrical circuits is done to aid with understanding the concept.

Generating enough elements to reflect all properties of a device on the one hand, while avoiding having too many elements that could unnecessarily slow down the computation without significantly gaining in accuracy, is the central idea in creating a magnetic equivalent circuit for a given electromagnetic device [120]. The compromise between the two contradictory requirements is a magnetic circuit that reduces calculation time for a given level of precision. In addition, the ultimate goal and motivation is not to completely replace the FEM but rather to provide an alternative method that can perform quicker computations with a decent level of accuracy. Usually, the computation time is not a serious concern if only one or two calculations are to be performed, but, practically, when designing an electromagnetic device an optimization study is performed to find the parameters that can provide the best performance. Conducting such studies means sweeping through multiple parameter values, and consequently there will be a lot of computations to be done; one for each set of values. Therefore, it is preferred to have a lightweight and quick method to perform the large number of calculations, and then when the parameters are fixed the FEM can be used to perform the final accurate predictions. Moreover, as shall be seen in the coming sections, nonlinear calculations are usually needed to take the magnetic saturation into account, and with large enough systems, the nonlinear calculations using FEM could take an extensive amount of time which rises another incentive to search for quicker methods to perform such calculations. Then, it is well known that when the size of the FEM model is large enough, the computer specification requirements increase significantly, so

when the computational resources are limited, another advantage arises from using the MEC method. Eventually, when using the term "lightweight" to describe the MEC method, the description not only points to the short computation time but also to the ability to run the model on personal computers with average specifications.

Flux tubes are the foundation of the MEC method, and it is assumed that the flux is constant throughout an elementary flux tube. They are considered as geometrical figures where no lines of flux cross their sides and all lines of flux are perpendicular to their bases (see Fig. II-9). Because lines of equal magnetic scalar potential, u, are perpendicular to lines of flux, φ, the bases of flux tubes are equipotential planes. The MMF drop is equivalent to the magnetic scalar potential difference between the bases. In general, in a flux tube with no current, the ratio of potential difference at the ends of the flux tube to the flux through it is a function of flux tube shape and medium properties. This ratio can be defined as the magnetic reluctance of the flux tube connecting equipotential planes holding nodes i and j and is equal to:

$$R_{ij} = \frac{u_i - u_j}{\varphi_{ij}} = \int_0^l \frac{dx}{\mu(x)\, A(x)} \tag{II-6}$$

where A is the cross-sectional area of the flux tube and it can be either constant throughout the whole tube or as a function of a position parameter, l is the total length of the tube, and μ is the magnetic permeability of the flux tube, where it can be constant, a function of position if the element's medium is nonhomogeneous, or a nonlinear function of the magnetic field in case of magnetic saturation. The magnetic permeance is the inverse of the reluctance and is given by:

$$P_{ij} = \frac{1}{R_{ij}} \tag{II-7}$$

The magnetic sources, like permanent magnets or coils with current, are also represented as circuit elements and are connected to the reluctance elements either in series as MMF sources or in parallel as flux sources. Consider the permanent magnet shown in Fig. II-10, where it has a rectangular shape with a cross-section A, perpendicular to its magnetization, and length l, and it can be represented using either a flux source φ_{pm} in parallel with its leakage reluctance R_{pm} or using an MMF source F_{pm} in series with R_{pm}. It is worth noting that the PM will be considered operating in the linear region of the 2nd magnetization quadrant.

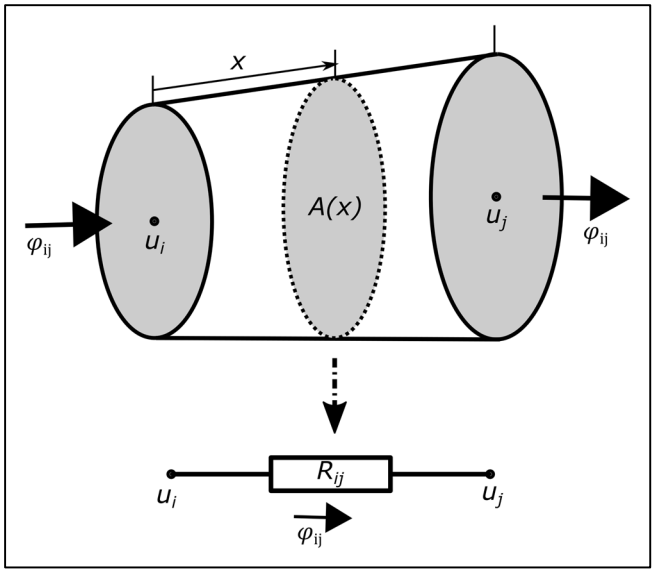

Fig. II-9 A flux tube delimited by two nodes and its equivalent circuital element representation.

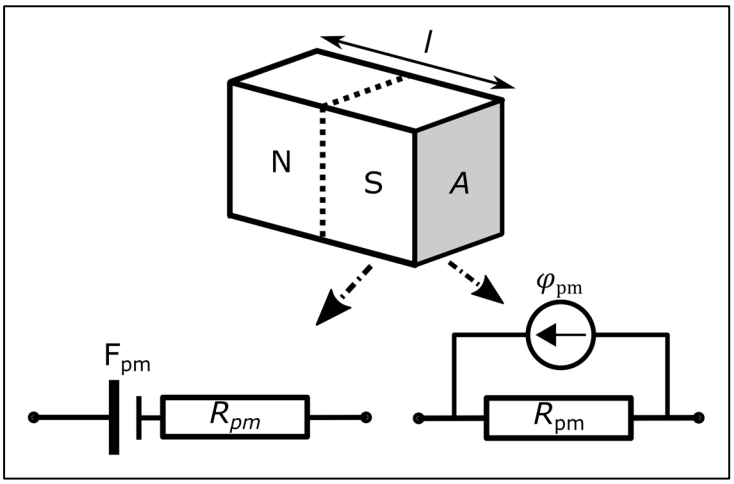

Fig. II-10 A permanent magnet and its equivalent circuital elements representations.

The equations of the circuit parameters related to the permanent magnet are given by:

$$\varphi_{pm} = B_r \cdot A \tag{II-8}$$

$$R_{pm} = \frac{l}{\mu_0 \cdot \mu_{rpm} \cdot A} \tag{II-9}$$

$$F_{pm} = R_{pm}\,\varphi_{pm} = \frac{B_r\,l}{\mu_0 \mu_{rpm}} \tag{II-10}$$

where B_r is the magnetic remanence of the PM, μ_0 is the vacuum's magnetic permeability, and μ_{rpm} is the relative permeability of the PM or the recoil permeability (refer to section 1.3).

Eventually, after getting introduced to the main elements that form the MEC, the study domain of the structure that is being modeled is divided or meshed into elementary elements, where the number of elements is chosen to be sufficient for obtaining results with good accuracy. As this work is mainly concerned with modeling magnetic gears, Fig. II-11 shows a 2D cross-section of a surface-mounted permanent magnet magnetic gear meshed using elementary reluctance elements and MMF sources. Some observations can be made when first looking at the sketch in Fig. II-11, for example, different regions hold different number of elements, and the elements at the air gaps seem to be not fully conformal. However, these questions will be tackled in the following sections, but for now, the next step is to introduce the formulations used to construct the system of equations and solve the problem. The work is aiming at constructing a 3D MEC model, and the next sections will try to treat the problem as so. Finally, a 3D MEC implementation and evaluation for a radial field magnetic gear has been proposed in [121], [122].

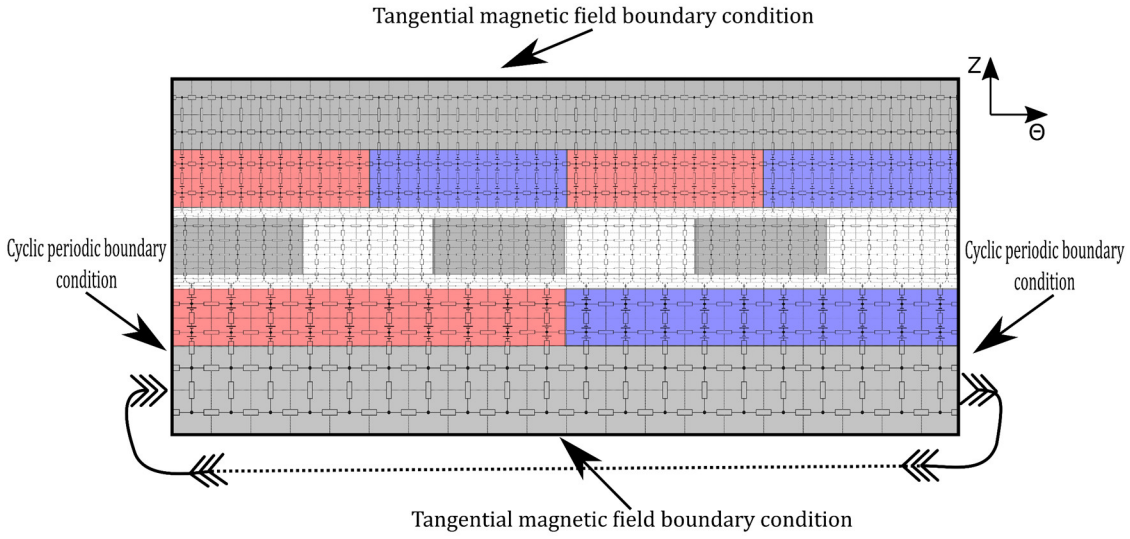

Fig. II-11 A 2D cross-section of a surface mounted PM magnetic gear meshed using reluctance elements.

3.1. The Nodal Formulation

Consider the sketch of a simple 3D MEC, shown in Fig. II-12, with nodes connected using permeances P_{ij}, and a magnetic scalar potential value is assigned to each node. The equivalent of Kirchhoff's Current Law for magnetics is given by:

$$\sum_{j=1}^{k} \varphi_{ij} = 0 \tag{II-11}$$

In other words, the sum of the magnetic fluxes entering or exiting a node i through a k number of branches is zero. Applying this law, in addition to the equivalent of ohm's law for magnetism (II-6), to each node of the magnetic circuit will generate a set of equations which will be used to get the magnetic potential value at each node of the defined domain. The permeances are the main parameters that characterize the flux tubes, and the unknowns to be found are the values of the magnetic scalar potential at each node, and since permeances are used for this formulation, a magnetic equivalent circuit using the nodal formulation will be called a Permeance Network (PN). The system of equations to be assembled and solved is given by:

$$[P]_{nnxnn}[U]_{nnx1} = [\varphi]_{nnx1} \tag{II-12}$$

where [P] is the permeance matrix containing all the permeance values constituting the flux connections across the whole network, [U] is the vector of unknowns representing the magnetic scalar potential at each node where the magnetic potential difference between two adjacent nodes i and j forming a flux tube equals to the MMF drop across this flux tube. Finally, $[\varphi]$ is the excitation vector representing the flux of the magnetic sources in the network (i.e., the flux of permanent magnets). The total number of nodes is represented by "nn", where a row "i" in the permeance matrix represents the nodal equation at node "i". This system of equations can be depending on the type of the permeances a linear or nonlinear system. For example, if the magnetic saturation is ignored and the values of the relative permeability in the regions are considered constant, the system can be treated as a linear system of equations. The nodal equation at node "i" is given by:

$$U_i \sum_{\substack{j=1 \\ j\neq i}}^{c} P_{ij} - \sum_{\substack{j=1 \\ j\neq i}}^{c} U_j P_{ij} = \sum_{\substack{j=1 \\ j\neq i}}^{c} \varphi_{ij}^{source} \tag{II-13}$$

where P_{ij} is the permeance connecting nodes i and j, φ_{ij}^{source} is the flux source, if present, in the branch connecting nodes i and j, and "c" is the number of the nodes directly adjacent to node i where it might vary depending on the position of node i.

For instance, if a tangential magnetic field border condition is present, then all nodes on the boundary will have fewer connections than nodes inside the network (see Fig. II-11). Usually, for rotating or moving machines, tangential magnetic field boundary conditions are applied two the lateral surfaces of the domain across two directions, and a cyclic periodic or anti-periodic boundary condition is applied to the lateral surfaces of the remaining direction. For example, taking the sketch in Fig. II-12, if a cyclic boundary condition is applied to the nodes on the ends of the circumferential θ direction, nodes 1 and 4 will be connected to nodes 3 and 6 respectively using permeances, and the same goes for all the nodes on the circumferential ends. The total number of nodes in a 3D PN then becomes equal to:

$$nn_U = nn_\theta \cdot nn_z \cdot nn_r \tag{II-14}$$

where nn_r, nn_θ, and nn_z represent the number of divisions in the radial, circumferential, and axial directions respectively. It is worth noting that the system followed for numbering the nodes in the network and the matrix is described in the sketch shown in Fig. II-12, and it will be adopted for the 3D PN models that will be presented throughout the work.

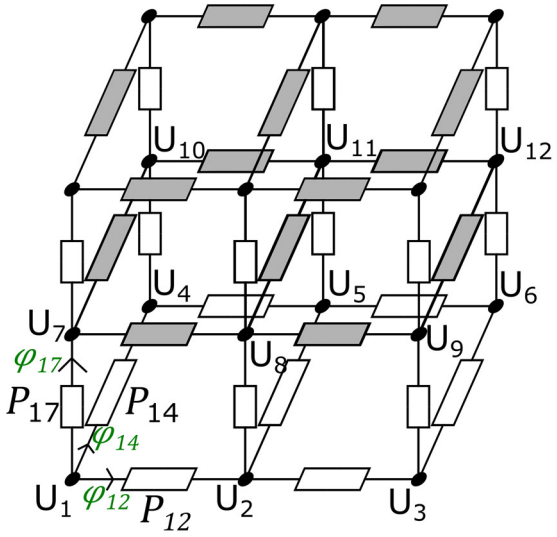

Fig. II-12 A simple sketch for a 3D PN with 18 nodes.

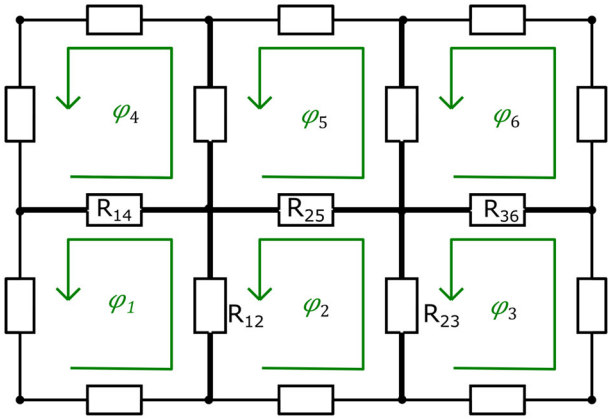

Fig. II-13 A simple sketch for a 2D RN showing its numbered flux loops.

3.2. The Mesh Formulation

Similarly, the equivalent of Kirchhoff's Voltage Law for magnetics is given by:

$$\sum_{\mu=1}^{k} F_{\mu} = 0 \tag{II-15}$$

where $F_{\mu} = u_i - u_j$, is the FMM drop across a branch in the network. Namely, the sum of magnetic potential differences around any closed loop is zero. Consider the sketch of a simple 2D network of reluctances shown in Fig. II-13, and by applying the laws in (II-6) and (II-15), a system of equations can be generated with the unknowns being the flux values around the loops, and the main matrix being composed of the reluctances that characterize the branches throughout the network. Since reluctances form the main parameter of this formulation, the term Reluctance Network (RN) will be used to describe an MEC that uses the mesh formulation. It is good to note that many references use the term "reluctance network" to name any MEC regardless of the formulation. Then, the system of equations for a RN can have the form:

$$[R]_{nnxnn}[\varphi]_{nnx1} = [E]_{nnx1} \tag{II-16}$$

where [R] is the permeance matrix containing all the permeance values constituting the flux connections across the whole network, $[\varphi]$ is the vector of unknowns representing the magnetic flux around any closed loop of the network. Finally, $[E]$ is the excitation vector representing the MMF of the magnetic sources in the network. The total number of nodes of the system is "nn",

where a row "i" in the reluctance matrix represents the mesh equation at loop "i". The mesh equation at loop "i" is given by:

$$\varphi_i \sum_{j=1}^{c} R_{ij} - \sum_{j=1}^{c} \varphi_j R_{ij} = \sum_{j=1}^{c} MMF_{ij}^{source} \tag{II-17}$$

where R_{ij} is the reluctance bordering both loops i and j, MMF_{ij}^{source} is the flux source (if present) in the branch adjacent to both loops i and j, and "c" is the number of the loops directly adjacent to loop i where it might vary depending on the position of loop i. The boundary conditions could be applied similar to the nodal formulation case. The 3D implementation of the mesh formulation is a little bit less trivial than the nodal formulation because flux loops should be assigned to certain surfaces in the third dimension, whereas for the nodal formulation it is just connecting the nodes of different planes. Under the assumption that a tangential magnetic field boundary condition is applied to the lateral surfaces of two axes directions, and a cyclic boundary condition is applied to the lateral surfaces of the remaining axis direction, the number of nodes of a 3D RN can be expressed as:

$$nn_{\varphi} = nn_{\theta} \cdot (nn_z - 1) \cdot (2nn_r - 1) \tag{II-18}$$

Hence, for a large number of divisions across the three directions, the number of nodes of a 3D RN becomes significantly greater than that of a 3D PN and that is for the same accuracy. Therefore, the nodal formulation approach will be adopted for creating 3D models in the following sections, and a quasi-3D approach using the mesh formulation will be presented at the end of this chapter. It is important to mention that this work's focus is more directed towards 3D modeling because it will tackle the modeling of structures with an axial field topology, where 3D effects are much more relevant and important usually. Before moving on to the next sections, some in-depth references that could be referred to on the subject of MEC are [120], [123]–[126]. In addition, a pedagogical reference on 2D MEC that includes a comparison between the two formulations and a full simulation code using MATLAB could be found in [127]. Finally, a comparison between the mesh and nodal formulations can be found in [128].

4. The Aspects of Implementing a 3D MEC

After presenting the theoretical basics and formulations of the MEC, it is important to discuss the actual implementation of this method. For simple small networks, the implementation is

quite straightforward and easy, but for the case of 3D modeling of axial field magnetic gears, the network can be quite complex with significantly large size. Hence, many numerical aspects should be addressed to optimize the code because the goal is still to acquire a lightweight modeling method. In addition, the treatment of many other important aspects like motion simulation, mesh sizing, and most importantly magnetic saturation should be conducted. The following sub-sections will try to address the implementation of all the important aspects, and although most of the details that will be mentioned are valid for the two MEC formulations, the following parts will mainly suppose the nodal formulation as the one that is being used. Moreover, the numerical implementation of the 3D MEC has been done exclusively using the MATLAB coding environment.

4.1. Non-Conformal Meshing and Motion Simulation

Similar to the principle of mesh relaxation presented previously for the FEM, changing the size of the MEC elementary blocks may be required to fit the components properly or to create a denser mesh in certain areas. In addition, there's something specific to MEC to facilitate the equations generation and permeances identification, one elementary block can't be a part of two regions at the same time, it should perfectly fit into a region with homogeneous medium properties. In this way the boundary between two regions can be treated easily as the series connection of two permeances of known values. Therefore, in structures like magnetic gears where there are three rotors where each rotor possesses different poles dimensions, it will be hard to find a single elementary dimension that fits all the regions, and if this element is found it will be so small where the total number of nodes of the system will be extremely high.

For the magnetic gear application, its geometry was divided into three zones corresponding to the three different rotors (i.e., the low-speed rotor, the high-speed rotor, and the fixed member). Each zone has a different number of circumferential and axial elements, and it is important to note that to maintain the mesh conformality in a single zone, all the elements in that zone should share the same dimension values in at least two directions. To illustrate, consider the example of an axial field magnetic gear whose 2D cross section is shown in Fig. II-11, the mesh elements of the same zone have the same length across the radial and circumferential directions, but different lengths across the axial direction could be found while still respecting the boundaries and conformality of the mesh in that zone. Eventually, this will create different meshes in the regions that don't conform at the interface surface, which is the

air gap that separates the rotors, and the mesh now is considered a non-conformal mesh across the circumferential direction. Having a non-conformal mesh is definitely not a weak point in the method, instead if treated properly it can be a very powerful technique to tune the size of the mesh and optimize the problem similar to the mesh relaxation in FEM. In fact, it might be even more optimal to have a non-conformal mesh across the two other directions, but the complexity of the method will increase in turn.

Now, the challenge becomes in connecting the permeance blocks at the air gap interface surface, and multiple approaches can be found in the literature on how to treat this issue. In [129], the authors proposed creating an interpolation surface at the interface between the two regions, with the nodes on both sides projected on it, then, compute the potential values using flux continuity equations and first-order interpolation. The issue with this method is that the system size will vary (slightly) at each motion step where the positions of the nodes will change, and its use is exclusive for the nodal formulation. The method proposed in [130] is what has been adopted for this work to treat the non-conformal interface. It is based on overlapping the permeances between immediately adjacent elements. Overlapping is done by multiplying the connecting permeance by a coefficient that depends on the overlapping distance (or angle) between the elements in contact. Fig. II-14 shows the air gap representing the interface between two regions with different element sizes. The position of every element at each side is defined by an interval ($[x_i, x_{i+1}]$ and $[y_j, y_{j+1}]$) where the intervals are in the range of $[0, L_{per}]$. Then, according to this position, the overlapping intervals, or the nodes that are in contact, from both sides can be determined. Finally, the permeance between any two nodes in contact (i and j) can be determined using the equations below:

$$P_{i1} = (2P_{z1}) \cdot \frac{y_{j+1} - x_i}{x_{i+1} - x_i} \tag{II-19}$$

$$P_{j2} = (2P_{z2})] \cdot \frac{y_{j+1} - x_i}{y_{j+1} - y_j} \tag{II-20}$$

$$P_{i,j} = \frac{P_{i1} \cdot P_{j2}}{P_{i1} + P_{j2}} \tag{II-21}$$

where P_{z1} and P_{z2} are the permeances in the axial direction for zones 1 and 2 respectively.

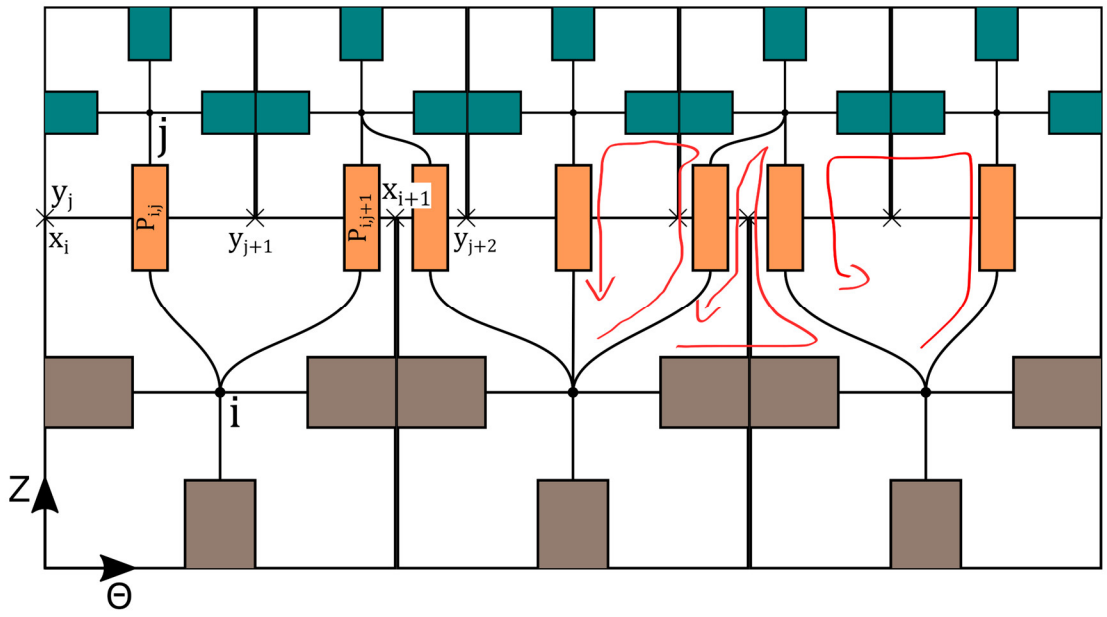

Fig. II-14 Interface between two regions with non-conformal meshes.

To simulate the motion of one of the rotors or even both, the connections between the two regions should be reset, and then the intervals defining the position of each node are edited according to the new position of the rotor. Consequently, the overlapping intervals are determined again, and the connection is done using the same equations defined. It is possible to apply this method to the mesh formulation approach by detecting the closed loops formed by the interpolated permeances connecting the two zones and treating them as new unknowns to be found. However, since the number of the closed loops at the interface will vary depending on the position of the two zones, the size of the system will vary slightly at each step which can be easily handled.

4.2. Choosing the 3D MEC Mesh Parameters

To choose the number of divisions in each region and direction, some testing is required to realize the satisfying results and performance. The three parameters to choose for the mesh of the network are the number of divisions in the radial direction (nn_r), circumferential direction (nn_θ), and axial direction (nn_z). Depending on the type and structure of the device, the configuration and the importance of each parameter will vary. For example, in an axial field flux focusing configuration, the most important and the largest of the three parameters is the number

of divisions in the circumferential direction, and the lower this number is the worse is the accuracy of the predicted torques and forces. On the other hand, for a surface-mounted PM axial field structure, nn_z and nn_θ are equally important for the quality of the results. The number of divisions in the radial direction is the least of the three ($nn_\theta, nn_z \gg nn_r$), but it will gain more importance and will increase when considering the air envelope surrounding the structure which is required to model the end-effects. A small increase in nn_r increases massively the total size of the system, so it is required to choose it as small as possible for any of the cases. To compare the effects of the 3D PN mesh size on the quality of the results, four mesh configurations are chosen to compute the torques developed in an axial field flux focusing magnetic gear, and values generated using a 3D FEM model were used as a reference for the comparison. The four mesh configurations are described in Table II-4, where it can be seen that the number of divisions in the axial and radial directions were maintained the same for the four meshes, and the variation parameter was the number of divisions in the circumferential direction which will highlight the importance of this parameter. The torques generated by the models with different meshes are shown in Fig. II-15.

Table II-4 The configuration of four different 3D PN meshes with the time consumed to compute 31 motion steps.

		nn_θ	nn_z	nn_r	nn_{3d}	Time consumed (sec)
Mesh 1	Zone 1	240	28	3	61056	43.16
	Zone 2	200	18			
	Zone 3	304	33			
Mesh 2	Zone 1	480	28	3	287640	293.9
	Zone 2	400	18			
	Zone 3	2280	33			
Mesh 3	Zone 1	1080	28	3	359640	566.4
	Zone 2	800	18			
	Zone 3	2280	33			
Mesh 4	Zone 1	1800	28	3	775440	2664.26
	Zone 2	3200	18			
	Zone 3	4560	33			

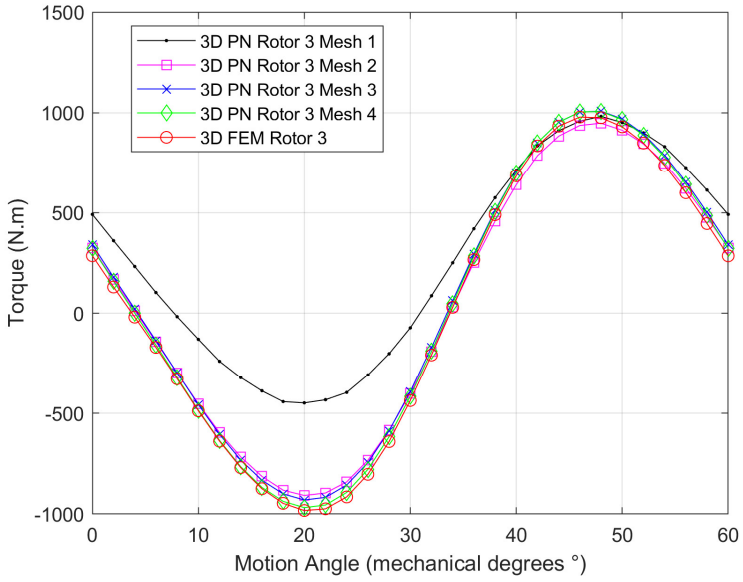

Fig. II-15 A comparison of the torques generated by multiple 3D PN models with different mesh configurations.

The results from Mesh 1 are totally unacceptable, and for the other meshes the results are all acceptable and slightly improving with the increase of the number of nodes. However, the increase in the number of nodes escalated rapidly the computation times, but, beyond the number of nodes of Mesh 2, the increase didn't provide a significant improvement in the results.

4.3. Maxwell Stress Tensor

The Maxwell Stress Tensor (MST) is used to calculate the total electromagnetic forces acting on a volume, and it is a very well-known and established method for calculating forces and torques in electromagnetic devices [131]–[134]. The tensor is a symmetric second-order tensor and can be derived by developing Maxwell's equations and Lorentz's force law. The tensor is expressed using 3D polar coordinates and shown in (II-22). Physically, $\overleftrightarrow{T}$ is the force per unit area or stress acting on a surface, and the entry T_{ij} is the force per unit area in the i^{th} direction acting on the element of surface oriented in the j^{th} direction, so diagonal elements represent pressures, off-diagonal elements represent shears. The more general form of the tensor contains elements related to the electric field, but they have been excluded considering the tensor will be applied on surfaces free of electric charges.

$$\overleftrightarrow{T} = \frac{1}{\mu_0}\begin{bmatrix} \frac{B_r^2 - B_\theta^2 - B_z^2}{2} & B_r B_\theta & B_r B_z \\ B_\theta B_r & \frac{B_\theta^2 - B_r^2 - B_z^2}{2} & B_\theta B_r \\ B_Z B_r & B_z B_\theta & \frac{B_z^2 - B_\theta^2 - B_r^2}{2} \end{bmatrix} \quad \text{(II-22)}$$

The force per unit volume acting on a body can be expressed (while excluding the Poynting vector) as:

$$\vec{f} = \nabla . \overleftrightarrow{T} \quad \text{(II-23)}$$

Then, by applying the divergence theorem, the total electromagnetic force acting on a volume ν becomes:

$$\vec{F} = \oint_S \overleftrightarrow{T} . \vec{n}\, ds \quad \text{(II-24)}$$

The torque developed by the total forces can expressed similarly as:

$$\vec{C} = \oint_S r \times (\overleftrightarrow{T} . \vec{n}\, ds) \quad \text{(II-25)}$$

Now consider the disc volume shown in Fig. II-16, where this volume represents a rotor of an axial field magnetic gear (or any other axial field discoidal electric machine). It is supposed that the magnetic flux density values at the lateral surfaces S_2, S_3, and S_4 are either zero due to boundary conditions or are negligible. Hence, the surface at which the magnetic induction should be evaluated is only the air gap surface S_1. Thus, the elementary electromagnetic force can be developed in the polar coordinates as:

$$dF = \begin{pmatrix} dF_r \\ dF_\theta \\ dF_z \end{pmatrix} = \left(\overleftrightarrow{T}\right)_{S1} . da_{S1} = \frac{1}{\mu_0}\begin{pmatrix} B_r B_z \\ B_\theta B_z \\ \frac{B_z^2 - B_\theta^2 - B_r^2}{2} \end{pmatrix}_{S1} \quad \text{(II-26)}$$

Then, surface integration is performed on every component of the elementary forces shown in (II-26), and since the force in the circumferential direction will develop a torque, the equation of the torque will be immediately applied to get the torque developed on this rotor structure. Finally, the equations of the forces and the torque are expressed in the following equations.

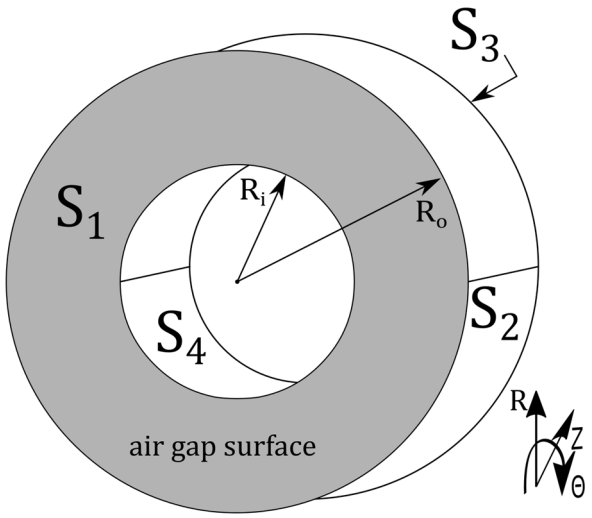

Fig. II-16 A discoidal structure representing a rotor of an axial field magnetic gear.

$$F_r = \frac{1}{\mu_0}\iint \left(B_r(r,\theta)B_z(r,\theta)\right)_{S1} r dr d\theta \tag{II-27}$$

$$C_\theta = \frac{1}{\mu_0}\iint \left(B_\theta(r,\theta)B_z(r,\theta)\right)_{S1} r^2 dr d\theta \tag{II-28}$$

$$F_Z = \iint \left(\frac{B_z^2(r,\theta) - B_\theta^2(r,\theta) - B_r^2(r,\theta)}{2\mu_0}\right)_{S1} r dr d\theta \tag{II-29}$$

Eventually, these equations can be applied numerically by using numerical integration and computing the magnetic induction components at a set of points on the air gap surface S_1, and the smaller the elementary surfaces are (i.e., the smaller the MEC mesh elements), the more accurate the results become. This method can be applied on the surfaces of the two air gaps of a magnetic gear to get the forces and torques on each rotor but by paying attention to the orientation of the air gap surface related to each rotor. It is worth noting that in axial field structures, the force acting in the radial direction is usually negligible and doesn't hold a great importance as compared to the forces in the circumferential and axial directions, where the force acting in the circumferential direction determine the torque developed by the rotor, and the force in the axial direction represents the attraction force between the rotors which holds a great

importance for the analysis of axial field structures. The torques and attraction forces acting on each rotor can be linked using the expressions:

$$F_{z1} + F_{z2} + F_{z3} = 0 \tag{II-30}$$

$$F_{\theta 1} + F_{\theta 2} + F_{\theta 3} = 0 \tag{II-31}$$

It is known that the MST is sensitive to the mesh quality especially at the air gap region which is one of the reasons that makes many people prefer using the virtual works method over it to calculate the forces. However, the main advantage that is acquired by using the MST is that the user is required calculate the magnetic induction values at one surface only and perform a surface integral to get the total forces, but in the virtual works method the computation of the magnetic induction and a volume integral is required over the whole domain. Hence, the easy implementation of the MST during the post-processing is one of the main reasons on why it has been chosen to be used in this work over the virtual works method.

4.4. Magnetic Saturation Consideration: Nonlinear Iterative Solvers

Design criteria should include consideration of magnetic saturation of the soft magnetic materials. It can have a significant impact on the estimation of specific quantities, and its significance varies according to the structure under study, the type of permanent magnets, the air gap length, and the materials being employed in the model. For example, in the case of magnetic gears using strong rare-earth magnets with small air gap length to acquire the highest torque, the magnetic saturation can have a large effect on the overall performance because the modular pieces of the middle member become highly saturated, and hence it can't be simply ignored. Another example is that in the flux focusing configuration the magnetic saturation can have a larger impact than in a surface-mounted PM configuration because the length magnetic equivalent air gap in the latter is much larger.

As a first step, a model for the B(H) curve has to be selected so that the relative permeability may be determined for any given magnetic field value H. An analytical B(H) curve model is selected to make the numerical implementation of the 3D MEC easier where the B(H) curve is plotted in Fig. II-17, and thus the relative magnetic permeability of the soft magnetic materials may be calculated using the formula shown in (II-32). This formula is provided by the FLUX software as well, and it has been used for the FEM models. Its parameters have been chosen to make the magnetic properties of the modeled material close to that of an isotropic silicon steel.

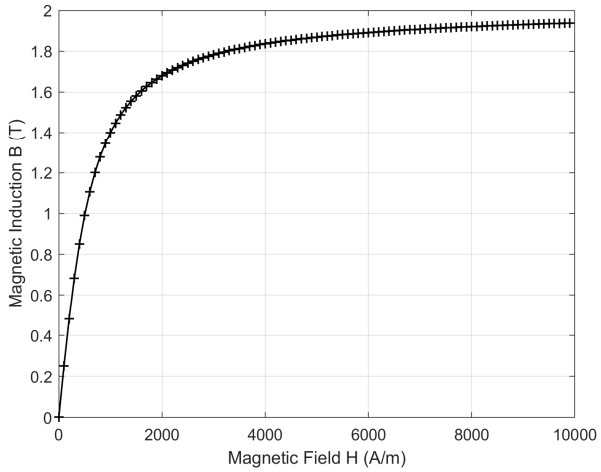

Fig. II-17 The adopted analytical B(H) curve used for representing the soft magnetic materials.

$$\mu_{rf} = 1 + \frac{2J_s}{\mu_0 \pi H} \arctan\left(\frac{\pi(\mu_{ri} - 1)\mu_0 H}{2J_s}\right) \tag{II-32}$$

where $J_s = 1.99T$ is the saturation magnetization and $\mu_{ri} = 2000$ is the relative permeability at the origin. Moreover, if the user wants to use experimental B(H) data plots, they can import the plot and use some form of interpolation like spline to get the relative permeability value for any magnetic field value. Meanwhile, implementing the nonlinear material properties into the MEC will turn the main system of equations into a nonlinear system that will require an iterative nonlinear solver because now the permeance values depend on the value of the magnetic field and eventually the value of the magnetic potential in the nodes. The development of the equations in the following sections will mainly treat the nodal formulation. Thus, the multivariate nonlinear function that is derived from (II-12) is given by:

$$\mathbf{F}(\mathbf{U}) = \mathrm{P}(\mathbf{U}) \cdot \mathbf{U} - \varphi(\mathbf{U}) = 0 \tag{II-33}$$

An important aspect to note and not miss is that the excitation vector $\boldsymbol{\varphi}$ is also dependent on the value of the magnetic potential which is not the case when developing the mesh formulation. The two nonlinear solvers that are selected for solving the problem and are discussed in the following subsections are the fixed-point iteration method and the Newton-Raphson method. Some in-depth references on the subject of nonlinear solvers can be found in [135]–[138].

4.4.1. Fixed-Point Iteration Method

When using the fixed-point iteration approach, the nonlinear system in (II-33) is rearranged to have the form $\mathrm{U} = \gamma(\mathrm{U})$ where $\gamma(\mathrm{U})$ is a nonlinear function in the components of the vector of unknows U. An initial solution or guess for the vector of unknowns is then chosen and the iteration starts by solving the system:

$$\mathbf{U}_{k+1} = \gamma(\mathbf{U}_k) = \mathrm{P}^{-1}(\mathbf{U}_k)\varphi(\mathbf{U}_k), \qquad k \geq 0 \tag{II-34}$$

where the initial solution $\mathbf{U_0}$ is determined by solving the system in (II-12) as a linear system of equations through setting a constant initial value into μ_{rf}. The choice of the initial starting point in the fixed-point method is not very crucial and might not impact the convergence unlike the situation in Newton's method, but it has been found that different starting points can change slightly the total computation time. Hence, after doing multiple tests with multiple starting points, the chosen initial value of μ_{rf} was 1. Then, the convergence of the method is determined when a chosen error value drops below a certain threshold. There are several error equations that can be chosen as a stopping criterion, and usually depending on the problem the user chooses the error equation and threshold value that best suit the requirements. For the problem in this work, two error criteria could be possibly used:

$$\epsilon_1 = \frac{\|\mathbf{U}_{k+1} - \mathbf{U}_k\|}{\|\mathbf{U}_{k+1}\|} < \epsilon_{th} \tag{II-35}$$

$$\epsilon_2 = \|\mathbf{F}(\mathbf{U}_k)\| < \epsilon_{th} \tag{II-36}$$

Both criteria worked properly with the fixed-point method, but it has been found that using ϵ_1 as the error equation of the fixed-point method provided more stability. To illustrate, after running multiple simulations and trying the two criteria, the error value provided by ϵ_1 reflected the accuracy state of the system in a better fashion because usually the lower the error value is the better the accuracy of the results, but this wasn't always the case when using ϵ_2 with the fixed-point method. The value of the error threshold was chosen at $\epsilon_{th} = 10^{-4}$, and it was the most reasonable value that provided relatively decent accuracy with good computation times. This method will be tested, and the results with computation times will be shown in the following sections. A flowchart of the process of using the fixed-point method to solve the nonlinear PN problem is shown in Fig. II-18.

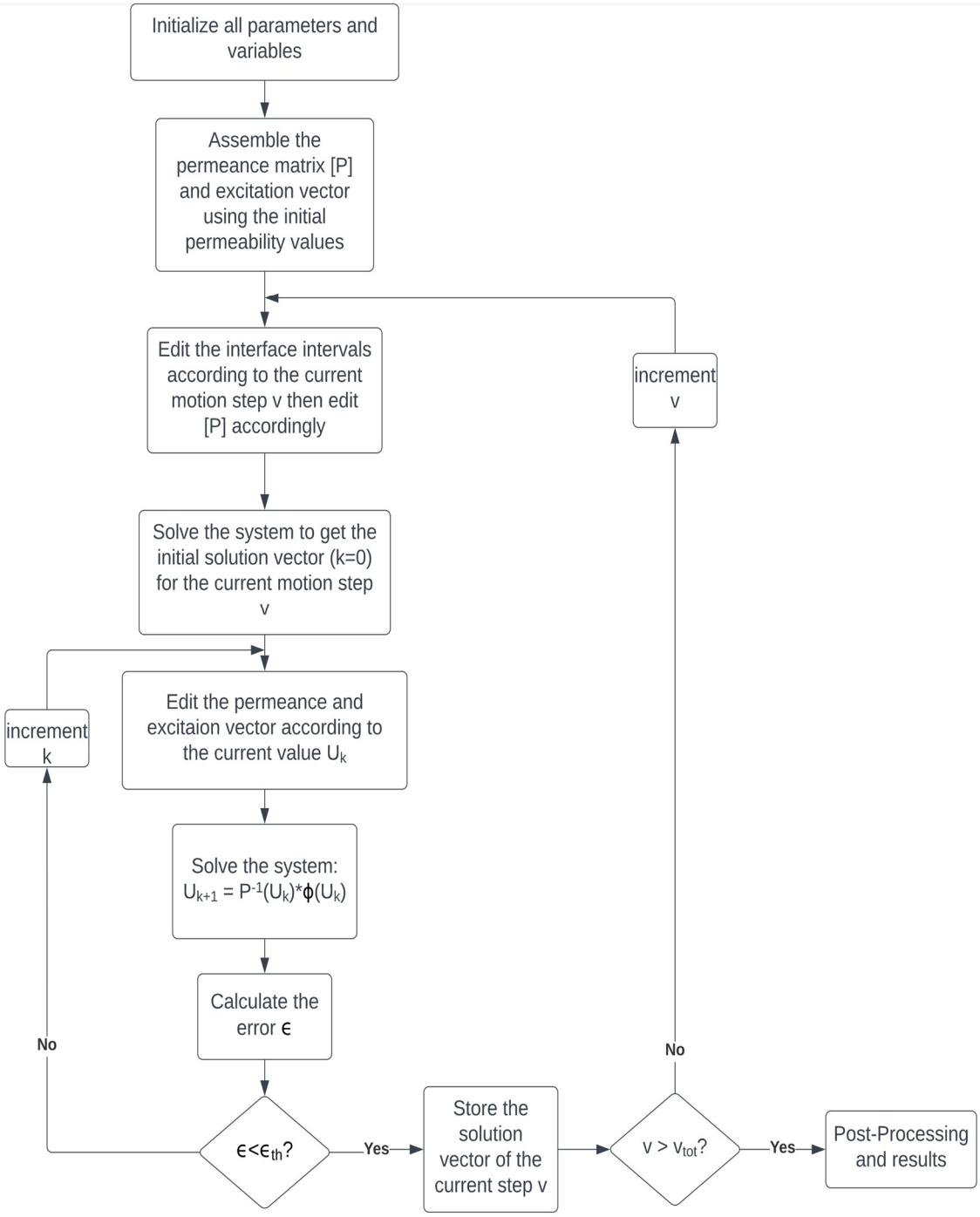

Fig. II-18 Flowchart of the algorithm to implement the fixed-point method for solving a nonlinear PN problem.

4.4.2. Newton-Raphson Method

The Newton-Raphson method or simply Newton's method is probably the most popular and efficient method for solving nonlinear systems of equations, and it will start by approximating the function $\mathbf{F}(\cdot)$ by its first-order Taylor expansion around $\mathbf{U}_k$:

$$\mathbf{F}(\mathbf{U}) \approx \mathbf{F}(\mathbf{U}_k) + \mathbf{J}(\mathbf{U}_k) \cdot (\mathbf{U} - \mathbf{U}_k) \tag{II-37}$$

where $\mathbf{J}(\mathbf{U}_k)$ is the (nn x nn) Jacobian matrix of $\mathbf{F}(\cdot)$ evaluated at $\mathbf{U}_k$:

$$\mathbf{J}(\mathbf{U}_k) = \frac{\partial \mathbf{F}}{\partial \mathbf{U}^{\mathrm{T}}}(\mathbf{U}_k) \tag{II-38}$$

with entries:

$$\mathrm{j}_{\mathrm{i,s}} = \frac{\partial F_i}{\partial U_s} \tag{II-39}$$

Consider the sketch shown in Fig. II-19 describing the connections of a node present in a 3D PN to its neighbors with an MMF source E_{pm} present at one of the branches. The development of the equations on node 1 of this sketch is just for demonstration, but the number of connections to the node and the number of excitation elements present might all vary throughout the network and the equations should be edited accordingly. Using (II-33), the elementary function F at node 1 can be expressed as:

$$F_1(U) = U_1 \sum_{\substack{j=0 \\ j\neq 1}}^{6} P_{1j} - \sum_{\substack{j=0 \\ j\neq 1}}^{6} U_j P_{1j} - P_{10} E_{pm} = 0 \tag{II-40}$$

The row number 1 of the Jacobian matrix has only 7 nonzero elements corresponding to the number of magnetic potential elements present in $F_1(U)$. The first nonzero element corresponding to the potential of node 1 can be expressed as:

$$\frac{\partial F_1}{\partial U_1} = \sum_{\substack{j=0 \\ j\neq 1}}^{6} P_{1j} + \sum_{\substack{j=0 \\ j\neq 1}}^{6} \frac{\partial P_{1j}}{\partial U_1} \cdot (U_1 - U_j) - \frac{\partial P_{10}}{\partial U_1} E_{pm} \tag{II-41}$$

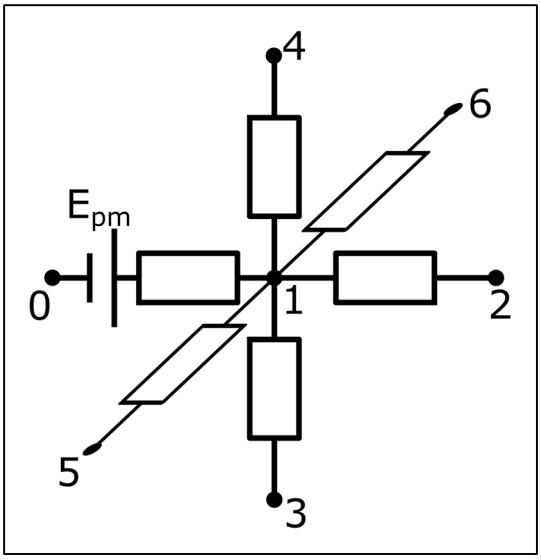

Fig. II-19 A magnetic potential node in a 3D PN connected to its neighbors.

Consider the partial derivative of the permeance P_{12} with respect to U_1, using the chain rule this term can be expressed as:

$$\frac{\partial P_{12}}{\partial U_1} = \frac{\partial P_{12}}{\partial \mu_{r_{12}}} \frac{\partial \mu_{r_{12}}}{\partial H_{12}} \frac{\partial H_{12}}{\partial \varphi_{12}} \frac{\partial \varphi_{12}}{\partial U_1} \tag{II-42}$$

where $\mu_{r_{12}}$, H_{12}, and φ_{12} are the relative permeability, magnetic field, and magnetic flux through branch connecting nodes 1 and 2.

Each one of these partial derivatives can then be calculated starting with the term $\frac{\partial P_{12}}{\partial \mu_{r_{12}}}$ which is a constant that can expressed as:

$$\frac{\partial P_{12}}{\partial \mu_{r_{12}}} = \frac{P_{12}}{\mu_{r_{12}}} = \alpha \tag{II-43}$$

Then, the derivative of the relative permeability with respect to the magnetic field can be deduced from the $\mu(H)$ relationship. If this relationship is not available analytically, the derivative can be found numerically from the data plot of the material. Hence, this term will be also a constant and will be called β. The derivative of the magnetic field with respect to the flux can be expressed as:

$$\frac{\partial H_{12}}{\partial \varphi_{12}} = \frac{1}{P_{12} \cdot \ l} \tag{II-44}$$

where l is the length of the permeance corresponding to the connection of nodes 1 and 2. Finally, the derivative of the flux through branch 1-2 with respect to the potential at node 1 is given by:

$$\frac{\partial \varphi_{12}}{\partial U_1} = \frac{\partial P_{12}}{\partial U_1} \cdot (U_1 - U_2) + P_{12} \tag{II-45}$$

At this stage combining the equations (II-42) to (II-45) leads to the final equation:

$$\frac{\partial P_{12}}{\partial U_1} = \frac{\alpha \, \beta \, P_{12}}{l \, P_{12} - \alpha \, \beta (U_1 - U_2)} \tag{II-46}$$

Similarly, all the terms of the $\frac{\partial F_1}{\partial U_1}$ equation can be calculated, and consecutively all the elements of the Jacobian can be found but considering the position of each node and the nature of each equation while paying attention to the treatment of the permeances connecting the iron regions to the PM regions.

The following step in Newton's method is considering that the next evaluation point $\mathbf{U}_{k+1}$ should be chosen so that the right-hand side of (II-37) equals to zero. Thus, the computation done at each iteration is:

$$\mathbf{U}_{k+1} = \mathbf{U}_k - \mathbf{J}^{-1}(\mathbf{U}_k)\mathbf{F}(\mathbf{U}_k) \tag{II-47}$$

The Jacobian matrix is not directly inverted, and the following linear system is solved instead:

$$\mathbf{J}(\mathbf{U}_k)\Delta\mathbf{U}_k = -\mathbf{F}(\mathbf{U}_k). \tag{II-48}$$

where $\Delta\mathbf{U}_k = \mathbf{U}_{k+1} - \mathbf{U}_k$. The conditioning of the Jacobian matrix is very important for this method and so is the choice of the initial solution. To improve the convergence rate of the system and avoid any divergence, a damping factor was introduced into the update equation. The damping factor λ was chosen separately at each iteration ensuring that the norm of $\mathbf{F(U)}$ is being minimized at each step ($\|\mathbf{F}(\mathbf{U}_{k+1})\| < \|\mathbf{F}(\mathbf{U}_k)\|$). With $0 < \lambda \leq 1$ the update equation becomes:

$$\mathbf{U}_{k+1} = \mathbf{U}_k + \lambda \, \Delta\mathbf{U}_k \tag{II-49}$$

Concerning the stopping criterion for this method, it has been found that the error ϵ_1 wasn't consistently decreasing with each step leading to divergence most of the times even with the damping factor. Hence, since the damping method is already ensuring the minimization of the norm of $\mathbf{F(U)}$ at each step, it was more suitable to use error equaiton ϵ_2 as the stopping criterion. The error threshold is again chosen to be at 10^{-4}. Meanwhile, the choice of the initial solution for the problem, or the initial value of the relative permeability of the soft magnetic materials. was trickier than the case of the fixed-point method because the convergence rate of the Newton's method is known to be dependent and sensitive to the initial solution value. Hence, after performing multiple simulations, it was found that a value between 500 and 1000 is the best choice for the value of the initial relative permeability, where a value in this range ensures convergence in the minimal number of iterations per step. Finally, the initial relative permeability value that was chosen to perform the simulations using the Newton's method was 500. Furthermore, one of the more concerning issues with the Newton's method usually is the evaluation of the Jacobian matrix because for some problems the derivation of the functions can be sometimes impossible or very hard to achieve numerically, and even if its computation is possible, sometimes the conditioning of the Jacobian matrix can be poor so its inversion can't be easily achievable. Hence, quasi-Newton approaches are proposed to evaluate an estimation of the Jacobian matrix, and to make the implementation of the whole method feasible. One of the more popular quasi-Newton approaches is the Newton-Broyden method which proposes an estimation of the Jacobian based on an initial guess. For this work and for the PN problem, the computation of the Jacobian matrix was feasible, but its conditioning was poor, so the use of Broyden's method was investigated to see the possibility of acquiring and inverting the Jacobian with a lower computational effort. However, the original Newton-Broyden method is not designed for sparse matrices and will not maintain the sparsity of the Jacobian which is very important for this work's problem (check section 4.6), so using it was not possible. Nevertheless, a modified Newton-Broyden method for sparse matrices was proposed in [138], and it was implemented to hopefully overcome the problems caused by the poor conditioning of the original Jacobian, but it didn't converge at all even when tried under different conditions and with different initial Jacobian guesses. Therefore, the original damped Newton's method described in this section was used and implemented for the nodal formulation, and a flowchart describing the implementation is shown in Fig. II-20.

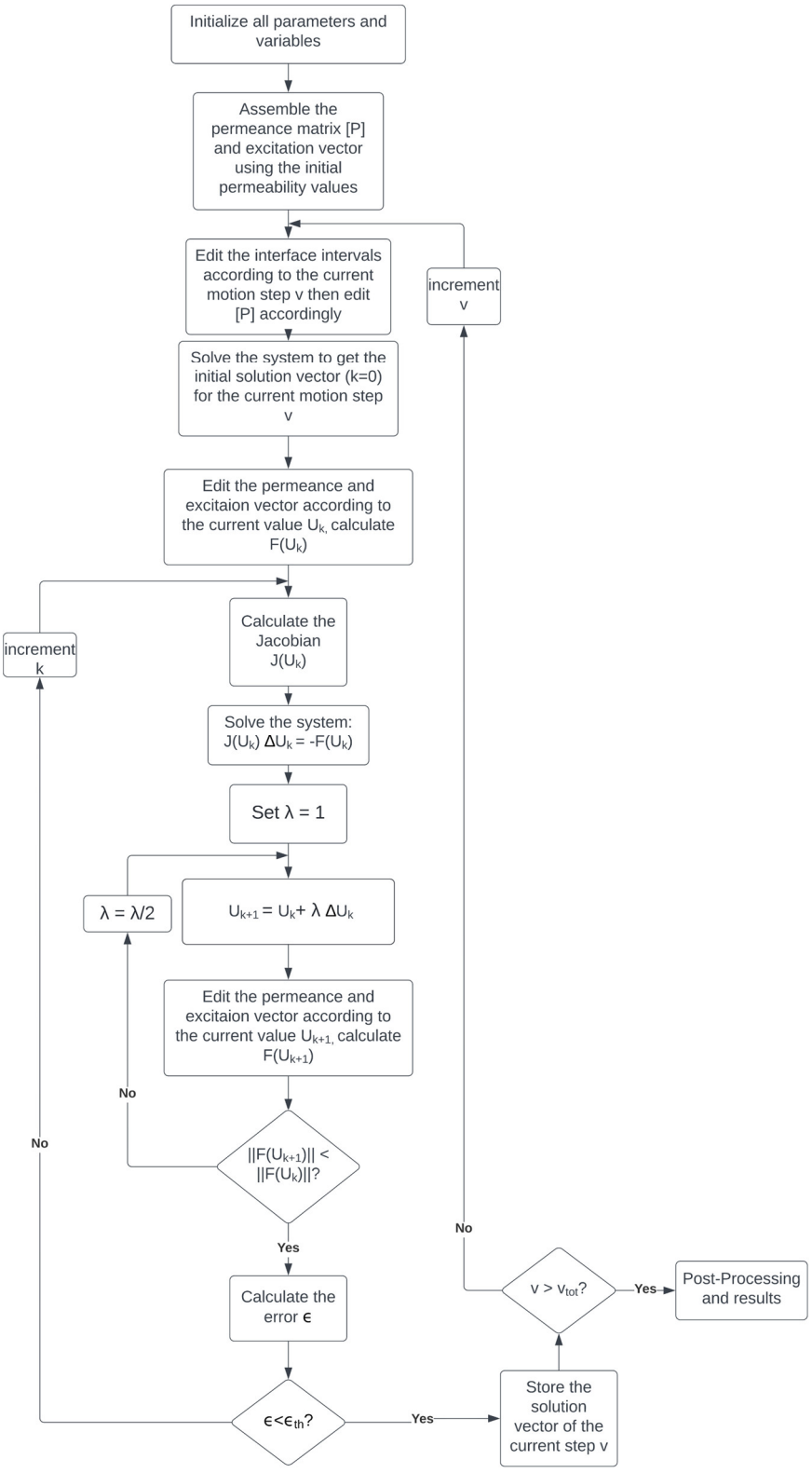

Fig. II-20 A flowchart for the algorithm to adapt the damped Newton's method to solve a nonlinear PN problem.

4.5. The End-Effects in Magnetic Gears

Depending on the application and the structure of the device, the "end-effects" might take on different forms and be caused by various elements, and it has been studied in magnetic gears by some references [139], [140]. End-effects will be described in this study as the flux leakages of the permanent magnets at the structure's lateral surfaces via the surrounding air area. In other words, the flux leakage can be considered as a form of wasted magnetic energy and thus causes reduction in the torque capability of the magnetic gear. End-effects occur along two directions and in two regions: a radial direction corresponding to the air regions at the inner and outer radii (Fig. II-21(a)), and an axial direction corresponding to the air regions at the axial ends of the structure (Fig. II-21(b)). The axial boundary air region could be represented through a 2D model, but the radial boundary air region requires a 3D model which reassures the importance of using 3D models for axial field structures. As for the significance of considering the end-effects in magnetic gears, it has been seen in the first chapter that some researchers reported poor performances from their prototypes as compared to what was predicted through calculations due to doing only 2D simulations and omitting the end-effects in their calculations. In addition, the importance of the end-effects consideration will be illustrated in a following section through a set of simulations and comparisons.

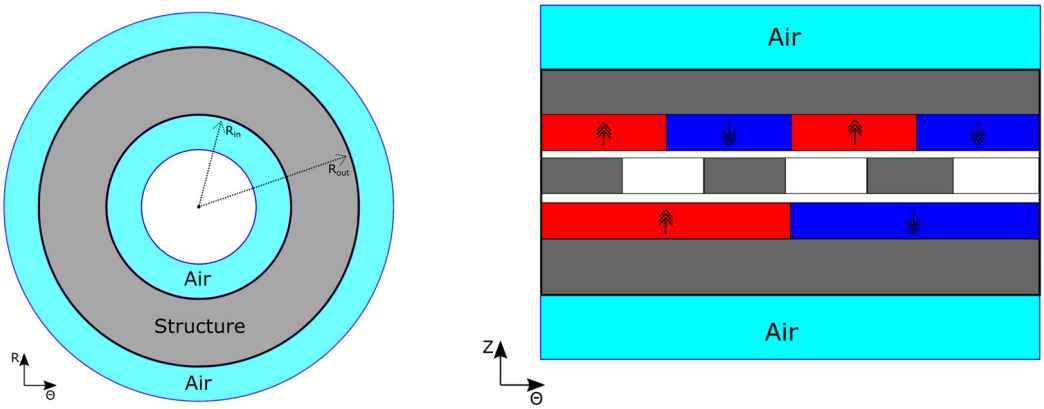

(a) (b)

Fig. II-21 2D projections of an axial field MG with the air envelope on the (a) (R, θ) plane and (b) (θ, Z) plane.

4.6. Numerical Aspects

The concept and equations of the MEC method are simple but applying them on a large scale and in a complex domain will introduce some serious numerical challenges that should be addressed. With having significantly large systems and matrices in the 3D MEC, it is very essential to consider optimizing the code and structuring it properly because if the programming of the MEC model is done without considering the numerical optimizations that accommodate the huge size of the system and the large number of operations, the whole purpose of the MEC method will be defied as it might become very slow or even seize to operate. Hence, below are some of the considerations that were followed to achieve a lightweight implementation of the MEC method knowing that the programming environment was MATLAB coding.

- **Matrix conditioning and rank deficiency:** one of the challenging numerical aspects is the bad conditioning of the matrix $[P]$ (or $[R]$), and the cause of this is the large difference between the singular values of these matrices. For example, in a 3D PN the largest singular value can be in the order of 10^{-4}, but the smallest singular value can reach values as small as 10^{-12}. This is due to the difference in the values of the permeances between the flux tubes with different medium properties and dimensions. The reciprocal condition number is a good way for estimating the condition of a matrix, where the closer this number is to 1 the better and the closer it is to zero the worse. The direct solver of MATLAB given by the function "$mldivide$" was found to be able to deal with the matrices generated by MEC that have a reciprocal condition number in the range of $10^{-7}\sim10^{-9}$. The algorithm of this solver was designed to treat matrix solving in a robust and efficient way, where it can treat each matrix according to its properties and apply suitable factorizations. For the $[P]$ (or $[R]$) matrix, the solver performs LU factorization as a form of preconditioning then proceed to solving. Moreover, an important detail that is good to mention for the solution of the PN models is the importance of defining a potential node that represents the ground of the network. If this step is omitted the matrix $[P]_{nnxnn}$ will have a rank of $nn-1$ which is not very good for an already poorly conditioned matrix. Hence, it is important to specify the potential of one of the nodes as zero which will make the matrix full rank. For example, the first row of matrix $[P]$ can be defined using the equation $10^{-6}\cdot U_1 = 0$ which sets the node number one as the ground point, and the use of the factor 10^{-6} is just to bring

the singular value of the first row closer to the range of the other singular values. In fact, the definition of a ground potential point doesn't contradict with the main PN theory because what is important is not the actual potential values of each node but rather the potential difference between the nodes which represents the MMF.

- **Sparse matrices and memory pre-allocation:** sparse matrices are frequently used in scientific computing, particularly for large-scale optimization, structural and circuit analysis [141]. Data with a large number of zero-valued elements may be stored more efficiently and processed faster in sparse matrices because when a matrix is stored as sparse, it allows the software to store only the nonzero elements and their indices and to eliminate the operations on zero elements. In the case of the 3D MEC, each row of the matrix will have a maximum of 8 to 10 nonzero elements out of nn number of total elements per row and given that nn could be in the order of hundreds of thousands, storing the permeance or reluctance matrix in full storage will be a complete waste if not impossible. For example, a matrix of size (500000 x 500000) will have $2.5 \cdot 10^{11}$ total number of elements, which if stored as single-precision variables will require $4 \cdot 2.5 \cdot 10^{11} = 931.32$ Gigabytes of RAM which is not available in the majority of PCs, and the memory requirement will increase rapidly with the increase of the size of the matrix and in case of using double-precision variables. Therefore, using sparse allocation is crucial for 3D MEC as it will allow to save a tremendous amount of memory and boost the overall performance of the model. It is worth noting that it is not enough to just do the default sparse declaration of the matrix in MATLAB because even though it will not use the full storage, it will reserve the space in memory required to store all the matrix elements. Hence, in addition to declaring the matrix as sparse in MATLAB, the expected number of nonzero elements should be specified, which is a form of memory pre-allocation that instructs the software to reserve only the space required for storing the nonzero elements. Thus, let's consider again the (500000 x 500000) matrix, but this time stored with double-precision variables and as a sparse matrix with memory pre-allocation, the amount of RAM memory required for storing this matrix becomes $500000 \cdot 8 \cdot 8 = 30.52$ Megabytes which is a monumental decrease in memory requirements. Finally, it is also a good practice to pre-allocate the memory for all the other arrays and matrices in the program even if their sizes are not significant.

- **Vectorization and matrix partitioning:** MATLAB is designed and optimized for treating vectors and matrices and replacing loop-based processes with vectorized operations can have a great impact on the overall performance of the program especially when operating on very large matrices. Then, there is the idea of matrix portioning which is very useful when working with large matrices. The concept is to operate on only a portion of the matrix at once, by extracting that portion from the original matrix storing it in a new matrix, performing the desired operations and edits, then returning it to its original place. The use of this concept necessitates that the algorithm treats only a specific part of the matrix at a time because if each operation requires the access of all the data in the matrix the portioning will not be possible. Moreover, matrix portioning is especially useful for the assembly of the permeance matrix in the 3D PN, where there are two levels of partitioning. The first level is extracting all the matrix rows for one radial mesh layer and putting them into a sub-matrix of size ($nn_{rlayer}\ x\ nn$) where $nn_{rlayer} = nn_\theta \cdot nn_z$ is the number of nodes in one radial layer. Then, the second partitioning level is by extracting from the sub-matrix the rows corresponding to one row of mesh nodes and putting it into a sub-sub-matrix that will have the size of ($nn_\theta\ x\ nn$) which will be operated on and returned it to its place in the sub-matrix. The second level of partitioning is done for all the mesh rows in one radial layer, then the sub-matrix of this layer is returned to the original matrix. Finally, the two-leveled partitioning process is repeated for all the radial mesh layers. This whole process might feel overcomplicated or wasteful, but in fact it improves the overall computation time significantly when treating large matrices $nn > 100000$.

5. Nonlinear 3D PN Modeling of an Axial Field Magnetic Gear

Now that the MEC method is properly presented and established, it can be put to the test by applying it to a magnetic gear structure and comparing its performance with respect to a typical 3D FEM model. Thus, a series of case studies will be presented through this section and the following sections to evaluate the potential of the MEC method as a lightweight alternative of the FEM for the 3D modeling of axial field magnetic gears. This section will be mainly concerned in evaluating a 3D nonlinear PN model for an axial field flux focusing magnetic gear (AFFMG) that takes into account the saturation of the soft magnetic materials, and at the same

time a comparison between the fixed-point and Newton's methods will be conducted. The end-effects will not be considered, and its study will be left for the next sections. Fig. II-22 shows the elementary flux tube that was used in the 3D PN models of the axial field magnetic gear structures. It is a six-directional flux tube where the flux is allowed to make an orthogonal contact with its lateral surfaces. The expressions of the permeances that characterize this elementary element are given by:

$$P_R(r) = \frac{\mu \theta_d z_d}{\ln\left(\frac{r + r_d}{r}\right)} \tag{II-50}$$

$$P_\theta(r) = \frac{\mu z_d}{\theta_d} \ln\left(\frac{r + r_d}{r}\right) \tag{II-51}$$

$$P_z(r) = \frac{\mu \theta_d (2.r.r_d + r_d^2)}{2 z_d} \tag{II-52}$$

The modeled AFFMG, shown Fig. II-23, has $p_1 = 6$ PM pole pairs on rotor 1, $p_3 = 19$ PM pole pairs on rotor 3, and $n_2 = 25$ modulating segments on rotor 2. Supposing that rotor 1 is chosen as the high-speed rotor (HSR) , rotor 2 is chosen as the low-speed rotor (LSR), and the rotor holding the modulating segments (rotor 2) is chosen as the fixed member, the gear ratio of the structure becomes $G_r = \frac{p_3}{p_1} = 3.16\dot{6}$. The parameters of the AFFMG were chosen based on an optimization study done in [48] and are summarized in Table II-5.

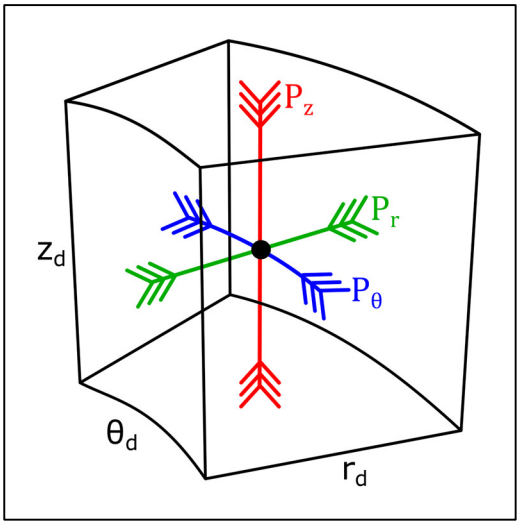

Fig. II-22 The elementary flux tube used in the MEC modeling of the axial field magnetic gear.

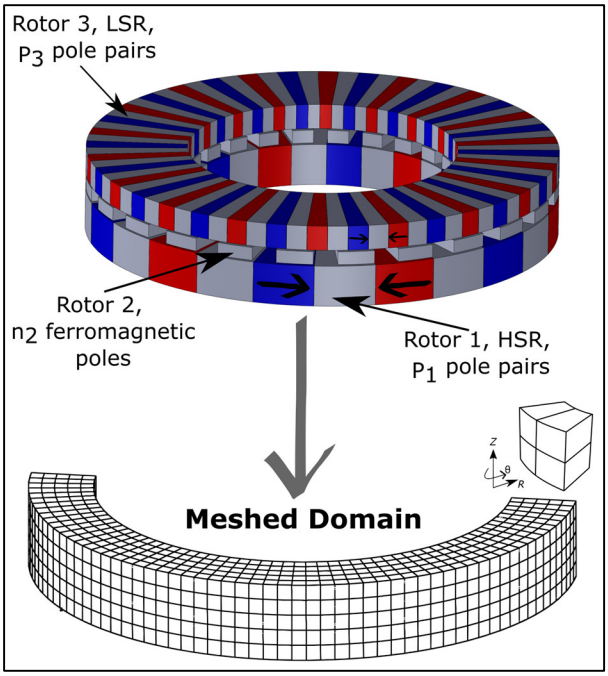

Fig. II-23 The modeled AFFMG with an illustration to the 3D meshing of its domain.

Table II-5 Geometrical dimensions and parameters of the studied AFFMG (design 1)

Rotor 1 (HSR)	Steel/magnet pole span θ_{1s}/θ_{1m}	15 °
	Axial Length l_{1s}	25 mm
	Airgap	1.5 mm
Rotor 2 (Stationary)	Steel pole span θ_{2s}	9 °
	Axial Length l_{2s}	8 mm
Rotor 3 (LSR)	Steel/magnet pole span θ_{3s}/θ_{3m}	4.74 °
	Axial Length l_{1s}	15 mm
	Airgap	1.5 mm
Radii	Inner Radius R_i	80 mm
	Outer Radius R_o	140 mm

An HSR pole-slipping motion test was simulated using the 3D PN and the 3D FEM. This test is done to observe the complete cycle of the forces on the three rotors, and it is achieved by fixing the LSR and rotating the HSR, knowing that the middle member is already fixed. The magnetic induction in the airgaps was computed at each step, and the test was conducted in a multi-static fashion, with each step evaluating the system and quantities independently of the preceding steps. Then, the magnetic induction values were fed to the MST to obtain the torque

sand attraction forces on each rotor. The magnetic saturation of the soft magnetic materials was taken into consideration where both the fixed-point and Newton's method were tested. The permanent magnets were considered as neodymium magnets with a linear demagnetization curve, a magnetic remanence $B_r = 1.2\ T$, and a relative permeability $\mu_{rm} = 1$. Finally, because the air outside the structure was ignored, a tangential magnetic induction boundary condition was imposed on all of the structure's lateral surfaces.

Calculated at a static position, Fig. II-24 and Fig. II-25 show the axial and circumferential components of the magnetic induction respectively calculated at the middle of the air gap splitting rotors 1 and 2 and at the mean radius position in the radial direction. Fig. II-26 and Fig. II-27 show the same components and at the same radial position but at the middle of the air gap splitting rotors 2 and 3. The results generated by the two nonlinear solving methods of the 3D PN and those generated from a 3D FEM nonlinear model are all presented in these figures. There can be seen a very good conformation between the curves generated using the 3D FEM and 3D PN, but with a slight difference in amplitudes at certain points especially noticeable in the axial induction component of Fig. II-26 where the saturation is higher and hence the slight accuracy deficiency will be observed. Moreover, an observation can be made regarding the circumferential components where there can be seen certain spikes in the values from the 3D PN at certain angular points, and these spikes might seem insignificant but can have some impact on the calculated torques. In addition, the severity of these spikes is dependent mainly on the number of the mesh divisions in the circumferential direction.

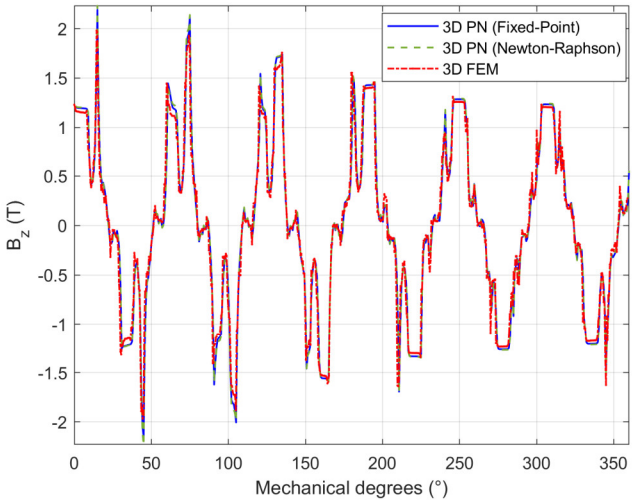

Fig. II-24 Axial magnetic induction component expressed as function of spatial angular position in the air gap between rotors 1 and 2.

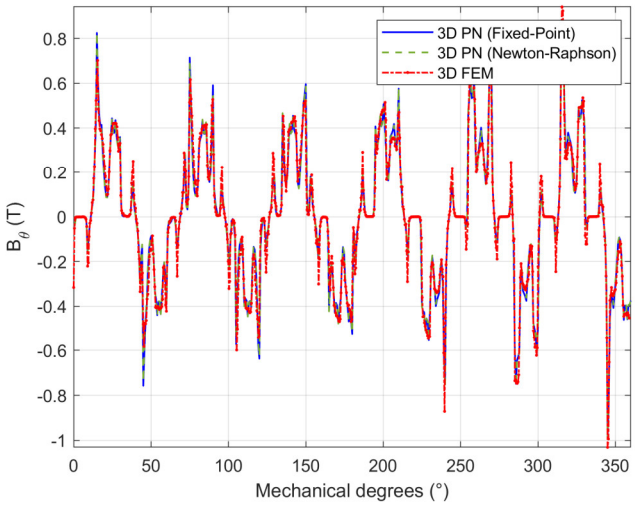

Fig. II-25 Circumferential magnetic induction component expressed as function of spatial angular position in the air gap between rotors 1 and 2.

The torques and axial attraction forces on the three rotors were evaluated and displayed in Fig. II-28 and Fig. II-29 when rotors 2 and 3 were fixed and rotor 1 was rotating. The differences are more noticeable for these quantities, nevertheless, the accuracy of the 3D PN is still acceptable. The results from the two nonlinear solvers of the PN were very close with the values provided by Newton's method slightly higher in amplitude at certain points.

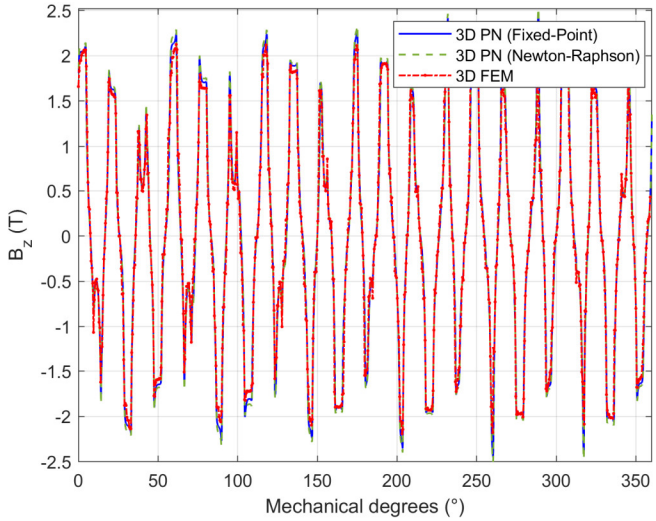

Fig. II-26 Axial magnetic induction component expressed as function of spatial angular position in the air gap between rotors 2 and 3.

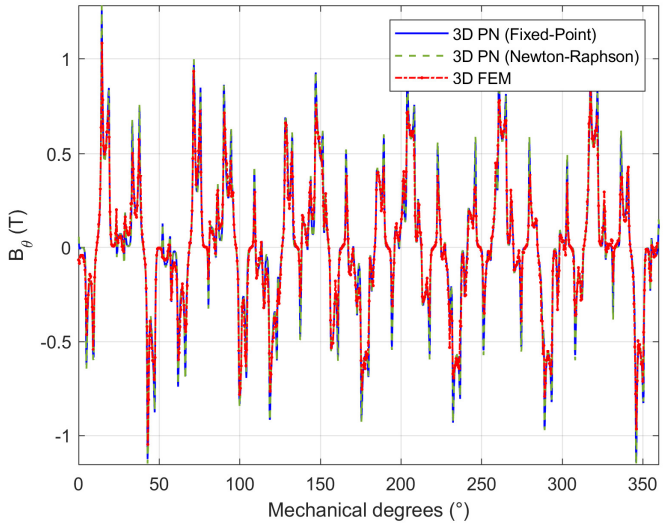

Fig. II-27 Circumferential magnetic induction component expressed as function of spatial angular position in the air gap between rotors 2 and 3.

The LSR stall torques evaluated by the 3D PN were 774.5 N m using the fixed-point method and 788 N m using Newton's method, whereas this value was 720.7 N m for the curve from the 3D FEM. Hence, the torque densities corresponding to the values from the MEC were 246.66 N m/L and 250.96 N m/L for the fixed-point method and Newton's method respectively, and the torque density estimated by the 3D FEM model was 229.52 N m/L. It is worth noting that the torque density estimated using a linear 3D PN supposing a constant permeability was 270.57 N m/L which shows a remarkable impact of the saturation on the performance.

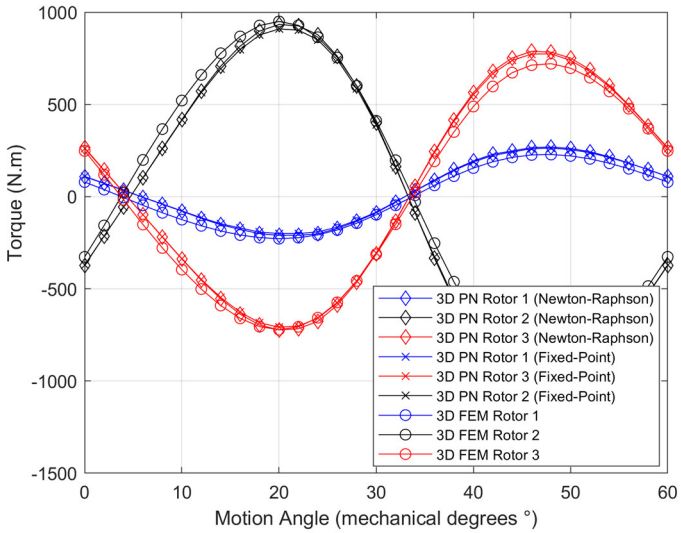

Fig. II-28 Torques developed by the three MG rotors during HSR pole-slipping.

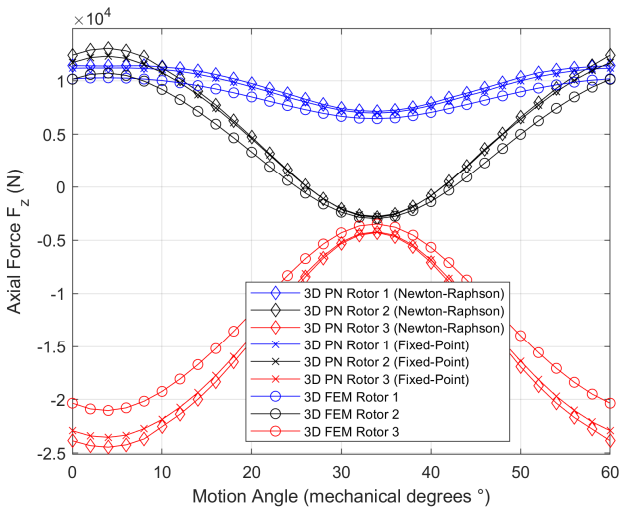

Fig. II-29 Attraction forces acting on the three MG rotors during HSR pole-slipping.

Table II-6 shows the size of each model and the time consumed to complete 31 motion steps. First, a comparison between the two nonlinear solving methods utilized by the 3D PN shows that the results obtained were very close but with the fixed-point method computation time being 1.84 times greater than the Newton's method computation time. This is an expected result considering the nature of the two methods, where the fixed-point method provided more stability but slower convergence rates than Newton's method. It is worth noting that the error used for the stopping criterion of the fixed-point method was ϵ_1, and for Newton's method it was ϵ_2. Fig. II-30 shows the variation of the error values ϵ_1 and ϵ_2 in function of time for one motion step. By comparing the two figures, one might suggest using ϵ_2 as an error criterion for the fixed-point method to reduce its computation time, and in this case the computation times of the two methods will get closer eliminating the significant gain from the use of Newton's method, but as mentioned earlier some reliability issues might be countered when using ϵ_2 with the fixed-point method which the user should be aware of. Hence, in the general case, Newton's method saved a good amount of time and provided almost the same level of accuracy as the fixed-point method, so it can be considered as the preferable choice, but using it also comes at a cost which is the complexity of constructing the Jacobian, so the use of each method is situational. Eventually, for the regular use, the user might prefer the fixed-point method when applying the 3D PN to a new structure because its implementation is much simpler and the gain from Newton's method might not appeal to everyone.

Table II-6 A summary of the characteristics and performance of the implemented 3D models.

		Total no. of nodes	Total time consumed
Linear	**3D PN**	345240	239 s
	3D FEM	1240574	5 h
Nonlinear	**3D PN fixed-point**	345240	19.69 h
	3D PN Newton-Raphson	345240	10.87 h
	FEM	949464	22.5 h

Comparing the 3D PN and the 3D FEM shows that the 3D PN probably achieved its goal of being a lightweight and fast model that provided relatively acceptable results. In terms of speed the 3D FEM, which uses Newton-Raphson as its numerical solver, consumed 65.2% more time than the 3D MEC with Newton's method. As for the computational resources, knowing that the models were running on a computer with 3.4 GHz CPU and 64 GB of RAM capacity, the 1240574 nodes 3D FEM model consumed up to 40 GB of RAM whereas the 3D PN required less than 1 GB of RAM, and even if the size of the 3D PN system increases to over a million nodes, it will still require much lower RAM capacity than the 3D FEM thanks to the efficient sparse storage of the matrices. The main disadvantage of the 3D PN model was the poorly conditioned system and Jacobian matrices, where the estimate for the 1-norm condition number of these two square matrices was in the order of 10^9. This explains why the nonlinear solvers used were stalling after a certain number of iterations, and very small error values were not possible to acquire without conducting a large unacceptable number of iterations.

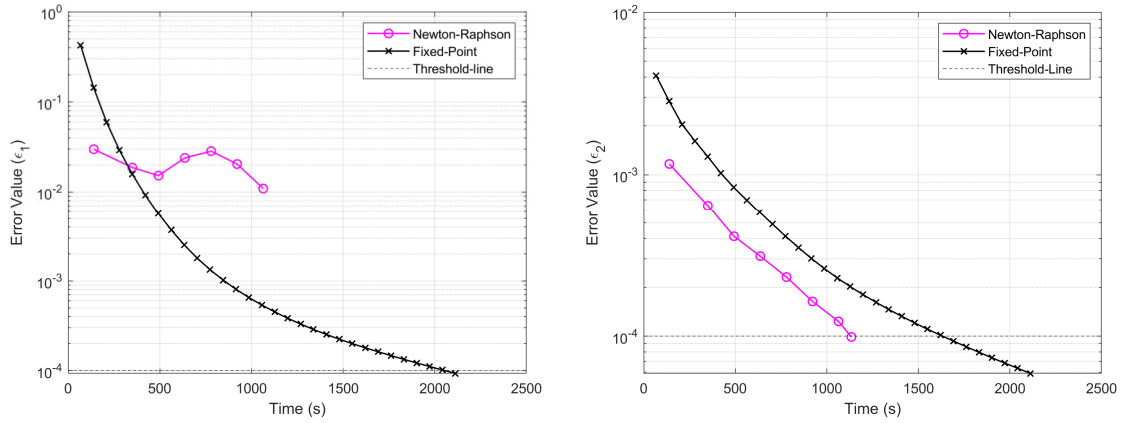

(a) (b)

Fig. II-30 The variation of the error values (a) ϵ_1 and (b) ϵ_2 in function of the elapsed time.

6. End-Effects Modeling in Magnetic Gears using 3D PN

Following the presentation of the end-effects concept in section 4.5, this section presents a 3D PN implementation for evaluating this aspect. In fact, a comparison between two magnetic gears topologies will be carried out concerning the magnetic saturation and the end-effects physical aspects. Therefore, an AFFMG and an axial field surface-mounted PM magnetic gear (SMPMG) were modeled using 3D PN under different physical conditions, and the comparison was carried out focusing on mainly comparing the variation of the torques and attraction forces of each structure with respect to the different operating conditions. In addition, accompanying every 3D PN model there will be a 3D FEM model serving as a reference for the comparison.

Meanwhile, to study the end-effects through the 3D PN or 3D FEM, an air envelope was considered around the magnetic gear structure as described in Fig. II-21. Concerning the dimensions of the envelope, there are many recommendations that are usually proposed by the FEM software to choose the dimensions of what could be called an "infinite box", but for this study a consideration should be made to the MEC method where it is better to choose the envelope as small as possible to reduce the total size of the system. Hence, a testing process was done running multiple simulations starting from a small thickness for the surrounding air region and increasing it gradually until the increase is no longer affecting the torque value significantly. Thus, the outer radius of the air envelope in the radial direction was chosen such that $R_{outAir} = 1.2 \cdot R_{out}$, and the interior radius was chosen such that the thickness of the air layer on the inner radial side is equal to that on the outer radial side. As for the air region in the axial direction, the defined axial length of that region on both axial sides was 30 mm. A tangential magnetic field boundary condition is set on the lateral surfaces of the air envelope.

Regarding the modeled structures, only two changes have been made to the studied AFFMG that was already presented in the previous section (check Fig. II-23 and Table II-5). Specifically, the two air gaps have now an axial length of 1 mm, and the relative magnetic permeability of the PMs is now 1.05. On the other hand, the studied SMPMG is shown in Fig. II-31, where it has the same number of pole pairs and gear ratio as the AFFMG, and it possesses the same material properties. The complete dimensions of the SMPMG are listed in Table II-7, and to keep the comparison valid, the dimensions were chosen such that the SMPMG has the same PM and iron volumes as the AFFMG. In addition, the permeance flux tube shape and permeance equations were the same for both structures (see Fig. II-22).

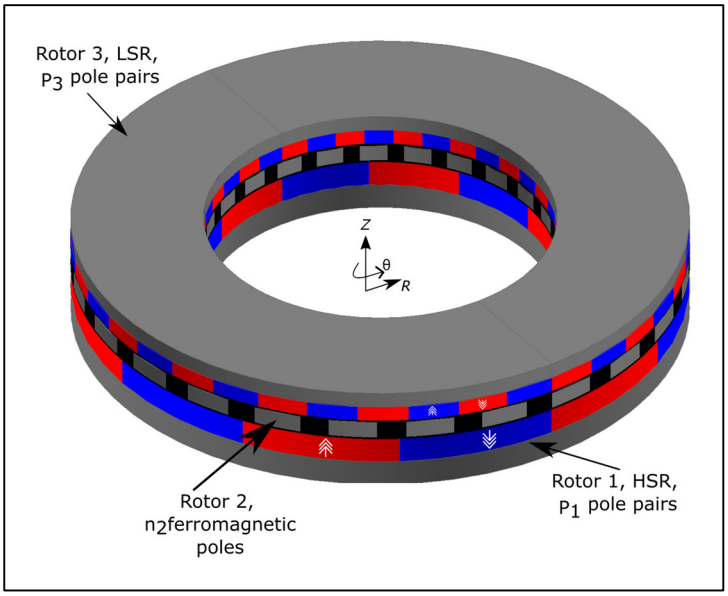

Fig. II-31 A drawing for the SMPMG that is being studied and modeled.

Table II-7 Geometrical dimensions and parameters of the studied SMPMG

Rotor 1 (HSR)	Magnet pole span θ_{1m}	30 °
	Back iron axial Length l_{1f}	12.5 mm
	Magnets axial length l_{1m}	12.5 mm
	Airgap	1 mm
Rotor 2 (Stationary)	Steel pole span θ_{2s}	9 °
	Axial Length l_{2s}	8 mm
Rotor 3 (LSR)	Magnet pole span θ_{3m}	9.47 °
	Back iron axial Length l_{3f}	7.5 mm
	Magnets axial length l_{3m}	7.5 mm
	Airgap	1 mm
Radii	Inner Radius R_i	80 mm
	Outer Radius R_o	140 mm

In essence, the two structures were modeled with and without considering the magnetic saturation; and with and without considering the end-effects. However, before going into the details of the evaluation and the results, a brief presentation of the meshes used for the 3D FEM models is good for the analysis. The elements used for the mesh of both structures were first-order regular tetrahedron elements, and a visualization for the mesh of the two structures can be seen in Fig. II-32. The mesh was constructed to have a good quality which could provide accurate results that will serve as a reference for judgement. The main mesh rules that were

applied for the two structures were having a double layered mesh in the air gaps and applying zero relaxation for all the volumes, surfaces, and lines that form the air gaps which is to try making all the mesh elements in the air gaps have uniform sizes. An evaluation of the 3D FEM meshes for the two structures generated by the FLUX software is shown in Fig. II-33.

6.1. Linear Case Results

In this case the magnetic saturation was ignored, and the relative permeability of the soft magnetic materials was constant at 10000. The torques and forces acting on the rotors of the two structures were calculated during HSR pole-slipping.

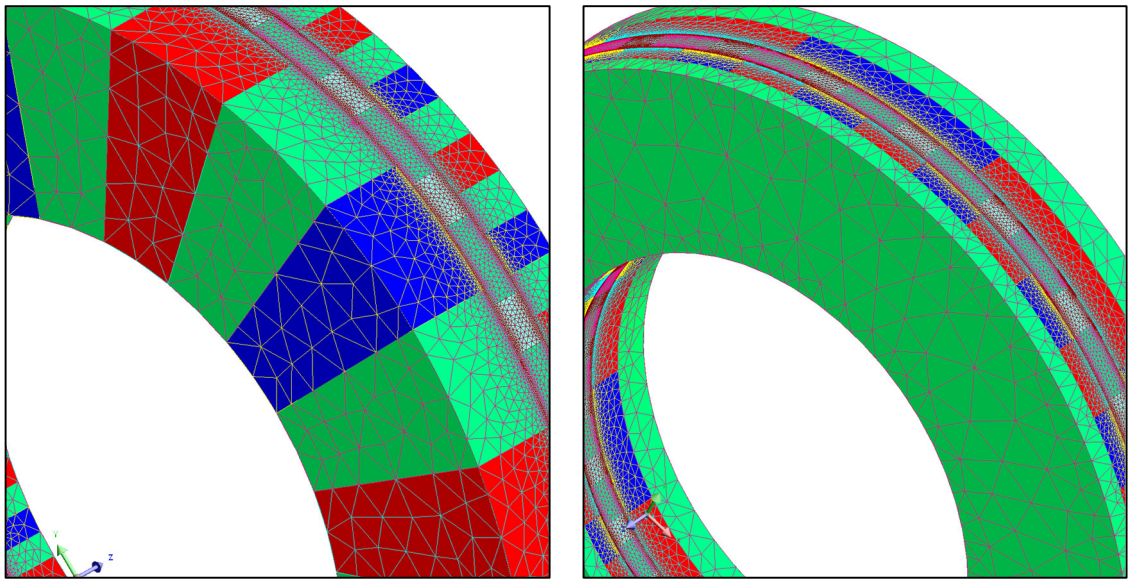

(a) (b)

Fig. II-32 A visualization of the 3D FEM mesh for the (a) AFFMG and (b) SMPMG.

```
Elements volumiques :
   Nombre d'elements non evalues          : 0  %
   Nombre d'elements d'excellente qualite : 66.59  %
   Nombre d'elements de bonne qualite     : 29.4  %
   Nombre d'elements de qualite moyenne   : 3.44  %
   Nombre d'elements de qualite mediocre  : 0.57  %

Nombre de noeuds : 2066965
Nombre d'elements lineiques : 50424
Nombre d'elements surfaciques : 2071074
Nombre d'elements volumiques : 10863925
Ordre de maillage : 1er ordre
```

(a)

```
Elements volumiques :
   Nombre d'elements non evalues          : 0  %
   Nombre d'elements d'excellente qualite : 64.79  %
   Nombre d'elements de bonne qualite     : 32.93  %
   Nombre d'elements de qualite moyenne   : 2.27  %
   Nombre d'elements de qualite mediocre  : 0.01  %

Nombre de noeuds : 2682757
Nombre d'elements lineiques : 44598
Nombre d'elements surfaciques : 2785944
Nombre d'elements volumiques : 14279123
Ordre de maillage : 1er ordre
```

(b)

Fig. II-33 The 3D FEM mesh evaluations generated by the FLUX software for the (a) AFFMG and (b) SMPMG.

The two cases of considering and ignoring the end-effects were evaluated for both structures. Fig. II-34 and Fig. II-35 show the torques and attraction forces experienced by the AFFMG during the HSR pole-slipping. In this case, the LSR stall torque decreased by 54.14%, only due to the end-effects, which is a significant drop, and the accuracy of the 3D PN slightly degraded in the case of the end-effects consideration especially the accuracy of the attraction forces.

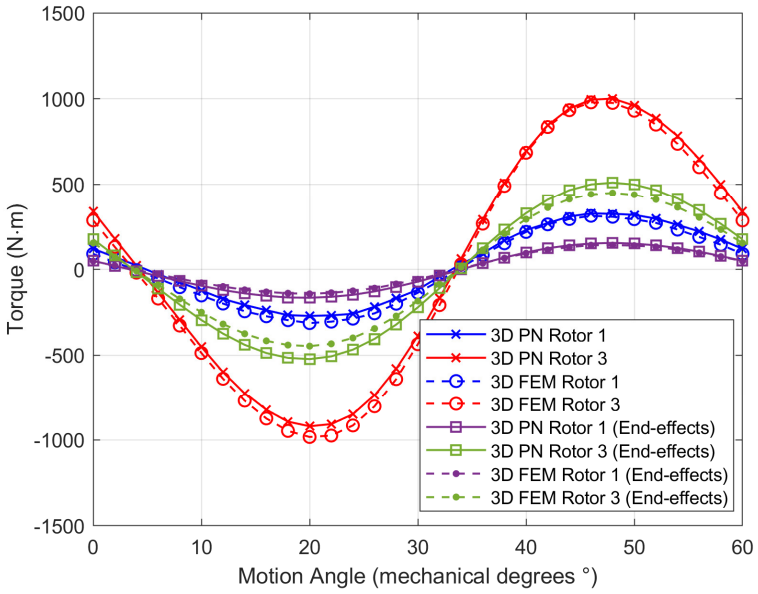

Fig. II-34 Torques experienced by the rotors of the AFFMG during HSR pole-slipping (linear case).

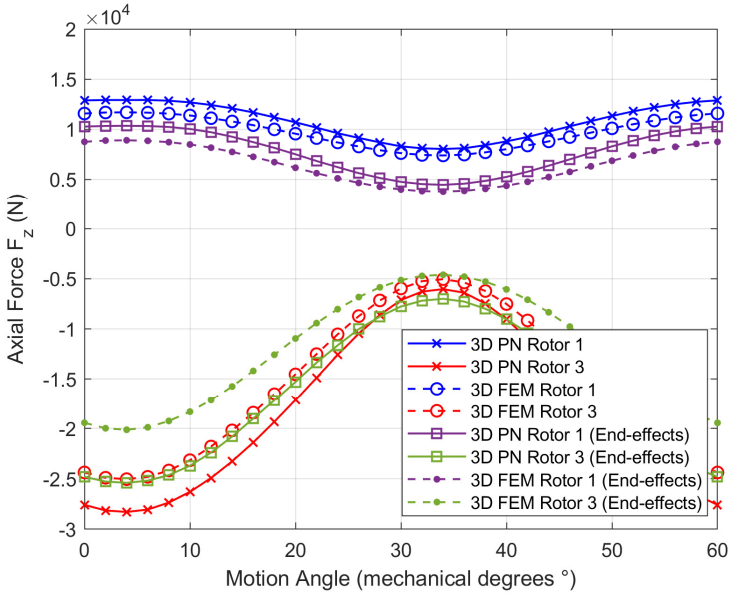

Fig. II-35 Attraction forces acting on the rotors of the AFFMG during HSR pole-slipping (linear case).

For the SMPMG linear case, the torques and attraction forces calculated are shown in Fig. 11 and Fig. 12. Here, the impact of the end-effects on the maximum torque is remarkably lower than what was observed with the AFFMG, where the maximum torque here decreased by 16.88%. The common between the two structures is that the accuracy of the 3D PN decreased when modeling the end-effects.

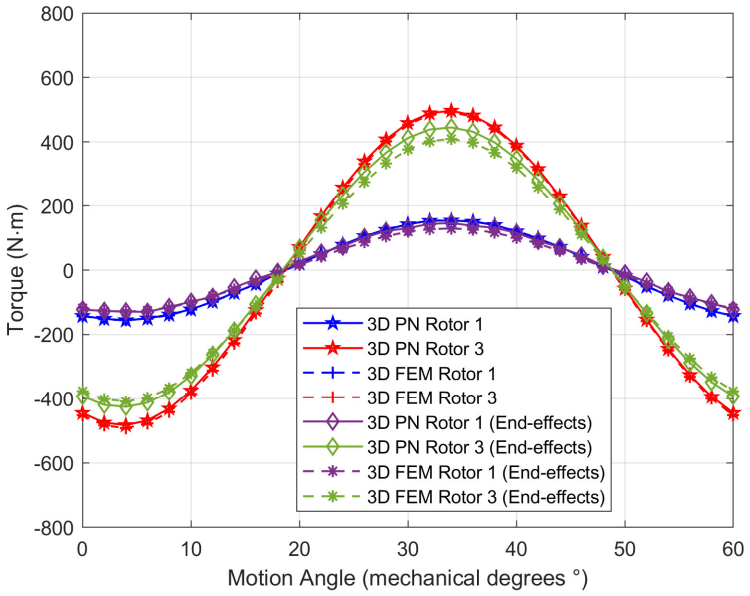

Fig. II-36 Torques experienced by the rotors of the SMPMG during HSR pole-slipping (linear case).

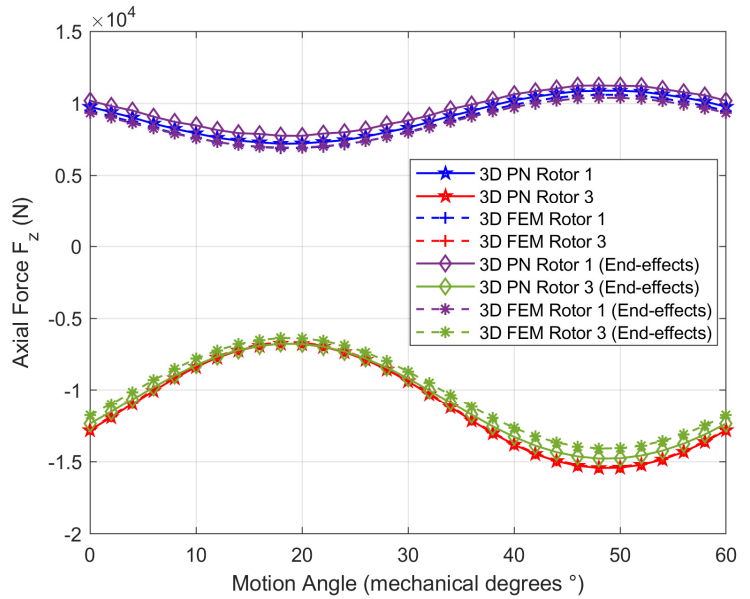

Fig. II-37 Attraction forces acting on the rotors of the SMPMG during HSR pole-slipping (linear case).

6.2. Magnetic Saturation Case Results

The magnetic saturation of the soft magnetic materials was considered for this case (see section 4.4). The nonlinear iterative solver chosen for the 3D PN was the fixed-point method where ϵ_2 was chosen as the error value for the stopping criterion. Moreover, for both structures, the two cases of considering and disregarding the end-effects were investigated.

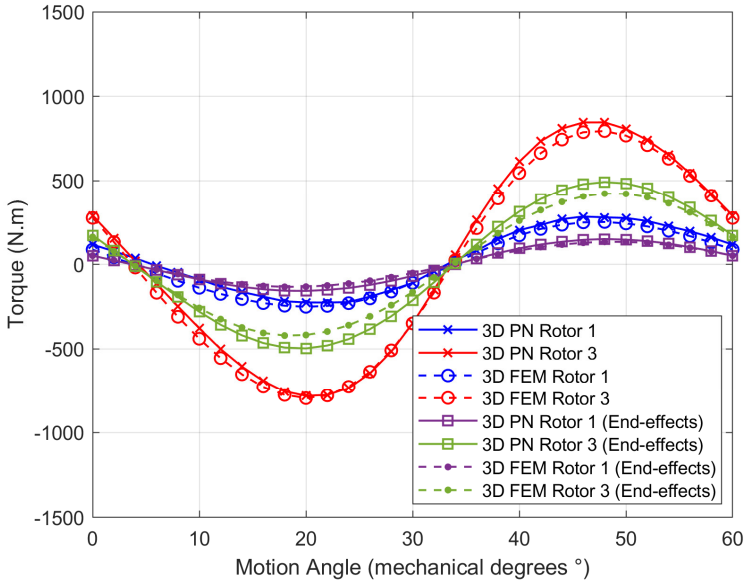

Fig. II-38 Torques experienced by the rotors of the AFFMG during HSR pole-slipping (saturation case).

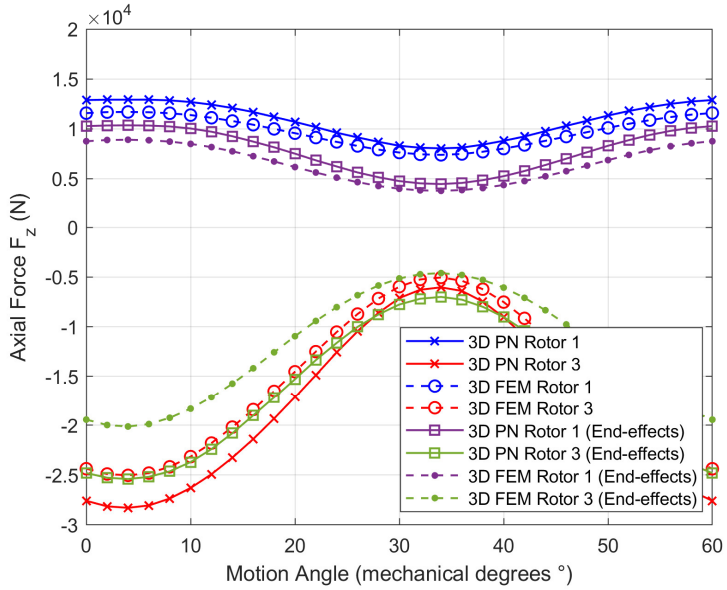

Fig. II-39 Attraction forces on the rotors of the AFFMG during HSR pole-slipping (saturation case).

Starting with the results from the AFFMG structure, the torques and attraction forces experienced by the AFFMG rotors during HSR pole-slipping are shown in Fig. II-38 and Fig. II-39. Two observations can be made here, first, the impact of the magnetic saturation on the AFFMG is significant and can't be ignored whether the end-effects are considered or not. Then, the end-effects affected remarkably the maximum torque where it decreased by 46.97%.

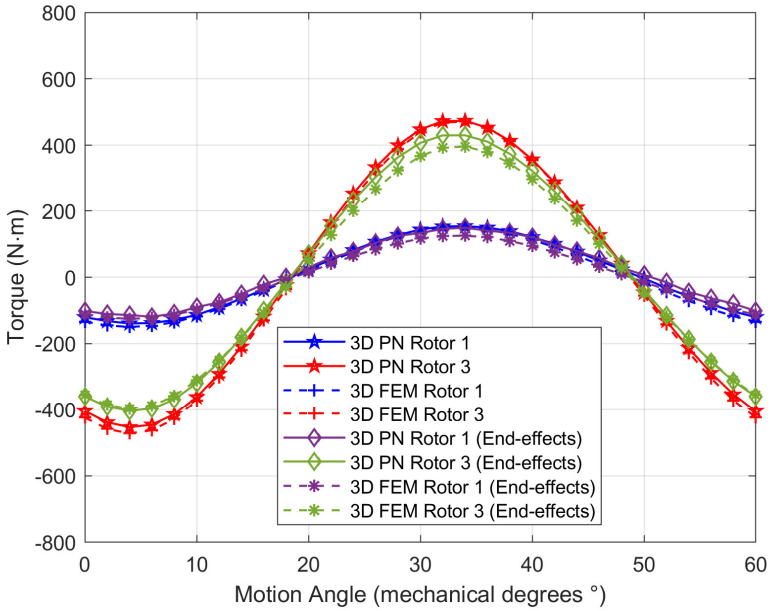

Fig. II-40 Torques experienced by the rotors of the SMPMG during HSR pole-slipping (saturation case).

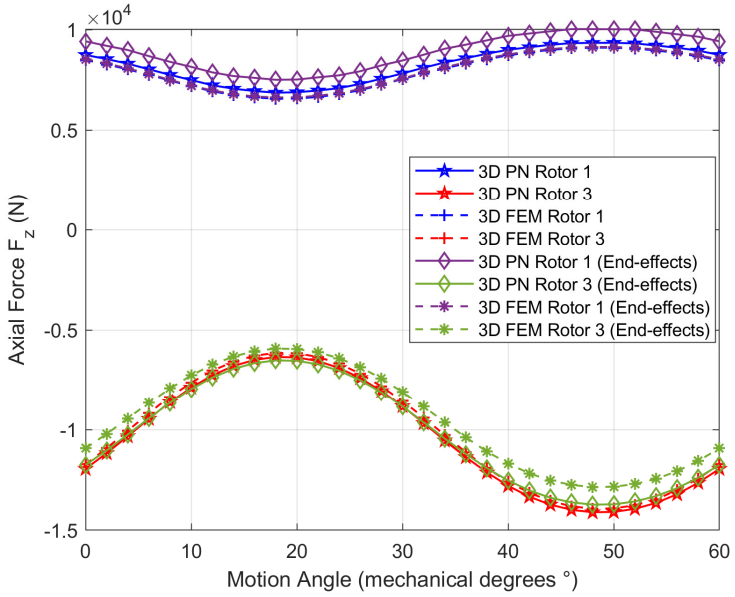

Fig. II-41 Attraction forces on the rotors of the SMPMG during HSR pole-slipping (saturation case).

Fig. II-40 and Fig. II-41 show the torques and axial forces estimated for the SMPMG in the magnetic saturation case, and with the presence and absence of the end-effects. By comparing these figures with those from the linear case, the magnetic saturation effect is not as severe as it was in the AFFMG. And due to the end-effects, the LSR stall torque dropped by 15.99% which is similar to the linear case and lower than the drop that occurred for the AFFMG.

6.3. Analysis and Discussion

The proper analysis of the results should address three main aspects: the magnetic saturation, the end-effects, and the accuracy and validity of the 3D PN model. The LSR stall torques of the two structures predicted by the 3D PN and 3D FEM models and the resulting VTDs for all the cases are summarized in Table II-8 and Table II-9. It is important to recall that the two studied structures, the AFFMG and the SMPMG, have the same active volume. Moreover, the percentage error between the stall torque values predicted by the 3D PN and their reference values generated by the 3D FEM is added in these tables for all cases. Furthermore, to enhance the analysis of the values in these two tables, Table II-10 is added to show the percentage decrease in the LSR stall torques of the two structures due to the different conditions. The values in Table II-10 show clearly how the two MG types are affected differently by the imposed conditions. Regarding the magnetic saturation, the SMPMG is only slightly affected by this aspect and hence, if a compromise is needed to cut off the computation time, magnetic saturation could be ignored for the SMPMG.

Table II-8 The AFFMG LSR stall torque predictions by the 3D PN and 3D FEM models for all the cases.

Simulation Conditions (AFFMG)		**LSR Stall Torque (N m)**		**VTD (N m/L)**		**Percentage Error (%)**
		3D PN	**3D FEM**	**3D PN**	**3D FEM**	
Linear	**Ignoring End-Effects**	1000.7	978.6	324.9	317.7	2.26
	With End-Effects	509.8	448.7	165.5	145.7	13.62
Saturation	**Ignoring End-Effects**	845.7	794.1	274.6	257.8	6.49
	With End-Effects	490.9	421.1	159.4	136.7	16.57

Table II-9 The SMPMG LSR stall torque predictions by the 3D PN and 3D FEM models for all the cases.

Simulation Conditions (SMPMG)		LSR Stall Torque (N m)		VTD (N m/L)		Percentage Error (%)
		3D PN	**3D FEM**	**3D PN**	**3D FEM**	
Linear	**Ignoring End-Effects**	497	492.64	161.4	159.95	0.89
	With End-Effects	445.1	409.46	144.5	132.94	8.7
Saturation	**Ignoring End-Effects**	473.6	471.66	153.8	153.14	0.4
	With End-Effects	430.1	396.21	139.6	128.64	8.6

Table II-10 Percentage decrease of the LSR stall torque caused by the different conditions for the two structures.

Simulation Conditions	3D FEM		3D PN	
	AFFMG	SMPMG	AFFMG	SMPMG
Magnetic Saturation Only	18.86%	4.26%	15.49%	4.71%
End-Effects Only	54.14%	16.89%	49.06%	10.44%
End-Effects & Saturation	56.97%	19.57%	50.94%	13.46%

On the other hand, the effect of the magnetic saturation on the AFFMG is more noticeable and can't be easily disregarded. This difference is caused by the nature of the two MG types, where the length of the effective magnetic air gap is much smaller in the case of the AFFMG which allows for higher magnetic field values to develop leading to the saturation region. Regarding the end-effects impact on the two structures, the impact on the AFFMG is much more severe where it lost over 50% of its potential torque density only due to the flux leakage at the outside air boundaries. Nonetheless, the end-effects influence on the SMPMG is higher than the magnetic saturation, but still much lower than the end-effects impact on the AFFMG. This goes back to the arrangement of the PMs in the two structures, where the AFFMG is prone to the magnetic flux leakage at both the axial and radial ends, whereas the flux leakage in the SMPMG is more likely to occur at the radial ends only. To illustrate, a heatmap of the magnetic induction in the two structures generated by FLUX 3D can be seen in Fig. II-42 and Fig. II-43. By observing the heatmaps, the two structures exhibit different magnetic flux activity patterns at their ends, where higher magnetic induction values can be observed at the ends of the

AFFMG structure. When observing the percentage drop of the stall torques due to both the end-effects and magnetic saturation, the same conclusions could be drawn out.

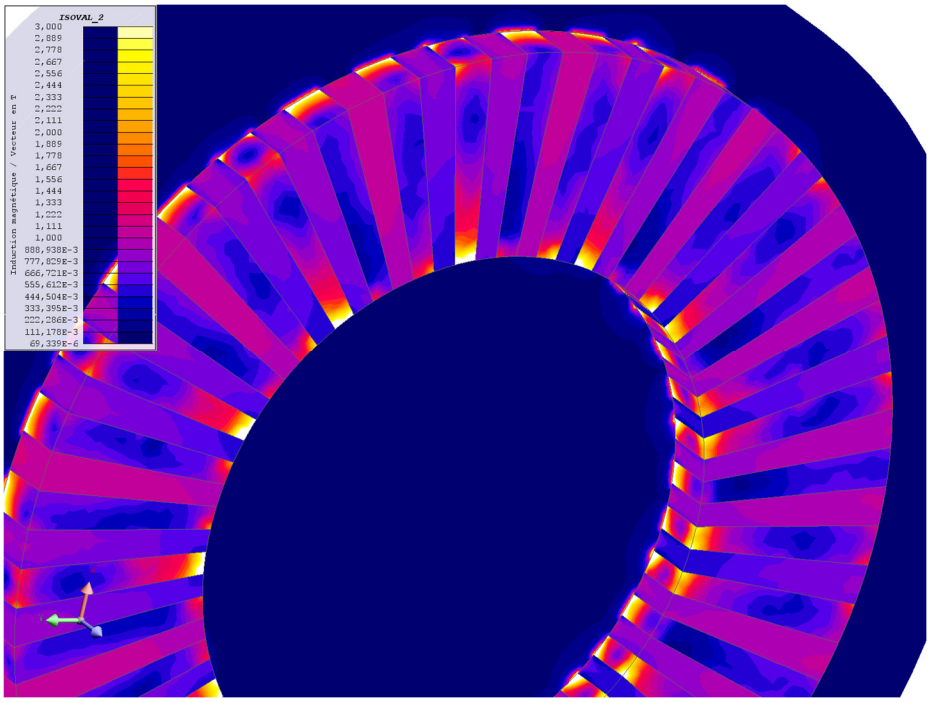

Fig. II-42 Magnetic induction heatmap illustrating the flux leakage at the ends of an AFFMG.

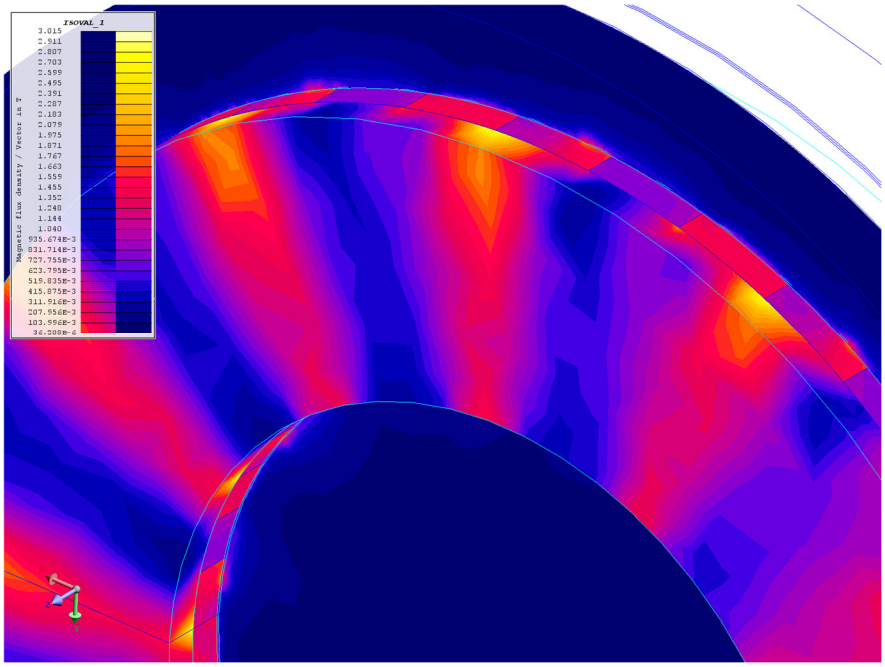

Fig. II-43 Magnetic induction heatmap illustrating the flux leakage at the ends of an SMPMG

For the evaluation concerning the performance of the 3D PN model in comparison to the 3D FEM model, Table II-11 and Table II-12 summarize the number of nodes and computation time for each case, knowing that all the models were run on a PC with 3.4 GHz CPU with 64 GB of RAM. The detailed 3D PN mesh dimensions for the two structures are described and summarized in Fig. II-44 and Table II-13. In an attempt to improve the accuracy of the AFFMG 3D PN model in the case of the end-effects, the mesh of each radial layer was redistributed by decreasing the number of divisions in the axial direction and increasing it in the circumferential direction while approximately maintaining the same mesh density in that layer, and this redistribution helped in slightly improving the results.

In general, from the results shown previously and summarized in Table II-8 and Table II-9, the accuracy of the 3D PN decreased when modeling the end-effects. In the AFFMG case, the mesh density in each layer was maintained the same after considering the air envelope, but the accuracy still deteriorated. A hypothesis to explain this behavior could be directly related to the distribution of the flux leakage paths at the ends of the AFFMG because it could be seen from Fig. II-42 that high magnetic induction values are appearing in small areas at some of the edges of the rotor, and this suggests that only a fine mesh around these edges could detect the flux leakage paths. In the current configuration of the 3D PN mesh, acquiring fine flux tubes around the edges of the rotors will increase the system size massively, but it is possible to acquire such a fine mesh without significantly affecting the system size if a more complex mesh configuration is implemented which will increase the complexity of the whole method and reduce its practicality. In fact, it has been noticed that increasing the number of radial divisions (g_{air}) improves the results, but increasing these divisions comes at the cost of remarkably increasing the system size. On the other hand, the accuracy of the 3D PN SMPMG models were better in general even though the mesh density per layer was reduced when modeling the end-effects, and it might be because the SMPMG is not too much affected by the end-effects.

Furthermore, the computation times of the models for the SMPMG are generally lower than those of the AFFMG, and it is mainly due to the fact that the PM rotors regions of the SMPMG are uniform in the circumferential direction. This property of the SMPMG structure is more suitable for the matrix assembly algorithm, and it facilitates the navigation of the nodes inside the structure.

Table II-11 Characteristics and performance of the models implemented for the AFFMG

		Number of Nodes		Computation Time	
		3D PN	**3D FEM**	**3D PN**	**3D FEM**
Linear	**Ignoring End-Effects**	345240	1858781	0.126 h	9 h
	With End-Effects	1464840	2744797	0.78 h	17 h
Saturation	**Ignoring End-Effects**	345240	1858781	13.94 h	37 h
	With End-Effects	1464840	2744797	17.90 h	60 h

Table II-12 Characteristics and performance of the models implemented for the SMPMG

		Number of Nodes		Computation Time	
		3D PN	**3D FEM**	**3D PN**	**3D FEM**
Linear	**Ignoring End-Effects**	794820	2427805	0.35 h	5 h
	With End-Effects	991440	2512444	0.54 h	6 h
Saturation	**Ignoring End-Effects**	794820	2427805	13.85 h	31.5 h
	With End-Effects	991440	2512444	16.80 h	48 h

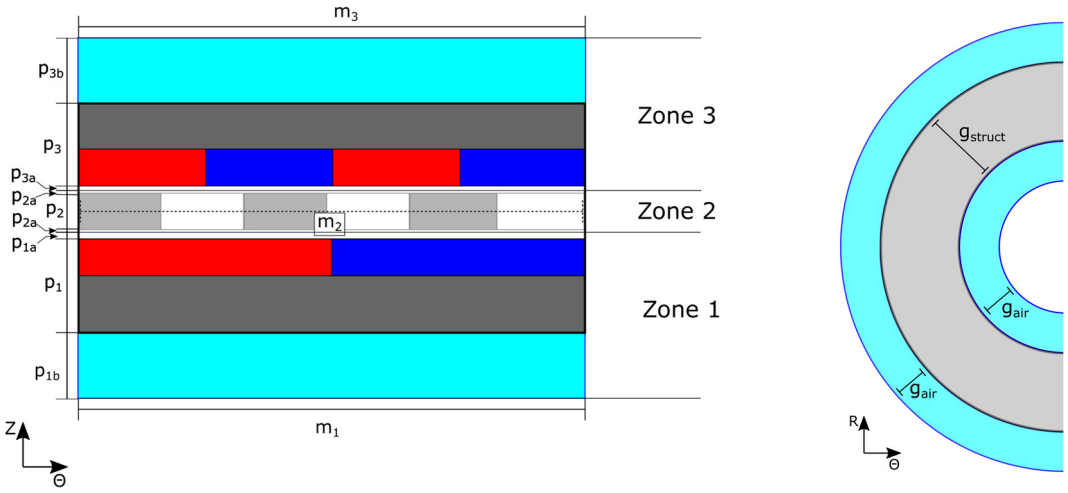

(a) (b)

Fig. II-44 2D cross-sections of an axial field MG illustrating the 3D PN mesh parameters on the (a) (R, θ) plane and (b) (θ, Z) plane.

Table II-13 Characteristics and performance of the models implemented for the SMPMG

		m_1	p_{1b}	p_1	p_{1a}	m_2	p_2	p_{2a}	m_3	p_{3b}	p_3	p_{3a}	g_{struct}	g_{air}
AFFMG	**Ignoring End-Effects**	480	n/a	50	3	800	16	1	2280	n/a	30	3	3	n/a
	With End-Effects	720	4	25	3	800	16	1	3420	4	15	3	3	5
SMPMG	**Ignoring End-Effects**	540	n/a	100	3	1600	32	1	2280	n/a	60	3	3	n/a
	With End-Effects	360	3	26	3	1600	16	1	1710	3	30	3	3	3

The main advantage obtained from using the 3D PN is the significant time saving achieved across all the cases and especially in the linear case. Then, the accuracy of the 3D PN was relatively acceptable across the different cases, and even though the error percentage became noticeable in the end-effects case, the time saving was still important which could mitigate the deficiency in the accuracy. In essence, the 3D PN could be considered a good candidate for early design optimization studies where it can perform very quick linear estimations, in addition to nonlinear estimations that can be faster than the nonlinear 3D FEM predictions. Hence, depending on the application and tools in hand, the user should choose the method that suits his constraints the most, knowing that a trade-off should be always done between accuracy and speed.

Finally, the comparison study has shown that the AFFMG is much more affected by the end-effects than the SMPMG, and, even if this aspect could be disregarded under certain conditions for the SMPMG, it might be highly important to consider for the AFFMG structures. The magnetic saturation, on the other hand, could be possibly ignored in the SMPMG structures, but it is better to always perform evaluations before ignoring such a condition. These conclusions were mainly derived from the case study that was presented, and a general conclusion on this subject that covers all the pole-pair combinations and structure dimensions requires more testing and investigation.

7. Quasi-3D RN for Modeling the End-Effects in Axial Field MGs

In addition to the 3D PN implementations, a quasi-3D RN (Q3D RN) approach is proposed, and the motivations behind using this approach were implementing the mesh formulation and testing a very well know technique that combines the simplicity of 2D modeling and the

advantages 3D modeling [142], [143]. In fact, the proposed Q3D RN model will be tested for the prediction of the quantities of an AFFMG considering the end-effects.

This approach can be considered as a multi-slice technique where the axial field structure is divided into several radial layers and each layer is treated as a standalone 2D RN model (see Fig. II-45). The reluctance values at each layer are dependent on the radial position of that layer, and the expressions for the axial and circumferential reluctances could be deduced as the reciprocal of the permeance equations in (II-51) and (II-52). The results from each layer are then combined using an activation function which will represent the radial dependence of the magnetic induction in the structure, and eventually this representation will mean the consideration of the end-effects in the axial field structure. Hence, the process to construct the quasi-3D multi-slice approach that can take into account both the radial and axial end-effects is as follows: first, the structure is divided into multiple layers in the radial direction. Next, each layer is solved as an independent 2D reluctance network model using the formulation presented in section 3.2. Then, the magnetic induction in the airgaps is calculated at the mean radius of each layer and then provided to the MST to compute the torques and axial forces applied on each layer. Finally, using the predetermined activation function, a weighted sum is performed on the obtained torques and forces to obtain the total quantities. The equations of the torques and axial forces acting on the whole structure are given in (II-53).

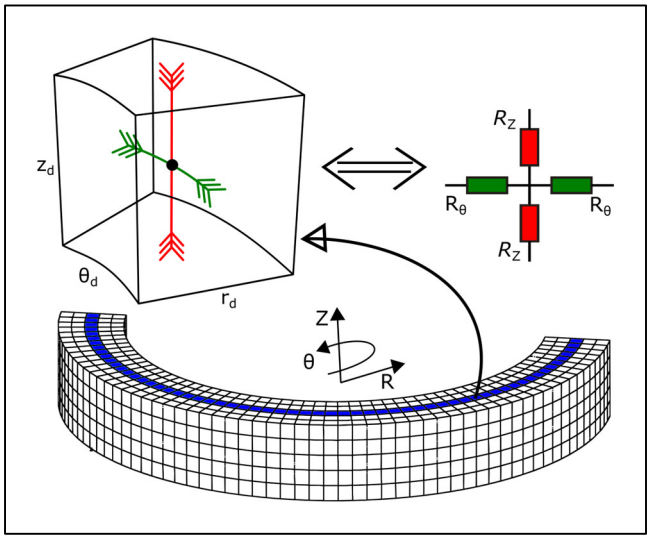

Fig. II-45 An illustration of the multi-slice approach applied to an axial field structure.

$$\begin{cases} C_k = \sum_{i=1}^{N} g_k^2(R_{mi}) \cdot C_{ki} \\ F_k = \sum_{i=1}^{N} g_k^2(R_{mi}) \cdot F_{ki} \end{cases} \quad \text{(II-53)}$$

C_k and F_k are the total torque and axial force, respectively, acting on rotor k such that $k \in \{1,3\}$, N is the total number of slices, R_{mi} is the mean radius of slice i, C_{ki} and F_{ki} are the elementary torque and axial force, respectively, from slice i acting on rotor k, and $g_k(r)$ is the activation function related to the airgap adjacent to rotor k. Thus, there will be two activation functions related to each air gap of the magnetic gear, and this is required since the behavior of the magnetic induction in the two airgaps is not the same and using one activation function for both will affect the accuracy. The determination or the choice of the activation function depends on the type of the structure. For this work, the approach followed in [143] was used to obtain the two activation functions required. The curves of the estimated activation functions for the two air gaps are shown in Fig. II-46.

The structure that is going to be modeled using the Q3D RN is again an AFFMG with a different gear ratio. The complete dimensions and specifications of the design are listed in Table II-14. Furthermore, the number of pair poles of the HSR is $p_1 = 4$, the number of pole pairs of the LSR is $p_3 = 15$, and the number of the ferromagnetic modulation segments of the fixed member is $n_2 = p_1 + p_3 = 19$. Moreover, as it is being supposed that the middle rotor (rotor 2) is going to be the fixed member, the gear ratio of this design becomes $G_r = \frac{p_3}{p_1} = 3.75$, where and the relation between the angular velocities of the rotors is $\omega_1 = -G_r\omega_3$.

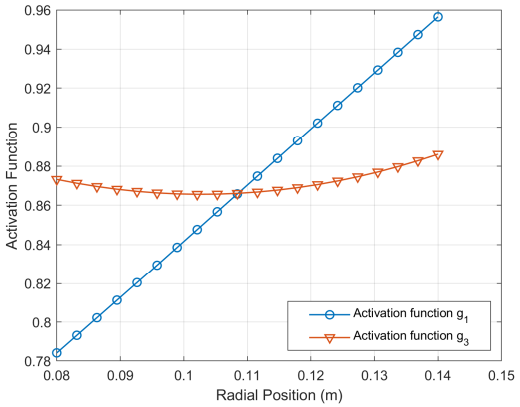

Fig. II-46 The activation functions for the two air gaps used for the Q3D RN model.

Table II-14 Geometrical dimensions and parameters of the studied AFFMG (design 2)

Rotor 1 (HSR)	Steel/magnet pole span $\boldsymbol{\theta_{1s}/\theta_{1m}}$	22.5 °
	Axial Length l_{1s}	25 mm
	Airgap	1.5 mm
Rotor 2 (Stationary)	Steel pole span θ_{2s}	12 °
	Axial Length l_{2s}	8 mm
Rotor 3 (LSR)	Steel/magnet pole span θ_{3s}/θ_{3m}	6 °
	Axial Length l_{1s}	15 mm
	Airgap	1.5 mm
Radii	Inner Radius R_i	80 mm
	Outer Radius R_o	140 mm

The same performance tests that were performed in the previous sections were repeated for this model and device, and the results were accompanied by reference results generated using a 3D FEM model for validation and comparison. In the linear case, the soft magnetic materials were considered linear isotropic with a constant relative permeability of 10000, and in the magnetic saturation case the B(H) curve presented in section 4.4 was adopted, and the fixed-point iteration method was used as a nonlinear solver with ϵ_1 being the error equation of the stopping criterion. In addition, the permanent magnets were considered as neodymium magnets with a linear demagnetization curve, a relative permeability $\mu_{rm} = 1$, and a magnetic remanence $B_r = 1.2\ T$.

First, to test the impact of the end-effects on this structure and to support the conclusion that was made in the previous chapter, two linear 3D FEM models were constructed for this design: one considers the end-effects through a surrounding air envelope, and another ignores the end-effects by applying tangential magnetic field boundary conditions to the lateral surfaces of its structure. Then, the torques generated by these models during HSR pole-slipping are shown in Fig. II-47. For this different AFFMG design also, it can be seen that the impact of the end-effects on the torque of the structure is significant where the LSR stall torque decreased by over 50.3%.

Meanwhile, the evaluation of the Q3D RN method will be carried out by comparing its results to results from 3D FEM models that consider the end-effects through an air envelope. While having rotors 2 and 3 fixed and moving rotor 1, the torques and attraction forces on the three rotors were evaluated and shown for the linear and saturation cases in Fig. II-48 and Fig. II-49.

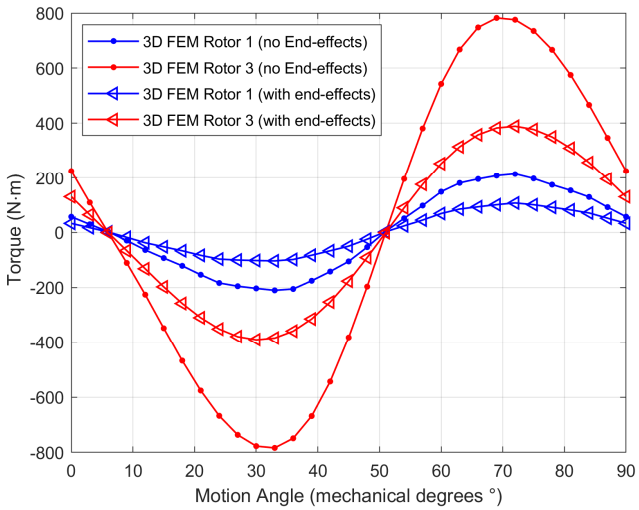

Fig. II-47 Torques experienced by the rotors of the AFFMG (design 2) during HSR pole-slipping and generated using 3D FEM models.

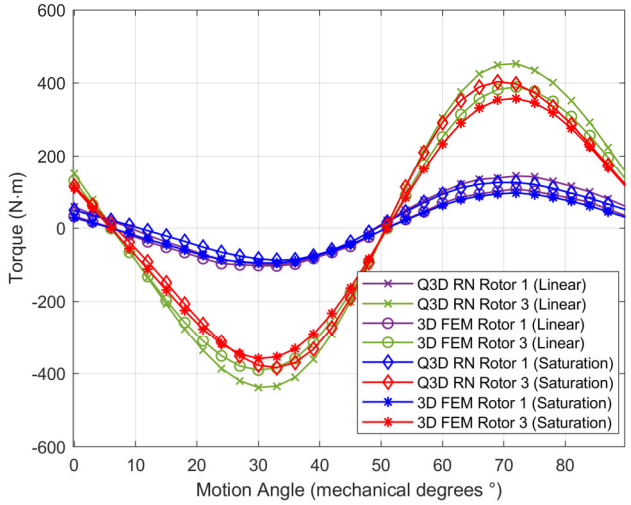

Fig. II-48 Torques experienced by the rotors of the AFFMG (design 2) during HSR pole-slipping (linear and saturation cases, end-effects considered).

A comparison between the results generated using the Q3D RN and 3D FEM shows that there is a noticeable but not significant difference between the amplitudes of the torques, whereas a much better agreement between the two models can be seen in the attraction forces curves. The values of the LSR stall torques and the respective VTDs are listed in Table II-15, and in addition to the percentage error between the stall torque values predicted using the 3D

FEM and Q3D RN. The difference in the values of the torque is mainly related to the nature of the activation functions, where the functions have been obtained using a method that depends only on the variation of the values of the axial induction component and doesn't consider how the circumferential components are being affected by the end-effects. Eventually, this leads to less accurate predictions for the circumferential components which affected the accuracy of the torque values knowing how it plays an important role in the formula of the torque derived from the MST. Nevertheless, the difference could be justified when observing the amount of time saved by using the Q3D RN. The computation times and number of nodes of the Q3D RN and 3D FEM models implemented are summarized in Table II-16.

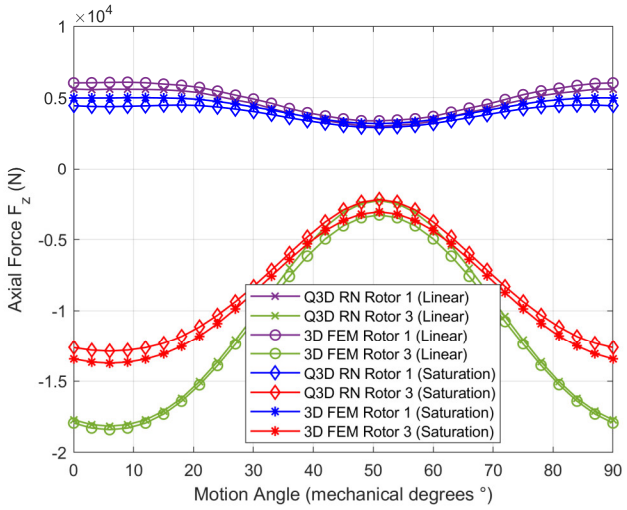

Fig. II-49 Attraction forces on the rotors of the AFFMG (design 2) during HSR pole-slipping (linear and saturation cases, end-effects considered).

Table II-15 The AFFMG (design 2) LSR stall torque predictions by the Q3D RN and 3D FEM models.

Simulation Conditions	**LSR Stall Torque (N m)**		**VTD (N m/L)**		**Percentage Error (%)**
	Q3D RN	**3D FEM**	**Q3D RN**	**3D FEM**	
Linear	453	388.9	144.3	123.9	16.48
Saturation	403.6	357.6	128.5	113.9	12.86

Table II-16 Characteristics and performance of the Q3D RN model and the reference 3D FEM models.

Simulation Conditions	Q3D RN			3D FEM	
	Nodes per 2D Layer	**No. of Layers**	**Computation Time**	**No. of nodes**	**Computation Time**
Linear	155700	9	0.417 h	1439817	7 h
Saturation	125100	5	8.375 h	1439817	29 h

In essence, the Q3D RN served as a good lightweight model that can provide relatively good results in a short time, where the compromise between speed and accuracy is always there to be considered. Moreover, there is still a room for improvement for this method by upgrading the activation functions to be able to consider the variations of the both the axial and circumferential induction components, and this upgrade will require a change or improvement for the original method used to obtain these functions. Finally, a proper comparison between the Q3D RN method and 3D PN method presented in the previous sections might not be valid due to the slight differences in their application. However, if some observations are to be done, then it has been seen that in the linear case the 3D PN performed better than the Q3D RN in terms of lower percentage error and shorter computation time, but in the saturation case the Q3D RN saved almost half the time consumed by the 3D PN and still provided lower percentage error.

Conclusion

The chapter started with an overview on the behaviors and kinds of magnetic materials. Then, a theoretical presentation for the modeling approaches that were employed was done. The implementation details of the magnetic equivalent circuit approach were then detailed through multiple sections. In addition, the MEC modeling technique was assessed by evaluating and comparing its nonlinear solvers. Then, the end-effects of axial field magnetic gears were investigated and modeled using a 3D MEC, and two magnetic gear types were compared. The chapter concluded with the presentation and evaluation of an alternate quasi-3D technique for modeling the end-effects. The evaluation and results of the MEC models have satisfied the main goal of this chapter which was to obtain a lightweight 3D modeling tool for axial field magnetic gears. Across the different cases and studies, the MEC provided quicker computation times than

the 3D FEM and maintained relatively good accuracy. The consideration of the end-effects in axial field magnetic gears was also possible using the MEC method but with decreased accuracy. Hence, there is a compromise to be made between the constraints, where the MEC could be used for early design optimization studies where multiple parameters are varying, and then the verification in the final stage could be done by using the FEM. Finally, the case studies have shown that the SMPMG and AFFMG structures were affected by magnetic saturation and end-effects differently, where the evaluation has shown the AFFMG could be severely affected by these aspects especially the end-effects.

Chapter III - Magnetic Gears for Marine Renewable Energy

Introduction

This chapter starts with an overview of the marine renewable energy technologies. Different conversion systems and energy sources will be briefly introduced, and a more detailed study will be done on offshore wind energy. The challenges and criteria of the offshore wind conversion systems will be explored. Next, an overview of the applications of magnetic gears in marine energy systems will be done showing the implementations reported in the literature of both magnetic gears and magnetically geared machines. Finally, a parametric sweep analysis will be done utilizing the modeling methods presented in the previous chapter, where the goal is to propose an axial field magnetic gear design that can be suitable for implementation in a marine renewable energy conversion system.

1. An Overview on Marine Renewable Energy Conversion Systems

Problems related to the use of fossil fuels have encouraged the societies to find viable and reliable alternatives for energy production. The controversial nuclear energy has lower greenhouse gases emissions but treating its radioactive wastes is rather complicated. Therefore, renewable energy sources are constituting a viable solution sought after by most countries. The French Agency for Ecological Transition (ADEME) ensures that France could produce, by 2050, 100% of its electrical energy from renewable sources at economically acceptable costs [144]. In addition, water covers more than 70% of the surface of our planet, so the potential of renewable marine energy is enormous. Different types of marine energy could be distinguished, and types that include electromechanical conversion systems could be tidal stream, tidal impoundment, wave, and offshore wind. Fig. III-1 shows resource maps from AQUARET of Europe for tidal stream and wave energy. The electromechanical conversion in these systems is usually done through an electric generator which could have linear or rotational motion. In addition, the generator could be connected directly to the energy source forming a direct drive system (DD) or through a gearbox.

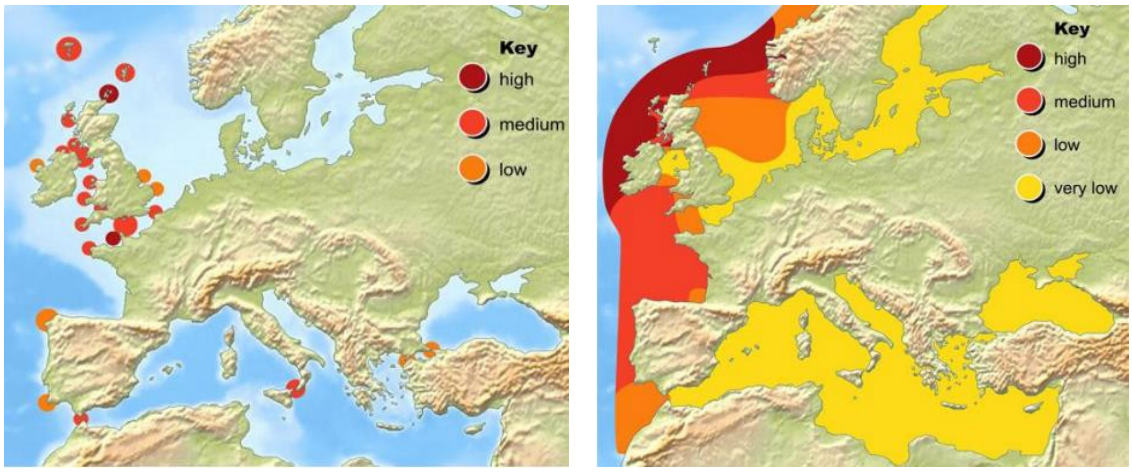

(a) (b)

Fig. III-1 Marine renewable energy potential in Europe (a) tidal stream (b) wave energy [145].

1.1. Tidal Stream Energy

Tidal stream technologies produce power by using the water flow caused by the tides and accelerated by the terrain of the shore. As is the case with wind and wave technologies in their development, several tidal stream designs have been and continue to be presented. Horizontal or vertical-axis rotors are used in the majority of turbines. Several devices have been or are being tested on a small scale, while others have been evaluated as full-scale prototypes. In the UK, Norway, Ireland, Italy, Sweden, Canada, and the United States, corporate, government, and university research initiatives on tidal power during the last half-decade have laid an essential basis for the burgeoning tidal power sector. Wind and tidal current generating systems share numerous elements and driving forces. Borrowing technology, components, and expertise from horizontal axis wind turbines is the easiest approach to develop tidal stream energy. A tidal stream turbine is comparable to a wind turbine, except seawater is 800 times denser than air and has one-fifth the flow rate. A properly rated tidal turbine would have half the rotor diameter of a comparable wind turbine. Tidal stream energy harnessing devices could be categorized into three types [145]–[147] (see Fig. III-2):

- Horizontal axis systems like the Free Flow Turbine designed by Verdant Power and installed in the USA as part of the RITE project [148], or those installed in the Bristol Channel between England and Wales [149].

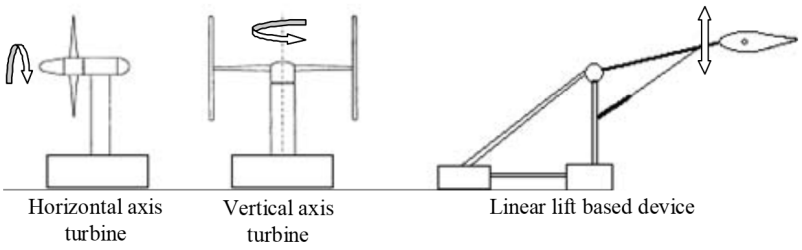

Fig. III-2 Tidal current turbines different types [146].

- Vertical axis systems like the GCK Gorlov Helical Turbine designed in the US [150] or the turbine of the ENERMAR project located along Sicilian coast [151].

- Oscillating hydrofoil systems such as the Stingray tidal stream energy device installed in the Shetland, UK [152].

1.2. Wave Energy

Wave energy technologies are meant to harvest energy from the wave motion. Wave energy systems are often categorized into shoreline (or coastal), near-shore, and offshore devices based on the features of their deployment areas. The physical factors pertinent to wave energy conversion vary based on ocean depth and distance from the coast. It is anticipated that floating systems anchored in deep water will have the greatest potential for large-scale application, since waves in deep water move across the ocean nearly without energy loss.

The Pelamis wave energy converter was the offshore wave energy technology that is closest to park-scale deployment, but the company was disbanded in 2014. Current wave energy clients that are working on wave energy technologies are like AWS Ocean Energy, Mocean Energy, SEABSED, Wello OY [153]. Wave energy technology types could be classified into different types like attenuator, axisymmetric point absorber, oscillating wave surge converters, oscillating water column, overtopping device, and submerged pressure differential. Each one of these categories might have typical power take-off (PTO) options, but the other options might also be suitable for them. An overview on wave energy conversion devices can be found in [154].

1.3. Tidal Impoundment Energy

Tidal impoundment power plants work by impounding enormous quantities of water at a location that may generate a head difference, and then directing the flow of this water into or out of the impoundment using low-head hydroelectric turbines. The plants may function on either ebb or flood tide, or both. The most prevalent technique is ebb generation. At this position, water would enter via sluice gates as the tide rises. Then, the sluices are shut, and the tide starts to recede. When the water level outside the barrage is low enough to provide a proper head, the sluices are opened and the water in the impoundment is released back into the sea through turbines. Like wind energy, this technology has achieved industrial and commercial maturity. However, there are few tidal power plants owing to the limited number of appropriate locations and the concerns on the potential harmful impact on the ecosystem. Table III-1 lists tidal power stations in operation around the world [155], [156]. The tidal power station in La Rance, France was the first in the world that was put in service in 1966, and it remains to this day one of the most important in the world. The electromechanical conversion systems used for this energy are like those used with wind turbines, and the electric machine structures are rotational.

1.4. Offshore Wind Energy

The offshore wind energy is probably the most mature and most developed out of the different marine renewable energy sources. This is mostly because this source of energy is basically the same as normal wind energy but with different conditions and constraints, and wind energy is a very well established and now widely used renewable energy source around the world. The literature is full of state-of-the-art reviews and discussions on wind energy and some important and interesting studies could be found in [157]–[164].

Table III-1 Tidal power centers in operation around the world.

Center	Power (MW)	Country
Sihwa	254	South Korea
La Rance	240	France
Annapolis Royal	20	Canada
MeyGen	6	USA
Jiangxia	3.2	China
Kislaya Guba	1.7	Russia
Uldolmok	1.5	Sout Korea
Eastern Scheldt	1.2	Netherlands

Some of the major criteria that wind power systems should address are:

- Reliability and ease of maintenance
- Total weight of the nacelle
- Total cost
- Energy efficiency and grid integration

These criteria should be considered when looking into increasing the unit power of wind turbines.

The 2022 Global Wind Report [165] has highlighted that 2021 was the second-best year for the global wind industry where almost 94 GW capacity was added. Europe, Latin America, and Africa & the Middle East experienced record-breaking years for new onshore installations, but the overall number of onshore wind installations in 2021 was 18% fewer than the previous year. The reduction was mostly attributable to the slowdown of onshore wind growth in China and the United States, the world's two biggest wind power markets. Last year, 21.1 GW of offshore wind capacity was installed, three times as much as in 2020. Making 2021 the greatest year in the history of offshore wind and increasing its market share of new installations worldwide to 22.5% in 2021. China contributed 80% of the world's offshore wind capacity additions in 2021, increasing its total offshore wind installations to 27.7 GW (see Fig. III-3). It took Europe 30 years to reach a comparable level of offshore wind capacity. The total worldwide wind power capacity has now reached 837 GW, allowing the world to avoid almost 1.2 billion tons of CO2 per year.

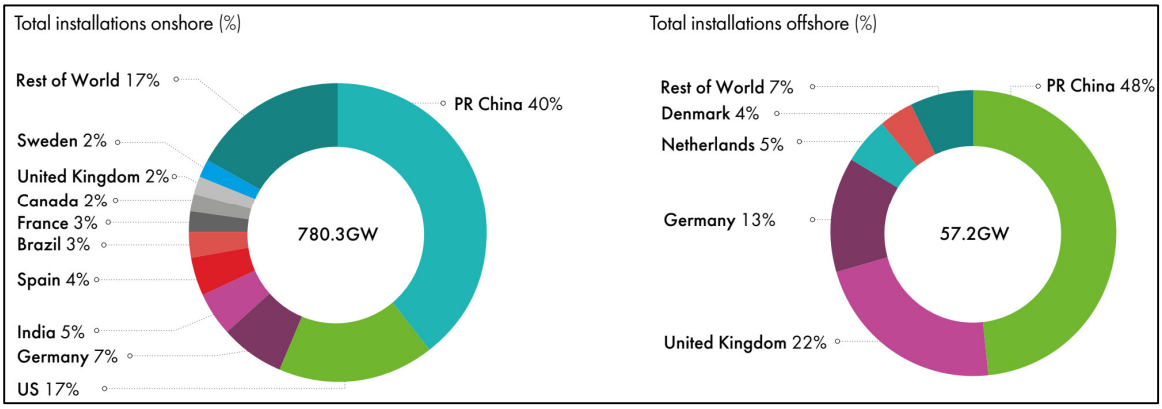

Fig. III-3 The distribution of the total onshore and offshore wind energy installations around the world [165].

A report from 2017 [166] summarized the principle manufacturers for offshore wind turbines (see Fig. III-4) and estimated the top 5 suppliers of wind turbines with over 5 MW of unitary power (see Fig. III-5). The aforementioned criteria support the construction of wind turbines with the highest feasible unitary power, essentially to reduce installation and maintenance costs. In fact, it is more economical to install a limited number of turbines with high unit power, than a larger number of turbines with lower power [167], [168].

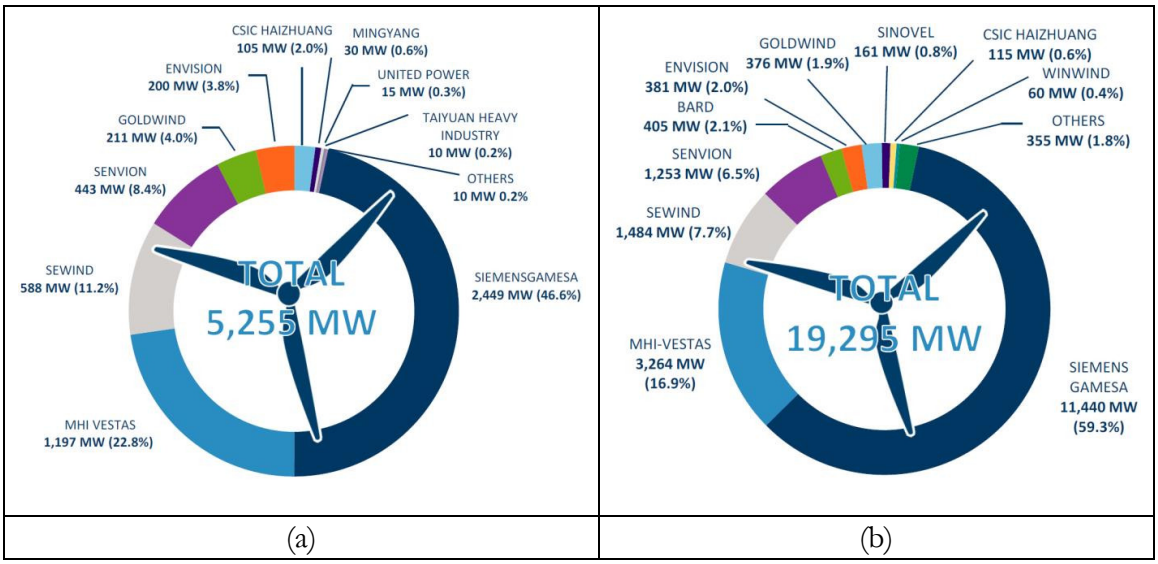

(a) (b)

Fig. III-4 Top 10 offshore wind turbine suppliers for (a) newly installed turbines in 2017 and for (b) the total turbines installed by the end of 2017 [166].

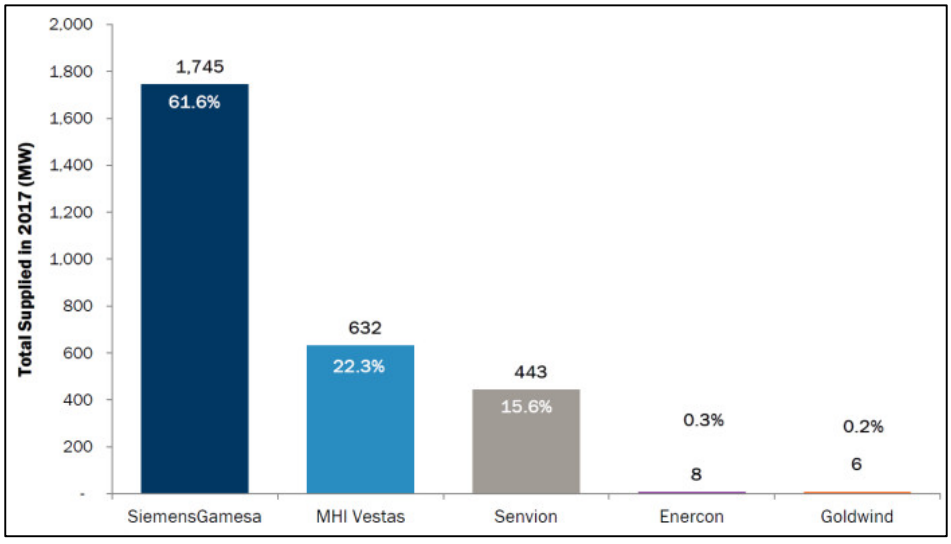

Fig. III-5 Top 5 suppliers for wind turbines with unitary power of over 5 MW in the year of 2017 [166].

The Haliade-X offshore wind turbines from GE Renewable Energy are the most powerful wind turbines in operation to date. The Haliade-X 14 MW was the industry's first offshore wind turbine to operate, and the only 12+MW offshore wind turbine platform that has been operating for over two years. It has a 220-meter radius rotor with three blades each measuring 107 meters. In addition, it uses a single direct drive permanent magnet synchronous generator [169]. Other powerful offshore wind turbines (14+ MW) are being developed currently by different manufacturers like bewind, Vestas, aerodyn Energiesysteme, Siemens Gamesa Renewable Energy, and Mingyang Defeng Energy Systems. For example, the V236-15.0 is a 15 MW offshore wind turbine that is being developed by Vestas, where it uses an indirect drive synchronous generator through a three-stage planetary gearbox, and the installation of its prototype is set to take place in the second half of 2022 [170]. Finally, the largest announced offshore wind turbine is the 16 MW MySE 16.0-242 from the Chinese manufacturer Mingyang. This wind turbine has a hybrid drive topology with a medium-speed planetary gearbox, and the installation of its prototype is scheduled for the first half of 2023 [171]. In the following subsections the criteria related to the wind turbines are discussed based on the overview presented in [159].

1.4.1. Reliability and ease of maintenance

Several recent studies have been devoted to the problem of the reliability of wind turbine systems [172]–[177]. This problem has a direct link with the operation and maintenance costs (O&M) of wind systems.

Fig. III-6 GE Haliade-X 14 MW offshore wind turbine prototype [169].

These studies are based on databases collected on wind turbine systems already installed "onshore" and "offshore". Note that the first offshore wind farm is the Vindeby wind farm in Denmark. This park was dismantled in 2017, the year in which the first floating wind farm "Hywind Scotland" was commissioned [178]. Moreover, a European project "RELIAWIND" bringing together players from the industrial and academic worlds has been devoted to this issue [179]. Detailed analyzes are made of the data collected. Some studies are also devoted to defining the best reading indicators of its bases in order to draw the right lessons [172], [173], [180]–[182]. Eventually, these studies make it possible to refine the monitoring campaigns. Some components like the generator are complex electromechanical systems that should not be treated as a single component, but as a set of subcomponents (bearings, windings, etc.) that should each be monitored [183].

Overall, data on power generation systems [173], [175], [176], [184] show that mechanical gearboxes, for the drive systems where they are present, are the components with the highest O&M costs. especially when they are implemented with multiple stages. On the other hand, for direct drive systems, where no mechanical gearboxes are installed, the failure rate for the generator increases [175], [176]. Essentially, the elimination of gearboxes shifts the problems to the level of the generator which is subjected to much greater mechanical stresses, and the current load increases at the same time (torque machines). In the direct drive systems, where the speed of rotation is relatively low, and thus the torque produced by the machine becomes relatively high, as well as the current of the armature (torque machines), and this causes mechanical problems and heating of the windings. In this situation, the use of magnetic gears is very plausible and could solve a lot of the reliability problems. Most of the marine energy types listed before in addition to the onshore and offshore wind energy systems are considered as applications with high torque and low speed, and as discussed in the first chapter, the magnetic gears are best suited for such operation because most of their losses are dependent on their rotational speed. However, there are still concerns raised around the heavy dependance of magnetic gears on rare-earth magnets which affects the availability of the materials and the economic feasibility of the devices.

1.4.2. Weight of the Nacelle

The weight of the nacelle is an important indicator of the technical and economic feasibility of a wind turbine concept. From the perspective of using direct drive generators, which are much heavier than those associated with gearboxes, and the inclusion of step-up transformers

in the nacelle, for offshore wind turbines, the mechanical load of the tower will be too high and may therefore compromise the technical and economic feasibility of higher power wind turbines. Regarding the reduction of the weight of the power transformer, some studies propose replacing it by a lighter power electronics converter. A state of the art concerning this aspect is presented in [185]. For the generator, innovative solutions that are more compact, and therefore less heavy, such as PDD systems, or generators based on superconductors are still being heavily investigated. These two solutions have been explored within the framework of the "InnWind" project. The development of a low-cost and lightweight superconducting generator demonstrator was recently carried out within the framework of the European "EcoSwing" project, which ended in April 2019. This prototype was placed in a wind turbine and tested with success [186].

1.4.3. Total Cost

Another aspect to consider when designing wind turbines is related to the investment and operating costs. The cost of the generator represents a non-negligible part of the total cost of the nacelle [187], [188], which itself constitutes a significant part of the investment and operating costs.

Permanent magnet generators have relatively high capital costs but are offset by relatively low O&M costs. Given the fluctuating prices of permanent magnets, one solution is to use wound excitation, or double excitation generators [189]. However, this would lead to an increase in O&M costs, given the additional excitation system. This issue of offshore wind costs is the subject of the European "ROMEO" project [190].

1.4.4. Energy efficiency and grid integration

The direct-drive fault-tolerant permanent magnet generator is probably the best solution for increasing the energy yield of a wind turbine. The direct drive concept allows mechanical gearbox losses to be eliminated, and permanent magnet generators have relatively higher efficiency than other machine technologies. Fault tolerance of the machine improves its availability and therefore its energy efficiency.

The spread of wind energy in the electrical energy system continues to increase, which implies that large wind farms are changing from the status of a simple energy source to the status of power plant with characteristics of support to the electricity network. The main grid code requirements can be summarized as follows: control of active and reactive power, control of the voltage quality (frequency and harmonics), and the voltage dip management [191]. While in

conventional thermal power plants the ability of the units to respond to the "grid code" is ensured by controlling the drive system, in the case of wind turbines this is not possible because the direction and intensity of the wind can't be controlled. The proposed solutions, to meet the requirements of electrical network operators, consist of adding power electronics systems often associated with energy storage systems [192].

2. Applications of Magnetic Gears in Marine Renewable Energy

Some literature overview studies have been done on the application of magnetic gears or magnetically geared machines in marine and wind energy [82], [193], [194]. In [82], the authors presented the different magnetically geared machines or PDD technologies that could be applied to wind energy whether onshore or offshore. The study started first by presenting the popular drive train topologies for wind energy systems and then made a comparison between these systems based mainly on their mass and cost, where the result of the comparison agrees with what have been discussed in the previous section concerning the high mass and cost of direct drive PM generators. Next, the study went on to present different magnetic gear and magnetically geared machine types, and then present their potential advantages like the compact size of the MGM with respect to a PM machine with a one-stage gearbox. Finally, the challenges associated with the MGMs were discussed like the complex mechanical structure of MGs and MGMs which might increase their manufacturing costs, the complexity of the optimization process required to match between the magnetic gear and the PM generator where the modeling of magnetic gears is already complicated and requires 3D modeling methods due to the severity of the end-effects which agrees with what have been presented in chapter 2 of this work. Moreover, another reported challenge was related to the low torsional stiffness of the mechanical parts which could lead to undesired oscillations [82].

A dedicated study to demonstrate the potential of MGs in marine energy was presented in [194]. The study first provided a brief overview on MGs in general and then discussed in detail the forms of implementation for magnetic gears in marine energy, specifically wave and tidal energy. One of the applications that was proposed for magnetic gears was to use it in oscillating wave surge converters (see Fig. III-7), where this proposed application was a high torque low speed one and required a gear ratio of around 10 [194], [195]. Furthermore, multiple gear ratio values of the MGs that could be proposed for wind energy applications, where the torque ripple was investigated for each individual value [193].

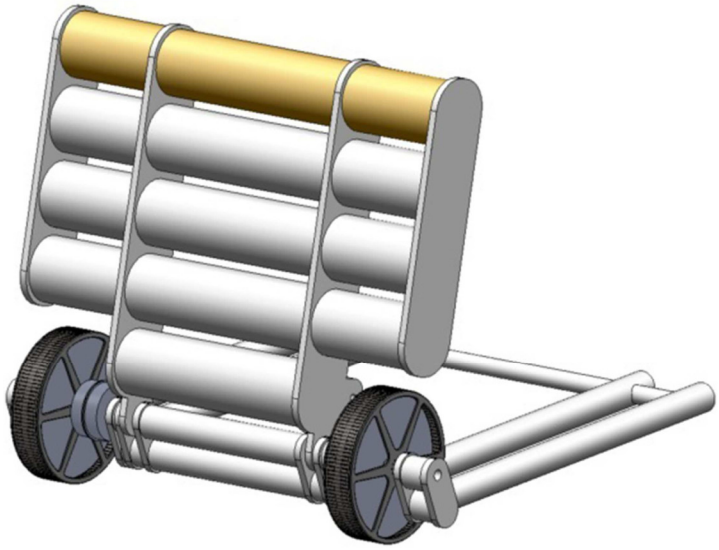

Fig. III-7 An oyster design proposed with two MGs connected to two generators [195].

Consequently, many MG and MGM designs were proposed for marine energy with different types and structures, and a briefing for some of these designs will be done in the following paragraphs.

1.5. Rotational Radial Field Structures

In [196], L. Shah proposed a coaxial radial field magnetic gear to be used for contra-rotating tidal turbine system which is a double rotor turbine system (see Fig. III-8). The proposed MG is a basic surface mounted PM but with no fixed rotor, where the outer and the pole pieces rotors rotate simultaneously at the same low speed in opposite directions while the inner rotor is the high-speed output shaft, and the resulting gear ratio for this mode of operation is 1:12. The design was theoretically supposed to provide a VTD of 74 N m/L, but the constructed prototype delivered 47.08 N m/L which according to the authors was due to the non-uniform air gaps of the constructed prototype.

A 1:63.3 dual-stage magnetic gearbox designed for a hydrokinetic generator application was presented through two studies [197], [198] (see Fig. III-9). The first study addressed the electromagnetic and mechanical design of the first stage of the magnetic gearbox which was chosen with a gear ratio of 6.67:1. The design requirements for the first stage were low torque ripple, high efficiency, input speed of less than 40 rpm (which is suitable for a hydrokinetic turbine), and a rated power of 5 kW (at 40 rpm) [198].

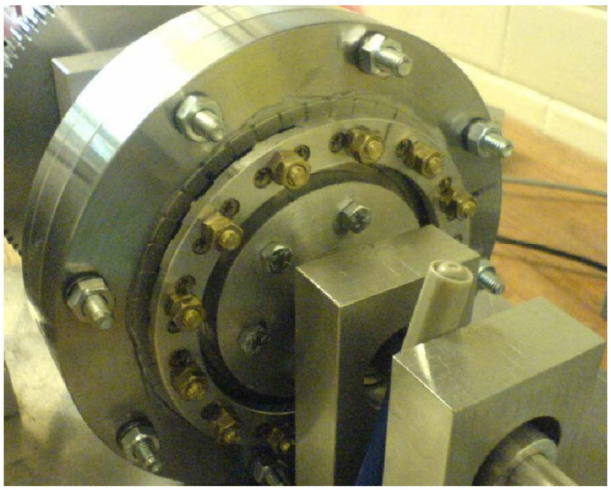

Fig. III-8 The MG prototype designed for a contra-rotating tidal turbine [196].

The study first investigated using flux focusing configuration on the inner and outer rotors and performed a parametric sweep analysis to determine the optimal parameters for a high mass and volume torque densities. Then, to increase the torque capability of the design without increasing the axial length, Halbach array configuration was used on the outer rotor. Furthermore, the study performed a deflection analysis to measure the feasibility of the mechanical design. The final estimated VTD using 3D FEM was 306.4 N m/L [198].

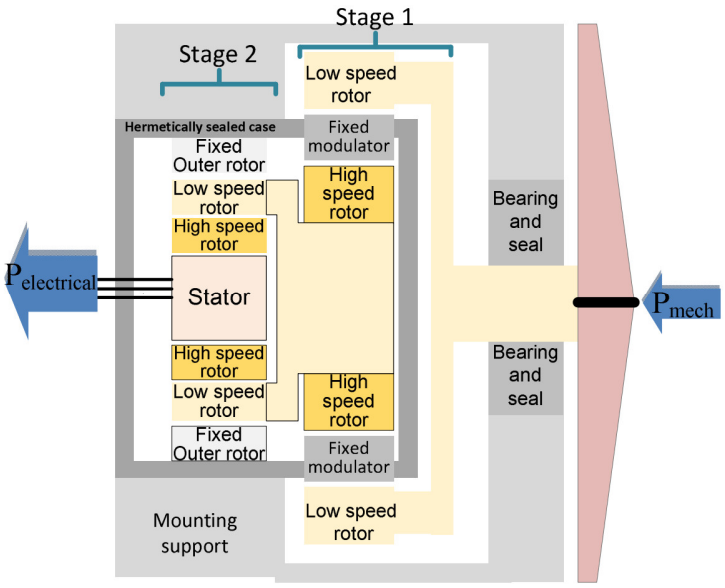

Fig. III-9 A sketch showing the proposed dual stage hermetically sealed magnetic gearbox designed for marine hydrokinetic applications [198]

Fig. III-10 The prototype constructed in [198] showing the (a) full assembly of the inner Halbach rotor, (b) the cage rotor, and (c) the half assembly of the outer Halbach rotor.

The design and prototyping of the second stage of the magnetic gearbox was done in [197]. The proposed design had a gear ratio of 9.5:1 and Halbach array configuration for the PM rotors, where the authors used for the Halbach rotor a new type of isosceles trapezoidal magnet shape to facilitate the assembly and manufacturing. The optimization study was done for two configurations regarding the multistage implementation: a nested configuration where the generator is included within the 2nd stage MG as shown in Fig. III-9, and a series configuration where the generator is cascaded externally to the magnetic gearbox. The comparison between the two configurations has shown that while the series MG design delivered greater volumetric torque density, both the series and nested configurations had comparable volumetric torque density characteristics. Eventually, a prototype was constructed testing the MG on its own in addition to testing it while in the series configuration with an off-the-shelf generator (see Fig. III-10). The experimental VTD for the MG was measured to be 236 N m/L while the measured VTD of the MG generator combination was 66 N m/L.

In their work [199] the authors investigated the possibility of using magnetically geared machines to harvest wave energy, and then demonstrated the design, analysis, and construction of a large scale magnetically decoupled inner stator radial flux magnetically geared machine prototype (see Fig. III-11). It was shown that the prototype could attain a significant stall torque of 3870 N m which matched the estimated values and corresponded to a VTD of 82.8 N m/L and an MTD of 14.5 N/kg. Furthermore, while running in steady state near its rated torque, the prototype was around 90% efficient with negligible torque ripple. As a result, the technology was reported to have enormous promise for high torque, low speed applications such as wave

and wind energy harvesting, traction, and oil and gas extraction. Additionally, the authors left some observations on their experience with this design like the necessity of the simultaneous evaluation for the magnetic gear and the generator when choosing the optimal gear ratio, and the severity of the end-effects where it was evaluated that it decreased the maximal VTD by 21%. On the other, the authors recommended that significant future work is still ahead to develop this technology, where the main concern is investigating the transient response of the device to oscillating input motion. In fact, studies on the transient response of MGMs are already starting to emerge [200], [201].

Additionally, a magnetically geared PDD generator for a floating tethered marine current turbine was proposed in [202]. The device was designed to have a rating of 6 kW at a speed of 100 rpm. The study first started by investigating different pole-pair combinations and different gear ratios where the selection criteria were obtaining a high pull-out torque, low torque ripple, and acceptable attraction forces (see Fig. III-12). After choosing the gear ratio to be 7.75:1, an optimization study aiming at maximizing the PDD efficiency at the rated operation point and reducing the total PM mass while limiting the 2-D active length of the machine to a maximum of 180 mm. Then, following the choice of the right parameters a prototype of the PDD generator was constructed and validated first using a dynamometer test setup, and later by integrating it into a marine current turbine where the outer case of the PDD was in direct contact with water flow (see Fig. III-13).

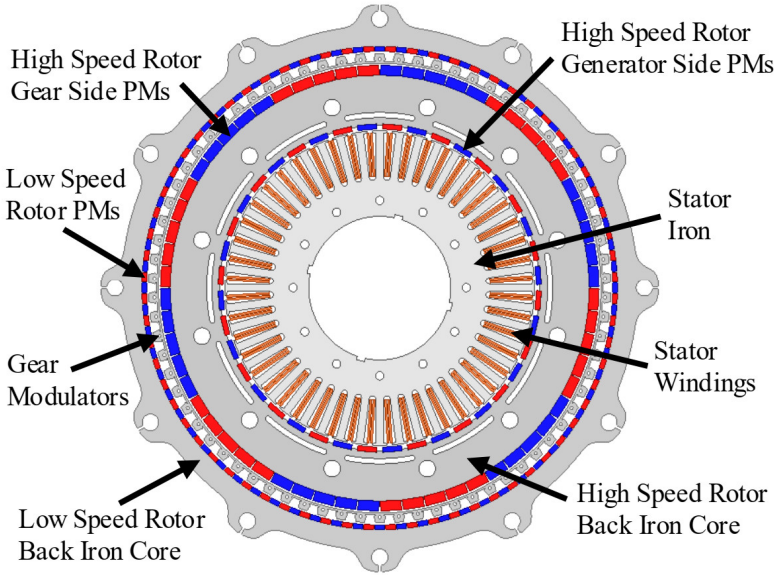

Fig. III-11 Cross-section view of the MGM proposed in [199] for wave energy harvesting.

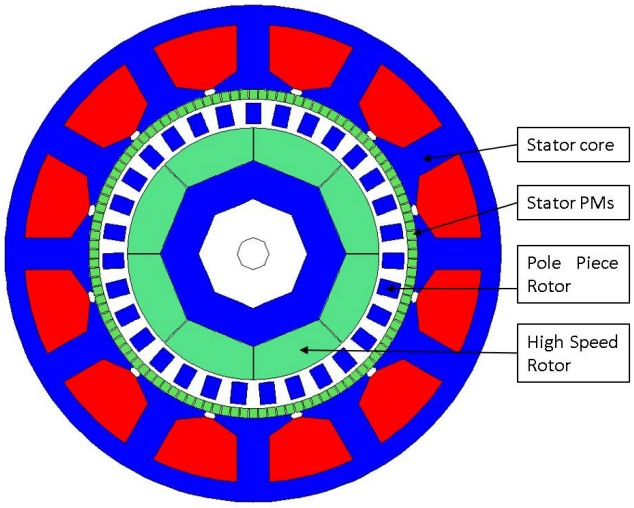

Fig. III-12 The PDD generator proposed for floating marine current turbine in [202].

The study has shown that this design exhibited high efficiency in a compact form that can be easily integrated into the marine turbine, and in addition it will assure a reduced maintenance rate due to the integration of the magnetic gear element. Finally, the study has discussed the effect of the unbalanced attraction forces on the machine performance [202].

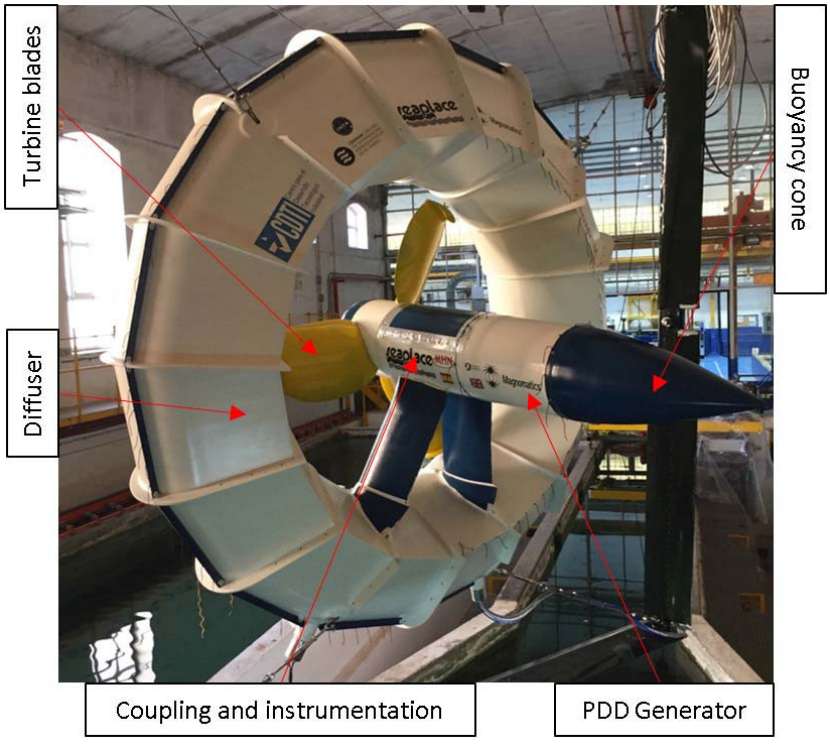

Fig. III-13 The PDD tidal turbine demonstrator presented in [202].

1.6. Rotational Axial Field Structures

There are some studies that discussed the use of axial field structures for wind or marine renewable energy, but the number of prototyped and experimentally tested axial field structures is still very little because the axial field topology still has a lot of challenges to address mainly related to the attraction forces. In[203], the authors designed and experimentally tested an axial field magnetically geared generator for wind energy applications (see Fig. III-14). The rated power of the machine was 4 kW, and the chosen gear ratio was 6.667:1 which for a rated input speed of 150 rpm could ensure an output frequency for the generator of 50 Hz. A prototype was constructed for the design after performing an optimization study and choosing the right parameters. It has been shown the active MG part could achieve a VTD of over 100 N m/L. In addition, two configurations were tested for the MGM, one where the MG is magnetically coupled to the generator and another when the two are magnetically decoupled. Moreover, the inherent overload protection was demonstrated for the device. On the other hand, high losses occurred at the LSR side caused by the flux leakage in the steel back plate which led to a poor overall efficiency for the prototype. Additionally, the axial field flux focusing MG of the study in [49] which was presented in the first chapter was designed for ocean generator applications, where the authors first performed a parametric sweep analysis to get the design parameters then constructed a prototype that was evaluated to have a VTD of 152.3 N m/L.

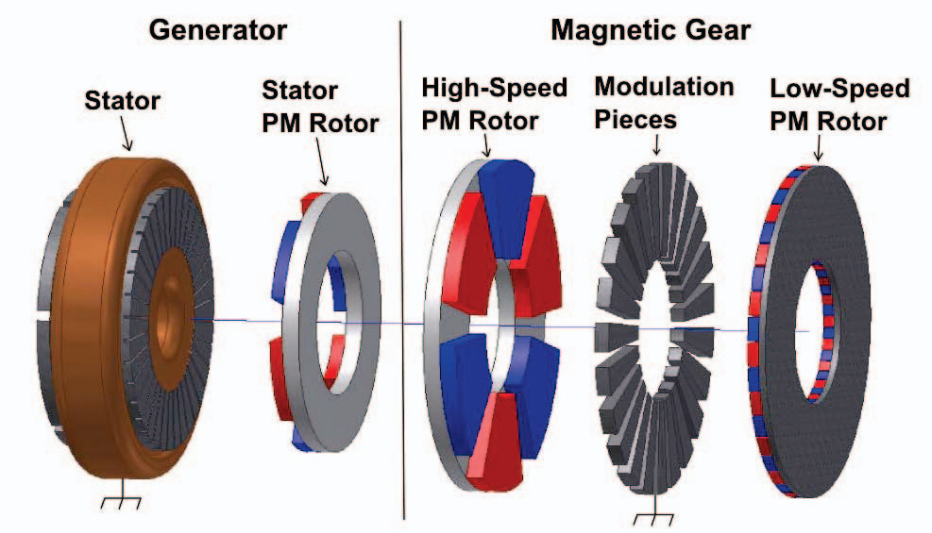

Fig. III-14 The layout of the axial field MGM proposed in [203].

1.7. Tubular Linear Structures

Linear magnetically geared machines were proposed for heaving buoy wave energy converters. A linear magnetic gear cascaded with a linear PM generator was proposed in [204] for such an application. The proposed system was serially integrated which enabled the gear's high-speed mover and the generator's translator to use the same shaft. The suggested design couples the MG's low-speed mover with the heaving buoy structure (see Fig. III-15). The speed of the high-speed mover linked to the linear generator is increased by a factor of the gear ratio when the buoy rises and falls with wave propagation. A comparably rated machine without the MG system would have a volume four times that of the proposed system and would cost much more due to increased quantities of PMs, iron cores, and copper windings (167, 214, and 271%, respectively). Furthermore, the copper losses for the gearless machine were projected to be greater. As a result, the suggested machine has higher efficiency and power density while drastically decreasing cost and bulk [194], [204].

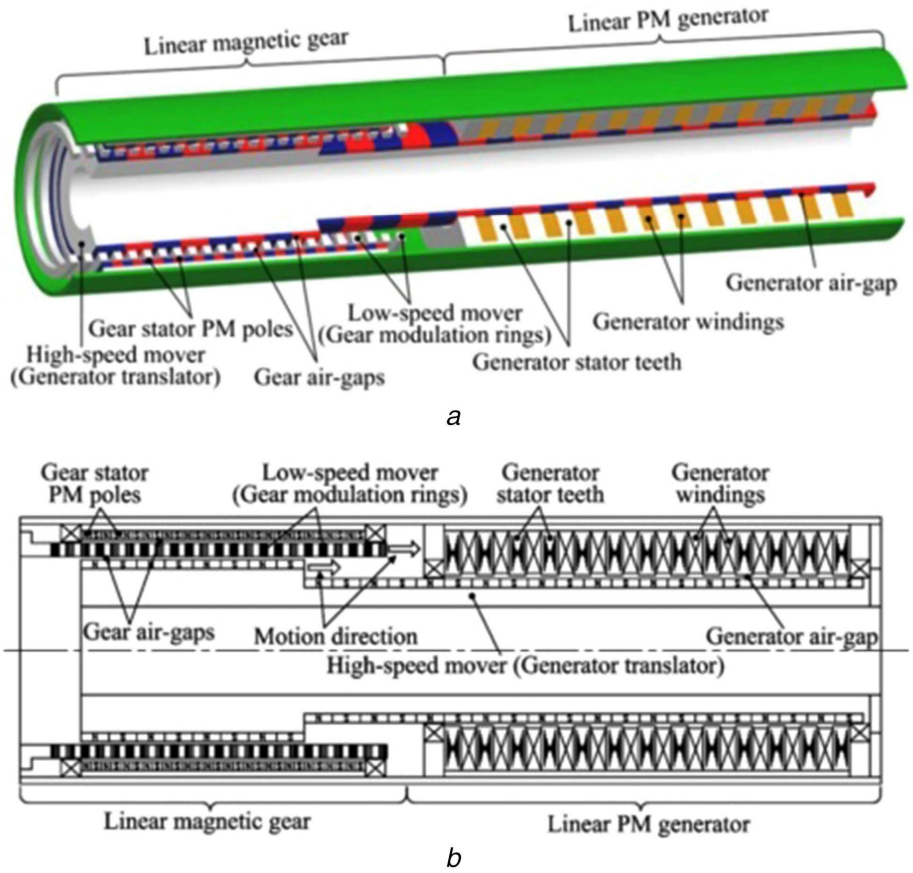

Fig. III-15 A linear MGM proposed for a heaving buoy converter ((a) 3D solid model (b) cross-section schematic) [204].

An adjustable gear ratio linear MGM design for wave energy extraction was proposed in [205], where the design used Alnico magnets (see Fig. III-16). The gear ratio variation was done by magnetizing and demagnetizing some of the Alnico magnet poles using DC excitation fields. The work included evaluation of the electromagnetic performance of the proposed design through FEM modeling. It was suggested that the variable gear ratio property of the MG would allow the wave energy converter to operate in resonance with the waves at different sea states to maximize the captured power.

Finally, some studies have discussed the use of trans-rotary MG or magnetic lead screw design for the wave energy convertors [206]–[209].

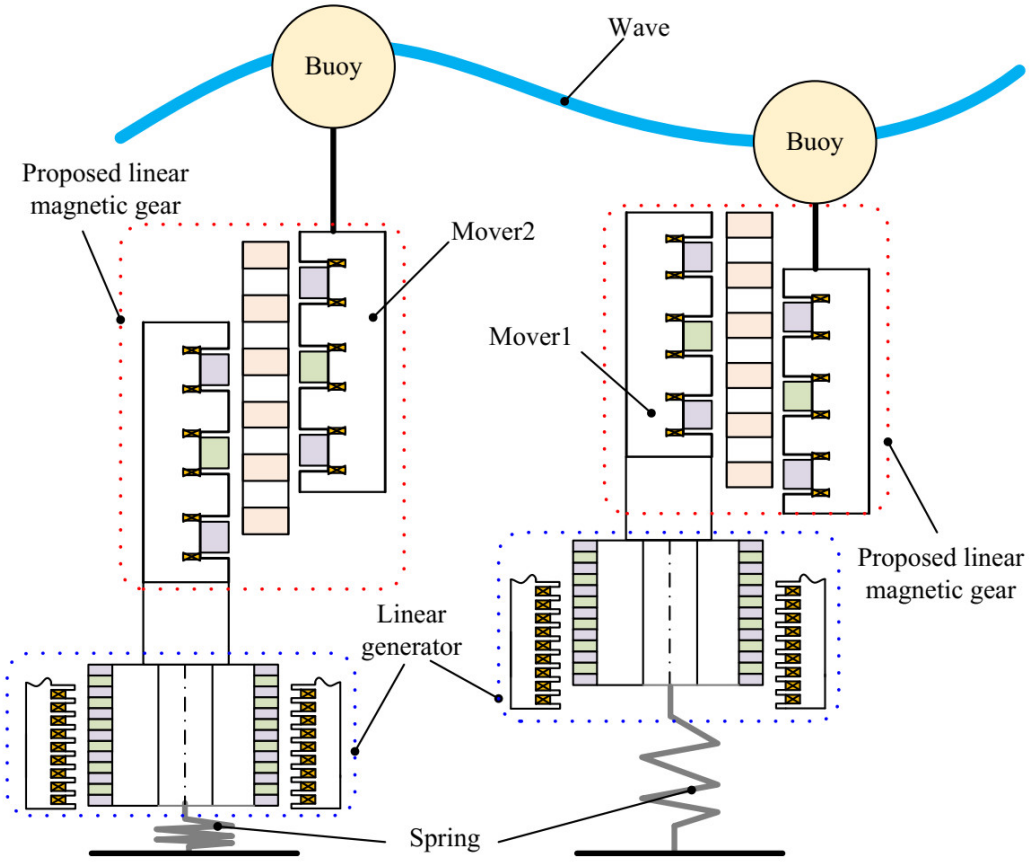

Fig. III-16 A drawing of the possible installation of the variable gear ratio linear MG proposed in [205].

3. Proposal of a MG for Marine Energy Conversion

To wrap up the investigation and put the modeling methods proposed in the previous chapter to practice, this section will carry out a parametric sweep analysis to determine the design parameters of an axial field flux focusing magnetic gear. This proposed design could be useful for multiple applications including tidal current, wave surge oscillator, and offshore wind turbines, and since there is no specific application certain criteria will be defined just to direct the selection of the parameters. The criteria defined were as follows:

- Gear ratio greater than 7 and smaller than 11
- Output torque greater than 600 N m
- Virtually ripple free torque transmission (i.e., the cogging torque factor = 1)

Based on these criteria, the first step is to choose the appropriate pole-pair combinations and gear ratio. The choice will be done by running simulations for the different combinations while fixing the main parameters of the magnetic gear (axial length, inner and outer radii, air gap length), and then doing the selection such as maximizing the output torque and minimizing the attraction forces. The simulations of this step and all the following steps will be done using the linear 3D PN method while considering the end-effects. The magnetic saturation was not considered to ensure the rapidity of the calculations, so the relative permeability of the soft magnetic materials was chosen constant at 10000. At each simulation step the rotors were moved into the maximum torque position and the torques and forces on each rotor were calculated.

Regarding the choice of the fixed and rotating members, to maximize the gear ratio for a given set of pole-pairs, the rotor with the higher number of magnetic pole-pairs was chosen as the fixed member, the modulation pole pieces rotor (PPR) was chosen as the LSR, and eventually the rotor with the lower number of magnetic pole-pairs becomes the HSR. The minimal number of the magnetic pole-pairs for the HSR was chosen at 4 according to the recommendation provided by the authors in [210]. The initial parameters that were used throughout this first step are summarized in Table III-2. It is worth noting that the chosen soft magnetic material was the laminated non-grain-oriented silicon steel M600-50A, and the chosen PM material was the sintered neodymium iron boron N35. Throughout the parametric sweep analysis, when using the 3D PN, only the mass density of the M600-50A steel will be considered but not its magnetic saturation behavior as mentioned earlier, and regarding the PM, the N35 has a linear

demagnetization curve, so its magnetic properties as well as its mass density can be considered by the 3D PN.

For different pole-pair combinations and gear ratios, the per unit stall torque of the LSR and the per unit attraction force on the LSR (at the maximum torque position) are shown in Fig. III-17 and Fig. III-18 respectively. From the figures below, the maximum stall torque is attributed to the gear ratio 8.25 and the HSR pole-pairs 4, but at the same time this combination also inherits the highest attraction force, so it can be chosen especially that there are other combinations that have reduced attraction force but slightly lower stall torque. Thus, this compromise between the maximum output torque and the attraction force can lead to choosing the gear ratio 8.1667:1 with $p_1 = 6$. The output torque of this combination is 4.2% less than the maximum possible output torque, but its attraction force is 36% less the attraction force of the combination that has the maximum output torque which is a very good trade-off. Hence, the number of pole pairs on each rotor becomes $p_1 = 6, n_2 = 49$, and $p_3 = 43$.

Table III-2 The initial chosen parameters of the AFFMG for the parametric sweep analysis.

Rotor 1 (HSR)	Number of pole-pairs	p_1
	Steel/magnet pole span $\theta_{1s} = \theta_{1m}$	$180°/2p_1$
	Axial Length l_{a1}	20 mm
	Air gap	1mm
Rotor 2 (LSR)	Number of modulating pole pieces	n_2
	Steel/slot pole span $\theta_{2f} = \theta_{2s}$	$180°/n_2$
	Axial Length l_{a2}	10 mm
Rotor 3 (Stationary)	Number of pole-pairs	p_3
	Steel/magnet pole span $\theta_{3s} = \theta_{3m}$	$180°/2p_3$
	Axial Length l_{a3}	20 mm
	Air gap	1 mm
Radii	Inner Radius R_i	80 mm
	Outer Radius R_o	140 mm
Materials	Steel mass density	7750 Kg/m^3
	PM mass density	7400 Kg/m^3
	PM relative permeability	1.05
	PM magnetic remanence	1.2 T

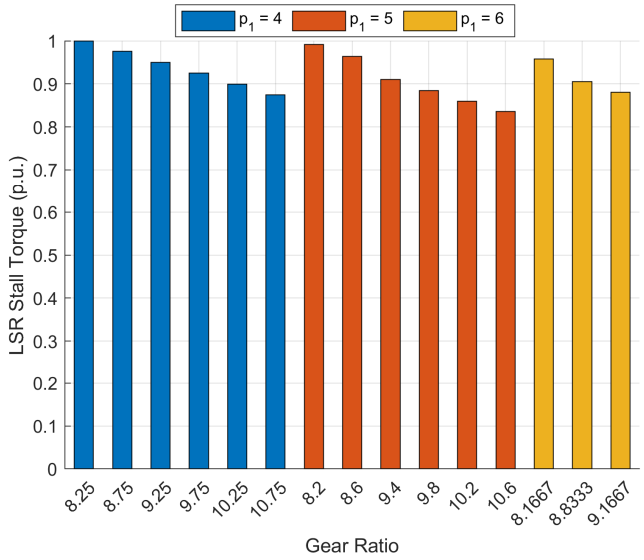

Fig. III-17 The LSR stall torque of the different tested pole-pair combinations and gear ratios.

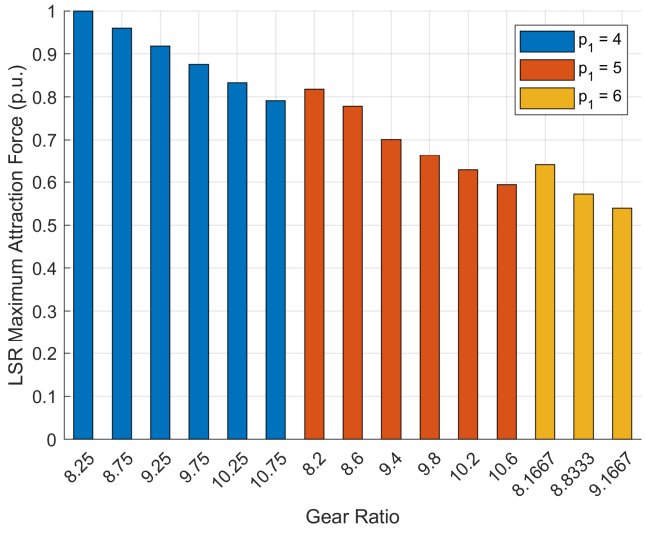

Fig. III-18 The maximum attraction force on the LSR for different gear ratios and pole-pair combinations.

After choosing the suitable gear ratio and pole-pair numbers, a parametric sweep analysis will be carried out to determine a good set of parameters. The two objectives are maximizing the active region volumetric torque density and mass torque density, where certain parameters will

be varied consecutively to satisfy the objectives. The equations of the VTD and MTD can be given by:

$$VTD = \frac{C_2}{(l_{a1} + l_{a2} + l_{a3} + 2 \cdot airgap) \cdot \pi \, R_o^2} \tag{III-1}$$

$$MTD = \frac{C_2}{m_{fer} + m_{pm}} \tag{III-2}$$

where C_2 is the stall torque of the LSR, m_{fer}, and m_{pm} are the total steel and PM masses. The first two parameters that will be varied are the inner and outer radii where all the other remaining parameters will remain constant according to the values of Table III-2.

The variation of the VTD and MTD with respect to the different inner and outer radii values is shown in Fig. III-19. By observing the figures, the VTD seems to be always increasing as the inner radius value decrease and the outer radius value increase. However, the MTD attains a peak value at a certain point and starts to decline beyond it. Thus, the inner and outer radii values at which the MTD attains its maximum will be chosen and specifying $\mathrm{R_i} = 70\ \mathrm{mm}$ and $\mathrm{R_o} = 150\ \mathrm{mm}$.

Consequently, the axial lengths of each rotor will be varied consecutively while fixing the other parameters including the newly chosen radii values. First, the axial length of the HSR (l_{a1}) is varied, and Fig. III-20 shows the variation of the VTD and MTD with respect to the different values of l_{a1}.

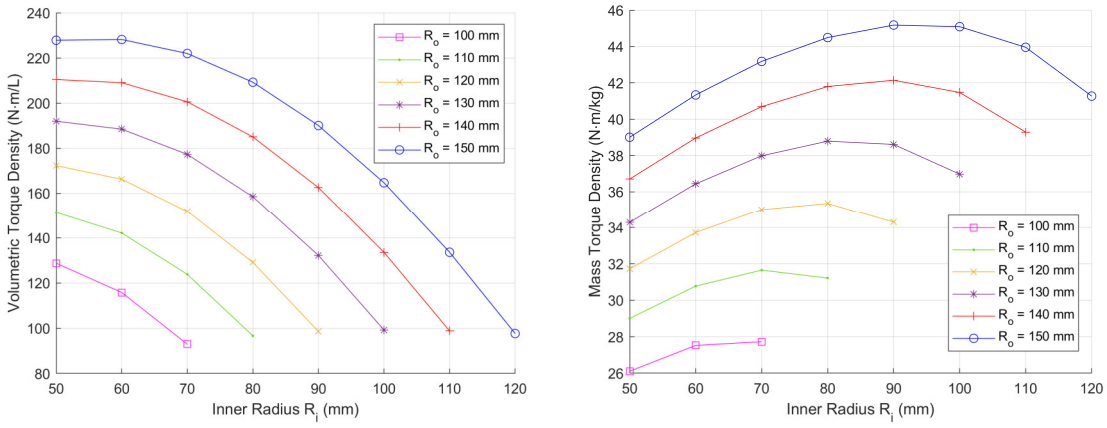

(a) (b)

Fig. III-19 The variation of the (a) VTD and (b) MTD as a function of the varying inner and outer radii.

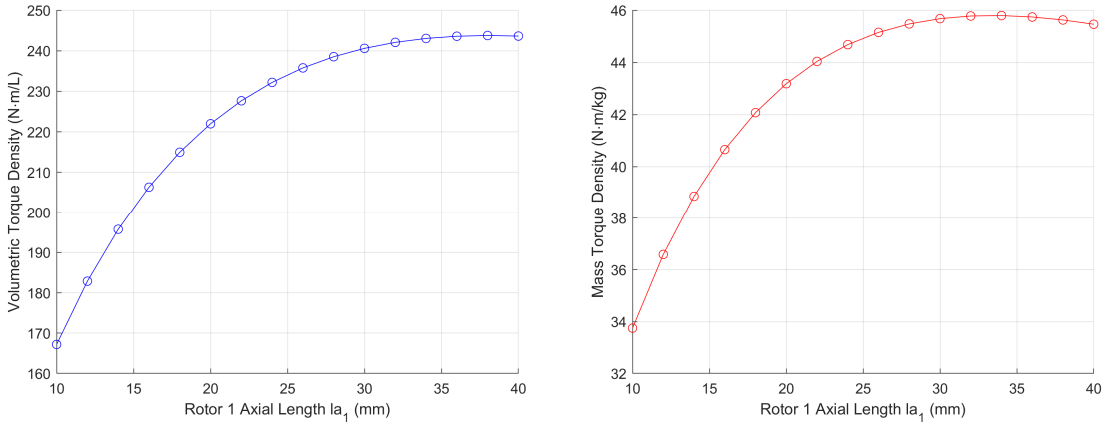

(a) (b)

Fig. III-20 The variation of the (a) VTD and (b) MTD as a function of the axial length of the HSR.

As the axial length of the HSR increases the VTD and MTD increase until they reach a certain maximum after which the MTD especially starts to decrease. Hence, the value chosen that corresponds to the maximum MTD was $l_{a1} = 32\ mm$.

Furthermore, after fixing the new value of l_{a1}, next the axial length of the fixed rotor l_{a3} is varied. The variation of the torque densities with respect to the multiple l_{a3} values is shown in Fig. III-21. With the increase of the axial length l_{a3}, the VTD and MTD start increasing and quickly attain their maximum values and then start to decrease and continue declining afterwards. Thus, the chosen value for the axial length of the fixed rotor which corresponds to the maximum VTD and MTD values was $l_{a3} = 15\ mm$.

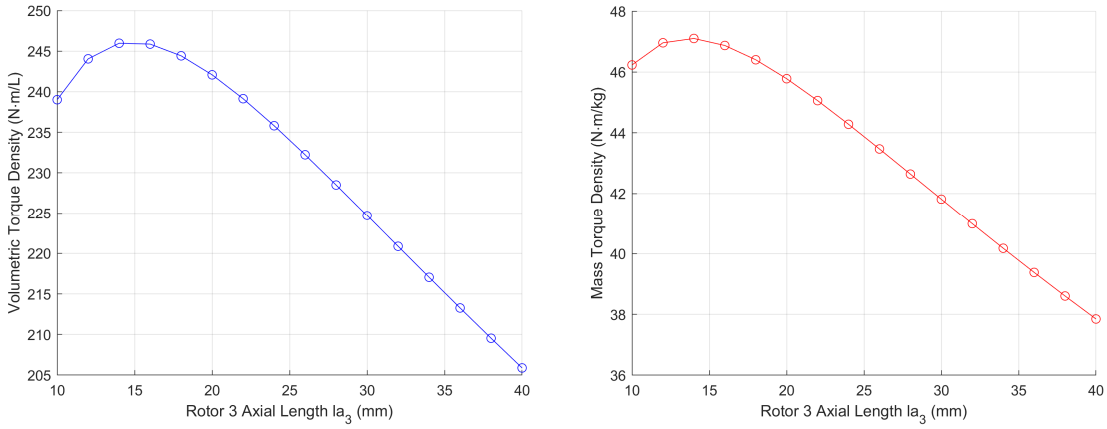

(a) (b)

Fig. III-21 The variation of the (a) VTD and (b) MTD as a function of the axial length of the fixed rotor.

Then, after choosing the axial lengths for the HSR and the fixed rotor and fixing them, the axial length of the LSR l_{a2} is varied. The figure showing the evolution the MTD and VTD as function of l_{a2} is Fig. III-22. The value of l_{a2} starts at 5 mm and as this value increases both the VTD and MTD decrease. This means that the increase in the axial length of the LSR is not significantly affecting the maximum torque of the structure, but it increases the active volume and mass of the device, so both the torque densities will decrease. Eventually, the value of 5 mm seems the best in terms of maximizing the torque densities, but because having such a small axial length for the LSR might risk the structural integrity of the rotor which will be subjected to high attraction forces. Thus, the value $l_{a2} = 10\ mm$ was chosen as a compromise. However, in any case a mechanical study that tests the structural integrity of the device and simulates the possible deflection under the attraction forces should be done on all the MG components before prototyping to test the feasibility of all the dimensions.

Finally, the last parameter to vary is the angle opening of the modulating pole-pieces of the LSR. A filling factor will be defined to control this angle opening and consequently the angle opening of the air slots in the LSR. The equation of θ_{2f} controlled by the filling factor is given by:

$$\theta_{2f} = \frac{ff_2 \cdot 360°}{n_2} \tag{III-3}$$

where $0 < ff_2 < 1$. Up until now this factor was set to 0.5 meaning that the angle opening of the modulating pieces is equal to the angle opening of the slots.

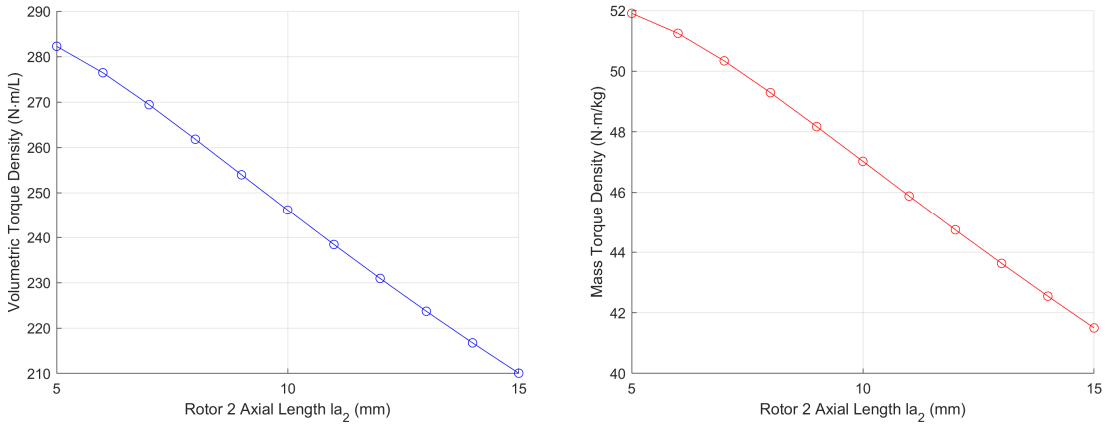

(a) (b)

Fig. III-22 The variation of the (a) VTD and (b) MTD as a function of the axial length of the LSR.

By varying the filling factor value around 0.5 while fixing all the other parameters that have been obtained until now, a variation curve for the VTD and MTD could be created (see Fig. III-23). By observing the curves, the VTD and MTD reach their maximum values for a filling factor of 0.575 which will be chosen to obtain the angle opening of the modulating pole pieces. By this choice, the sweep analysis is done where all the parameters were obtained. It is worth noting that the angle opening of the PMs of rotors 1 and 3 was kept equal to the angle opening of the steel in those rotors. Studies that are concerned with reducing the PM volume in a MG might have to investigate this parameter. Therefore, the final parameters obtained from this parametric sweep analysis are summarized in Table III-3. For the final parameters, the estimated VTD and MTD using the linear 3D PN (with end-effects) were 254.5 N m/L and 48 N m/kg respectively.

These parameters are expected to decrease when using the final parameters to create a 3D FEM that takes the end-effects and the magnetic saturation into account. Even though the end-effects were already considered in the parametric analysis, there is still a margin of error to be expected between the 3D PN and the 3D FEM which was illustrated in chapter 2. Additionally, the magnetic saturation will have its impact on the performance as well.

Therefore, to validate the design a nonlinear 3D FEM (with end-effects) was created using the final obtained parameters (see Fig. III-24). The torques and attraction forces experienced by the rotors during the pole-slipping of the HSR are shown in Fig. III-25 and Fig. III-26 respectively. The evaluated LSR stall torque using the 3D FEM was 768.9 N m which yields 184.35 N m/L VTD and 34.7 N m/kg MTD. The error between this value and the value estimated by the linear 3D PN is 27.6% which is an anticipated value.

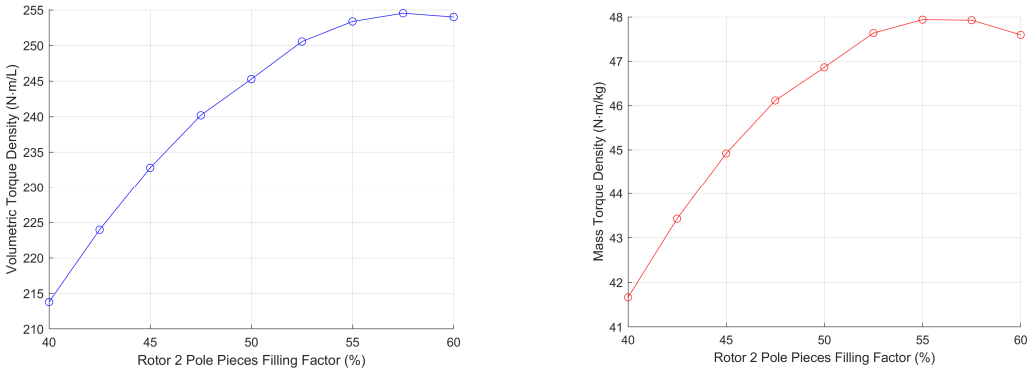

(a) (b)

Fig. III-23 The variation of the (a) VTD and (b) MTD as a function of the LSR pole pieces filling factor.

Table III-3 Final chosen parameters of the AFFMG after the parametric sweep analysis.

Rotor 1 (HSR)	Number of pole-pairs	6
	Steel/magnet pole span $\theta_{1s} = \theta_{1m}$	15°
	Axial Length l_{a1}	32 mm
	Air gap	1mm
Rotor 2 (LSR)	Number of modulating pole pieces	49
	Steel pole span θ_{2f}	4.22°
	Axial Length l_{a2}	10 mm
Rotor 3 (Stationary)	Number of pole-pairs	43
	Steel/magnet pole span $\theta_{3s} = \theta_{3m}$	2.09°
	Axial Length l_{a3}	15 mm
	Air gap	1 mm
Radii	Inner Radius R_i	70 mm
	Outer Radius R_o	150 mm

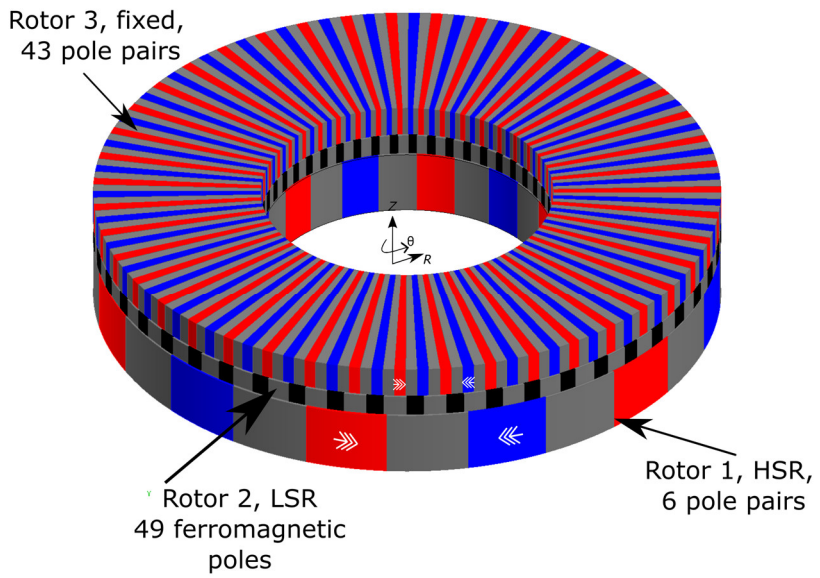

Fig. III-24 A drawing of the final proposed AFFMG design.

Although the error between the two methods might be considered relatively high, it was expected because the 3D PN didn't take the saturation into account, and, from the previous chapter, it was observed that an error of around 20% was present between the estimations of the 3D PN and the 3D FEM when modeling the end-effects. Thus, overall, the results achieved

could be considered satisfactory given that the 3D PN allowed to perform a large amount of simulations with changing parameters for a low computational cost

Finally, the torques on each rotor during the normal operation (rotation of the HSR and LSR) of the MG at maximum torque are shown in Fig. III-27. The torque transmission is as expected virtually ripple free, where the torque ripple was 0.76% for the HSR and 0.09% for the LSR.

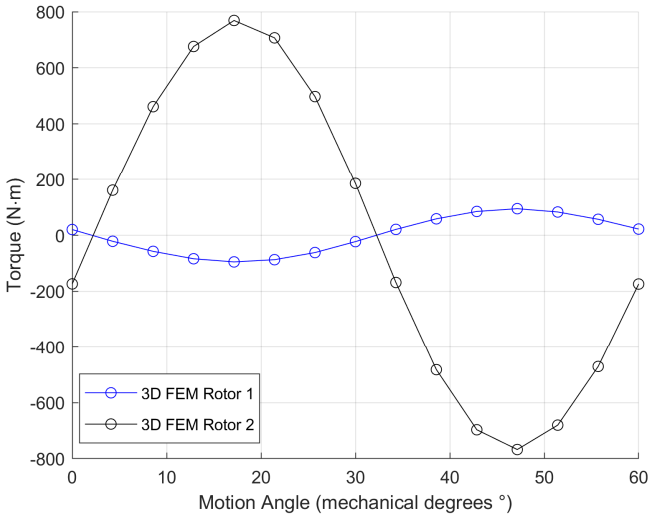

Fig. III-25 Torques experienced by the rotors of the proposed MG during HSR pole-slipping and estimated using 3D FEM.

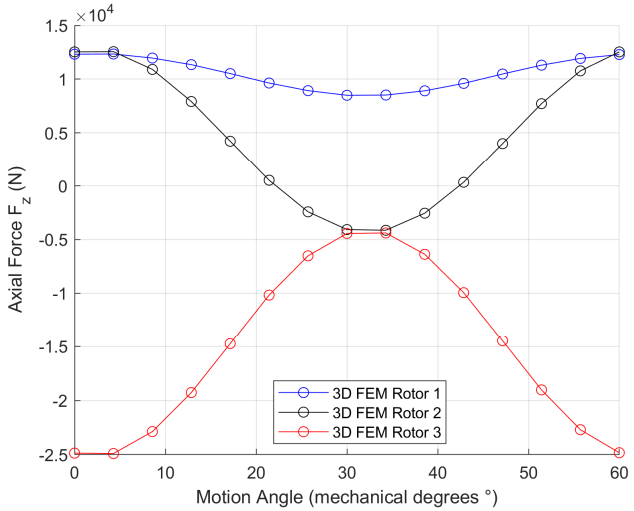

Fig. III-26 Attraction forces acting on the rotors of the proposed MG structure during HSR pole-slipping and estimated using 3D FEM.

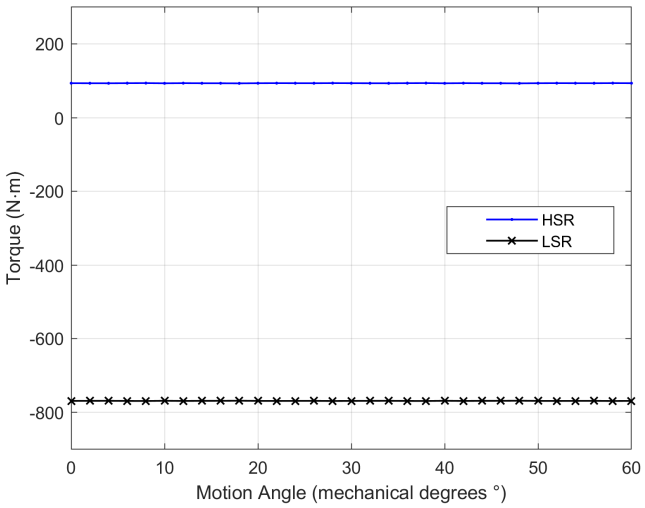

Fig. III-27 Loaded operation of the proposed MG showing the estimated torques on the HSR and LSR.

Conclusion

The chapter began with an overview of sustainable marine energy technologies. Diverse conversion technologies and energy sources were described briefly, and offshore wind energy was analyzed in depth because it could be considered currently as the most mature out of the other marine technologies due to the similarities it has with the developed onshore wind energy systems. Then, an overview of the uses of magnetic gears in maritime energy systems was presented, highlighting the literature-reported implementations of both magnetic gears and magnetically geared machines. Knowing that magnetic gears best operate in high torque low speed applications, it was found that MGMs could provide a very good alternative for direct drive marine renewable energy systems, where they can reduce the total mass and volume of the system and provide very high efficiency. Magnetic gears were also proposed in multiple studies to replace mechanical gears to improve the reliability of the system while avoiding the direct drive solutions. Lastly, a parametric sweep analysis was conducted employing the modeling techniques given in the preceding chapter. The objective of this study was to propose an axial field magnetic gear design appropriate for deployment in a maritime renewable energy conversion system. During the sweep analysis the structure was modeled using the 3D PN while taking the end-effects, and after all the parameters were found, a nonlinear 3D FEM model was constructed, where it has been found that an error of 26% was present between the estimations done by the 3D PN and the 3D FEM which was an expected value.

Chapter IV - Translator Eccentricity in Tubular Linear Structures

Introduction

The problem of eccentricity in tubular linear structures is addressed in this chapter. First, the eccentricity issue is defined and specified. Next, the 3D FEM model used to analyze the eccentricity impact is discussed. Then, two tubular linear permanent magnet machines with different structures are analyzed under different eccentricity and operating conditions, and a comparison between the structures is carried put. Afterwards, a quasi-3D FEM modeling technique for analyzing eccentricity in tubular linear machines is presented and explained. Then, it is applied to the structures that were already introduced and compared with the 3D FEM. Finally, eccentricity is analyzed in two tubular linear magnetic gear structures using 3D FEM.

1. Tubular Linear Machines and Eccentricity

Tubular linear permanent magnet machines (TLPM) have gained increasing popularity over the past years due to their versatile nature. Whether used as actuators for linear motion applications or as generators for energy production applications, these machines can provide accurate and precise motion with relatively compact structures and simpler control systems [211]–[218]. This made them perfect for high-precision industrial applications and even applications where pneumatic and hydraulic linear actuators are being used but not inherently required. As generators, TLPMs are also very popular among different energy conversion and production applications especially renewable energy applications. For instance, ocean and wave energy applications use TLPMs translational motion to extract energy directly without the need for an intermediary motion conversion system.

Like any other mechanical device, TLPMs might suffer from different structural deformations during either operation or assembly. The moving part of the machine called the translator is the most vulnerable to such mechanical deformations. One commonly occurring deformation happens at the level of the translator shaft and is usually called a translator eccentricity where the translator shaft is no longer aligned perfectly with the central axis of the machine's cylindrical structure.

In tubular linear structures the translator eccentricity can take different forms as can be shown in Fig. IV-1 [219]. The work in this chapter is concerned only by static translator eccentricity where the axis of the primary (stator) and the secondary (translator) are parallel but offset by constant distance ε Fig. IV-1(a) and Fig. IV-2. The value of this offset distance determines the level of impact of the translator eccentricity on the machine. Greater ε values mean that the air gap is getting very small across a certain area and very large at the radially opposite area.

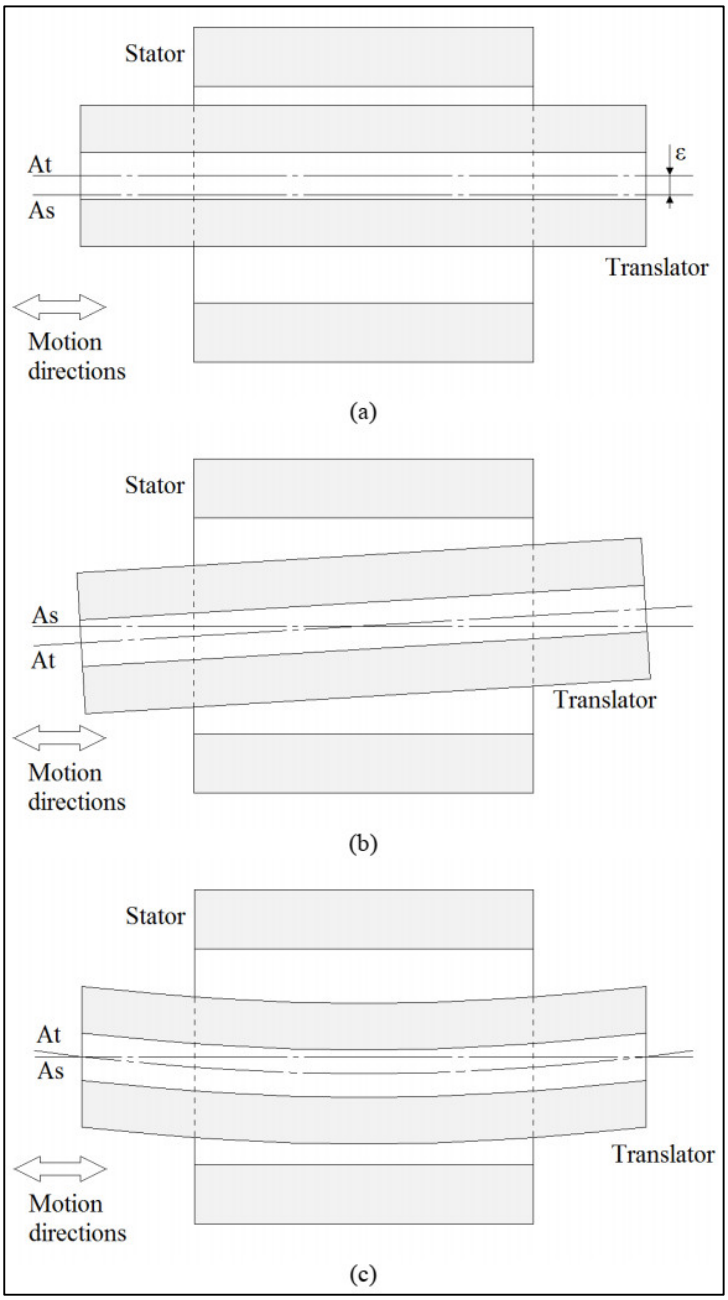

Fig. IV-1 Different forms of translator eccentricity in tubular linear structures [219].

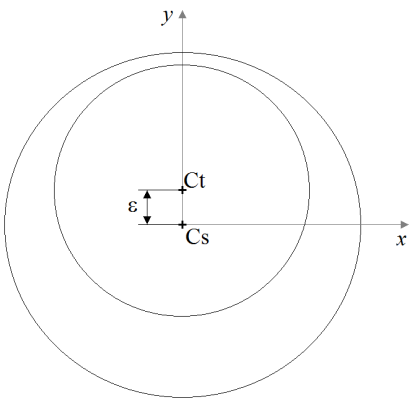

Fig. IV-2 Illustration showing a 2D plane view of a tubular linear machine with the eccentricity form that is considered in this chapter.

In normal and simple situations where no eccentricity is present, tubular linear structures could be modeled using 2D axisymmetric models which are computationally cheap and effective. However, with eccentricity the symmetry in the structure is lost which necessitates the use of 3D methods to model and analyze the effect of the eccentricity on the performance of the structure.

Eccentricity for linear or rotational structures has been studied previously by some authors [219]–[223]. In [220], [221], eccentricity analysis was done using analytical and 3D FEM modeling, and the calculated results were compared and validated by experimental results. Then, a superposition-based modeling method targeting eccentricity in rotary machines was presented in [222]. In [219], the authors analyzed the eccentricity in a tubular linear surface-mounted PM machine using 3D FEM modeling. Different eccentricity values were studied, and the impact of eccentricity on quantities like the electromotive forces (EMF), cogging force, and attraction forces was investigated.

2. Eccentricity Analysis in TLPM using 3D FEM

This section will be a continuation and extension of the work done in [219]. Two TLPM structures will be modeled under different eccentricity, load, and saturation conditions, and then a comparison between the two structures will be carried out to show how eccentricity and other conditions affect their performance.

The two TLPM structures are shown in Fig. IV-3. Structure A is a surface-mounted PM tubular linear machine, and Structure B is a flux focusing inserted PM tubular linear machine. Both structures have the same stator and armature windings specifications. The windings are installed as distributed windings, so for one pole pitch with three stator teeth, there is one coil for each phase, and the coils are oriented and positioned in such a way to maintain a 3-phase balanced system. Also, both structures have the same PM grades and volumes, where the PMs are considered to have a linear demagnetization curve with relative permeability equal to 1 and magnetic remanence equal to 1 T. The dimensions and specifications of the two structures were kept similar to make the comparison valid and reasonable. Fig. IV-4 shows the dimensions of the two structures in (mm) illustrated on 2D cross-sections for one pole-pitch.

The stator and rotor cores for the two structures (colored in grey in Fig. IV-3) are built from a soft magnetic material. This material will be studied in two cases: the ideal case considering a linear magnetization curve with constant relative magnetic permeability ($\mu_{rf} = 10000$), and a more realistic case that takes the magnetic saturation into account and treats the material as M330-35A silicon-steel.

The modeling method to be used to analyze the eccentricity in the two structures is the 3D FEM. The FLUX software is again used, and the calculations were performed on a couple of high-end PCs with a RAM capacity varying from 64 GB to 767 GB.

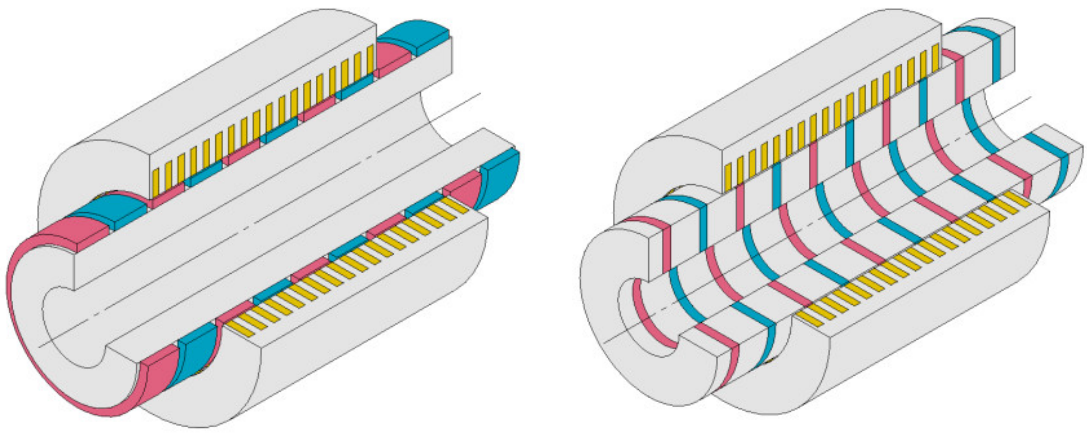

Structure A Structure B

Fig. IV-3 The two TLPM structures studied.

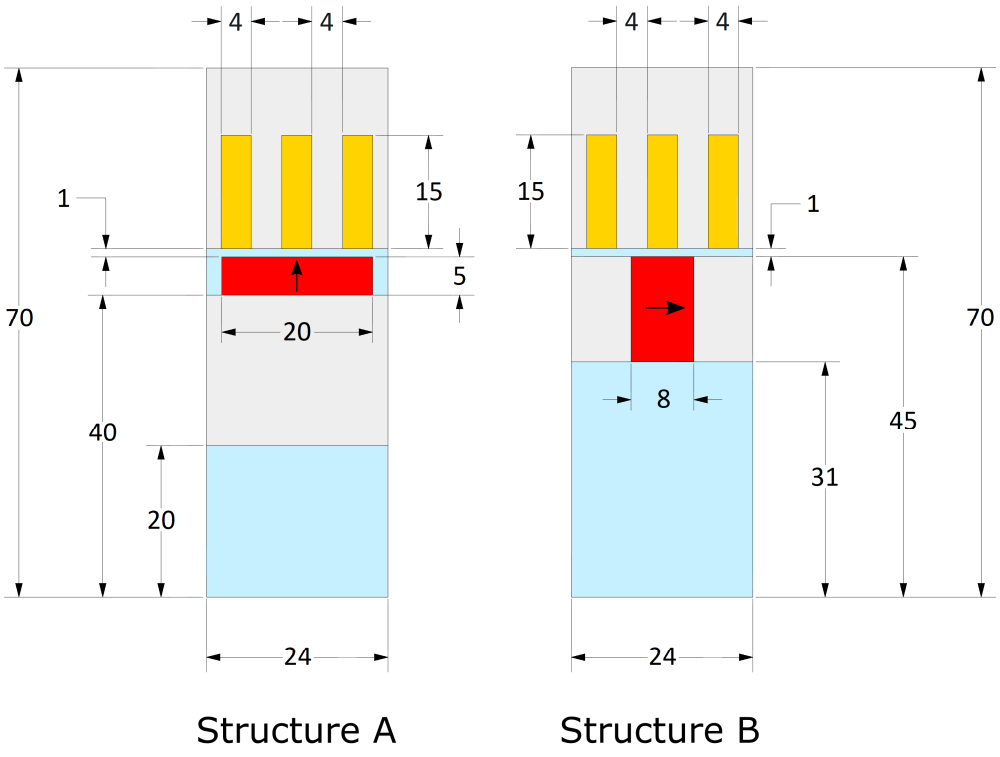

Fig. IV-4 2D axial cross-section views of structures A and B with the dimensions shown in (mm).

In order to reduce the computation cost as much as possible, only one pole pitch was modeled for the two structures. Four eccentricity values (ε) were studied: 0 mm eccentricity (no eccentricity), 0.25 mm, 0.5 mm, and 0.75 mm. For each eccentricity value, open circuit and on-load conditions were studied, as well as linear and non-linear (taking magnetic saturation into account) behaviors of the soft magnetic material. Studying the linear and nonlinear cases can measure the effect of the magnetic saturation on the performance of the two machines in general, and whether the assumption of the linear magnetization could be considered as valid for modeling these machines. The end-effects were ignored for this study.

The 3D meshing of both structures was done by extruding a 2D mesh (see Fig. IV-5). Extrusion meshes are usually easier to manage and control but can't be applied to all structures. The mesh technique used for these structures was already tested and verified in [219]. The air gap mesh in the zero-eccentricity model had two layers which are the minimum to ensure the model accuracy. As the eccentricity value increase, the air gap thickens at one side and thins at the radially opposite side (see Fig. IV-6) which means more fine layers are required to mesh the air gap region resulting in a higher number of nodes for the models representing higher

eccentricity values. For example, the different number of nodes in structure B models for each eccentricity value are shown in Table IV-1. As the number of nodes increases in a FEM model, the size of the linear/nonlinear system to be solved increases, and hence the computation time increases. It took 33 calculation steps around one week to be solved for the on-load 3D FEM model of structure B with 0.75 mm translator eccentricity while considering the magnetic saturation. Knowing that this model was running on a high-end computer (48 cores CPU and 767 GB of RAM). This shows the huge computation resources that should be reserved in order to solve such models, and the amount of time required to get the results.

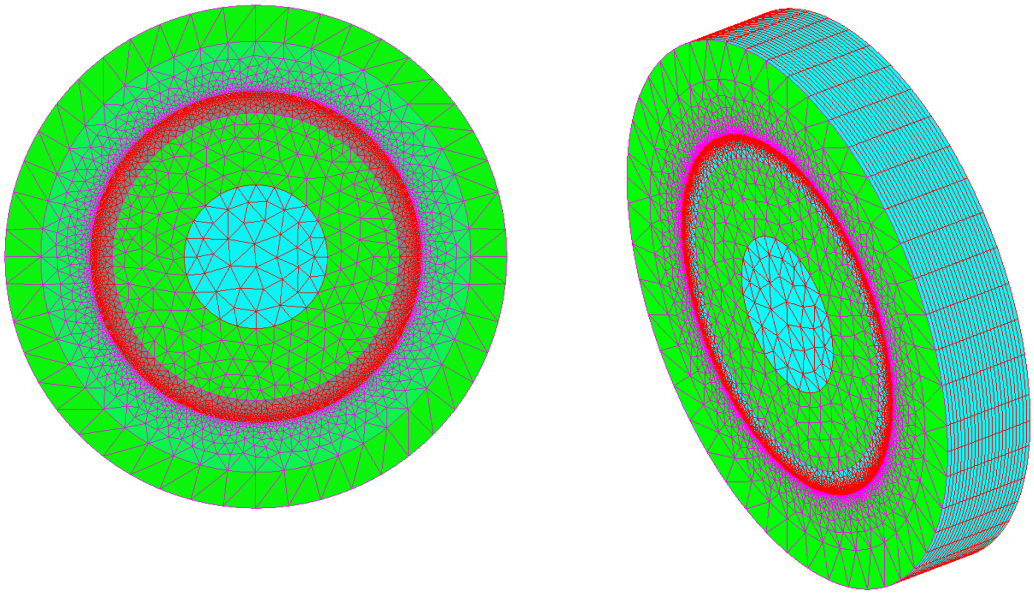

(a) (b)

Fig. IV-5 The (a) 2D mesh that has been extruded to obtain the (b) 3D mesh of the whole structure.

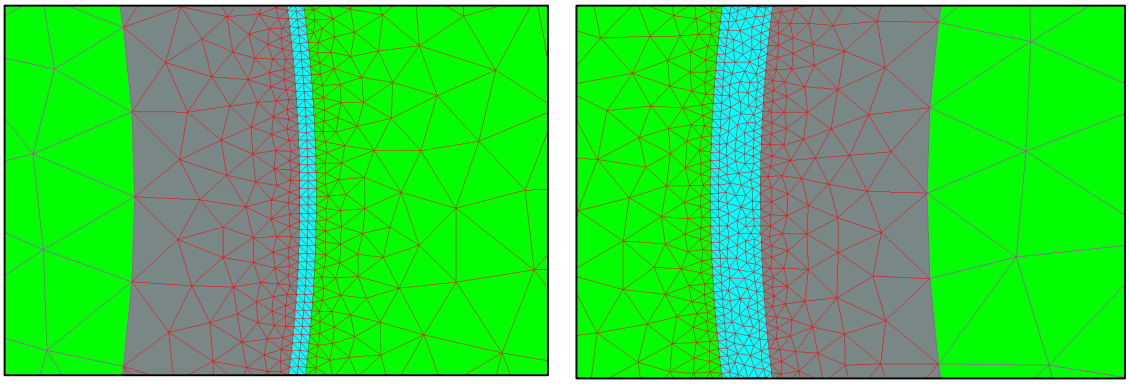

(a) (b)

Fig. IV-6 Air gap thickness variation in the case of 0.5 mm eccentricity with the (a) minimum and (b) maximum air gap thickness sides.

Table IV-1 Number of nodes in a 3D FEM model for structure B for different eccentricity values.

Eccentricity value (mm)	Number of nodes
0	1 468 484
0.25	2 079 188
0.5	3 172 788
0.75	6 569 684

2.1. Open-Circuit Case

This section will present the performance of structures A and B for open circuit conditions and under the effect of different eccentricity. Both the linear and magnetic saturation cases will be presented.

2.1.1. Linear Case

Fig. IV-7 shows the EMF waveforms of the two structures for the different eccentricity values. As the eccentricity value increased, a very slight increase in the EMF amplitude can be observed for Structure A, this increase is more noticeable for Structure B where the EMF amplitude for the 0.75 mm eccentricity case increased by 24.95 % w.r.t the reference model (no eccentricity). Similarly, the variation of the cogging forces of the two structures with respect to the increasing eccentricity is shown in Fig. IV-8. The increasing tendency of the cogging forces can be noted for both structures, but for Structure B the cogging force increased by 36.65% for the 0.75 mm eccentricity case.

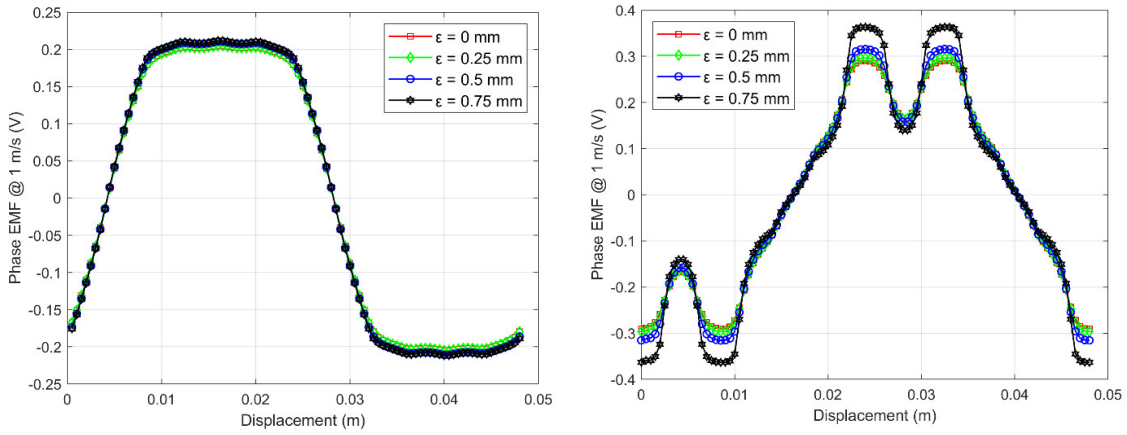

(a) Structure A (b) Structure B

Fig. IV-7 EMF waveforms comparison for the two structures under open-circuit conditions (linear case).

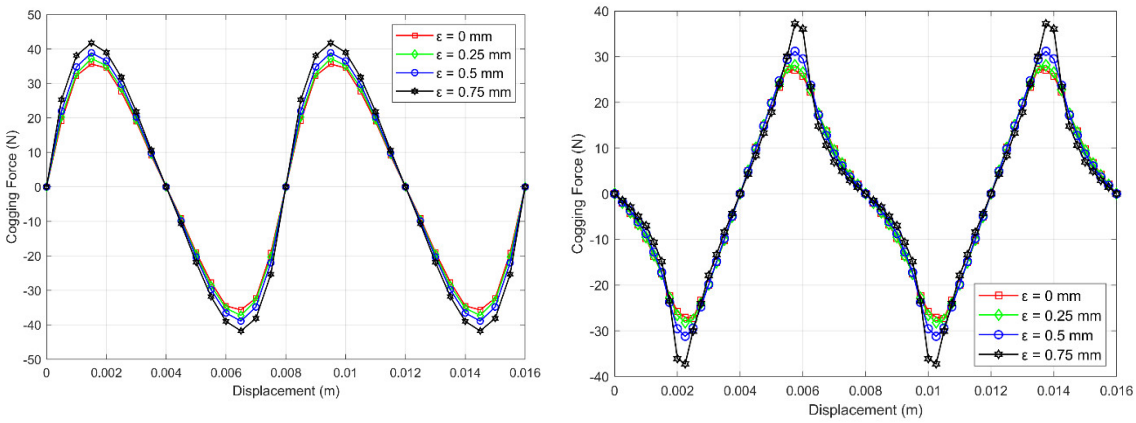

(a) Structure A (b) Structure B

Fig. IV-8 Cogging forces comparison for the two structures under open-circuit conditions (linear case).

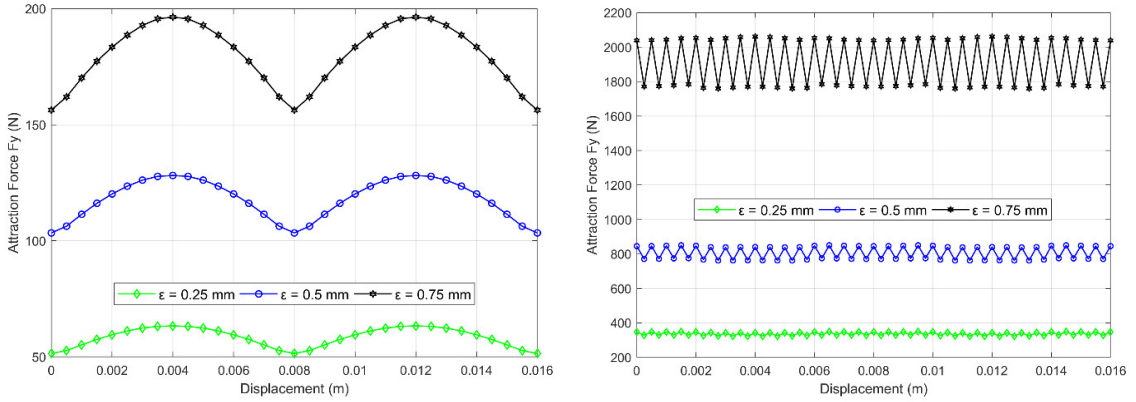

(a) Structure A (b) Structure B

Fig. IV-9 Attraction forces between the translator and stator for the two structures under open-circuit conditions (linear case).

Finally, Fig. IV-9 shows the attraction force between the stator and translator acting along the axis that holds the minimum and maximum air gap thicknesses which in this case is the y-axis (see Fig. IV-2). For structure A, the attraction force almost doubles (increased by 100%) when the eccentricity value increased from 0.25 mm to 0.5 mm, but it increased by 50% when the eccentricity value increased from 0.5 mm to 0.75 mm. However, for structure B, a larger increasing jump can be observed when the eccentricity increases from one value to another where the increase rate is around 150% between two consecutive eccentricity values.

2.1.2. Magnetic Saturation Case

For different eccentricity values, the EMF, cogging force, attraction force waveforms for the case of the open-circuit magnetic saturation are shown in Fig. IV-10, Fig. IV-11, and Fig. IV-12 respectively. For structure A, the increasing tendencies and rates are the same as the linear case, where only a slight decrease in amplitude is observed for all the quantities. However, for structure B, the magnetic saturation affected the behavior of the EMF waveforms with the increase of the eccentricity value. Unlike the noticeable increase seen in the linear case, here the maximum EMF values increased slightly with the increase of the eccentricity value.

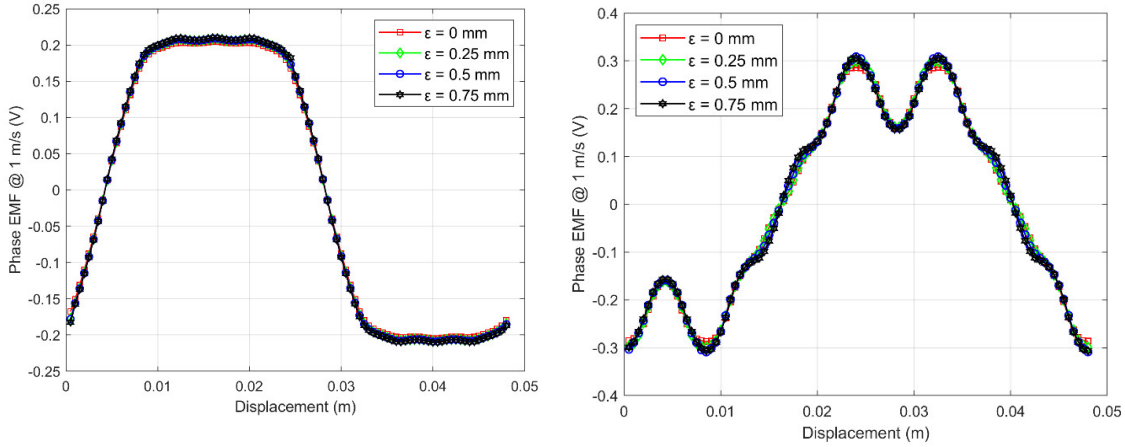

(a) Structure A (b) Structure B

Fig. IV-10 EMF waveforms comparison for the two structures under open-circuit conditions (saturation case).

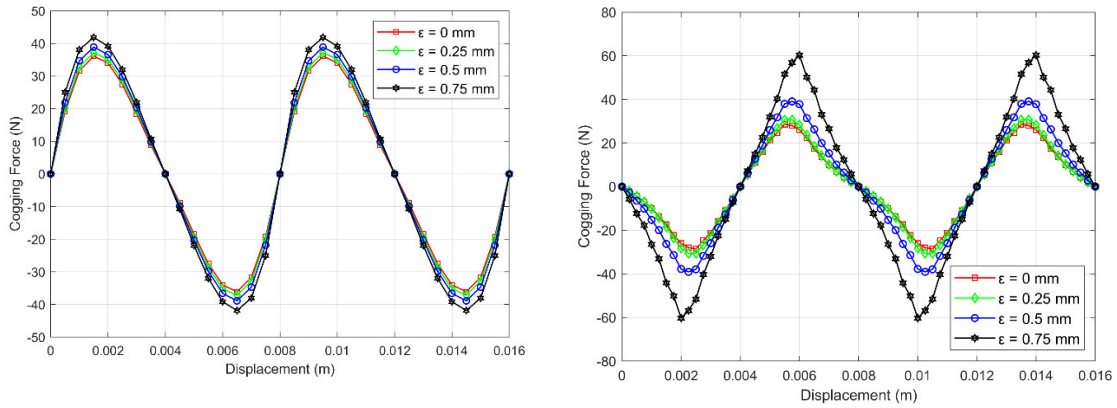

(a) Structure A (b) Structure B

Fig. IV-11 Cogging forces comparison for the two structures under open-circuit conditions (saturation case).

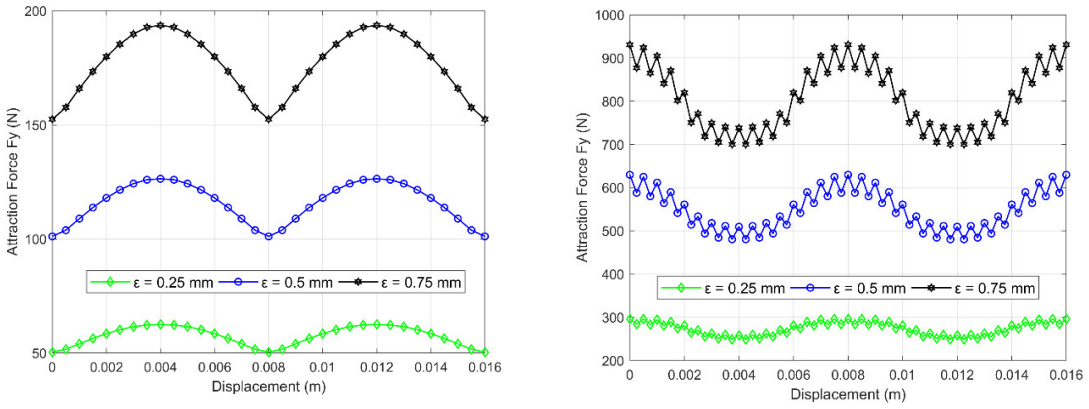

(a) Structure A (b) Structure B

Fig. IV-12 Attraction forces between the translator and stator for the two structures under open-circuit conditions (saturation case).

Additionally, compared to the linear case, the cogging force values increased remarkably. A kind of exponential increasing behavior for the maximum cogging force values with the increase of the eccentricity values can be observed. The maximum cogging force value for the 0.75 mm eccentricity model reached 60.28 N and it increased by 110.82 % w.r.t the reference model (these values were 37.227 N and 36.65 % in the linear case). The values of the attraction force decreased w.r.t the linear case and showed a clear oscillation behavior. The maximum value of the attraction force for the 0.5mm eccentricity model increased by 112.52% w.r.t the 0.25mm one, and for the 0.75mm eccentricity model, it increased by 47.78% w.r.t 0.5mm one.

2.2. On-Load Case

On-load performances of structures A and B under the effect of different eccentricity values are presented in this section. The eccentricity values and the reference model will be the same as values used for the open circuit performance. The on-load computations are conducted with a maximum armature current density of 5 A/mm2, while the maximum force control strategy is adopted, i.e., a null phase shifting between phase EMF and armature phase current. The quantities that were computed for this case were the thrust forces and the attraction forces.

2.2.1. Linear Case

The linear magnetization case is first considered. The computed thrust forces and attraction forces are shown in Fig. IV-13 and Fig. IV-14 respectively. The quantities of structure A have

the same increasing tendencies and rates as the open-circuit case. In fact, the attraction forces are almost the same as in the open circuit case.

Changes in the increasing rates and behaviors occurred again for structure B as compared to the linear open-circuit case. The maximum value of the thrust force for structure B increased in an exponential manner, which is eventually an increase in the force ripple. The maximum thrust force value for the 0.75 mm eccentricity model increased by 25.37 % with respect to the reference model. The maximum value of the attraction force for the 0.5 mm eccentricity model increased by 147.87 % w.r.t the 0.25 mm one, and for the 0.75 mm eccentricity model, it increased by 151.21 % w.r.t the 0.5 mm one. These increasing rates are similar to the linear case, but here significant change in the shape can be observed as the eccentricity value increased.

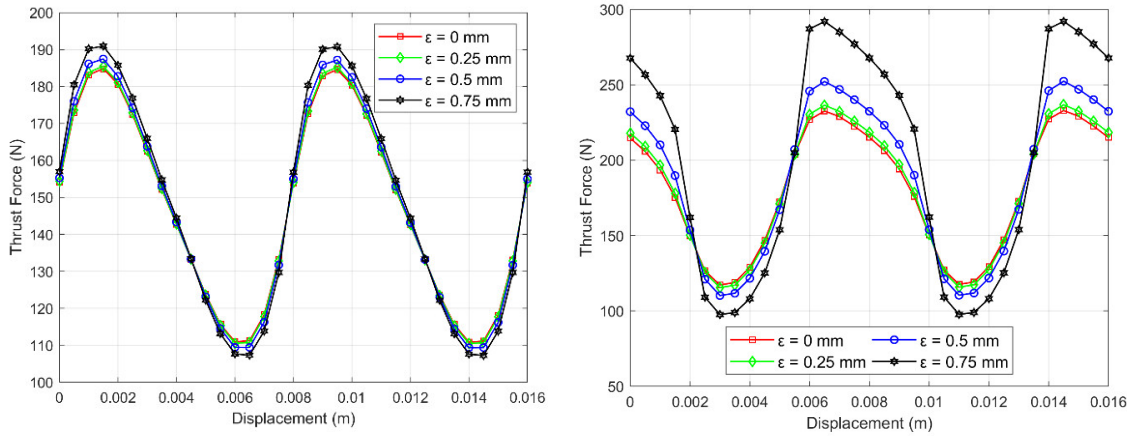

(a) Structure A (b) Structure B

Fig. IV-13 Thrust forces comparison for the two structures under load conditions (linear case).

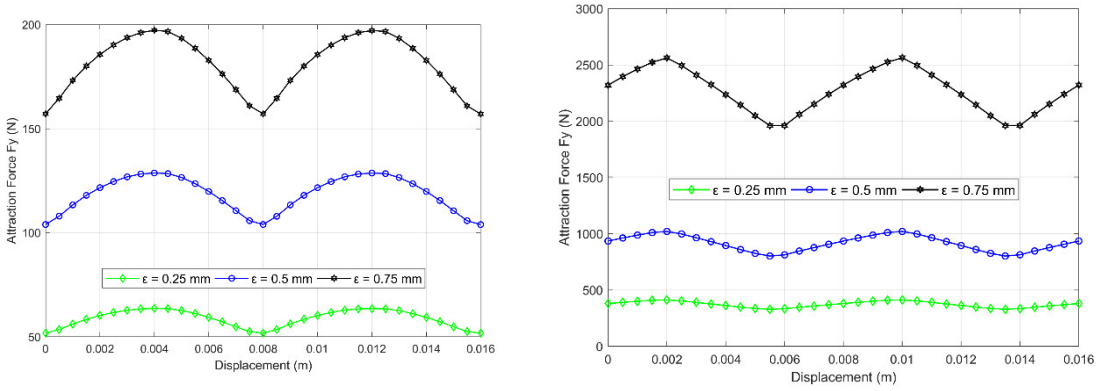

(a) Structure A (b) Structure B

Fig. IV-14 Attraction forces between the translator and stator for the two structures under load conditions (linear case).

2.2.2. Magnetic Saturation Case

In the case of the magnetic saturation consideration the variations of the thrust and attraction forces with different eccentricity values are shown in Fig. IV-15 and Fig. IV-16.

For structure A, the thrust force waveforms were affected by magnetic saturation. The thrust force maximum value of the reference model decreased compared to the linear case, while the general behavior of the thrust waveforms with the eccentricity increase is still similar to the linear case. The maximum value of the thrust force for the 0.75 mm eccentricity model increased by 5.66 % with respect to the reference model. On the other hand, the amplitudes of the attraction forces and the increasing tendencies remained almost the same for all the cases that have been discussed till now.

Concerning structure B, the exponential increase of the thrust forces amplitudes is still there but the maximum attained value is now lower than the linear case. The maximum thrust force ripple recorded in the saturation case was 31.18%, which is lower than the linear case value 36.29%. The attraction forces are similar to the open-circuit magnetic saturation case, where only the maximum values decreased with respect to the linear case, but the increasing rates remained the same.

2.3. Discussion and Comparison of the Results

It was noticed that the magnetic saturation didn't have a noticeable effect on the different results generated from the eccentricity models of structure A.

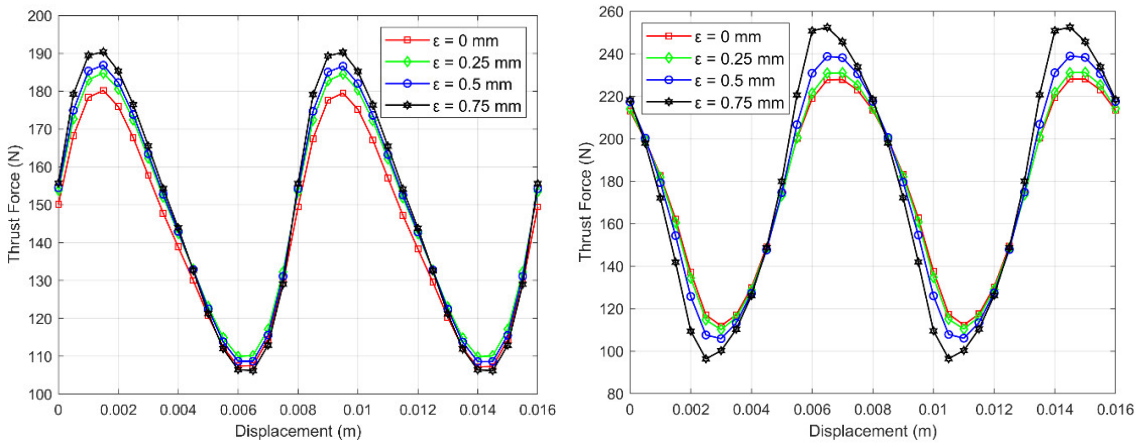

(a) Structure A (b) Structure B

Fig. IV-15 Thrust forces comparison for the two structures under load conditions (saturation case).

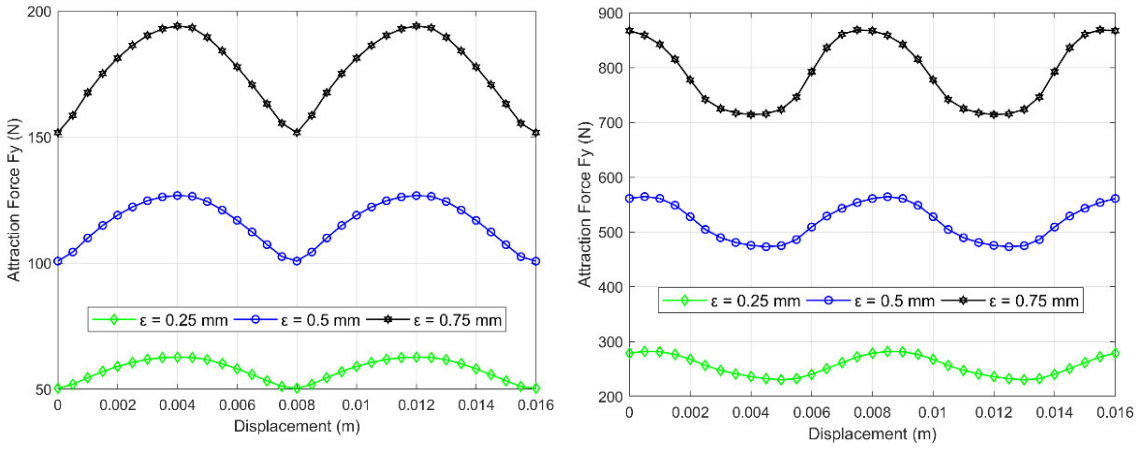

(a) Structure A (b) Structure B

Fig. IV-16 Attraction forces between the translator and stator for the two structures under load conditions (saturation case).

To be more specific, there were no noticeable effects for the magnetic saturation on the open circuit performance of structure A. However, for the on-load performance, the thrust force values slightly decreased due to the magnetic saturation. Mainly, the maximum thrust force value of the reference model decreased from 184.862 N in the linear case to 180.197 N in the saturation case. So, assuming linear magnetization behavior for structure A instead of magnetic saturation behavior would decrease the computation time while maintaining a high level of accuracy.

In contrast, the magnetic saturation had a remarkable effect on the results generated for structure B. The shapes and maximum values of the waveforms changed significantly between the linear and saturation cases (especially when talking about the attraction forces waveforms). For example, for the on-load performance the maximum value of the attraction forces in the linear case was 2563.6 N, and in the magnetic saturation case it decreased to 868.74 N. Another important observation for structure B was the increase of the maximum cogging force values in the open circuit performance from 37.23 N in the linear case to 60.28 N in the magnetic saturation case. Thus, ignoring magnetic saturation for this structure should be considered carefully by the user.

Eccentricity didn't noticeably affect the EMF values for both structures A and B, but if an observation is to be made, then the EMF of structure B was slightly more affected.

For both structures A and B, the cogging force increased with the increase of the eccentricity value. When taking the magnetic saturation into account, the recorded maximum cogging force value for structure A was 41.85 N for the 0.75 mm eccentricity model with an increase of 13.86 % w.r.t the reference model, while the maximum cogging force value for structure B reached 60.28 N for the 0.75 mm eccentricity model where it increased by 110.82 % w.r.t the reference model. Hence, the impact of the eccentricity value increase on the cogging force values of structure B was remarkably higher than it was on structure A.

The attraction forces along the y-direction increased with the increase of the eccentricity value for both the structures. However, it reached much higher values in structure B than in structure A. For example, in the open-circuit magnetic saturation case, for 0.75 mm eccentricity, the maximum value of the attraction force corresponding to structure B was 930.55 N, whereas it was 193.58 N for structure A.

Moreover, the thrust force increased with the increase of the eccentricity value for both structures. The increase rate and maximum thrust force values for structure B were higher than they were for structure A. For the 0.75 mm eccentricity model, the maximum thrust force value for structure A was 190.39 N where it increased by 5.66 % w.r.t the reference model, while these numbers were 252.48 N and 10.69 % respectively for structure B.

In essence, the impact of eccentricity on structure B was remarkably higher than on structure A across all the cases. This might be mainly due to the fact that the magnetic equivalent air gap for structure B is much smaller than that of structure A. In structure A, the magnetic equivalent air gap can be considered as the thickness of the mounted PMs and the mechanical air gap combined as the relative permeability of the PM are very close to 1. In contrast, the equivalent air gap for structure B is only equal to the mechanical air gap, and thus with the increase of the eccentricity this value becomes very small. In fact, the eccentricity values considered are theoretical only, and their investigation is only to provide some insight that helps in dealing with any case, but realistically, many tubular linear designs might fail mechanically even at low eccentricity values due to the attraction forces that will occur.

3. Eccentricity Analysis in TLPM using Quasi-3D FEM

Very high computation times were observed for the 3D FEM models from the previous section, and with the need to have multiple models to span all operating conditions, using 3D FEM on its own to study eccentricity in a certain structure might be very time extensive and

require a lot of resources. Thus, the idea is to propose a quasi-3D FEM method that can model eccentricity in tubular linear structures for a low computational cost.

The proposed quasi-3D model is achieved by dividing the 3D structure in the tangential direction (θ direction) into a certain number of sections (see Fig. IV-17). Since the air gap is non-uniform around the translator in the tangential direction, there is a different air gap value e for each θ along the tangential direction where $\theta \in [0, 2\pi]$. Hence, each section in the tangential direction is modeled as a standalone 2D linear machine having an air gap equal to the air gap value at the central angle of the corresponding section. Then, for each 2D linear machine model, the magnetic induction in the air gap is calculated where it will have two components x and y corresponding to the axial (z-direction) and radial (r-direction) cylindrical components of the 3D model respectively. The tangential component (B_t) can't be associated with a component from the 2D model, so it can't be represented and will be considered as zero. It will be seen later that the nullification of the tangential component will affect the accuracy and a correction function will be required to compensate for that.

The total number of sections in the tangential direction was chosen to be 32. When increasing the number of sections beyond this value, no significant increase in accuracy was noticed. Due to the symmetry with respect to the eccentricity axis, there will be only 17 unique air gap values and hence reducing the total number of 2D models to 17 instead of 32.

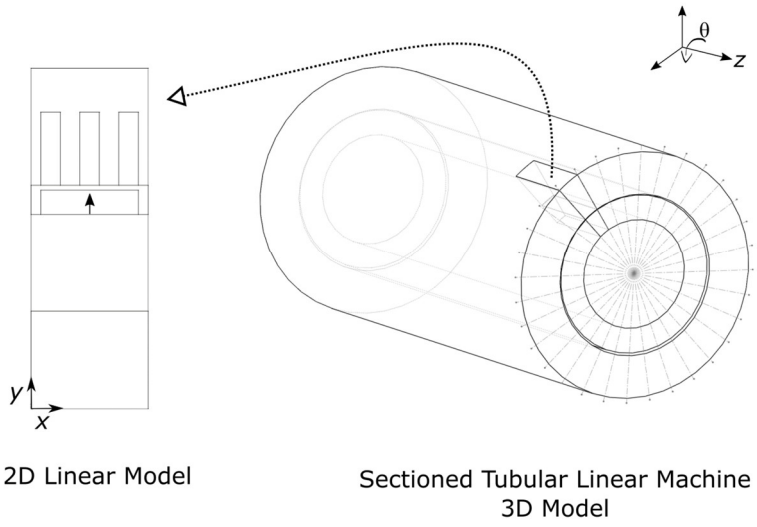

Fig. IV-17 A 3D TLPM structure divided in the tangential direction with a 2D axial cross-section view.

After gathering the results from all the 2D modeled sections, the total electromagnetic force acting on the translator is calculated using Maxwell's Stress Tensor. The attraction force to be calculated acts along the y-axis which is the axis that contains the maximum and minimum air gap values. The cogging and thrust forces act along the z-axis which is the axis of translation.

The two structures that will be studied are the same as the ones studied in the previous section and will have the same dimensions and physical properties (see Fig. IV-3 and Fig. IV-4). In addition, the linear and magnetic saturation cases will be considered as well as the open circuit and on-load operations. The on-load operation will have the same conditions it had from the previous section. Moreover, the same eccentricity values will be imposed: 0.25 mm, 0.5 mm, and 0.75 mm. It is worth noting that the curves of the linear magnetization case will be omitted and not shown as the comparison between the two magnetization conditions was done in the previous section. However, for the purpose of evaluating the proposed model, the linear results will be summarized in a table later.

2.4. Modeling of Structure A

Under the open-circuit conditions, Fig. IV-18 shows the curves of the cogging forces and attraction forces calculated using the 3D and the quasi-3D models for all the eccentricity cases and while considering the magnetic saturation. The amplitudes of the cogging forces calculated using the quasi-3D model seem to be higher than the values from the 3D models, but the results from both models seem to have the same tendencies. For all the eccentricity cases, the average error rate between the amplitudes of the two models was 13.3%.

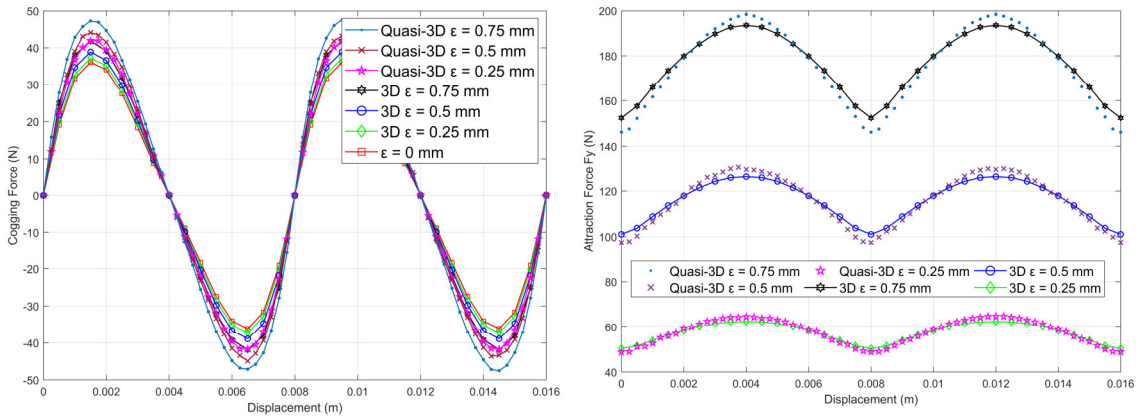

(a) (b)

Fig. IV-18 Results evaluated using the proposed models with open-circuit and magnetic saturation conditions: (a) cogging forces, (b) attraction forces.

Regarding the attraction forces, a very good conformation can be observed between the two models can be observed. The average error rate between the amplitudes was 3.16%.

For the on-load performance, the generated thrust and attraction forces are shown in Fig. IV-19. Similar to the open-circuit case, the amplitudes, as well as the DC components of the thrust forces calculated using the quasi-3D model, seem to be higher than the 3D calculated ones. The average error rate between the amplitudes of the thrust forces of the two models is 7.67%. However, the quasi-3D model curves maintained the same tendencies observed in the 3D model. For structure A, the attraction forces don't seem to be affected in general by the on-load conditions, and the quasi-3D attraction force calculations in this case also provided very good confirmation with the 3D model calculated values with the average error rate being 1.35% only.

Under the load conditions, the combined computation time of these 3D models (for all the eccentricity cases) is around 7 days whereas it's only about an hour for the quasi-3D models. So, the quasi-3D approach, with a much lower computation time and a low error rate, provided the same thrust force curve tendencies and predicted accurately the attraction forces.

Table IV-2 summarizes the error rates between the quasi-3D and 3D models of the cogging, thrust, and attraction forces calculated for structure A for all the conditions.

2.1. Modeling of Structure B

For structure B, the quasi-3D model had to be improved to compensate for the tangential magnetic components that have been nullified.

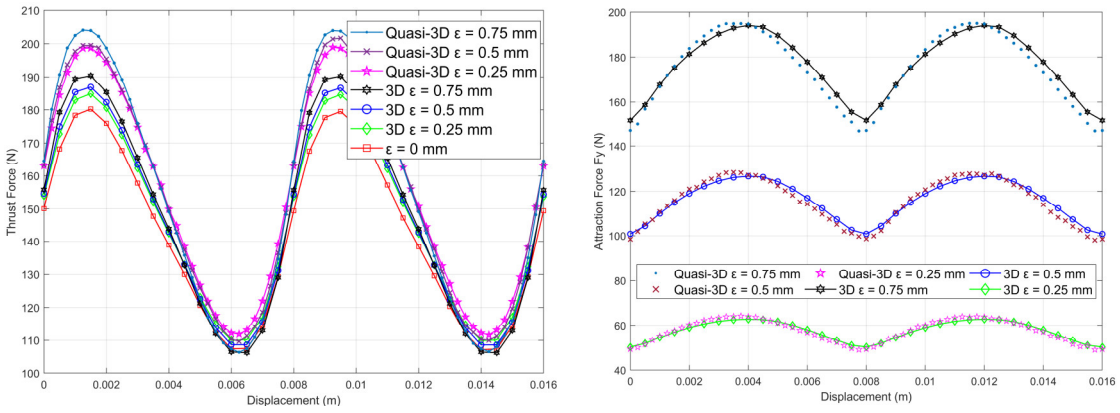

(a) (b)

Fig. IV-19 Results evaluated using the proposed models with on-load and magnetic saturation conditions: (a) thrust forces, (b) attraction forces.

Table IV-2 Error rates between the quasi-3D and 3D models for the quantities generated for structure A.

	Eccentricity (mm)	Open Circuit		On-Load	
		Linear	Non-Linear	Linear	Non-Linear
Cogging/Thrust Forces	0.25	10.34%	12.69%	7.81%	7.63%
	0.5	10.32%	13.53%	8.09%	7.92%
	0.75	9.69%	13.66%	7.51%	7.47%
Attraction Forces	0.25	6.96%	3.71%	7.04%	2.34%
	0.5	6.56%	3.27%	6.82%	1.41%
	0.75	5.98%	2.49%	5.80%	0.30%

The first calculation campaign carried out for structure B followed the same methodology described till now and applied for structure A. The generated results showed some relatively high error rates and inconsistent tendencies across the different running conditions and eccentricity cases. The error rates of the cogging, thrust, and attraction forces calculated during the first campaign are summarized in Table IV-3.

The error rates represent the difference between the amplitudes of the calculated quantities by the 3D and the quasi-3D models with the 3D model considered as the reference. It can be seen that some error rates are pretty high, especially for the attraction forces. The error rates of the cogging and thrust forces were in general acceptable except for the open circuit non-linear case.

Table IV-3 Error rates between the quasi-3D and 3D models for the quantities generated for structure B (without correcting coefficients).

	Eccentricity (mm)	Open Circuit		On-Load	
		Linear	Non-Linear	Linear	Non-Linear
Cogging/Thrust Forces	0.25	13.61%	45.32%	9.77%	10.17%
	0.5	6.04%	33%	7.20%	8.72%
	0.75	-15.48%	9.51%	2.08%	7.88%
Attraction Forces	0.25	-44.40%	-44.16%	-39.67%	-45.99%
	0.5	-49.06%	-43.99%	-44.56%	-44.00%
	0.75	-60.60%	-36.78%	-54.98%	-39.72%

A solution to the high error rates was found by introducing correcting coefficients to the radial magnetic induction (B_r) values. The correcting coefficients serve as compensation to the neglected component (Bt) and help in estimating the true behavior of the magnetic field in the air gap affected by eccentricity. It is the same as the "activation function" concept that has been used for the quasi-3D RN model in chapter 2. The determination of the correcting coefficients was done using another 2D FEM model (correction model) which happened to be a model for a radial field flux focusing machine suffering from rotor eccentricity. Eccentricity can be modeled in this structure using a simple 2D model and hence the reason why it was chosen. By observing the behavior of B_t in the air gap of the correction model, a series of correcting coefficients can be generated and used to compensate for the absence of the B_t component from the quasi-3D model. The method for finding the correcting coefficients is summarized in Fig. IV-20.

After multiplying the B_r values that were acquired from the quasi-3D model by the correcting coefficients, another calculation campaign was done, and the cogging and attraction forces were calculated using the same formulas as before except that now each B_r value is now multiplied by a correcting coefficient. Error rates of the cogging and thrust forces haven't improved in the second computation campaign due to the nature of the equation related to their calculation (Maxwell Stress Tensor), so the results from the first campaign were maintained. However, the error rates of the attraction forces have improved significantly, so the values calculated from the second campaign were the ones adopted.

Table IV-4 Error rates between the quasi-3D and 3D models for the quantities generated for structure B (with correcting coefficients).

	Eccentricity (mm)	**Open Circuit**		**On-Load**	
		Linear	**Non-Linear**	**Linear**	**Non-Linear**
Cogging/Thrust Forces	**0.25**	13.61%	45.32%	9.77%	10.17%
	0.5	6.04%	33%	7.20%	8.72%
	0.75	-15.48%	9.51%	2.08%	7.88%
Attraction Forces	**0.25**	9.01%	16.11%	11.90%	18.32%
	0.5	3.93%	22.25%	7.53%	26.48%
	0.75	-8.07%	57.24%	1.10%	57.05%

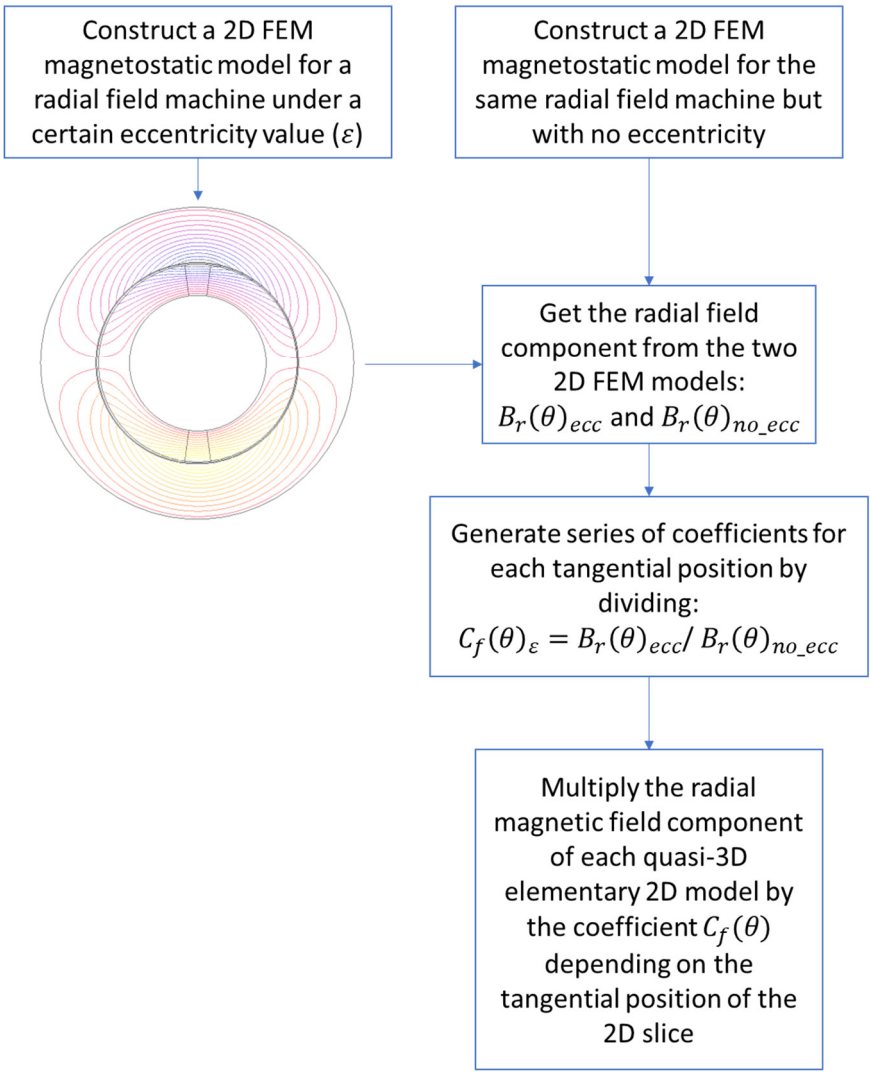

Fig. IV-20 The process to obtaining and applying the correcting coefficients to the quasi-3D FEM model.

The correcting coefficients method was good in improving the accuracy of the attraction forces but was not enough for some of the cogging and thrust forces. Table IV-4 summarizes the error rates of the attraction forces calculated using the correcting coefficients method.

Eventually, for open-circuit magnetic saturation conditions the final obtained cogging and attraction forces are shown in Fig. IV-21. The increasing rates of the cogging forces calculated using the quasi-3D models have changed to what they have been at in the 3D models, but the values from the quasi-3D model can be still considered as acceptable. Meanwhile, for the

attraction forces it can be seen that the error rate for the ε = 0.75 mm case is very high, but for the other cases the estimation is acceptable.

Concerning the on-load performance, Fig. IV-22 shows the estimated thrust and attraction forces. The tendencies and increasing rates of the thrust forces from the quasi-3D model are very similar to the tendencies and increasing rates recorded for the 3D model. The average error rate between the amplitudes of the thrust forces of the two models is 8.92%. The quasi-3D attraction forces seem to have a behavior similar to the ones observed for the open circuit case.

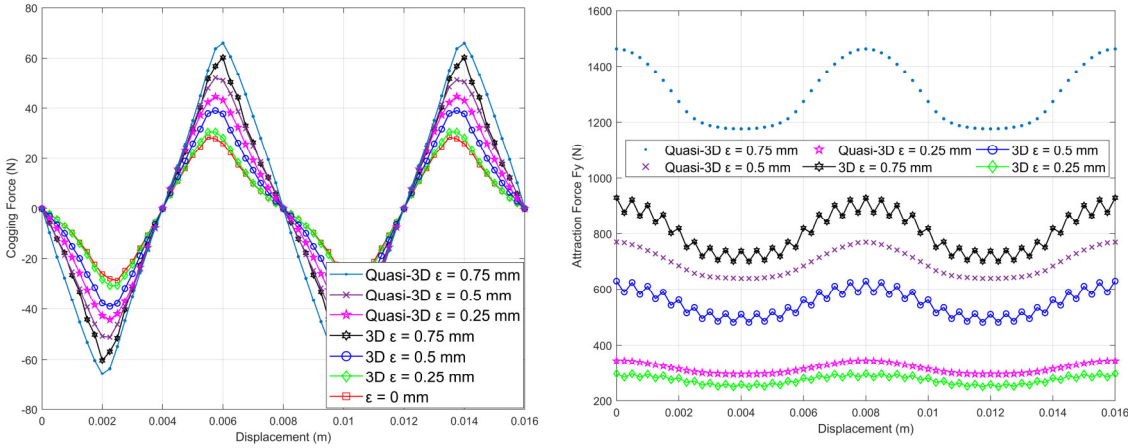

(a) (b)

Fig. IV-21 Results evaluated using the proposed models with open-circuit and magnetic saturation conditions: (a) cogging forces, (b) attraction forces.

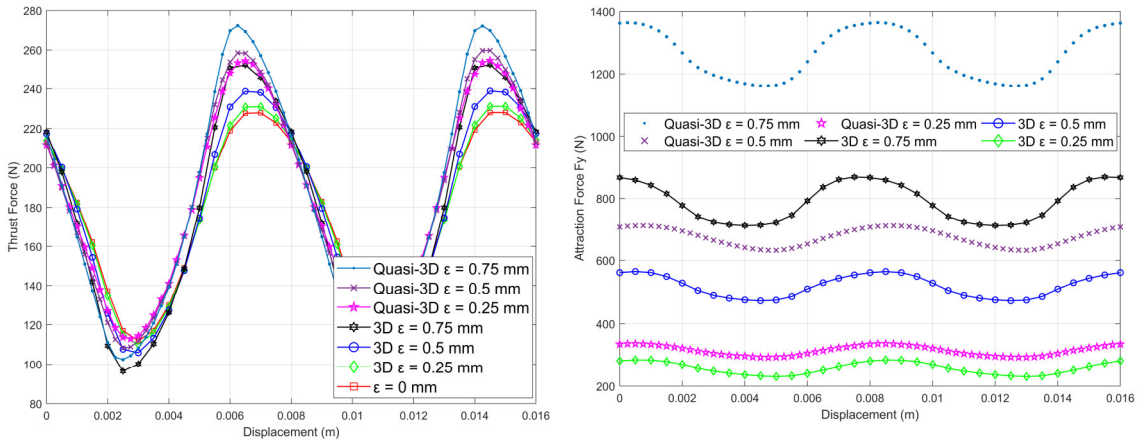

(a) (b)

Fig. IV-22 Results evaluated using the proposed models with on-load and magnetic saturation conditions: (a) thrust forces, (b) attraction forces.

The non-linear 3D FEM model of the ε = 0.75 mm on-load case took more than 7 days to finish computing 33-time steps with a huge number of computational resources allocated. However, the quasi-3D model can be computed in around an hour only and with fewer computational resources. By observing the error rates, the accuracy-time tradeoff is worth it, and it makes the quasi-3D approach a plausible choice even for structure B.

2.2. Discussion and Evaluation

After presenting the error rates and analyzing the results from the two structures and for the different operating conditions, a judgment can be passed on our quasi-3D model. First, the computation times and efforts are massively reduced from what was required by the 3D modeling approach. Second, non-linear computations can be done easily at no significant cost when using the quasi-3D approach. It follows that the quasi-3D approach provided pretty accurate results for structure A, and it provided results with relatively acceptable accuracy for structure B. The difficulties that might face the user when using this modeling technique are mainly the investigation and testing needed to find the best way to estimate the results, especially for structures similar to structure B where ignoring the tangential components might have a huge impact on the accuracy of the model. The quasi-3D modeling technique itself is based on the simple superposition principle, but its usage for the TLPM eccentricity analysis application is much more complicated. There's still a lot of room for improving the proposed quasi-3D model but it might, as it stands, serve as a good starting point and an effective tool for modeling eccentricity in different tubular linear structures.

4. Eccentricity Analysis in Tubular Linear Magnetic Gears

Tubular linear magnetic gears (TLMG) might be even more susceptible to translator eccentricity due to the presence of two air gaps and two moving parts. Thus, it might be also very interesting to analyze the impact of eccentricity on the performance of a TLMG.

The analysis will be carried out using 3D FEM modeling, where the performance of two different TLMG structures will be studied for different eccentricity values. The structures to be studied are presented in Fig. IV-23, where "Structure C" has a surface-mounted PM configuration, and "Structure D" has a flux focusing inserted PM configuration. The dimensions and parameters of structure C and D are summarized in Table IV-5 and Table IV-6 respectively.

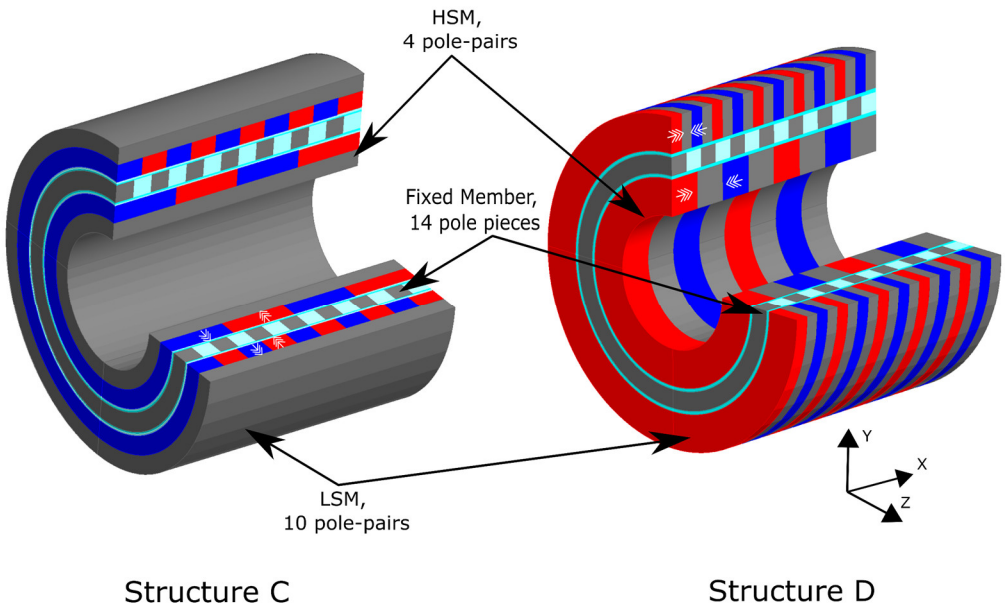

Fig. IV-23 The two TLMG structures under study.

Table IV-5 The parameters and dimensions of structure C.

HSM	Number of pole-pairs	4
	Magnet axial length w_{1m}	18.75 mm
	Steel radial thickness h_{1f}	5 mm
	Magnet radial thickness of h_{1m}	5 mm
	Air gap	1mm
Fixed Member	Number of modulating pole pieces	14
	Steel/slot axial length $w_{2f} = w_{2s}$	5.36 mm
	Radial thickness h_2	5 mm
LSM	Number of pole-pairs	10
	Magnet axial length w_{3m}	7.5 mm
	Steel radial thickness h_{3f}	5 mm
	Magnet radial thickness of h_{3m}	5 mm
	Air gap	1 mm
General Parameters	Inner radius R_i	18 mm
	Outer radius R_o	45 mm
	Axial length	150 mm
	PM relative permeability	1.05
	PM magnetic remanence	1.2 T

Table IV-6 The parameters and dimensions of structure D.

HSM	Number of pole-pairs	4
	Steel/magnet axial length $w_{1f} = w_{1m}$	9.375 mm
	Radial thickness h_1	10 mm
	Air gap	1mm
Fixed Member	Number of modulating pole pieces	14
	Steel/slot axial length $w_{2f} = w_{2s}$	5.36 mm
	Radial thickness h_2	5 mm
LSM	Number of pole-pairs	10
	Steel/magnet axial length $w_{3f} = w_{3m}$	3.75 mm
	Radial thickness h_3	10 mm
	Air gap	1 mm
General Parameters	Inner radius R_i	18 mm
	Outer radius R_o	45 mm
	Axial length	150 mm
	PM relative permeability	1.05
	PM magnetic remanence	1.2 T

The dimensions of the two structures were kept similar to compare between them, where they both have similar PM volume and type. The PM magnetic properties are listed in the tables above where they are considered neodymium PMs with linear demagnetization curve. In addition, the soft magnetic material in the two structures will be studied in two cases: linear magnetization case with constant relative magnetic permeability ($\mu_{rf} = 10000$), and a magnetic saturation case treating the material as M330-35A silicon-steel.

In addition, the eccentricity type that will be considered is similar to the one considered in the previous sections, where the axes of the three magnetic gear members will remain parallel but will have a constant offset between them denoted as the eccentricity value ε. Fig. IV-24 illustrates the eccentricity value and the state of the air gaps surrounding each member. The center of the fixed member which carries the modulating pole-pieces remains in its place, whereas the two moving members: the high-speed mover (HSM) and the low-speed mover (LSM) have their centers move in a way forming a minimum and maximum air gap regions aligned along the y-axis. Thus, when considering the members that carry the PM as moving and fixing the modulating member, the gear ratio becomes 2.5:1 with an opposite translation movement for

the HSM and LSM. This gear ratio and pole-pair combination allowed to have periodicity in the structure, so only one half of the total structure will be modeled using the 3D FEM. Moreover, this combination allowed for having zero attraction forces between the members when no eccentricity is present. Thus, the attraction forces will only appear when there is eccentricity where it will be acting along the axis that holds the minimum and maximum air gap regions (y-axis).

The methodology followed with the 3D FEM is the same as the previous sections except for the 3D mesh, where no extrusion was done and instead regular tetrahedrons were used to mesh the whole domain. A snapshot of the mesh used for structure C is shown in Fig. IV-25.

The eccentricity values that will be considered in this section are different from the previous sections, where the values investigated will be 0.2 mm, 0.4 mm, and 0.6 mm. A reference model with no eccentricity will be used also for the comparison.

The performance of the TLMGs for different eccentricity values was evaluated during the HSM pole-slipping (HSM moving and the LSM and modulating member being fixed). The moving forces of the HSM and LSM acting along the x-direction (motion direction) for structures C and D are summarized in Fig. IV-26 and Fig. IV-27 respectively. The figures show the results from both the linear and saturation cases. It can be observed that the moving forces of structure C are only very slightly affected by both the magnetic saturation and the eccentricity.

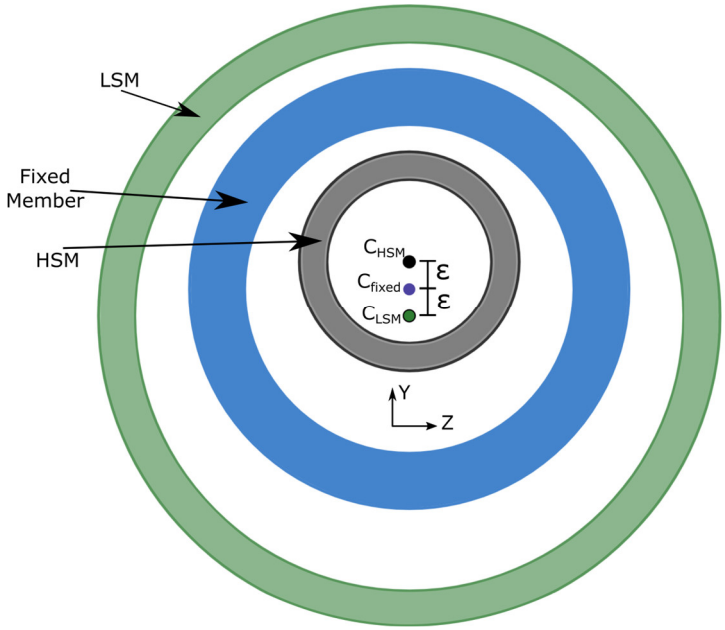

Fig. IV-24 An illustration on the eccentricity consideration in a TLMG.

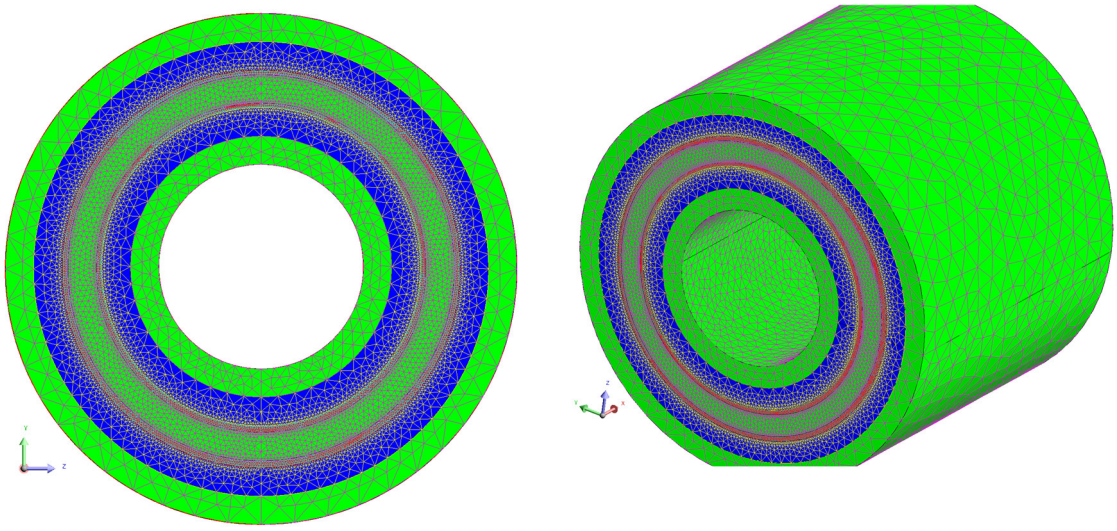

(a) (b)

Fig. IV-25 The 3D meshing of the TLMG (structure C): (a) 2D and (b) 3D views.

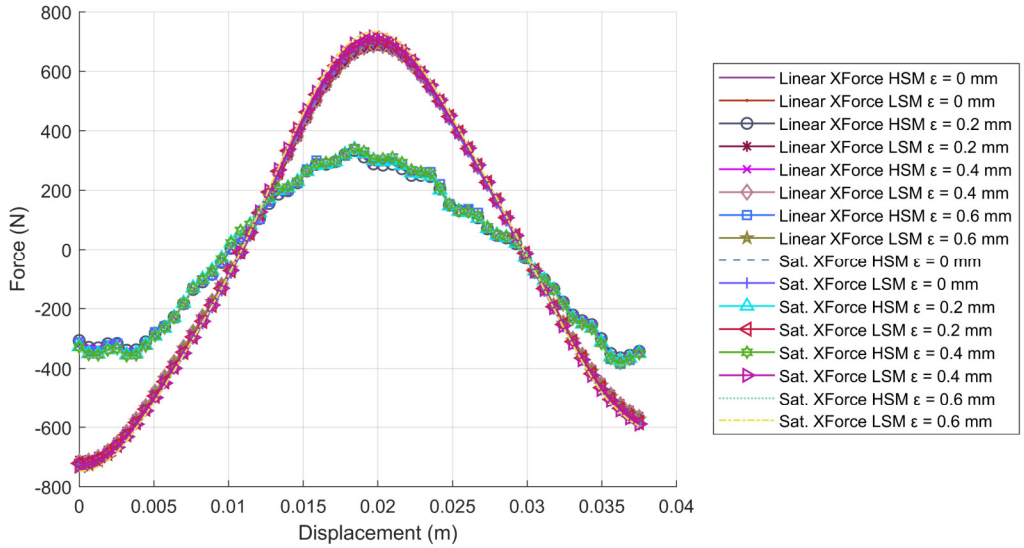

Fig. IV-26 The forces in the x-direction experienced by the HSM and LSM of **structure C** under different eccentricity values during the HSM pole-slipping (linear and saturation cases).

Fig. IV-28 reports the maximum values of the forces in the x-direction as function of the eccentricity value. The figure confirms the observations made for structure C as the values from linear and saturation cases are close and have the same linear increasing rate. In addition, the x-force of the HSM is barely affected by the eccentricity and saturation.

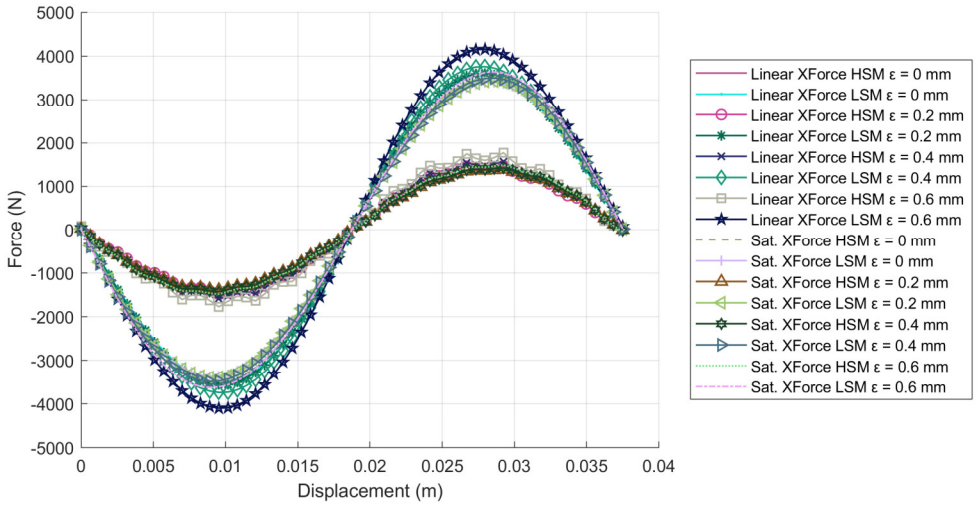

Fig. IV-27 The forces in the x-direction experienced by the HSM and LSM of **structure D** under different eccentricity values during the HSM pole-slipping (linear and saturation cases).

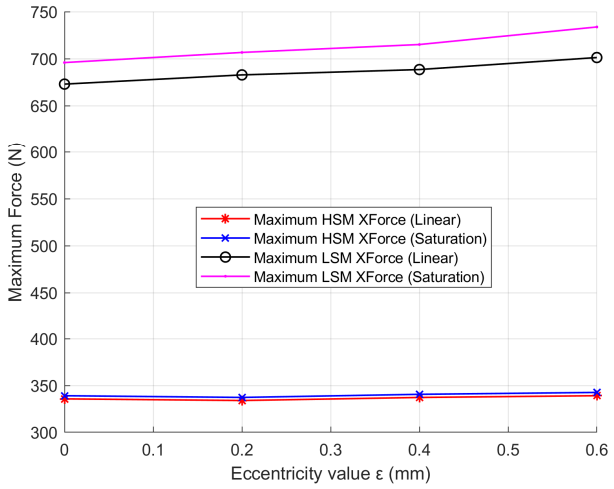

Fig. IV-28 Variation of the maximum moving forces acting in the x-direction for **structure C** as function of eccentricity.

The estimated increasing rates of structure C HSM and LSM moving forces per mm of eccentricity were 6.72 N/mm and 45.25 N/mm respectively. In addition, an interesting observation for structure C is that the moving forces in the saturation case were higher than the linear case.

For structure D it seems from Fig. IV-27 that eccentricity and saturation affected the moving forces maximum values and increasing tendencies. The variation of the maximum HSM and LSM moving forces as function of eccentricity is shown in Fig. IV-29. In the linear case, the moving forces had higher amplitudes and were increasing in an exponential fashion with the increase of eccentricity, but in the saturation case the increasing tendencies became closer to linear. For the saturation case in structure D, the estimated increasing rates of the HSM and LSM moving forces per mm of eccentricity were 196.22 N/mm and 388.28 N/mm respectively.

Moving to the more important quantity which is the attraction force that is occurring due to eccentricity and might lead to different mechanical and wear problems. The attraction forces caused by eccentricity and acting along the axis that holds the minimum and maximum air gap regions (y-axis) for structure C and D are shown in Fig. IV-30 and Fig. IV-31 respectively.

The attraction forces in structure C had a linear increasing tendency with the increasing eccentricity, and the saturation had a small but noticeable impact on these values as compared to the impact it had on the moving forces of structure C. The variation of structure C's maximum attraction force as a function of eccentricity is shown in Fig. IV-32. The increasing tendencies are linear and almost the same for the saturation and linear magnetization cases. The estimated increasing rates of the attraction forces in structure C acting on the HSM and LSM per mm of eccentricity were 634.7 N/mm and 1594.6 N/mm respectively.

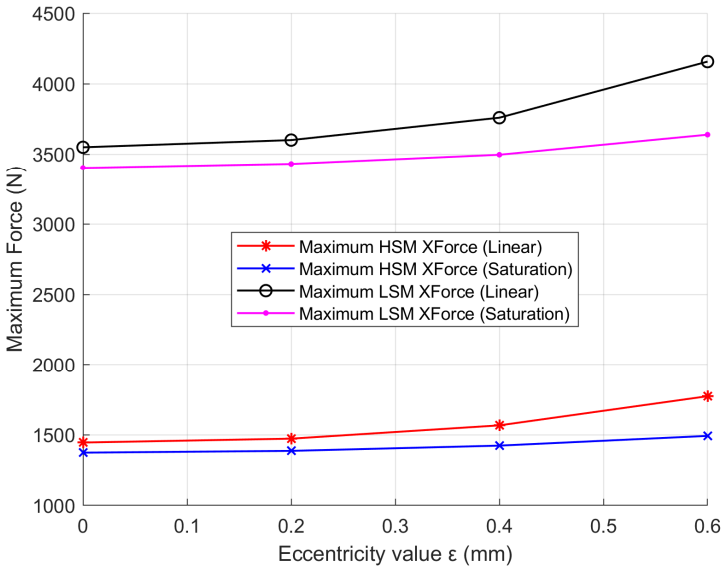

Fig. IV-29 Variation of the maximum moving forces acting in the x-direction for **structure D** as function of eccentricity.

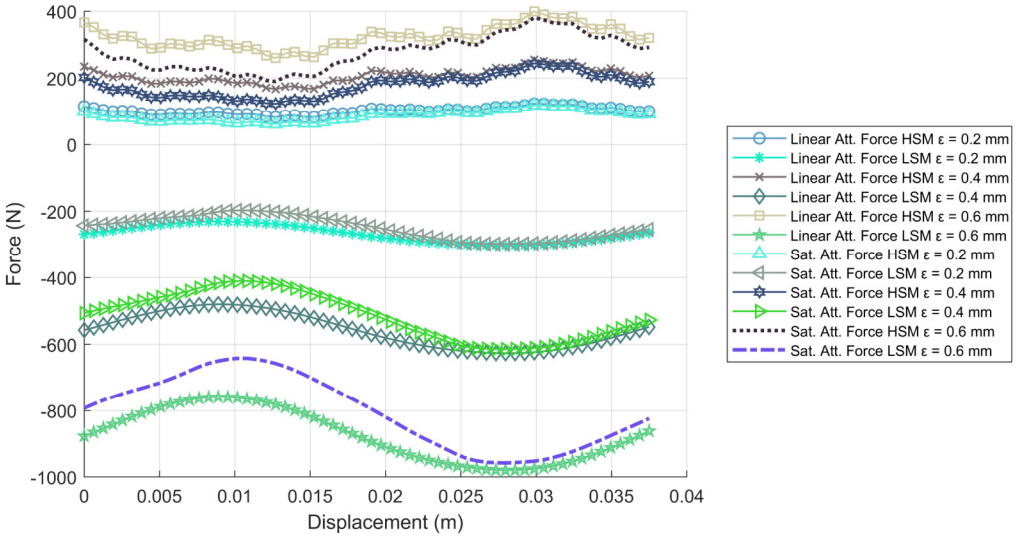

Fig. IV-30 The attraction forces in the y-direction acting on the HSM and LSM of **structure C** under different eccentricity values during the HSM pole-slipping (linear and saturation cases).

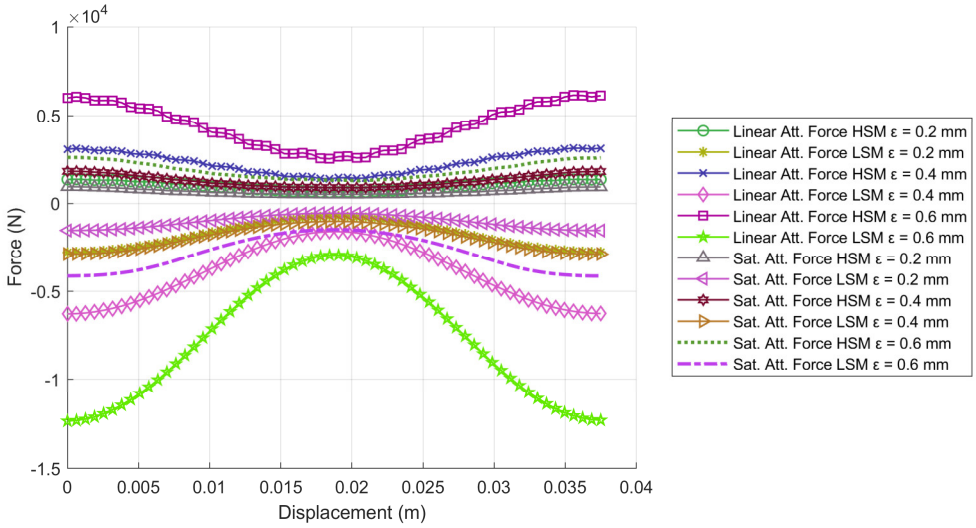

Fig. IV-31 The attraction forces in the y-direction acting on the HSM and LSM of **structure D** under different eccentricity values during the HSM pole-slipping (linear and saturation cases).

Concerning structure D, almost the same observations done for the moving forces can be repeated for the attraction forces. The saturation seems to have a big impact on the estimation of these forces. Fig. IV-33 shows the variation of the maximum attraction force for each

eccentricity case. In the linear case, the attraction forces were increasing exponentially, but the increasing tendency in the saturation case was linear. For the saturation case, the estimated increasing rates of the attraction forces in structure C acting on the HSM and LSM per mm of eccentricity were 4355.5 N/mm and 6868 N/mm respectively.

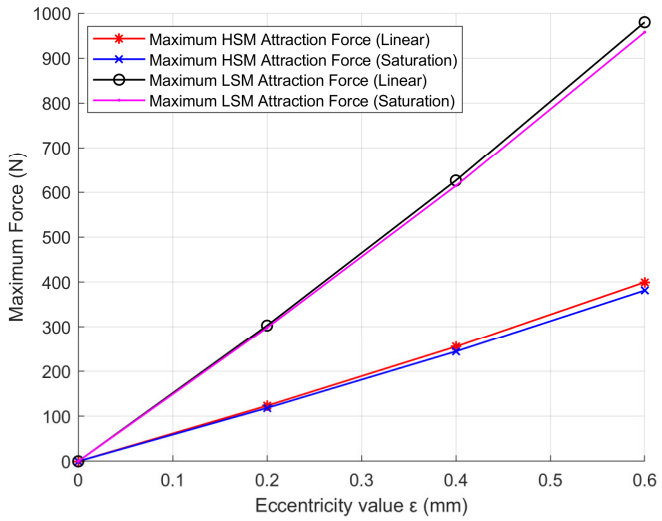

Fig. IV-32 Variation of the maximum attraction forces acting along the y-direction for **structure C** as function of eccentricity.

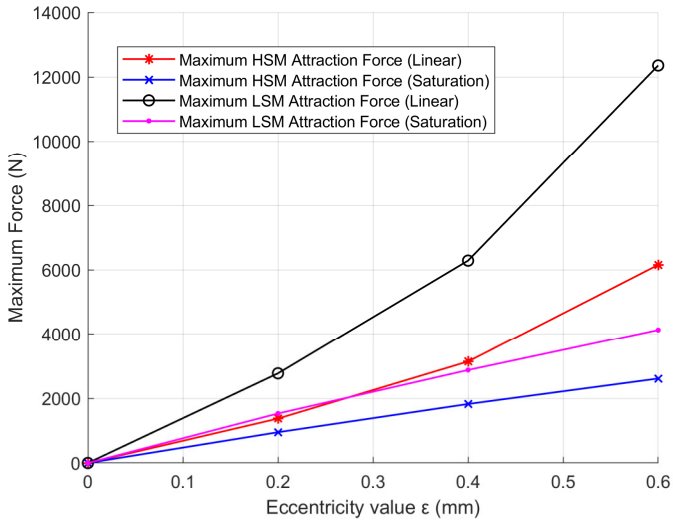

Fig. IV-33 Variation of the maximum attraction forces acting along the y-direction for **structure D** as function of eccentricity.

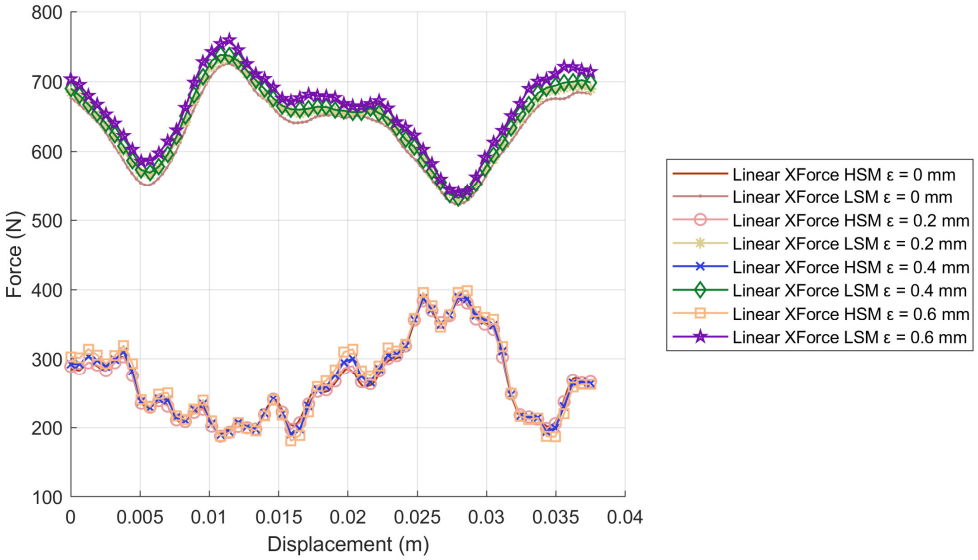

Fig. IV-34 The moving forces in the x-direction of the HSM and LSM of **structure C** during loaded operation at maximum force for different eccentricity values.

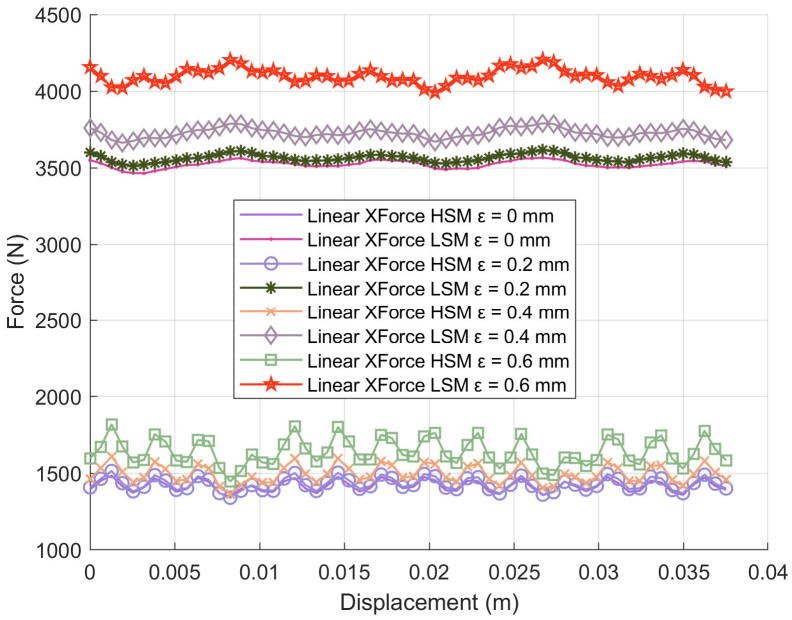

Fig. IV-35 The moving forces in the x-direction of the HSM and LSM of **structure D** during loaded operation at maximum force for different eccentricity values.

Finally, a loaded performance at maximum force was simulated for the two structures to evaluate the impact of eccentricity on the force ripple. In other words, the LSM and HSM were

shifted to maximum moving force position, then they were simulated while moving according to the gear ratio while having the modulating pieces fixed. For multiple eccentricity values, the evaluated moving forces during this operation for structure C and D are shown in Fig. IV-34 and Fig. IV-35. It appears by observing the figures that the general shape of the forces was not affected by eccentricity, as only an increase in the mean value of the waveforms was happening when the eccentricity is applied.

Therefore, once again it has been shown that the flux focusing configuration is more affected by saturation than the surface mounted PM. Additionally, unlike the TLPM case, it seems that the two structures are affected similarly by eccentricity when considering the realistic saturation case because when normalizing the increasing rates for the two structures they become relatively close. It is worth noting that although the two structures had similar dimensions, the forces recorded by the flux focusing structure were much higher, and this is mainly due to ignoring the end-effects in that structure because the end-effects are also ignored in structure C but are expected to have much lower impact than the impact they could have on structure D. Thus, a future study could be done by considering the end-effects in both structures and then attempting the eccentricity analysis.

Conclusion

This chapter addressed the issue of eccentricity in tubular linear machines. First, the problem of eccentricity was defined and described alongside the 3D FEM modeling used for its analysis. The eccentricity in two tubular linear permanent magnet machines with different structures was then analyzed then compared under varying operating conditions. It was found that the flux focusing configuration is more affected by eccentricity and magnetic saturation than the surface mounted PM. Following that, a quasi-3D FEM modeling approach was shown and discussed for assessing eccentricity in tubular linear machines. It was then applied to the previously mentioned structures and compared to the 3D FEM. The proposed quasi-3D model performed well when applied to structure A, but it required special modification through a correcting function to improve its accuracy when modeling structure B. Finally, eccentricity in two tubular linear magnetic gear systems was investigated using 3D FEM, where it was found that the two different structures were affected similarly by eccentricity, but the flux focusing structure much more affected by magnetic saturation.

GENERAL CONCLUSION

Many observations and deductions could be drawn out from this work. Starting with the first chapter which included a literature overview on magnetic gears and an analysis of the data extracted. First, to this date, radial field topology appears to be the prevalent structure for magnetic gears, since most successful prototypes are of this kind, and they have the highest observed VTDs. This doesn't imply axial field topology isn't studied. Researchers have paid a lot of attention to axial field topology and offered numerous solutions, but the key problem has been building a successful prototype and implementing the concept. More effort is needed to enhance the structural and mechanical integrity of the design to overcome construction obstacles. Moreover, among the several magnetic arrangements, flux focusing and the Halbach array appear to be the best. This doesn't prohibit any other potential arrangement or configuration from having high-performance when properly modeled and optimized. In addition, the design and shape of the ferromagnetic pole-pieces affect total performance, and the way to support them should be considered throughout the design process. Next, by comparing the simulated and experimental VTD, one can observe that only a few designs have kept the predicted and measured values near enough. Unaccounted-for end-effects are a common reason of this difference. Additionally, there is a trend for standard magnetic gear structures where the torque density would decrease with the increase of the gear ratio. However, some investigations have shown that cycloidal magnetic gears might be a solution for achieving a high gear ratio while maintaining a high torque density. Finally, it was reported that losses in a magnetic gear depend on rotational speed rather than torque load. Losses which could be split into mechanical related to bearings and friction and electromagnetic losses related to iron core and PM losses, seem lower at full torque load than at no load or decreased load. Thus, this makes magnetic gears more suited for low-speed high-torque applications.

In the second chapter where the magnetic equivalent circuit method was presented and its implementation was illustrated for modeling axial field magnetic gears, it has been shown that this method could achieve an important time gain against 3D FEM and perform calculations for low resources allocation. A nonlinear implementation of the MEC to consider the magnetic saturation was presented where two nonlinear solving methods were tested: the fixed-point iteration method and Newton’s method. After presenting the details of the implementation of

the two methods in the 3D MEC, they were tested to model an axial field magnetic gear while comparing their results to a 3D FEM. The two methods achieved lower computation time, but a slightly reduced accuracy as compared to the 3D FEM. On the other hand, the fixed-point method was slower than the Newton's method but achieved better accuracy. Hence, with the complexity that comes with the implementation of Newton's method as compared to the simplicity of the fixed-point method, the question rises on whether using Newton's method is worth it, especially that the time gain against the fixed-point method was marginal. In addition, in the linear magnetization case the MEC provided very good accuracy with a significant time gain against the 3D FEM. Thus, to evaluate the practicality of using the MEC for the 3D modeling of magnetic gears, it can be said that in the linear case the use of the MEC is undoubtedly a good choice due to the significant time saving it can provide, but in the nonlinear case it is considered situational. To illustrate, if the user has the time and resources required to create and use nonlinear 3D FEM modeling, they could start with the linear MEC to perform the largest number of computations for a low computational cost and effort, and then when most of their parameters are fixed, they could use the nonlinear 3D FEM. However, in case the computational resources or time are not available, the nonlinear MEC could provide relatively good results at a low computational cost and in reduced time.

Then, the issue of end-effects in axial field magnetic gears is addressed by proposing a 3D and quasi-3D MEC to model it. The proposed 3D MEC is applied to two axial field magnetic gear structures: flux focusing and surface mounted PM. This served as an evaluation for the 3D MEC model and as a comparison between the two structures. The evaluation of the 3D MEC has shown that it can achieve lower computation times but when considering the end-effects its accuracy drops. An error margin of around 15% was observed between results estimated using the 3D MEC and the 3D FEM when modeling the end-effects. This error was mainly attributed to the fact that very fine meshing elements are needed at the radial ends of the axial field magnetic gear to model properly the end-effects, and the 3D MEC that was proposed couldn't acquire such a fine mesh at the edges without significantly increasing the total size of the systems which affects the computation time. Regarding the comparison between the modeled structures, the influence of the end-effects and the magnetic saturation was measured. It was found that the axial field flux focusing configuration was significantly more affected by the end-effects and the magnetic saturation. In fact, the impact of the end-effects on that structure was greater than the impact of the magnetic saturation which makes the end-effects a very important aspect to

consider when modeling. Finally, the quasi-3D MEC model that was proposed to model the end-effects in axial field utilized an activation function that compensates for the radial dependence of the magnetic induction in the air gaps. In terms of accuracy and computation time, it performed similarly to the 3D MEC.

The next chapter began with an overview of renewable marine energy conversion systems. Diverse conversion methods and energy sources were briefly presented, and offshore wind energy was investigated in more detail since it is one of the quickly growing and prominent marine energy technologies. It has been found that most of the marine energy conversion systems could benefit from a magnetic gear implementation to improve their reliability and maybe reduce their mass and volume by replacing the direct drive topologies. However, the heavy dependance of magnetic gears on rare-earth magnets introduces a set of concerns on the economic feasibility and availability of the materials for mass producing and adopting this technology. Furthermore, an overview of the applications of magnetic gears in marine energy systems was provided, emphasizing the implementations of magnetic gears and magnetically geared machines documented in the literature. Knowing that magnetic gears perform best in low-speed, high-torque situations, it was discovered that MGMs might serve as an excellent option for direct-drive maritime renewable energy systems, where they can lower the system's overall mass and volume while increasing its efficiency. Also, multiple studies have recommended magnetic gears to replace mechanical gears in order to increase system reliability while avoiding direct drive solutions. Using the modeling approaches described in the prior chapter, a parametric sweep analysis was then performed. Its purpose was to develop an axial field magnetic gear suitable for use in a marine renewable energy conversion system. During the sweep analysis, the structure was modeled using the 3D PN while considering the end-effects. Once all the parameters were determined, a nonlinear 3D FEM model was constructed to predict the performance as accurately as possible. The proposed MG which had a gear ratio of 8.1667:1 and an outer radius of 150 mm was shown to be capable of delivering an active region volumetric torque density of 184.35 N m/L with virtually torque ripple free operation.

This last chapter covered the topic of eccentricity in linear tubular structures. First, the problem of eccentricity was presented in addition to the 3D FEM model that was used to analyze the impact of eccentricity on the performance of the structures. Next, under various operating conditions, the eccentricity in two tubular linear permanent magnet machines with distinct structures was analyzed and compared. The flux focusing design was shown to be remarkably

more affected by eccentricity and magnetic saturation than the surface mounted PM. In addition, the 3D modeling of eccentricity was reported to be time extensive, as the computation time of a single model was high and multiple models were required to cover all the cases. Hence, this motivated the development of a quasi-3D FEM modeling technique for analyzing eccentricity in tubular linear machines for a low computation cost and time. The proposed method was then applied to the structures previously specified and compared to the 3D FEM. The suggested quasi-3D model functioned well when applied to the surface-mounted PM structure, but it needed particular adjustment by means of a correction function in order to improve its accuracy when modeling the flux focusing structure. Overall, the proposed quasi-3D method showed a lot of potential, but it could still benefit from a lot of improvements. Finally, eccentricity in two tubular linear magnetic gear systems was explored using 3D FEM. The two structures studied were also surface-mounted PM and flux focusing. It was discovered that both structures were equally impacted by eccentricity, but the flux-focusing structure was much more influenced by magnetic saturation. Thus, the work in this chapter and the previous chapters might have provided more insight for the user when choosing between the surface mounted PM and flux focusing configurations. To illustrate, the flux focusing configuration seems to have higher overall performance, but to properly estimate its performance, it requires more complex modeling methods that consider the magnetic saturation and the end-effects aspects. This doesn't mean that these aspects can be simply disregarded when modeling surface-mounted PM structures, but if they are to be ignored due to time or resources limitation, their impact on the predicted performance will not be as significant.

Finally, many perspectives can be listed which might be directly related to parts of this work or to the magnetic gears in general. First, although a brief overview on magnetically geared machines was done in the first and third chapters, a more detailed investigation on all the literature available on this subject could be done. Then, for the MEC method a couple of improvements could be listed: the investigation of another approach for the consideration of the magnetic saturation to see if its implementation could be more numerically adequate than the current used method, the implementation of a more advanced meshing method for the 3D MEC that will allow it to have fine elements at the radial edges without significantly affecting the system's size, the use of an alternative or more advanced method to get the activation function used in the quasi-3D MEC model to improve its overall accuracy, and finally investigating methods or approaches that can improve the conditioning of the MEC matrices.

Next, in the third chapter, the proposal of the MG design can benefit from more advanced optimization methods to find the optimal designs. In addition, the proposal was only concerned with maximizing the torque densities which is only one aspect to be considered when modeling MGs, so more aspects like minimizing the losses and reduction of PM volume could be considered. Furthermore, multiple aspects could be improved and addressed in the last chapter regarding the topic of eccentricity. First, the work could benefit from the consideration of a different eccentricity type and linking the electromagnetic model with a mechanical model to detect exactly how the eccentricity shape could be. Second, the utilization of the MEC to model the eccentricity whether through a 3D or a quasi-3D approach is very plausible and could indeed help in solving the problem of the high computation time needed. Then, studying the eccentricity effects in tubular linear magnetically geared machines might be appealing, especially that this type of structures is being proposed in different configurations and considered seriously for renewable energy applications.

Additionally, the study of the non-uniform air gap or rotor deflection in axial field structures is very interesting, and it might be a good idea to apply the 3D MEC to model such a state. Moreover, transient behavior of magnetic gears seems to be really important as reported by some authors, thus an investigation into modeling this aspect could be done. The thermal behavior of magnetic gears is another important topic that needs investigation and might make use of the lumped parameters network approach. Equally important, more efforts should be made into designing high-performance magnetic gear structures that don't heavily rely on rare-earth magnets by using hybrid excitation or ferrite magnets, where the ultimate aim is to overcome some of the economical obstacles currently facing the wide integration of magnetic gears. Finally, an interesting topic for investigation might be the magnetic noise and vibration in magnetic gears.

REFERENCES

[1] C. G. Armstrong, "Power transmitting device," 687,292, 1901

[2] A. H. Neuland, "Apparatus for transmitting power," 1,171,351, 1916

[3] G. A. Reese, "Magnetic gearing arrangement," 3,301,091, 1967

[4] T. B. MARTIN, "Magnetic transmission," 3,378,710, 1968

[5] D. E. Hesmondhalgh and D. Tipping, "A multielement magnetic gear," *IEE Proceedings B Electric Power Applications*, vol. 127, no. 3, p. 129, 1980, doi: 10.1049/ip-b.1980.0017.

[6] K. Tsurumoto and S. Kikuchi, "A new magnetic gear using permanent magnet," *IEEE Trans Magn*, vol. 23, no. 5, pp. 3622–3624, Sep. 1987, doi: 10.1109/TMAG.1987.1065208.

[7] S. Kikuchi and K. Tsurumoto, "Design and characteristics of a new magnetic worm gear using permanent magnet," *IEEE Trans Magn*, vol. 29, no. 6, pp. 2923–2925, Nov. 1993, doi: 10.1109/20.280916.

[8] T. Teragaki and H. Kobayashi, "A new rotary speed converter," *IEEE Trans Magn*, vol. 23, no. 5, pp. 2200–2202, Sep. 1987, doi: 10.1109/tmag.1987.1065637.

[9] K. Ikuta, S. Makita, and S. Arimoto, "Non-contact magnetic gear for micro transmission mechanism," in *Proceedings. IEEE Micro Electro Mechanical Systems*, 1991, pp. 125 – 130. [Online]. Available: https://www.scopus.com/inward/record.uri?eid=2-s2.0-0025840975&partnerID=40&md5=43ccb0a78ea1ca2be3b7f3f4e371c2e6

[10] B. Ackermann and L. Honds, "Magnetic drive arrangement comprising a plurality of magnetically cooperating parts which are movable relative to one another," 5,633,555, 1997

[11] Bernd Ackermann, "Magnetic drive arrangement," 5,994.809, 1999

[12] E. Shipely, "Gear Failures," 1967. Accessed: Jul. 08, 2022. [Online]. Available: https://www.xtek.com/wp-content/uploads/2018/05/xtek-gear-failures.pdf

[13] B. A. Miller, R. J. Shipley, R. J. Parrington, A. S. M. International, and A. S. M. International, Eds., *ASM handbook. Volume 11: Failure analysis and prevention*. Materials Park, Ohio: ASM International, 2021.

[14] S. Q. A. Rizvi, *A Comprehensive Review of Lubricant Chemistry, Technology, Selection, and Design*. 100 Barr Harbor Drive, PO Box C700, West Conshohocken, PA 19428-2959: ASTM International, 2009. doi: 10.1520/MNL59-EB.

[15] American Gear Manufacturers Association and American National Standards Institute, *Appearance of gear teeth: terminology of wear and failure*. 2014.

[16] K. Atallah and D. Howe, "A novel high-performance magnetic gear," *IEEE Trans Magn*, vol. 37, no. 4, pp. 2844–2846, Jul. 2001, doi: 10.1109/20.951324.

[17] K. Atallah, S. D. Calverley, and D. Howe, "Design, analysis and realisation of a high-performance magnetic gear," *IEE Proceedings - Electric Power Applications*, vol. 151, no. 2, p. 135, 2004, doi: 10.1049/ip-epa:20040224.

[18] K. Atallah, J. Wang, S. D. Calverley, and S. Duggan, "Design and Operation of a Magnetic Continuously Variable Transmission," *IEEE Trans Ind Appl*, vol. 48, no. 4, pp. 1288–1295, Jul. 2012, doi: 10.1109/TIA.2012.2199451.

[19] J. Wang, K. Atallah, and S. D. Carvley, "A Magnetic Continuously Variable Transmission Device," *IEEE Trans Magn*, vol. 47, no. 10, pp. 2815–2818, Oct. 2011, doi: 10.1109/TMAG.2011.2157470.

[20] Z. Q. Zhu and D. Howe, "Influence of design parameters on cogging torque in permanent magnet machines," in *1997 IEEE International Electric Machines and Drives Conference Record*, p. MA1/3.1-MA1/3.3. doi: 10.1109/IEMDC.1997.604060.

[21] K. Li and J. Z. Bird, "A Review of the Volumetric Torque Density of Rotary Magnetic Gear Designs," in *2018 XIII International Conference on Electrical Machines (ICEM)*, Sep. 2018, pp. 2016–2022. doi: 10.1109/ICELMACH.2018.8507059.

[22] P. M. Tlali, R.-J. Wang, and S. Gerber, "Magnetic gear technologies: A review," in *2014 International Conference on Electrical Machines (ICEM)*, Sep. 2014, pp. 544–550. doi: 10.1109/ICELMACH.2014.6960233.

[23] O. S. Chirila, D. Stoia, M. Cernat, and K. Hamayer, "High-performance magnetic gears topologies," in *2010 12th International Conference on Optimization of Electrical and Electronic Equipment*, May 2010, pp. 1091–1096. doi: 10.1109/OPTIM.2010.5510496.

[24] Y. Wang, M. Filippini, N. Bianchi, and P. Alotto, "A Review on Magnetic Gears: Topologies, Computational Models, and Design Aspects," *IEEE Trans Ind Appl*, vol. 55, no. 5, pp. 4557–4566, Sep. 2019, doi: 10.1109/TIA.2019.2916765.

[25] X. Li, K.-T. Chau, M. Cheng, and W. Hua, "COMPARISON OF MAGNETIC-GEARED PERMANENT-MAGNET MACHINES," *Progress In Electromagnetics Research*, vol. 133, pp. 177–198, 2013, doi: 10.2528/PIER12080808.

[26] D. Fodorean, "State of the Art of Magnetic Gears, their Design, and Characteristics with Respect to EV Application," in *Modeling and Simulation for Electric Vehicle Applications*, InTech, 2016. doi: 10.5772/64174.

[27] S. Gerber and R.-J. Wang, "Evaluation of a prototype magnetic gear," in *2013 IEEE International Conference on Industrial Technology (ICIT)*, Feb. 2013, pp. 319–324. doi: 10.1109/ICIT.2013.6505692.

[28] A. Matthee, S. Gerber, and R.-J. Wang, "A high performance concentric magnetic gear," Aug. 2015. doi: 10.13140/RG.2.1.1493.6167.

[29] P. O. Rasmussen, T. O. Andersen, F. T. Jorgensen, and O. Nielsen, "Development of a High-Performance Magnetic Gear," *IEEE Trans Ind Appl*, vol. 41, no. 3, pp. 764–770, May 2005, doi: 10.1109/TIA.2005.847319.

[30] K. Uppalapati and J. Bird, "A flux focusing ferrite magnetic gear," in *6th IET International Conference on Power Electronics, Machines and Drives (PEMD 2012)*, 2012, pp. B151–B151. doi: 10.1049/cp.2012.0303.

[31] K. K. Uppalapati, W. Bomela, J. Z. Bird, M. Calvin, and J. Wright, "Construction of a low speed flux focusing magnetic gear," in *2013 IEEE Energy Conversion Congress and Exposition*, Sep. 2013, pp. 2178–2184. doi: 10.1109/ECCE.2013.6646976.

[32] K. K. Uppalapati, W. B. Bomela, J. Z. Bird, M. D. Calvin, and J. D. Wright, "Experimental Evaluation of Low-Speed Flux-Focusing Magnetic Gearboxes," *IEEE Trans Ind Appl*, vol. 50, no. 6, pp. 3637–3643, Nov. 2014, doi: 10.1109/TIA.2014.2312551.

[33] K. K. Uppalapati, M. D. Calvin, J. D. Wright, J. Pitchard, W. B. Williams, and J. Z. Bird, "A Magnetic Gearbox With an Active Region Torque Density of 239 N·m/L," *IEEE Trans Ind Appl*, vol. 54, no. 2, pp. 1331–1338, Mar. 2018, doi: 10.1109/TIA.2017.2779418.

[34] N. W. Frank and H. A. Toliyat, "Analysis of the Concentric Planetary Magnetic Gear With Strengthened Stator and Interior Permanent Magnet Inner Rotor," *IEEE Trans Ind Appl*, vol. 47, no. 4, pp. 1652–1660, Jul. 2011, doi: 10.1109/TIA.2011.2154291.

[35] X. Liu, K. T. Chau, J. Z. Jiang, and C. Yu, "Design and analysis of interior-magnet outer-rotor concentric magnetic gears," *J Appl Phys*, vol. 105, no. 7, p. 07F101, Apr. 2009, doi: 10.1063/1.3058619.

[36] H. Y. Wong, J. Z. Bird, D. Barnett, and W. Williams, "A High Torque Density Halbach Rotor Coaxial Magnetic Gear," in *2019 IEEE International Electric Machines & Drives Conference (IEMDC)*, May 2019, pp. 233–239. doi: 10.1109/IEMDC.2019.8785188.

[37] L. Jing, Z. Huang, J. Chen, and R. Qu, "An Asymmetric Pole Coaxial Magnetic Gear With Unequal Halbach Arrays and Spoke Structure," *IEEE Transactions on Applied Superconductivity*, vol. 30, no. 4, pp. 1–5, Jun. 2020, doi: 10.1109/TASC.2019.2962687.

[38] H. Mafi, E. Afjei, and A. Ghaheri, "Design of coaxial magnetic gear utilising a novel permanent magnet Halbach array structure," *IET Electr Power Appl*, vol. 15, no. 3, pp. 299–309, Mar. 2021, doi: 10.1049/elp2.12021.

[39] L. Jing, J. Gong, J. Chen, Z. Huang, and R. Qu, "A Novel Coaxial Magnetic Gear With Unequal Halbach Arrays and Non-Uniform Air Gap," *IEEE Transactions on Applied Superconductivity*, vol. 30, no. 4, pp. 1–5, Jun. 2020, doi: 10.1109/TASC.2020.2968043.

[40] L. Jing, T. Zhang, Y. Gao, R. Qu, Y. Huang, and T. Ben, "A Novel HTS Modulated Coaxial Magnetic Gear With Eccentric Structure and Halbach Arrays," *IEEE Transactions on Applied Superconductivity*, vol. 29, no. 5, pp. 1–5, Aug. 2019, doi: 10.1109/TASC.2019.2892152.

[41] L. Jian and K. T. Chau, "A Coaxial Magnetic Gear With Halbach Permanent-Magnet Arrays," *IEEE Transactions on Energy Conversion*, vol. 25, no. 2, pp. 319–328, Jun. 2010, doi: 10.1109/TEC.2010.2046997.

[42] T. Fujita *et al.*, "Surface Magnet Gears with a New Magnet Arrangement and Optimal Shape of Stationary Pole Pieces," *Journal of Electromagnetic Analysis and Applications*, vol. 05, no. 06, pp. 243–249, 2013, doi: 10.4236/jemaa.2013.56039.

[43] M. C. Gardner, D. A. Janak, and H. A. Toliyat, "A Parameterized Linear Magnetic Equivalent Circuit for Air Core Radial Flux Coaxial Magnetic Gears with Halbach Arrays," in *2018 IEEE Energy Conversion Congress and Exposition (ECCE)*, Sep. 2018, pp. 2351–2358. doi: 10.1109/ECCE.2018.8557915.

[44] K. Aiso, K. Akatsu, and Y. Aoyama, "A Novel Reluctance Magnetic Gear for High-Speed Motor," *IEEE Trans Ind Appl*, vol. 55, no. 3, pp. 2690–2699, May 2019, doi: 10.1109/TIA.2019.2900205.

[45] M. C. Gardner, M. Johnson, and H. A. Toliyat, "Comparison of Surface Permanent Magnet Axial and Radial Flux Coaxial Magnetic Gears," *IEEE Transactions on Energy Conversion*, vol. 33, no. 4, pp. 2250–2259, Dec. 2018, doi: 10.1109/TEC.2018.2865200.

[46] S. Mezani, K. Atallah, and D. Howe, "A high-performance axial-field magnetic gear," *J Appl Phys*, vol. 99, no. 8, p. 08R303, Apr. 2006, doi: 10.1063/1.2158966.

[47] V. M. Acharya, J. Z. Bird, and M. Calvin, "A Flux Focusing Axial Magnetic Gear," *IEEE Trans Magn*, vol. 49, no. 7, pp. 4092–4095, Jul. 2013, doi: 10.1109/TMAG.2013.2248703.

[48] V. M. Acharya, J. Z. Bird, and M. Calvin, "A low torque ripple flux focusing axial magnetic gear," in *7th IET International Conference on Power Electronics, Machines and Drives (PEMD 2014)*, 2014, pp. 2.12.02-2.12.02. doi: 10.1049/cp.2014.0476.

[49] M. Bahrami Kouhshahi, V. M. Acharya, M. Calvin, J. Z. Bird, and W. Williams, "Designing and experimentally testing a flux-focusing axial flux magnetic gear for an ocean generator application," *IET Electr Power Appl*, vol. 13, no. 8, pp. 1212–1218, Aug. 2019, doi: 10.1049/iet-epa.2018.5931.

[50] M. Johnson, A. Shapoury, P. Boghrat, M. Post, and H. A. Toliyat, "Analysis and development of an axial flux magnetic gear," in *2014 IEEE Energy Conversion Congress and Exposition (ECCE)*, Sep. 2014, pp. 5893–5900. doi: 10.1109/ECCE.2014.6954210.

[51] M. Johnson, M. C. Gardner, and H. A. Toliyat, "Analysis of axial field magnetic gears with Halbach arrays," in *2015 IEEE International Electric Machines & Drives Conference (IEMDC)*, May 2015, pp. 108–114. doi: 10.1109/IEMDC.2015.7409045.

[52] M.-C. Tsai and L.-H. Ku, "3-D Printing-Based Design of Axial Flux Magnetic Gear for High Torque Density," *IEEE Trans Magn*, vol. 51, no. 11, pp. 1–4, Nov. 2015, doi: 10.1109/TMAG.2015.2435817.

[53] H. Weh and H. May, "Achievable force densities for permanent magnet excited machines in new configurations," in *Proc. Int. Conf. Electrical Machines*, 1986, vol. 3, pp. 1107–1111.

[54] M. F. J. Kremers, J. J. H. Paulides, and E. A. Lomonova, "Toward Accurate Design of a Transverse Flux Machine Using an Analytical 3-D Magnetic Charge Model," *IEEE Trans Magn*, vol. 51, no. 11, pp. 1–4, Nov. 2015, doi: 10.1109/TMAG.2015.2444994.

[55] M. Kremers, J. J. Paulides, and E. Lomonova, "Design and optimization of a transverse flux machine using an analytical 3-D magnetic charge model," in *2015 IEEE Magnetics Conference (INTERMAG)*, May 2015, pp. 1–1. doi: 10.1109/INTMAG.2015.7156613.

[56] M. F. J. Kremers, J. J. H. Paulides, and E. A. Lomonova, "Analytical 3-D design of a Transverse Flux Machine with high power factor," in *2015 International Conference on Sustainable Mobility Applications, Renewables and Technology (SMART)*, Nov. 2015, pp. 1–5. doi: 10.1109/SMART.2015.7399243.

[57] K. Ramakrishnan, M. Curti, D. Zarko, G. Mastinu, J. J. H. Paulides, and E. A. Lomonova, "A comparison study of modelling techniques for permanent magnet machines," in *2016 Eleventh International Conference on Ecological Vehicles and Renewable Energies (EVER)*, Apr. 2016, pp. 1–6. doi: 10.1109/EVER.2016.7476424.

[58] W. Bomela, J. Z. Bird, and V. M. Acharya, "The Performance of a Transverse Flux Magnetic Gear," *IEEE Trans Magn*, vol. 50, no. 1, pp. 1–4, Jan. 2014, doi: 10.1109/TMAG.2013.2277431.

[59] M. Desvaux, M. Chauwin, B. Multon, S. Sire, and H. ben Ahmed, "Experimental validation of a transverse flux magnetic gear," *J Magn Magn Mater*, vol. 536, p. 168139, Oct. 2021, doi: 10.1016/j.jmmm.2021.168139.

[60] L. Yong, X. Jingwei, P. Kerong, and L. Yongping, "Principle and simulation analysis of a novel structure magnetic gear," in *2008 International Conference on Electrical Machines and Systems*, 2008, pp. 3845–3849.

[61] X. Yin, P.-D. Pfister, and Y. Fang, "A Novel Magnetic Gear: Toward a Higher Torque Density," *IEEE Trans Magn*, vol. 51, no. 11, pp. 1–4, Nov. 2015, doi: 10.1109/TMAG.2015.2436058.

[62] Cheng-Chi Huang, Mi-Ching Tsai, D. G. Dorrell, and Bor-Jeng Lin, "Development of a Magnetic Planetary Gearbox," *IEEE Trans Magn*, vol. 44, no. 3, pp. 403–412, Mar. 2008, doi: 10.1109/TMAG.2007.914665.

[63] R.-J. Wang, A. Matthee, S. Gerber, and P. Tlali, "Calculation of Torque Performance of a Novel Magnetic Planetary Gear," *IEEE Magn Lett*, vol. 7, pp. 1–5, 2016, doi: 10.1109/LMAG.2016.2564948.

[64] K. Davey *et al.*, "Rotating Cylinder Planetary Gear Motor," *IEEE Trans Ind Appl*, vol. 52, no. 3, pp. 2253–2260, May 2016, doi: 10.1109/TIA.2016.2532286.

[65] L. Xu and X. Zhu, "Magnetic planetary gear drive," *Proc Inst Mech Eng C J Mech Eng Sci*, vol. 223, no. 9, pp. 2167–2181, Sep. 2009, doi: 10.1243/09544062JMES1441.

[66] F. T. Joergensen, T. O. Andersen, and P. O. Rasmussen, "The cycloid permanent magnetic gear," in *Conference Record of the 2006 IEEE Industry Applications Conference Forty-First IAS Annual Meeting*, Oct. 2006, pp. 373–378. doi: 10.1109/IAS.2006.256549.

[67] G. Duan *et al.*, "Cycloidal Magnetic Gear Combining Axial and Radial Topologies," *IEEE Transactions on Energy Conversion*, pp. 1–1, 2022, doi: 10.1109/TEC.2022.3171105.

[68] K. Davey, L. McDonald, and T. Hutson, "Axial Flux Cycloidal Magnetic Gears," *IEEE Trans Magn*, vol. 50, no. 4, pp. 1–7, Apr. 2014, doi: 10.1109/TMAG.2013.2287181.

[69] S. Hasanpour, M. Johnson, M. C. Gardner, and H. A. Toliyat, "Cycloidal Reluctance Magnetic Gears for High Gear Ratio Applications," *IEEE Trans Magn*, vol. 58, no. 6, pp. 1–10, Jun. 2022, doi: 10.1109/TMAG.2022.3163419.

[70] M. Johnson, S. Hasanpour, M. C. Gardner, and H. A. Toliyat, "Analysis and Benchmarking of Radial Flux Cycloidal Magnetic Gears with Reduced Permanent Magnet Piece Count Using Consequent Poles," in *2021 IEEE Energy Conversion Congress and Exposition (ECCE)*, Oct. 2021, pp. 4334–4341. doi: 10.1109/ECCE47101.2021.9595788.

[71] B. Praslicka *et al.*, "Practical Analysis and Design of a 50:1 Cycloidal Magnetic Gear with Balanced Off-Axis Moments and a High Specific Torque for Lunar Robots," in *2021 IEEE International Electric Machines & Drives Conference (IEMDC)*, May 2021, pp. 1–8. doi: 10.1109/IEMDC47953.2021.9449504.

[72] H. Huang, R. Qu, and J. Bird, "Performance of Halbach Cycloidal Magnetic Gears with Respect to Torque Density and Gear Ratio," in *2019 IEEE International Electric Machines & Drives Conference (IEMDC)*, May 2019, pp. 1977–1984. doi: 10.1109/IEMDC.2019.8785259.

[73] K. Li, J. Bird, J. Kadel, and W. Williams, "A Flux-Focusing Cycloidal Magnetic Gearbox," *IEEE Trans Magn*, vol. 51, no. 11, pp. 1–4, Nov. 2015, doi: 10.1109/TMAG.2015.2440218.

[74] J. Rens, K. Atallah, S. D. Calverley, and D. Howe, "A novel magnetic harmonic gear," in *2007 IEEE International Electric Machines & Drives Conference*, May 2007, pp. 698–703. doi: 10.1109/IEMDC.2007.382752.

[75] K. Atallah, J. Wang, and D. Howe, "A high-performance linear magnetic gear," *J Appl Phys*, vol. 97, no. 10, p. 10N516, May 2005, doi: 10.1063/1.1853900.

[76] K. Atallah, J. Wang, S. Mezani, and D. Howe, "A Novel High-Performance Linear Magnetic Gear," *IEEJ Transactions on Industry Applications*, vol. 126, no. 10, pp. 1352–1356, 2006, doi: 10.1541/ieejias.126.1352.

[77] R. C. Holehouse, K. Atallah, and J. Wang, "A linear magnetic gear," in *2012 XXth International Conference on Electrical Machines*, Sep. 2012, pp. 563–569. doi: 10.1109/ICElMach.2012.6349925.

[78] R. C. Holehouse, K. Atallah, and J. Wang, "Design and Realization of a Linear Magnetic Gear," *IEEE Trans Magn*, vol. 47, no. 10, pp. 4171–4174, Oct. 2011, doi: 10.1109/TMAG.2011.2157101.

[79] W. Li, K. T. Chau, and J. Li, "Simulation of a Tubular Linear Magnetic Gear Using HTS Bulks for Field Modulation," *IEEE Transactions on Applied Superconductivity*, vol. 21, no. 3, pp. 1167–1170, Jun. 2011, doi: 10.1109/TASC.2010.2080255.

[80] A. B. Kjaer, S. Korsgaard, S. S. Nielsen, L. Demsa, and P. O. Rasmussen, "Design, Fabrication, Test, and Benchmark of a Magnetically Geared Permanent Magnet Generator for Wind Power Generation," *IEEE Transactions on Energy Conversion*, vol. 35, no. 1, pp. 24–32, Mar. 2020, doi: 10.1109/TEC.2019.2951998.

[81] M. Johnson, M. C. Gardner, and H. A. Toliyat, "Design and Analysis of an Axial Flux Magnetically Geared Generator," *IEEE Trans Ind Appl*, vol. 53, no. 1, pp. 97–105, Jan. 2017, doi: 10.1109/TIA.2016.2603962.

[82] R.-J. Wang and S. Gerber, "Magnetically geared wind generator technologies: Opportunities and challenges," *Appl Energy*, vol. 136, pp. 817–826, Dec. 2014, doi: 10.1016/j.apenergy.2014.07.079.

[83] K. Atallah, J. Rens, S. Mezani, and D. Howe, "A Novel 'Pseudo' Direct-Drive Brushless Permanent Magnet Machine," *IEEE Trans Magn*, vol. 44, no. 11, pp. 4349–4352, Nov. 2008, doi: 10.1109/TMAG.2008.2001509.

[84] L. Jian, K. T. Chau, and J. Z. Jiang, "A Magnetic-Geared Outer-Rotor Permanent-Magnet Brushless Machine for Wind Power Generation," *IEEE Trans Ind Appl*, vol. 45, no. 3, pp. 954–962, 2009, doi: 10.1109/TIA.2009.2018974.

[85] S. Gerber and Rong-Jie Wang, "Design and Evaluation of a Magnetically Geared PM Machine," *IEEE Trans Magn*, vol. 51, no. 8, pp. 1–10, Aug. 2015, doi: 10.1109/TMAG.2015.2421474.

[86] Z. Q. Zhu, H. Y. Li, R. Deodhar, A. Pride, and T. Sasaki, "Recent developments and comparative study of magnetically geared machines," *CES Transactions on Electrical Machines and Systems*, vol. 2, no. 1, pp. 13–22, Mar. 2018, doi: 10.23919/TEMS.2018.8326448.

[87] A. Penzkofer and K. Atallah, "Analytical Modeling and Optimization of Pseudo-Direct Drive Permanent Magnet Machines for Large Wind Turbines," *IEEE Trans Magn*, vol. 51, no. 12, pp. 1–14, Dec. 2015, doi: 10.1109/TMAG.2015.2461175.

[88] P. O. Rasmussen, T. v. Frandsen, K. K. Jensen, and K. Jessen, "Experimental Evaluation of a Motor-Integrated Permanent-Magnet Gear," *IEEE Trans Ind Appl*, vol. 49, no. 2, pp. 850–859, Mar. 2013, doi: 10.1109/TIA.2013.2242423.

[89] W. N. Fu and S. L. Ho, "A Quantitative Comparative Analysis of a Novel Flux-Modulated Permanent-Magnet Motor for Low-Speed Drive," *IEEE Trans Magn*, vol. 46, no. 1, pp. 127–134, Jan. 2010, doi: 10.1109/TMAG.2009.2030677.

[90] S. Mezani, T. Hamiti, L. Belguerras, T. Lubin, and C. Gerada, "Magnetically geared induction machines," in *2015 IEEE Magnetics Conference (INTERMAG)*, May 2015, pp. 1–1. doi: 10.1109/INTMAG.2015.7156627.

[91] B. Bidouche, T. Lubin, and S. Mezani, "Design and Analysis of a Magnetically Geared Induction Machine," in *2018 XIII International Conference on Electrical Machines (ICEM)*, Sep. 2018, pp. 629–634. doi: 10.1109/ICELMACH.2018.8507009.

[92] B. E. B. Bidouche, T. Lubin, and S. Mezani, "Etude d'une Machine à Induction integrant un Réducteur de Vitesse Magnétique," Jul. 2018. [Online]. Available: https://hal.archives-ouvertes.fr/hal-01910639

[93] M. C. Gardner, B. Praslicka, M. Johnson, and H. A. Toliyat, "Optimization of Coaxial Magnetic Gear Design and Magnet Material Grade at Different Temperatures and Gear Ratios," *IEEE Transactions on Energy Conversion*, vol. 36, no. 3, pp. 2493–2501, Sep. 2021, doi: 10.1109/TEC.2021.3054806.

[94] M. C. Gardner, B. E. Jack, M. Johnson, and H. A. Toliyat, "Comparison of Surface Mounted Permanent Magnet Coaxial Radial Flux Magnetic Gears Independently Optimized for Volume, Cost, and Mass," *IEEE Trans Ind Appl*, vol. 54, no. 3, pp. 2237–2245, May 2018, doi: 10.1109/TIA.2018.2803039.

[95] M. C. Gardner, M. Johnson, and H. A. Toliyat, "Performance Impacts of Practical Fabrication Tradeoffs for a Radial Flux Coaxial Magnetic Gear with Halbach Arrays and Air Cores," in *2019 IEEE Energy Conversion Congress and Exposition (ECCE)*, Sep. 2019, pp. 3129–3136. doi: 10.1109/ECCE.2019.8912286.

[96] M. C. Johnson, "Design and Analysis of Axial and Radial Flux Magnetic Gears and Magnetically Geared Machines," 2017.

[97] M. Calvin, "A comparative study between axial and radial fluxfocusing magnetic gear topologies and mechanical gearboxes," The University of North Carolina at Charlotte, 2015.

[98] F. T. Jørgensen, *Design and construction of permanent magnetic gears*. Department of Energy Technology, Aalborg University, 2010.

[99] D. Som *et al.*, "Analysis and Testing of a Coaxial Magnetic Gearbox With Flux Concentration Halbach Rotors," *IEEE Trans Magn*, vol. 53, no. 11, pp. 1–6, Nov. 2017, doi: 10.1109/TMAG.2017.2715799.

[100] Linni Jian, K. T. Chau, Yu. Gong, J. Z. Jiang, Chuang Yu, and Wenlong Li, "Comparison of Coaxial Magnetic Gears With Different Topologies," *IEEE Trans Magn*, vol. 45, no. 10, pp. 4526–4529, Oct. 2009, doi: 10.1109/TMAG.2009.2021662.

[101] K. Uppalapati, J. Kadel, J. Wright, K. Li, W. Williams, and J. Z. Bird, "A low assembly cost coaxial magnetic gearbox," in *2016 IEEE 2nd Annual Southern Power Electronics Conference (SPEC)*, Dec. 2016, pp. 1–6. doi: 10.1109/SPEC.2016.7846207.

[102] K. Nakamura, M. Fukuoka, and O. Ichinokura, "Performance improvement of magnetic gear and efficiency comparison with conventional mechanical gear," *J Appl Phys*, vol. 115, no. 17, p. 17A314, May 2014, doi: 10.1063/1.4863809.

[103] Libing Jing, Lin Liu, Min Xiong, and da Feng, "Parameters Analysis and Optimization Design for a Concentric Magnetic Gear Based on Sinusoidal Magnetizations," *IEEE Transactions on Applied Superconductivity*, vol. 24, no. 5, pp. 1–5, Oct. 2014, doi: 10.1109/TASC.2014.2340460.

[104] L. Bronn, R.-J. Wang, and M. Kamper, "Development of a shutter type magnetic gear," Aug. 2010. doi: 10.13140/RG.2.1.5032.5606.

[105] L. Shah, A. Cruden, and B. W. Williams, "A Variable Speed Magnetic Gear Box Using Contra-Rotating Input Shafts," *IEEE Trans Magn*, vol. 47, no. 2, pp. 431–438, Feb. 2011, doi: 10.1109/TMAG.2010.2097273.

[106] E. Gouda, S. Mezani, L. Baghli, and A. Rezzoug, "Comparative Study Between Mechanical and Magnetic Planetary Gears," *IEEE Trans Magn*, vol. 47, no. 2, pp. 439–450, Feb. 2011, doi: 10.1109/TMAG.2010.2090890.

[107] M. Johnson, M. C. Gardner, H. A. Toliyat, S. Englebretson, W. Ouyang, and C. Tschida, "Design, Construction, and Analysis of a Large-Scale Inner Stator Radial Flux Magnetically Geared Generator for Wave Energy Conversion," *IEEE Trans Ind Appl*, vol. 54, no. 4, pp. 3305–3314, Jul. 2018, doi: 10.1109/TIA.2018.2828383.

[108] E. P. Furlani, *Permanent Magnet and Electromechanical Devices: Materials, Analysis, and Applications*. Elsevier Science, 2001. [Online]. Available: https://books.google.fr/books?id=irsdLnC5SrsC

[109] R. J. Parker, *Advances in Permanent Magnetism*. Wiley, 1990.

[110] J. Sykulski, *Computational Magnetics*. Springer Netherlands, 2012. [Online]. Available: https://books.google.fr/books?id=tr70CAAAQBAJ

[111] "Tata Steel Europe." https://www.tatasteeleurope.com/engineering/products/electrical-steel (accessed Aug. 29, 2022).

[112] "Imphy Aperam." https://www.aperam.com/alloys/markets/electronics-electrical/ (accessed Aug. 29, 2022).

[113] "Magnetics USA Kool Mu." https://www.mag-inc.com/Products/Powder-Cores/Kool-Mu-Cores (accessed Aug. 29, 2022).

[114] "Imphy AFK1 Aperam." https://www.aperam.com/product/imphy-afk-1/ (accessed Aug. 29, 2022).

[115] "Magnetics USA Ferrites J ." https://www.mag-inc.com/Products/Ferrite-Cores/J-Material (accessed Aug. 29, 2022).

[116] "Thyssenkrupp Carbon Steel." https://www.thyssenkrupp-materials.fr/en/products/mechanical-steels/unalloyed-engineering-steels/carbon-steel (accessed Aug. 29, 2022).

[117] D. C. Jiles, *Introduction to Magnetism and Magnetic Materials, Second Edition*. Taylor & Francis, 1998. [Online]. Available: https://books.google.fr/books?id=axyWXjsdorMC

[118] "CY Magnets ." http://www.cy-magnetics.com/Mag_Industrial.htm (accessed Sep. 01, 2022).

[119] J. N. Reddy, *Introduction to the Finite Element Method*, 3rd edition. New York: McGraw-Hill Education, 2006.

[120] V. Ostović, *Dynamics of Saturated Electric Machines*. New York, NY: Springer New York, 1989. doi: 10.1007/978-1-4613-8933-0.

[121] M. Johnson, M. C. Gardner, and H. A. Toliyat, "A Parameterized Linear 3D Magnetic Equivalent Circuit for Analysis and Design of Radial Flux Magnetic Gears–Part II: Evaluation," *IEEE Transactions on Energy Conversion*, vol. 36, no. 4, pp. 2903–2911, Dec. 2021, doi: 10.1109/TEC.2021.3061638.

[122] M. Johnson, M. C. Gardner, and H. A. Toliyat, "A Parameterized Linear 3D Magnetic Equivalent Circuit for Analysis and Design of Radial Flux Magnetic Gears–Part I: Implementation," *IEEE Transactions on Energy Conversion*, vol. 36, no. 4, pp. 2894–2902, Dec. 2021, doi: 10.1109/TEC.2021.3061635.

[123] J. Turowski, M. Turowski, and M. Kopec, "Method of three-dimensional network solution of leakage field of three-phase transformers," *IEEE Trans Magn*, vol. 26, no. 5, pp. 2911–2919, 1990, doi: 10.1109/20.104906.

[124] E. R. Lwithwaite, "Magnetic equivalent circuits for electrical machines," *Proceedings of the Institution of Electrical Engineers*, vol. 114, no. 11, p. 1805, 1967, doi: 10.1049/piee.1967.0344.

[125] J. WOROTYŃSKI, M. TUROWSKI, and E. A. MENDRELA, "THE ACCURACY OF CALCULATION OF MAGNETIC FIELDS, INDUCTANCE AND FORCES IN ELECTROMAGNETIC DEVICES USING THE RELUCTANCE NETWORK METHOD (RNM)," *COMPEL - The international journal for computation and mathematics in electrical and electronic engineering*, vol. 13, no. 1, pp. 159–162, Jan. 1994, doi: 10.1108/eb051864.

[126] J. K. Sykulski, Ed., *Computational Magnetics*. Dordrecht: Springer Netherlands, 1995. doi: 10.1007/978-94-011-1278-9.

[127] S. Yang *et al.*, "Introduction to mesh based generated lumped parameter models for electromagnetic problems," *CES Transactions on Electrical Machines and Systems*, vol. 5, no. 2, pp. 152–162, Jun. 2021, doi: 10.30941/CESTEMS.2021.00019.

[128] H. W. Derbas, J. M. Williams, A. C. Koenig, and S. D. Pekarek, "A Comparison of Nodal- and Mesh-Based Magnetic Equivalent Circuit Models," *IEEE Transactions on Energy Conversion*, vol. 24, no. 2, pp. 388–396, Jun. 2009, doi: 10.1109/TEC.2008.2002037.

[129] S. Asfirane *et al.*, "Scalar Magnetic Potential Interpolation for Non-Conformal Meshing in Mesh-Based Generated Reluctance Networks," *IEEE Trans Magn*, vol. 55, no. 7, pp. 1–8, Jul. 2019, doi: 10.1109/TMAG.2019.2899820.

[130] M. Amrhein and P. T. Krein, "3-D Magnetic Equivalent Circuit Framework for Modeling Electromechanical Devices," *IEEE Transactions on Energy Conversion*, vol. 24, no. 2, pp. 397–405, Jun. 2009, doi: 10.1109/TEC.2009.2016134.

[131] K. J. Meessen, J. J. H. Paulides, and E. A. Lomonova, "Force Calculations in 3-D Cylindrical Structures Using Fourier Analysis and the Maxwell Stress Tensor," *IEEE Trans Magn*, vol. 49, no. 1, pp. 536–545, Jan. 2013, doi: 10.1109/TMAG.2012.2206821.

[132] M. Marinescu and N. Marinescu, "Numerical computation of torques in permanent magnet motors by Maxwell stresses and energy method," *IEEE Trans Magn*, vol. 24, no. 1, pp. 463–466, 1988, doi: 10.1109/20.43957.

[133] D. J. Griffiths, *Introduction to Electrodynamics*. Cambridge University Press, 2017. doi: 10.1017/9781108333511.

[134] K. Reichert, H. Freundl, and W. Vogt, "The calculation of forces and torques within numerical magnetic field calculation methods," in *Compumag*, 1976, pp. 64–73.

[135] É. Walter, *Numerical Methods and Optimization*. Cham: Springer International Publishing, 2014. doi: 10.1007/978-3-319-07671-3.

[136] W. H. Press, S. A. Teukolsky, W. T. Vetterling, and B. P. Flannery, *Numerical Recipes in C (2nd Ed.): The Art of Scientific Computing*. USA: Cambridge University Press, 1992.

[137] C. T. Kelley, *Solving Nonlinear Equations with Newton's Method*. Society for Industrial and Applied Mathematics, 2003. [Online]. Available: https://books.google.fr/books?id=MpgVAuR4wJkC

[138] J. E. Dennis and R. B. Schnabel, *Numerical Methods for Unconstrained Optimization and Nonlinear Equations*. Society for Industrial and Applied Mathematics, 1987. [Online]. Available: https://books.google.is/books?id=9dIXzQEACAAJ

[139] S. Gerber and R.-J. Wang, "Analysis of the end-effects in magnetic gears and magnetically geared machines," in *2014 International Conference on Electrical Machines (ICEM)*, Sep. 2014, pp. 396–402. doi: 10.1109/ICELMACH.2014.6960211.

[140] X. Li, S. Liu, Y. Wang, and Y. Fan, "Investigation of the flux leakage effects in transverse-flux magnetic gear," in *2017 20th International Conference on Electrical Machines and Systems (ICEMS)*, Aug. 2017, pp. 1–5. doi: 10.1109/ICEMS.2017.8056382.

[141] J. R. Gilbert, C. Moler, and R. Schreiber, "Sparse Matrices in MATLAB: Design and Implementation," *SIAM Journal on Matrix Analysis and Applications*, vol. 13, no. 1, pp. 333–356, Jan. 1992, doi: 10.1137/0613024.

[142] J. Azzouzi, G. Barakat, and B. Dakyo, "Quasi-3-D Analytical Modeling of the Magnetic Field of an Axial Flux Permanent-Magnet Synchronous Machine," *IEEE Transactions on Energy Conversion*, vol. 20, no. 4, pp. 746–752, Dec. 2005, doi: 10.1109/TEC.2005.845538.

[143] H. Tiegna, Y. Amara, and G. Barakat, "A New Quasi-3-D Analytical Model of Axial Flux Permanent Magnet Machines," *IEEE Trans Magn*, vol. 50, no. 2, pp. 817–820, Feb. 2014, doi: 10.1109/TMAG.2013.2285739.

[144] ADEME, "Vers un mix électrique 100% renouvelable en 2050," 2015.

[145] "AQUARET." https://aquaret.com/indexea3d.html?option=com_content&view=article&id=203&Itemid=344&lang=en (accessed Sep. 22, 2022).

[146] S. E. ben Elghali, M. E. H. Benbouzid, and J. F. Charpentier, "Marine Tidal Current Electric Power Generation Technology: State of the Art and Current Status," in *2007 IEEE International Electric Machines & Drives Conference*, May 2007, pp. 1407–1412. doi: 10.1109/IEMDC.2007.383635.

[147] I. G. Bryden and S. J. Couch, "ME1—marine energy extraction: tidal resource analysis," *Renew Energy*, vol. 31, no. 2, pp. 133–139, Feb. 2006, doi: 10.1016/j.renene.2005.08.012.

[148] "Free Flow Turbine Verdant."

[149] "SIMEC Atlantis Energy." https://simecatlantis.com/tidal-stream/

[150] "GCK Turbine." https://www.northeastern.edu/cri/spinouts/gck-technology-inc/ (accessed Sep. 23, 2022).

[151] "ENERMAR Project." https://tethys.pnnl.gov/project-sites/enermar-project (accessed Sep. 23, 2022).

[152] "Stingray." https://tethys.pnnl.gov/sites/default/files/publications/Stingray_Tidal_Stream_Energy_Device.pdf (accessed Sep. 23, 2022).

[153] "Wave Clients." https://www.emec.org.uk/about-us/wave-clients/ (accessed Sep. 23, 2022).

[154] G. A. Aggidis and C. J. Taylor, "Overview of wave energy converter devices and the development of a new multi-axis laboratory prototype," *IFAC-PapersOnLine*, vol. 50, no. 1, pp. 15651–15656, Jul. 2017, doi: 10.1016/j.ifacol.2017.08.2391.

[155] B. Multon, *Marine Renewable Energy Handbook*. Wiley, 2013. [Online]. Available: https://books.google.fr/books?id=yv6cYlKjk5cC

[156] *Tidal Energy Systems*. Elsevier, 2019. doi: 10.1016/C2017-0-02279-6.

[157] Zhaoqiang Zhang, A. Matveev, S. Ovrebo, R. Nilssen, and A. Nysveen, "State of the art in generator technology for offshore wind energy conversion systems," in *2011 IEEE*

International Electric Machines & Drives Conference (IEMDC), May 2011, pp. 1131–1136. doi: 10.1109/IEMDC.2011.5994760.

[158] H. Polinder, F. F. A. van der Pijl, G.-J. de Vilder, and P. J. Tavner, "Comparison of Direct-Drive and Geared Generator Concepts for Wind Turbines," *IEEE Transactions on Energy Conversion*, vol. 21, no. 3, pp. 725–733, Sep. 2006, doi: 10.1109/TEC.2006.875476.

[159] H. Tiegna, Y. Amara, G. Barakat, and B. Dakyo, "Overview of high power wind turbine generators," in *2012 International Conference on Renewable Energy Research and Applications (ICRERA)*, Nov. 2012, pp. 1–6. doi: 10.1109/ICRERA.2012.6477341.

[160] F. Rasmussen, J.-C. Grivel, M. H. Faber, N. Mijatovic, and A. B. Abrahamsen, "Emerging wind energy technologies," in *DTU International Energy Report 2014*, H. Hvidtfeldt Larsen and L. Sønderberg Petersen, Eds. Technical University of Denmark, 2014, pp. 52–62.

[161] O. Keysan, "Future Electrical Generator Technologies for Offshore Wind Turbines," *Engineering & Technology Reference*, Jan. 2015, doi: 10.1049/etr.2014.0020.

[162] V. Yaramasu, B. Wu, P. C. Sen, S. Kouro, and M. Narimani, "High-power wind energy conversion systems: State-of-the-art and emerging technologies," *Proceedings of the IEEE*, vol. 103, no. 5, pp. 740–788, May 2015, doi: 10.1109/JPROC.2014.2378692.

[163] A. Bensalah, M. A. Benhamida, G. Barakat, and Y. Amara, "Large wind turbine generators: State-of-the-art review," in *2018 XIII International Conference on Electrical Machines (ICEM)*, Sep. 2018, pp. 2205–2211. doi: 10.1109/ICELMACH.2018.8507165.

[164] K. Rohrig *et al.*, "Powering the 21st century by wind energy—Options, facts, figures," *Appl Phys Rev*, vol. 6, no. 3, p. 031303, Sep. 2019, doi: 10.1063/1.5089877.

[165] "GWEC 2022." https://gwec.net/global-wind-report-2022/ (accessed Sep. 25, 2022).

[166] FTI Consulting, "Global Wind Market Update – Demand & Supply 2017: Part One – Supply Side Analysis," 2018.

[167] S. S. Gjerde and T. Undeland, "Power conversion system for transformer-less offshore wind turbine," in *Proceedings of the 2011 14th European Conference on Power Electronics and Applications*, 2011, pp. 1–10.

[168] European Wind Energy Association, *Wind Energy - The Facts, Earthscan*. 2009.

[169] "Haliade-X GE Renewable Energy ." https://www.ge.com/renewableenergy/wind-energy/offshore-wind/haliade-x-offshore-turbine

[170] "Vestas V236." https://www.vestas.com/en/products/offshore/V236-15MW/V236-15MW (accessed Sep. 25, 2022).

[171] "MySE 16.0-242." http://www.myse.com.cn/en/jtxw/info.aspx?itemid=825 (accessed Sep. 25, 2022).

[172] S. Pfaffel, S. Faulstich, and K. Rohrig, "Performance and Reliability of Wind Turbines: A Review," *Energies (Basel)*, vol. 10, no. 11, p. 1904, Nov. 2017, doi: 10.3390/en10111904.

[173] M. D. Reder, E. Gonzalez, and J. J. Melero, "Wind Turbine Failures - Tackling current Problems in Failure Data Analysis," *J Phys Conf Ser*, vol. 753, p. 072027, Sep. 2016, doi: 10.1088/1742-6596/753/7/072027.

[174] C. Kaidis, B. Uzunoglu, and F. Amoiralis, "Wind turbine reliability estimation for different assemblies and failure severity categories," *IET Renewable Power Generation*, vol. 9, no. 8, pp. 892–899, Nov. 2015, doi: 10.1049/iet-rpg.2015.0020.

[175] J. Carroll, A. McDonald, and D. McMillan, "Reliability Comparison of Wind Turbines With DFIG and PMG Drive Trains," *IEEE Transactions on Energy Conversion*, vol. 30, no. 2, pp. 663–670, Jun. 2015, doi: 10.1109/TEC.2014.2367243.

[176] K. Hart, A. McDonald, H. Polinder, E. Corr, and J. Carroll, *Improved cost of energy comparison of permanent magnet generators for large offshore wind turbines*. 2014.

[177] Bill Chun Piu Lau, Eden Wai Man Ma, and M. Pecht, "Review of offshore wind turbine failures and fault prognostic methods," in *Proceedings of the IEEE 2012 Prognostics and System Health Management Conference (PHM-2012 Beijing)*, May 2012, pp. 1–5. doi: 10.1109/PHM.2012.6228954.

[178] "Wind Europe." https://windeurope.org/about-wind/history/ (accessed Sep. 25, 2022).

[179] "RELIAWIND." https://cordis.europa.eu/project/id/212966/reporting (accessed Sep. 25, 2022).

[180] J. Carroll, A. McDonald, and D. McMillan, "Failure rate, repair time and unscheduled O&M cost analysis of offshore wind turbines," *Wind Energy*, vol. 19, no. 6, pp. 1107–1119, Jun. 2016, doi: 10.1002/we.1887.

[181] C. Dao, B. Kazemtabrizi, and C. Crabtree, "Wind turbine reliability data review and impacts on levelised cost of energy," *Wind Energy*, vol. 22, no. 12, pp. 1848–1871, Dec. 2019, doi: 10.1002/we.2404.

[182] B. Hahn *et al.*, "Recommended practices for wind farm data collection and reliability assessment for O&M optimization," *Energy Procedia*, vol. 137, pp. 358–365, Oct. 2017, doi: 10.1016/j.egypro.2017.10.360.

[183] C. Zhu and Y. Li, "Reliability Analysis of Wind Turbines," in *Stability Control and Reliable Performance of Wind Turbines*, InTech, 2018. doi: 10.5772/intechopen.74859.

[184] J. Carroll, A. McDonald, I. Dinwoodie, D. McMillan, M. Revie, and I. Lazakis, "Availability, operation and maintenance costs of offshore wind turbines with different drive train configurations," *Wind Energy*, vol. 20, no. 2, pp. 361–378, Feb. 2017, doi: 10.1002/we.2011.

[185] Md. R. Islam, Y. Guo, and J. Zhu, "A review of offshore wind turbine nacelle: Technical challenges, and research and developmental trends," *Renewable and Sustainable Energy Reviews*, vol. 33, pp. 161–176, May 2014, doi: 10.1016/j.rser.2014.01.085.

[186] X. Song *et al.*, "Designing and Basic Experimental Validation of the World's First MW-Class Direct-Drive Superconducting Wind Turbine Generator," *IEEE Transactions on Energy Conversion*, vol. 34, no. 4, pp. 2218–2225, Dec. 2019, doi: 10.1109/TEC.2019.2927307.

[187] R. Scott Semken *et al.*, "Direct-drive permanent magnet generators for high-power wind turbines: benefits and limiting factors," *IET Renewable Power Generation*, vol. 6, no. 1, p. 1, 2012, doi: 10.1049/iet-rpg.2010.0191.

[188] G. Shrestha, H. Polinder, and J. A. Ferreira, "Scaling laws for direct drive generators in wind turbines," in *2009 IEEE International Electric Machines and Drives Conference*, May 2009, pp. 797–803. doi: 10.1109/IEMDC.2009.5075295.

[189] A. S. McDonald, "Hybrid excitation of synchronous generators for wind turbines," in *2nd IET Renewable Power Generation Conference (RPG 2013)*, 2013, pp. 3.55-3.55. doi: 10.1049/cp.2013.1861.

[190] "ROMEO ." https://www.romeoproject.eu/ (accessed Sep. 26, 2022).

[191] M. Tsili and S. Papathanassiou, "A review of grid code technical requirements for wind farms," *IET Renewable Power Generation*, vol. 3, no. 3, p. 308, 2009, doi: 10.1049/iet-rpg.2008.0070.

[192] A. Oshnoei, R. Khezri, S. Muyeen, and F. Blaabjerg, "On the Contribution of Wind Farms in Automatic Generation Control: Review and New Control Approach," *Applied Sciences*, vol. 8, no. 10, p. 1848, Oct. 2018, doi: 10.3390/app8101848.

[193] N. W. Frank and H. A. Toliyat, "Gearing ratios of a magnetic gear for wind turbines," in *2009 IEEE International Electric Machines and Drives Conference*, May 2009, pp. 1224–1230. doi: 10.1109/IEMDC.2009.5075359.

[194] B. McGilton, M. Mueller, and A. McDonald, "Review of Magnetic Gear Technologies and their Applications in Marine Energy," in *5th IET International Conference on Renewable Power Generation (RPG) 2016*, 2016, pp. 14 (6 .)-14 (6 .). doi: 10.1049/cp.2016.0535.

[195] O. Keysan, A. McDonald, and M. Mueller, "Aquamarine power oyster - C-GEN rotary machine design," 2009.

[196] L. Shah, A. Cruden, and B. W. Williams, "A Magnetic Gear Box for application with a Contra-rotating Tidal Turbine," in *2007 7th International Conference on Power Electronics and Drive Systems*, Nov. 2007, pp. 989–993. doi: 10.1109/PEDS.2007.4487824.

[197] H. Baninajar, S. Modaresahmadi, H. Y. Wong, J. Z. Bird, W. Williams, and B. Dechant, "Designing a Halbach Rotor Magnetic Gear for a Marine Hydrokinetic Generator," *IEEE Trans Ind Appl*, pp. 1–11, 2022, doi: 10.1109/TIA.2022.3180705.

[198] H. Baninajar, J. Z. Bird, S. Modaresahmadi, and W. Williams, "Electromagnetic and Mechanical Design of a Hermetically Sealed Magnetic Gear for a Marine Hydrokinetic Generator," in *2018 IEEE Energy Conversion Congress and Exposition (ECCE)*, Sep. 2018, pp. 4987–4993. doi: 10.1109/ECCE.2018.8557386.

[199] M. Johnson, M. C. Gardner, H. A. Toliyat, S. Englebretson, W. Ouyang, and C. Tschida, "Design, Construction, and Analysis of a Large-Scale Inner Stator Radial Flux Magnetically Geared Generator for Wave Energy Conversion," *IEEE Trans Ind Appl*, vol. 54, no. 4, pp. 3305–3314, Jul. 2018, doi: 10.1109/TIA.2018.2828383.

[200] B.-E.-B. Bidouche, T. Lubin, and S. Mezani, "Transient performance of a magnetically geared induction machine," *COMPEL - The international journal for computation and mathematics in electrical and electronic engineering*, vol. 39, no. 5, pp. 1113–1130, Jul. 2020, doi: 10.1108/COMPEL-12-2019-0485.

[201] B.-E.-B. Bidouche, "Étude et réalisation d'une machine asynchrone basse vitesse à réducteur magnétique intégré," Université de Lorraine, 2019. [Online]. Available: https://hal.univ-lorraine.fr/tel-02552469

[202] R.-S. Dragan, R. Barrett, S. Calverley, J. Moreu, and K. Atallah, "Pseudo-Direct-Drive Electrical Machine for a Floating Marine Turbine," *IEEE Trans Magn*, vol. 58, no. 2, pp. 1–5, Feb. 2022, doi: 10.1109/TMAG.2021.3075904.

[203] R.-J. Wang, L. Bronn, S. Gerber, and P. M. Tlali, "Design and evaluation of a disc-type magnetically geared PM wind generator," in *4th International Conference on Power Engineering,*

Energy and Electrical Drives, May 2013, pp. 1259–1264. doi: 10.1109/PowerEng.2013.6635793.

[204] W. Li, K. T. Chau, and J. Z. Jiang, "Application of Linear Magnetic Gears for Pseudo-Direct-Drive Oceanic Wave Energy Harvesting," *IEEE Trans Magn*, vol. 47, no. 10, pp. 2624–2627, Oct. 2011, doi: 10.1109/TMAG.2011.2146233.

[205] W. Li, K. T. Chau, C. H. T. Lee, T. W. Ching, M. Chen, and J. Z. Jiang, "A new linear magnetic gear with adjustable gear ratios and its application for direct-drive wave energy extraction," *Renew Energy*, vol. 105, pp. 199–208, May 2017, doi: 10.1016/j.renene.2016.12.026.

[206] S. Pakdelian, Y. Deshpande, and H. A. Toliyat, "An electric machine integrated with trans-rotary magnetic gear," in *2012 IEEE Energy Conversion Congress and Exposition (ECCE)*, Sep. 2012, pp. 3356–3362. doi: 10.1109/ECCE.2012.6342332.

[207] S. Pakdelian and H. A. Toliyat, "Trans-Rotary Magnetic Gear for Wave Energy applicaion," in *2012 IEEE Power and Energy Society General Meeting*, Jul. 2012, pp. 1–4. doi: 10.1109/PESGM.2012.6345582.

[208] R. K. Holm, N. I. Berg, M. Walkusch, P. O. Rasmussen, and R. H. Hansen, "Design of a magnetic lead screw for wave energy conversion," in *2012 XXth International Conference on Electrical Machines*, Sep. 2012, pp. 618–626. doi: 10.1109/ICElMach.2012.6349934.

[209] S. Pakdelian and H. A. Toliyat, "Dynamic modeling of the trans-rotary magnetic gear for the point-absorbing wave energy conversion systems," in *2014 IEEE Energy Conversion Congress and Exposition (ECCE)*, Sep. 2014, pp. 3163–3170. doi: 10.1109/ECCE.2014.6953830.

[210] N. W. Frank and H. A. Toliyat, "Gearing ratios of a magnetic gear for marine applications," in *2009 IEEE Electric Ship Technologies Symposium*, Apr. 2009, pp. 477–481. doi: 10.1109/ESTS.2009.4906554.

[211] S. Eriksson, "Design of Permanent-Magnet Linear Generators with Constant-Torque-Angle Control for Wave Power," *Energies (Basel)*, vol. 12, no. 7, p. 1312, Apr. 2019, doi: 10.3390/en12071312.

[212] Haiwei Lu, Jianguo Zhu, and Youguang Guo, "A tubular linear motor for micro robotic applications," in *IEEE International Conference on Mechatronics, 2005. ICM '05.*, pp. 596–601. doi: 10.1109/ICMECH.2005.1529326.

[213] L. Szabo, C. Oprea, I.-A. Viorel, and K. A. Biro, "Novel Permanent Magnet Tubular Linear Generator for Wave Energy Converters," in *2007 IEEE International Electric Machines & Drives Conference*, May 2007, pp. 983–987. doi: 10.1109/IEMDC.2007.382809.

[214] J. Wang and W. Wang, "Testing and experimental characterization of a linear permanent magnet actuator for active vehicle suspension," in *2011 International Conference on Electrical Machines and Systems*, Aug. 2011, pp. 1–7. doi: 10.1109/ICEMS.2011.6073386.

[215] N. Bianchi, S. Bolognani, D. Dalla Corte, and F. Tonel, "Tubular linear permanent magnet motors: an overall comparison," *IEEE Trans Ind Appl*, vol. 39, no. 2, pp. 466–475, Mar. 2003, doi: 10.1109/TIA.2003.809444.

[216] B. L. J. Gysen, K. J. Meessen, J. J. H. Paulides, and E. A. Lomonova, "3-D Analytical and Numerical Modeling of Tubular Actuators With Skewed Permanent Magnets," *IEEE Trans Magn*, vol. 47, no. 9, pp. 2200–2212, Sep. 2011, doi: 10.1109/TMAG.2011.2139220.

[217] M. Kleijer, L. A. J. Friedrich, B. L. J. Gysen, and E. A. Lomonova, "Dynamic Analysis of a Tubular Generator for Automotive Suspension Applications," in *2019 12th International Symposium on Linear Drives for Industry Applications (LDIA)*, Jul. 2019, pp. 1–5. doi: 10.1109/LDIA.2019.8771025.

[218] L. A. J. Friedrich, J. J. H. Paulides, and E. A. Lomonova, "Modeling and Optimization of a Tubular Generator for Vibration Energy Harvesting Application," *IEEE Trans Magn*, vol. 53, no. 11, pp. 1–4, Nov. 2017, doi: 10.1109/TMAG.2017.2710232.

[219] D. Sarr Lo, H. Lawali Ali, Y. Amara, G. Barakat, and F. Chabour, "3D Finite Element Analysis of Eccentricity in a Tubular Linear Permanent Magnet Machine," in *2018 XIII International Conference on Electrical Machines (ICEM)*, Sep. 2018, pp. 1996–2001. doi: 10.1109/ICELMACH.2018.8507202.

[220] F. Marignetti, P. Cancelliere, and M. Scarano, "Analytical formulation of the no-load magnetic field in IPM tubular machines with translator eccentricity," in *IECON 2006 - 32nd Annual Conference on IEEE Industrial Electronics*, Nov. 2006, pp. 829–835. doi: 10.1109/IECON.2006.347268.

[221] L. Cappelli, Y. Coia, F. Marignetti, and Z. Q. Zhu, "Analysis of Eccentricity in Permanent-Magnet Tubular Machines," *IEEE Transactions on Industrial Electronics*, vol. 61, no. 5, pp. 2208–2216, May 2014, doi: 10.1109/TIE.2013.2271598.

[222] Y. Li, Q. Lu, Z. Q. Zhu, D. Wu, and G. Li, "Superposition Method for Cogging Torque Prediction in Permanent Magnet Machines With Rotor Eccentricity," *IEEE Trans Magn*, vol. 52, no. 6, pp. 1–10, Jun. 2016, doi: 10.1109/TMAG.2016.2533361.

[223] S. T. Boroujeni, N. Takorabet, and S. Mezani, "Dynamic Simulation of Unbalanced Magnetic Force in Induction Machines with Static Eccentricity," in *2020 International Conference on Electrical Machines (ICEM)*, Aug. 2020, pp. 151–156. doi: 10.1109/ICEM49940.2020.9271055.

Haidar DIAB

Contribution à l'étude des engrenages électromagnétiques pour les applications énergies renouvelables

Résumé

Les systèmes de conversion d'énergie pour les énergies renouvelables reposent sur des boîtes de vitesses mécaniques pour transmettre la puissance mécanique à la machine électrique à des vitesses plus élevées et pour éviter d'avoir de très gros générateurs. Le principal problème des engrenages mécaniques est leur faible fiabilité et la nécessité d'une lubrification et d'un entretien réguliers. Les engrenages magnétiques assurent la transmission de puissance entre deux ports grâce à l'interaction sans frottement des forces magnétiques. Certains avantages potentiels de l'utilisation d'engrenages magnétiques sont une maintenance réduite, une isolation possible entre les arbres d'entrée et de sortie et une protection inhérente contre les surcharges. Afin de couvrir l'ensemble des objectifs définis, le travail a été divisé en quatre chapitres. L'aperçu de la littérature du premier chapitre a montré que des engrenages magnétiques remarquablement performants ont été développés. Dans le deuxième chapitre, des modèles de circuits équivalents magnétiques efficaces en calcul 3D et quasi-3D qui pourraient prendre en compte la saturation magnétique et les effets de bord ont été présentés. Il a été constaté que ces méthodes pouvaient réaliser un gain de temps important par rapport à la méthode des éléments finis, mais avec une légère réduction de la précision. Le troisième chapitre comprenait un aperçu des systèmes d'énergie marine renouvelable et des applications des engrenages magnétiques dans ce domaine, puis une étude d'optimisation a été réalisée pour proposer une conception d'engrenage magnétique qui pourrait convenir aux applications des énergies marines renouvelables. Le quatrième chapitre a présenté une étude et une analyse sur le défaut d'excentricité qui pourrait se produire dans les machines linéaires tubulaires, où un modèle de méthode d'éléments finis 3D a d'abord été utilisé, puis pour réduire le temps de calcul un élément fini quasi-3D outil méthodologique a été développé.

Mots clés: Engrenages magnétiques, modélisation électromagnétique, circuit magnétique équivalent, méthode des éléments finis, énergies marines renouvelables, machines linéaires tubulaires.

Résumé en anglais

Energy conversion systems for renewable energy rely on mechanical gearboxes to transmit mechanical power to the electrical machine at higher speeds and to avoid having very large generators. The main issue with mechanical gears is their low reliability and requirement for regular lubrication and maintenance. Magnetic gears perform power transmission between two ports through the frictionless interaction of magnetic forces. Some potential advantages of using magnetic gears are reduced maintenance, possible isolation between input and output shafts, and inherent overload protection. To cover all the objectives defined, the work was divided into four chapters. The literature overview of the first chapter has shown that remarkably high-performance magnetic gears were developed. In the second chapter, 3D and quasi-3D computationally efficient magnetic equivalent circuit models that could consider the magnetic saturation and the end-effects were presented. It was found that these methods could achieve an important time gain against the finite element method, albeit with a slight reduction in the accuracy. The third chapter included an overview of the marine renewable energy systems and the magnetic gear applications in this field, and then an optimization study was done to propose a magnetic gear design that could be suitable for marine renewable energy applications. The fourth chapter presented a study and analysis on the eccentricity defect that could occur in tubular linear machines and magnetic gears, where a 3D finite element method model was used in the analysis first, and then to reduce the computation time a quasi-3D finite element method tool was developed.

Keywords: Magnetic gears, electromagnetic modeling, magnetic equivalent circuit, finite element method, marine renewable energy, tubular linear machines.